Virginia Commonwealth University

VCU Scholars Compass

2022

Innovative Techniques of Neuromodulation and Neuromodeling Based on Focal Non-Invasive Transcranial Magnetic Stimulation for Neurological Disorders

Ivan C. Carmona-Tortolero
Virginia Commonwealth University

Follow this and additional works at: https://scholarscompass.vcu.edu/etd

Part of the Bioelectrical and Neuroengineering Commons

Downloaded from

https://scholarscompass.vcu.edu/etd/7073

Innovative Techniques of Neuromodulation and Neuromodeling Based on Focal Non-Invasive Transcranial Magnetic Stimulation for Neurological Disorders

A dissertation submitted in partial fulfillment of the requirements for the degree of Doctor of Philosophy in Mechanical and Nuclear Engineering

by

Ivan C. Carmona Tortolero, M.Sc.

Advisor: Dr. Ravi L. Hadimani

Associate Professor

Department of Mechanical and Nuclear Engineering

College of Engineering

Virginia Commonwealth University

Richmond, Virginia 23284

July 2022

1. Acknowledgments

I would like to start these few words by saying that completing this Ph.D. program is probably the most challenging, fruitful, and satisfactory professional achievement that I have ever had the opportunity to experience in my professional life. None of that would have been possible without the invaluable help and meaningful contribution of many people and institutions that I want to take the time to thank, one by one, as they deserve.

To the Virginia Commonwealth University, the institution that believed in me, and recognized the professional value of my background to bring me the opportunity to belong to an undoubtedly privileged staff of research. These people are currently making history positioning the institution as one of the most recognized emerging leaders national wide in fields of research such as biomedical engineering and biomedical applications, and I could not feel more proud to be a part of such an important moment. Thanks to all the staff, faculty members, service personnel, students, alumni, and sponsors who made part of my life during these years doing research here in Richmond.

To the Department of Mechanical and Nuclear Engineering. During my years in the department, I always felt at home. The tremendously collaborative environment we breathe among us, and the willingness to support every member on what he/she/they may need to have a satisfactory job performance has allowed me to work in the most pleasant manner possible. You all have a part in this. During these years I can say nothing was missing for me to do my job, and I did it happy among you all. Special thanks to Dr. Gary Tepper, Dr. Karla Mossi, and Mrs. Denisse Ivey for all the support uncountable times in which I received your best willingness.

To IEEE R3, IEEE Richmond Section, and the IEEE Magnetics and Engineering in Medicine and Biology Societies Joint Chapter. All the support provided by this network was of very important and meaningful help to my development as a professional during these years.

To my professors, who demonstrated to me once and again that knowledge is infinite and that passion for learning is a constant flame that we keep on every day in academia.

To my coauthors, who contributed to this work with their valuable insights, recommendations, comments, and guidance. Without their help, the success of this work would not have been possible. Infinite thanks for your dedicated time and patience during these years.

To my colleagues in the field, from whom I have learned so much during these years. This includes all the reviewers I have had (even those who were not so kind), who contributed to my training as a Ph.D. student, helping to improve each published paper.

To my collaborators, who have been part of the executing arm of this work. This includes my external collaborator from outside the Biomagnetics Laboratory and lab coworkers inside. Special thanks to Dr. Deepak Kumbhare, for his dedicated contribution to my work through his feedback and technical discussions, and George Weistroffer for his continuous support during the experimental stage of my work. Thank you also to Shawn DiRocco for your kind collaboration during my experimental work at the VA Medical Center.

To my advisor, Dr. Ravi Hadimani, for his continued guidance and support. I always felt the greatest independence in the laboratory to propose new methods and lines of research, as well as great respect for my previous knowledge in other subfields as a source of possible contributions to the purpose of the laboratory. My most sincere words of gratitude to you and your invaluable contribution to my career.

To my colleagues in the laboratory who helped me along the way throughout this doctoral work with their direct participation or their emotional support. Special thanks to my personal friend Hamza Magsood, who showed me all that I needed to learn to become a Ph.D. student and who gave me significant personal support in difficult times throughout these years. Also, thanks to Mohannad Tashli,

another of my valuable friends in the lab, whose friendship during this last year has been of major importance during probably the most critical stage of my doctoral work.

To my friends in Richmond, who made my life easier and happier, and who gave me the emotional support that somehow compensates for the absence of my family. Special thanks to my friends Johane, Zindia, Santiago, Diana, and their new blessings Zia and Mateo. Thank you, guys,

To my family (mom, dad, and brother), who despite the distance, have been always present, supporting me and celebrating every achievement. I dedicate every success to you all. I would like to also thank my parents-in-law and brother-in-law and sister-in-law, who have been also a part of this process and who have been every day there to also support me.

And finally, a very special thanks to Rocko, my doggy, and to my beloved wife, whose unconditional support has meant everything to me to be able to overcome difficult times. You have been always my inspiration and I dedicate this work in a very special manner to you.

Thank you all.

2. Contents

3. List of Figures

12

13

4. List of Tables

5. Abstract

In recent decades, neuromodulation has become one of the main techniques for neurologists and neuroscientists to investigate and bring effective treatment to several neurological conditions and psychiatric disorders. One of such conditions is Parkinson's disease (PD), whose mechanisms and symptoms are still a matter of extensive investigation nowadays. PD is characterized by the death of dopaminergic neurons in the *substantia nigra pars compacta (SNc)*, and the subsequent dopamine depletion in the dopaminergic pathways to the *striatum*. As a consequence, the firing rates, firing patterns, and synchrony of neurons in different subpopulations of the *basal ganglia-thalamocortical circuit* (BGTCC) are affected in time, leading to abnormal neural behaviors in the motor cortex in advanced stages of the disease. This constitutes what the scientific community currently understands as the main cause of PD symptoms. Nevertheless, the underlaying mechanisms that connect the lack of dopamine with the abnormal neural activity that produces such symptoms are not completely understood yet.

As a manner to find answers to questions related to mechanisms in PD, neuroscientists have been exploring different computational approaches. Most of these approaches are based on computational neural networks, a part of the artificial intelligence subdiscipline in charge to replicate the neural behavior of real biological systems for problem-solving. These types of networks are powerful at the time to compute complex systems. However, one of their main drawbacks is the level of abstraction between the computational level and the semantic level, making the system lose coherence for the user in his/her search for answers. For applications intending to find causes of phenomena within a system, this does not seem to be the best approach, since computational neural networks will tend to act as a "black box" between the inputs and the outputs.

Aiming to improve the existing resources to investigate PD, and the development of new treatments based on neuromodulation, this works introduces a new neuromodeling approach based on the oscillatory network of the basal ganglia thalamocortical circuit. The model developed in state space representation describes, for the first time to our knowledge, the progression of PD throughout the entire patient's timeline, based on average values of firing rates and firing patterns of healthy subjects and PD patients reported in the literature. This allowed us to study the oscillatory nature of the BGTCC and determine the regulatory role of what we believe is the natural response of the system to dopamine depletion in advanced PD states: burstiness.

Our model describes, from a mathematical point of view, the mechanisms that would explain abnormal neural activity in PD such as altered firing rates, increased synchrony, and raised burstiness. The model matched the parkinsonian conditions and allowed us to model the role of neuromodulation techniques such as *deep brain stimulation* (DBS) and *transcranial magnetic stimulation* (TMS) in PD treatments. It also permitted us to define the type of stimulation that would be required in one or more nuclei, by developing novel neurostimulation coefficients as parameters to be extracted from the model. The results are helping us to investigate new manners to treat PD that aim to novel non-invasive treatments based on the application of TMS.

In order to experimentally validate analytical models such as ours, as well as study other aspects related to PD, it was necessary to address different technical difficulties from the beginning of this work, concerning limitations with current neuromodulation technologies. One of such difficulties was how to accurately stimulate nuclei within the BGTCC with non-invasive TMS technology that can be focal enough to reach cortical and subcortical targets without significant overstimulation of the surroundings. This is currently a problem with the existing technology since TMS coils are not

designed for small animals. In addition, high stimulation currents make it difficult to reduce the coil sizes to make them more focal as it is required.

Transcranial magnetic stimulation (TMS) is a popular non-invasive neuromodulation technique with proven efficacy in the treatment of other conditions such as depression. At the Biomagnetics Laboratory, Virginia Commonwealth University, we study the current technologies behind TMS, and how to improve the existing neuromodulation techniques to provide better non-invasive treatment to PD symptoms, as we investigate its evolution through novel neuromodeling techniques.

Based on the context so far provided of unknown mechanisms in PD, and the technical limitations in the development of novel treatments, the general aim of this dissertation is to develop alternative technology that improves the current range of application of TMS, on a scale that would permit defining specific non-invasive treatment for Parkinson's disease and other neurological disorders. This aim is accomplished through the completion of three specific objectives. 1) The design of a neurostimulation system that increases the focality in TMS to regions of narrow target areas and variable depths in the brain cortex. 2) The assessment of the feasibility of novel high-frequency neuromodulation techniques that would allow increasing the focality in deeper areas beyond the cortical surface, concerning the current TMS technology. 3) The development of a computational model of the motor pathway that allows studying the underlying mechanisms that originate PD symptoms, as well as evaluating the effects of TMS on cortical regions for the development of new treatments.

Throughout the document, the problem statement, hypothesis, rationale, and methodology are shown for each of the objectives, along with illustrative figures. The methodology shows the development of novel high-frequency neurostimulation equipment using analog modulations to shift the stimulation energy out of the commercial TMS frequency band and audible range, to exploit the advantages of operating at high frequency with reduced currents. This concept also allowed making

other developments concerning the increase of the focality in TMS coils. Hence, we develop an innovative *quintuple AISI 1010 carbon steel core coil* for highly focused TMS in small targets with a novel control mechanism of the E-field location based on the path of the highest current density. Similarly, we developed a new coil configuration called *figure-of-flower coil* with a central solenoid and multiple adjacent solenoids (petals). This coil is operated with our also novel *space-varying E-field vector modulation*, a neuromodulation technique conceived to vary the location of the stimulating hotspot dynamically and by electronic means.

The results successfully demonstrated the feasibility of using the novel high-frequency neuromodulation technique as an effective manner to reduce the necessary current in TMS coils. This reduction, which reached an order of magnitude of 100 times compared to commercial TMS technology, made it possible to reduce the coil sizes, making them more focal to targets (in the order of a few millimeters square).

Finally, we present the results of our innovative oscillatory model of the motor pathway, which allowed us to conclude that an internal regulatory mechanism that we believe neurons activate in advanced PD stages seems to be the pathological response of some neural subpopulation to the dopamine depletion, trying to compensate for the downstream effects in the system. We also found that such a mechanism seems to the burstiness in PD.

While we keep working toward the development of more and better technology for the modeling of neurological diseases, as well as the improvement of the existing non-invasive neuromodulation alternatives, we hope that the content of this work can have a significant contribution to the readers and the scientific community in the neuromodulation, neurostimulation and neuromodeling areas.

6. Introduction

Being one of the more promising stimulation techniques in the neuromodulation field, transcranial magnetic stimulation (TMS) has become an important matter of study for neuroscientists and bioengineers in the last few years. Its non-invasive characteristic, based on the external application of time-varying magnetic fields, makes TMS a suitable alternative to treat several neurological conditions and psychiatric disorders, versus other existing neurostimulation technologies –such as deep brain stimulation (DBS) – or the implementation of drug-based therapies.

TMS requires the variation in time of magnetic fields –generated by currents circulating through coils– to induce an electric field (E-field) in the brain tissue able to regulate the synaptic activity of neurons (Fig. 1). This E-field normally needs to reach a certain magnitude threshold to stimulate the neurons, with a referential value within the TMS area of around 100 V/m [1]–[8]. This value is the average required E-field in the *First Dorsal Interosseous (FDI)* region of the motor cortex to induce an involuntary thumb twitch in a human subject, and is considered as a reference of the required magnitude to stimulate most of the neurons in humans and other species.
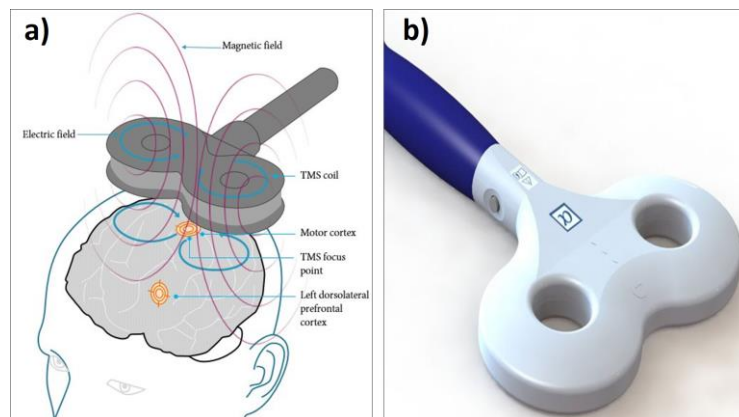
Figure 1 – a) Illustration of transcranial magnetic stimulation using a figure-of-eight coil. Notice how the magnetic field lines penetrate the different layers of the human head to induce an electric field of a circular shape whose intensity is higher toward the center. Source: [9]. b) Commercial figure-of-eight coil, model D70 Alpha Flat of the manufactured MAGSTIM, used in clinical settings [10].

The precision and effectiveness in the stimulation of intended areas during TMS depends on the ability of the coil to produce a focal E-field over a selected target in the brain tissue. In the last decades,

big efforts have been made to design coils able to increase the focality and reduce the size of the stimulated area [11]–[16] (Fig. 2). However, those efforts are limited when the target area is not located over the more superficial layers of the brain cortex, but in subsequent layers. Studies about the spatial distribution of the *E*-fields during TMS report that the relationship between the focality and the penetration depth in the brain tissue is a trade-off [15], [17]. For this reason, the stimulation of targets at bigger depths with the current technology will tend to produce non-focal *E*-field and, therefore, overstimulation of the surrounding tissues.
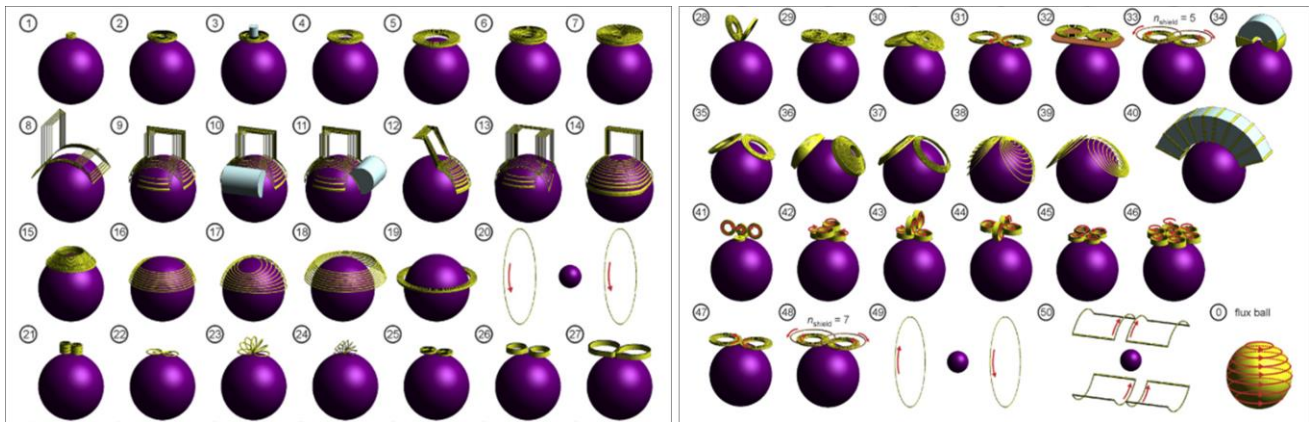
Figure 2 – Simulation of 50 TMS coils designed by different authors, made by Deng et al in [17]. This image illustrates the efforts made in the TMS field throughout the years to produce coils with better E-field patterns, since its appearance for the first time back in 1985.

Although the existence of numerous TMS coil designs so far, very few of these works have considered the use of ferromagnetic cores as an alternative to increase the focality in TMS coils, and reduce other technical requirements [18]–[20]. Moreover, the calculation or estimation of such focality with the current methodologies [11]–[14], [17], [21]–[24] does not allow to determine how well the stimulated area fits the target area, and how much of the surrounding tissue is overstimulated.

To address these identified gaps in the field, this work investigates the use of ferromagnetic materials as cores in TMS coils, and the implementation of new methods to estimate their focality, considering the precise stimulation of the target and the minimal overstimulation of unintended regions.

As part of the partial objectives of this work, we have applied this acquired knowledge to the development of a novel focal coil for the stimulation of small experimental animals (rats). This part of the research seeks to improve the existing technology for TMS in rodents, for which several coils have been proposed in the literature [24]–[28] (Fig. 3), with a current focality limit of around 1 cm^2.
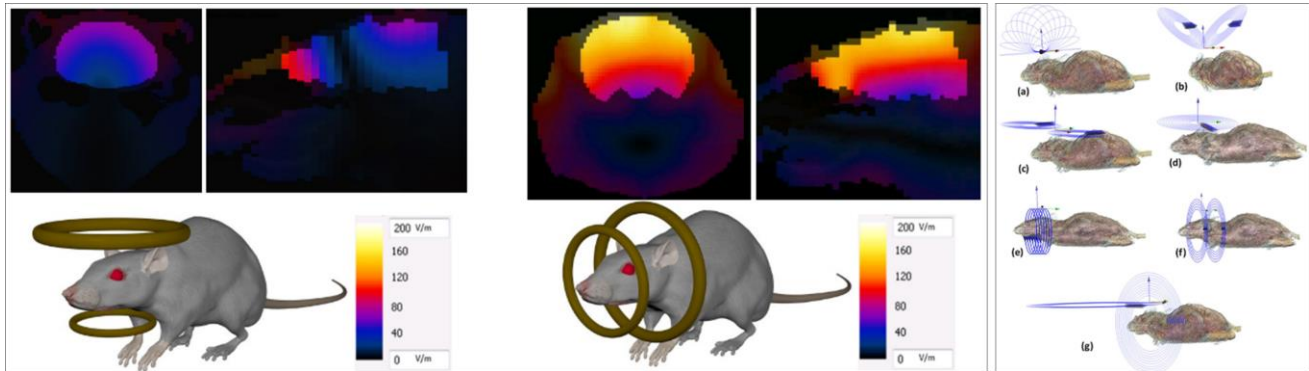
Figure 3 – Different animal coils presented by a) March et al in [24], [27] and b) Rastogi et al in [25]. Notice in a) how the distribution of the electric field is poorly focal, with overstimulation of a big part of the entire rat brain.

Our results in this particular topic will allow us to obtain the appropriate equipment for the focal stimulation of the rat brain, in areas as small as 1 mm^2. This constitutes a first step in obtaining focal stimulation of the motor cortex in rats, with an expected impact on the improvement of TMS technology for humans.

In addition to the discussed aspects concerning the coil design, current TMS technology is restricted by big hardware and power dissipation requirements in stimulators and coils, because of the high currents and voltages required to achieve the *E*-field magnitudes needed in the target (see Fig. 4). These restrictions, along with the uncomfortable sound from TMS coils exposed to magnetic fields in audible frequencies, have also focused the attention of this work on the feasibility of using high frequency for the development of novel techniques of neuromodulation and neurostimulation. The successful development of these techniques would not only allow the creation of a silent and low-power stimulation system, but it would also permit the focality and penetration depth to be increased, essentially through the size reduction of the coils, not possible with the existing technology.
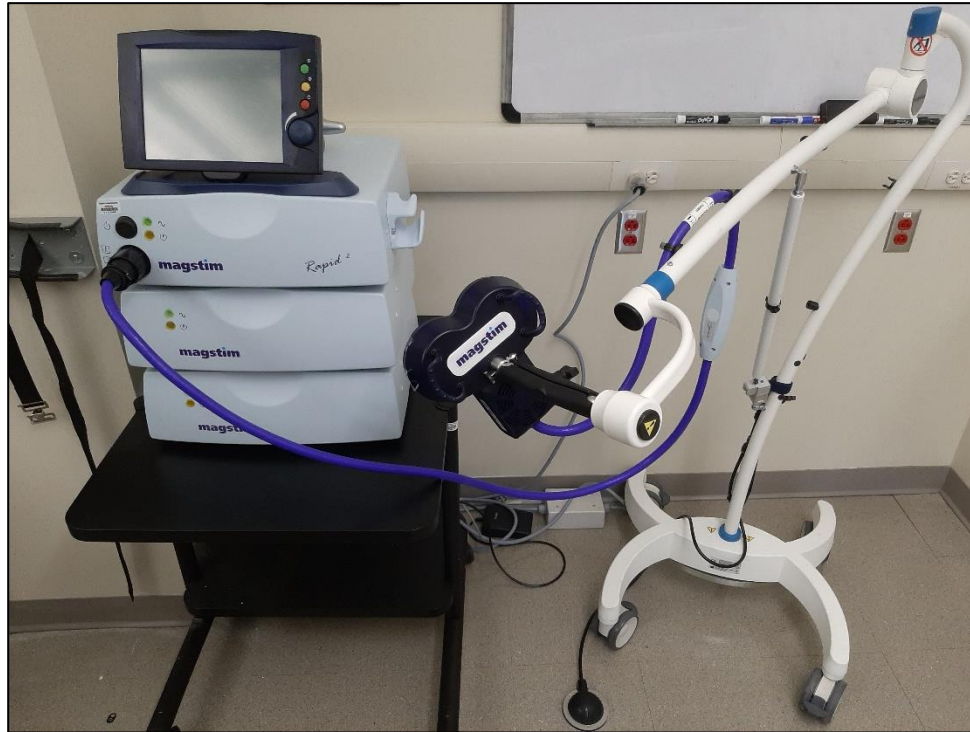
Figure 4 – Photograph of the commercial TMS stimulator, model *Rapid 2* of the manufacturer *MAGSTIM*, used for experimentation at the Biomagnetics Laboratory, Virginia Commonwealth University. Notice the figure-of-eight coil connected to it and the relatively big size of the stimulator. This size is a consequence of the power electronics and heat dissipation system required to manage currents in the order of several kilo-amps and voltages of serval hundreds of volts.

On the other hand, modern modeling techniques for neural networks are based on the modeling of thousands of individual neurons in a topology. This demands significant computational requirements and processing time to observe a convergence and a statistical behavior that is representative of what occurs in the network. In this work, we show the development and results of an innovative model of the motor pathways based on the oscillatory nature of the basal ganglia-thalamocortical circuit [Fig. 5] (neural network responsible for the motion of the musculoskeletal system), seeking to contribute to the understanding of Parkinson's disease (PD) in patients, and the role of the lack of dopamine in the development of the symptoms. This model also makes it possible to investigate novel TMS-based treatments for PD, based on the stimulation of cortical regions, as an alternative to the invasive, yet effective, deep brain stimulation (DBS).

The previously mentioned topics of research are compiled in this dissertation as an effort to develop innovative techniques for neuromodulation, neurostimulation, and neuromodeling for complex

neurological disorders, based on the use of TMS. The dissertation document contains the aim and objectives of the research; problem, hypothesis, rationale, and methodology for each objective; as well as the results and the planned work for the next stages (including experimental activities in real specimens).
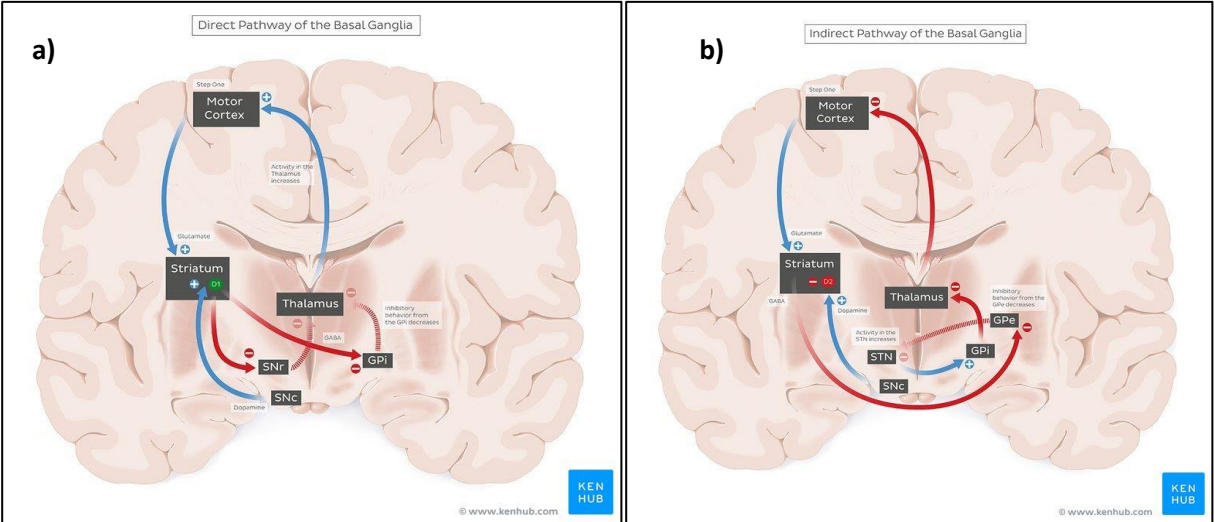
Figure 5 – Anatomical structure and functional connection of the direct (a) and indirect (b) pathways of the basal ganglia. These structures are normally represented through computational neural networks to investigate the relationship between different neural subpopulations (nuclei). Source: [29].

7. Aim and Objectives

General Aim

To develop alternative technology to improve the current range of application of TMS on a scale that would permit defining specific non-invasive treatment for Parkinson's disease, usable for other neurological conditions involving malfunction of sub-surface neurons in the brain cortex.

In this context, "**alternative technology**" refers to the <u>set of equipment, techniques, and methods</u> that would differ partially or totally from the ones currently used for TMS, both in research and clinical settings. This includes –but is not limited to– <u>neurostimulation equipment</u> (such as TMS coils and pulse-generators/stimulators); <u>neuromodulation techniques and parameters</u> (e.g. pulse amplitude, frequencies, and waveforms); <u>and neuromodeling methods</u> that would allow to better understand, predict, and assess the effects of the stimulation with this equipment.

Also in the context of this general aim, **"to improve the current range of application"** means <u>to enhance the up-to-date scope of TMS in terms of the set of brain regions focally achievable and effectively stimulable</u>. These regions are currently limited to very superficial targets in the cortex due to: a) a low focality of the existing commercial TMS-coils; b) a restricted penetration depth of the induced E-fields (because of the magnetic field spreading and safety limits); c) the very high power requirements to induce such fields with magnitudes able to stimulate relatively deep regions below the cortical surface.

Specific Objective # 1:

To develop a computational model of the motor pathway -based on the statistical characteristics and parameters of its different neural subpopulations- that allows hypothesizing the underlying mechanisms that originate the PD symptoms, as well as to evaluate the effects of neuromodulation techniques applied to different nuclei (particularly TMS over the cortex).

The basal ganglia's indirect and direct motor pathways (MP) constitute the neural network that commands the musculoskeletal system, responsible for the voluntary and involuntary motion in mammals. This is the exact network in which PD generates and develops, and where most of the PD symptoms have their origin [30]–[37].

The modern scientific literature shows a well-defined topology for what is understood up-to-date as the connections between the different nuclei (neuron subpopulations) of the motor pathway. Based on published works, significant knowledge about the firing rates, firing patterns and synchrony has been collected from PD patients, as well as from experimental animals with induced PD via the inactivation of the *nigrostriatal dopamine tract*. Other *in-vitro* studies have revealed intrinsic characteristics and values for different types of neurons within the MP nuclei, whose results are interesting for our computational approach [32], [38], [39].

It is well known that PD originates when the dopamine levels in the *substantia nigra pars compacta* (*SNc*) decrease in its connections to the striatum cells. However, though changes in firing rates, firing patterns, and synchrony are reported in PD patients compared to healthy subjects, the underlying mechanisms that explain these changes and relate them to PD symptoms are not well understood.

The above-explained argument has been the motivation for the development of a novel oscillatory approach (explained in the next section), that aims to characterize the system from a physical and mathematical point of view, using the described data. With the oscillatory model of the motor pathway, we will seek the following sub-objectives:

a) To hypothesize the underlying mechanism that directly connects low dopamine levels to PD symptoms.

b) To describe the effect of therapies based on Deep Brain Stimulation (DBS) within the basal ganglia, which alleviates PD symptoms in patients with an implanted DBS probe and an implantable pulse generator (IPG).

c) To predict the effects of novel experimental non-invasive therapies based on TMS over the motor cortex, substitutive of those based on DBS, to alleviate some of the PD symptoms.

Specific Objective # 2:

To assess the feasibility of developing novel high-frequency neuromodulation techniques – outside the typical TMS range– that allow increasing the focality in deeper areas beyond the cortical surface with respect to the current technology, reducing the power requirements for the stimulator and making the TMS therapy soundless for the comfort of the patients.

Current TMS technology is restricted to frequencies in which neurons have demonstrated to respond under electrical/electromagnetic stimulation, typically in a range from 0 to 2.5 kHz, sometimes up to 3kHz [40]–[42]. Under this assumption, both existing commercial equipment and experimental research developments seem to focus on this as the only range of frequencies physically usable to induce a neural response and obtain the subsequent regulation of the firing rhythms and patterns.

Using specific knowledge brought from the telecommunications and electronics sub-fields, we have enough evidence to believe that high-frequency analog modulation techniques would produce effective stimulation of the neurons (see next sections), even when the range of frequencies used to stimulate is out of the TMS band.

The positive verification of our inference –converted into a hypothesis in the next section- would complement the neurostimulation system to be designed for objective # 3, providing it with the possibility to significantly increase the range of penetration into the cerebral cortex, as well as into deep brain structures. In addition, it would have a very high impact on the current conception of neurostimulation devices, due to the significantly reduced power requirements.

Finally, the operation of this neuromodulation technique in frequencies above the audible range (typically up to 22 kHz) would turn this technology, not only noiseless but theoretically soundless. This would represent significant progress in the comfort of the patient, increasing the positive perception and acceptance of the TMS technologies in the future.

Specific Objective # 3:

To design a neurostimulation system that increases the focality in TMS to regions of narrow target areas and variable depths in the brain cortex. This technology should be conceived to be usable both in small experimental animals such as rats and in human subjects with appropriate modifications.

For this first objective, the neuromodulation system we will seek to develop will be composed of the set of equipment, methods, and specific knowledge applied to improve both the focality of the

induced E-field and the controllability of the penetration depth during TMS sessions. The objective includes:

a) Study of the phenomena and parameters involved in the focality and penetration depth of TMS coils, identifying key factors for their controllability.

b) Design of a highly focal TMS coil for small targets –around 1 mm^2– that allows precise stimulation of the primary and secondary motor cortex (M1 and M2 regions, respectively) in rats, with extensible usability to humans.

c) Development of the associated control mechanism(s) that will assure the controllability of the electric field in terms of the focality, penetration depth, and direction.

The successful accomplishment of this objective would enable neuroscientists to focally stimulate very specific locations within these two regions of the motor cortex in experimental animals (rats). That would allow observing the projections of the stimulated neurons deep into brain structures such as the basal ganglia. This information is critical for the study and better understanding of network where the Parkinson's disease (PD) originates, taking into consideration the anatomical similarities in neural circuits between rats and the human species.

On the other hand, with a better understanding of the connections between the deep brain structures of the motor pathway (basal ganglia and thalamus), and the motor cortex, the technology developed within this objective would also allow neurologists to define specific treatments to alleviate symptoms in PD patients such as tremors, muscular stiffness, and speech difficulties/impediment, among others.

8. Flowchart of Project

Scope of this work

Projects Objective #3
- Study of the tip sharpening and ferromagnetic materials as cores in TMS coils.
- Development of the Quintuple AISI Carbon Steel Core Coil (QCC)
- Study of the focality in coils and overstimulation of biological tissues
- Development of a novel spatial modulation technique of the *E*-field
- Experimental work with two coils at high frequency.

Outcomes:
- QCC Coil
- Oriented Control of the Path of Highest Current Density and E-field
- Novel methodology for the estimation of the focality in TMS
- Space-varying E-field Vector Modulation

Products:
- **AIP ADVANCES Jan 2021** — Quintuple AISI 1010 carbon steel core coil for highly focused transcranial magnetic stimulation in small animals
- **PATENT** — System and Method For Multi-Coil Steerable And Selectively Focused Transcranial Magnetic Stimulation
- **IEEE Transactions on Magnetics May 2021** — Estimation of the Focality of Coils and Quality of Stimulation of Biological Tissues During Transcranial Magnetic Stimulation
- **In-progress Publication (submitted)** — Space-varying E-field Vector Modulation with Oriented Control Using Multi-Core Figure of Flower Coil for TMS

Goals:
- Focality in areas as small as 1 mm²
- Controllability of the E-field
- Big penetration depth without reducing focality

Conclusions. Accomplishment of the specific objective #1

Projects Objective #2
- Conceptualization of the high-frequency neuromodulation technique
- MATLAB simulations of the high-frequency neuromodulation system
- Design and construction of the high-frequency neuromodulator
- Workbench experimentation and measurements over the high-frequency neurostimulator and coils.

Outcomes:
- High-frequency neuromodulation techniques
- High-frequency neuromodulator
- Animal experimentation with the high-frequency neurostimulator and coils

Products:
- **PATENT** — High Frequency Neuromodulation Methods and Equipment for Transcranial Magnetic Stimulation
- **In-progress Publication (In draft)** — High-frequency neuromodulator and power reduction Using Amplitude Modulation
- **In-progress Publication (In draft)** — Ultra Low-power, Soundless TMS Using High-frequency neuromodulation techniques

Goals:
- Reduced hardware requirements and power dissipation
- Soundless TMS comfortable for patients

Conclusions. Accomplishment of the specific objective #2

Projects Objective #1
- Conceptualization of the *Oscillatory Model of the Motor Pathway*
- MATLAB Simulations of the *Model*
- Simulations of DBS and TMS over the model

Outcomes:
- Stochastic model of the motor pathway
- Theory of the auto-regulation of the firing rates

Products:
- **In-progress Publication (Drafted)** — A Novel Modeling for Parkinson's Disease Based on the Oscillatory Nature of the Basal Ganglia Thalamocortical Circuit

Goals:
- Prediction of the PD evolution in time
- Theorization of the mechanisms that relate low dopamine to symptoms
- Prediction of the effects of TMS in the Motor Pathway

Conclusions. Accomplishment of the specific objective #3

← **Beginning**   **End** →

| Conceptual stage | Analysis and design stage | Experimental stage |

9. **Chapter I: A Novel Modeling of the Basal Ganglia-Thalamocortical Circuit for Parkinson's Disease**

9.1. Problem # 1:

The modeling of neural networks often referred to as *neuromodeling*, has become one of the more important instruments for neurologists and neuroscientists to study the complex connections between sub-regions of the brain to form functional circuits. In this type of technique, many are the variables of interest that can be monitored to observe evolution patterns in the progression of a neurological condition or psychiatric disorder, highlighting the firing rates, firing patterns, and synchrony of the neuron spikes.

To date, it is well known that *Parkinson's disease* (PD) arises as a consequence of the death of neurons in the *substantia nigra pars compacta* (SNc), and the resulting low levels of dopamine in the *nigrostriatal pathway*. However, the mechanisms that relate this lack of dopamine to symptoms, and that explain the pattern changes in different neuronal nuclei, are not fully understood.

On the other hand, the technologies behind most of the existing software for neuromodeling rely on complex simulations of neuronal populations. On them, every single neuron needs to be represented with a set of equations and parameters, which must be repeated as many times as it is required by the number of simulated neurons for each population. This normally represents a significantly high consumption of computational resources, including memory, processing capacity, storage, and computing time.

Previous attempts in the scientific community to simulate the Motor Pathway[1] (MP) have suggested interesting results when the firing rate in the subthalamic nucleus or some basal ganglia structures is forced to vary with rhythmic stimulating pulses [43]–[48]. This method simulates the role

---

[1] The *Motor Pathway*, alternatively called "*pyramidal tract*", is an association of neurons of different subpopulations in a neural circuit responsible for the movement in the musculoskeletal system. The network is mainly in charge of the transport of the neural impulses that control the motion, originated over the motor cortex in the forebrain, to the structures below the brain through the spinal cord.

that *Deep Brain Stimulation* (DBS) plays in the neuromodulation of the structures of the *basal ganglia[2]*, in the treatment of PD. Nevertheless, though the predictions of the changes in firing rates and synchrony are consistent with what is reported in the literature, for PD patients with the stimulator turned on and off, these models do not explain the reasons for these changes to occur, and the evolution of the disease in the patient's timeline.

A new oscillatory approach that considers the varying characteristic of the parameters involved in the modeling of the MP, would help neuroscientists to investigate the evolution of the PD in patients, defining indicators for the stage of the disease, as well as for early diagnosis.

When statistical parameters are required (such as the firing rate of a neuron population), we usually find restrictions in the amount and quality of information available from the scientific literature. These restrictions are given by the complexity of extracting real values from real PD patients or healthy subjects with *in-vivo* techniques, for which many times *in-vitro* results are useful. In this sense, a new approach is necessary with a flexibility that allows making use of both types of data, admitting boundary conditions for healthy subjects and PD patients to obtain a full representation of the evolution of the disease in the time domain.

In addition to the aforementioned, for the particular purpose of this work, the new neuromodeling approach should allow us to investigate the effects of novel TMS-based treatment applied in the motor cortex to alleviate PD symptoms. This non-invasive technique would be an alternative to the existing *deep brain stimulation (DBS)*, effective but invasive by nature.

---

[2]

9.2. Hypothesis # 1:

An oscillatory approach to modeling the motor pathway, based on statistical information of the neuron subpopulations that compound it, allows obtaining a detailed description of the evolution of Parkinson's disease in a patient's timeline, with predictions of both future stages of the disease and the effects of novel non-invasive TMS-based treatment to alleviate the symptoms.

9.3. Rationale # 1:

The new approach for the modeling of the motor pathway departs from the understanding of the relationship between the firing rates of the different subpopulations. Because any rhythmic phenomenon can be represented using an equivalent (or predominant) frequency of occurrence, the motor pathway can be represented as an oscillatory network formed by different nodes operating at different frequencies.

Taking into consideration the nature of a single neuron, described as a system with *multiple inputs* (dendrites) *and one single output* (axon), *MISO*, we can find ways to represent the outgoing firing rate (frequency) as a linear combination of those rates present in the inputs. The firing rates in the inputs, coming from neighbor regions, should then contribute to the output in the same ratios as the number of incoming synaptic connections represent over the total for one neuron. Now, assume that all the neurons of one population have similar characteristics and that they all can be grouped and referred to as a *subpopulation*. Then, we can say that the outgoing firing rate of a *subpopulation* can be expressed as a linear combination of the incoming firing rates from *neighbor subpopulations*, with coefficients equal to the average synaptic weights of the connections between each *neighbor subpopulation* and the *subpopulation under study*.

Departing from the representation previously explained, it is possible to obtain a system of equations that include all the subpopulations and firing rates in the motor pathway, and that can match average values for both healthy subjects and PD patients, as boundary conditions. These boundary conditions denote an evolution in time, the reason why a temporary representation is also required.

The *state-space representation* is an appropriate mathematical form to describe systems evolving in time. Nonetheless, one of the main characteristics of the *state space representation* is that the dependency on *time* as a variable is not explicit, but implicit. This means that the variable *time* will not appear in the system of equations, but is implicit in the evolution of the rest of the variables expressed as vectors. Meanwhile, some other explicit variables changing in time will act as the independent variable and will determine the change in the rest of the dependent variables of the system. Under this description, every instant in the timeline will describe the *state of the system*, with a set of values for the dependent variables organized in vectors, which will depend on the *state of the system* in the previous instant.

Because the change in the dopamine levels is the critical factor in the evolution of the PD in a patient, the use of this variable as the explicit independent variable in the *state space representation* modeling the motor pathway should allow finding the evolution of the firing rates for the rest of the *subpopulations*. Hence, the ratio between the number of active cells (alive or functionally active) to the total number of cells in the *substantia nigra pars compacta* (SNc) –to be called *Active Cell Ratio (ACR)* – will be the *independent state variable* of the model.

According to the previous description, the firing rates in the model for each subpopulation will depend on the specific ACR value in the SNc, the firing rates of their neighbors in the network topology at the previous instant, and the weights of the incoming synaptic connections. Then, if a curve is provided with the behavior of the ACR in the patient's lifetime (or a fraction of it), with the correct

modeling of the system <u>it is theoretically possible to inspect, or predict, the firing rates at any point in the patient's life, in the past, present or future</u>.

<u>A similar analysis can be made for the synchrony of the neurons</u>, taking into account that the ability of the neurons of a subpopulation to fire at different times is lost for some subpopulations in advanced stages of PD. Then, the synchrony should also have a relationship with the firing rates and the dopamine level, and such a relationship can be explored and theorized through the oscillatory model in state space.

Another frequent factor of interest in the study of PD is the set of possible firing patterns. In this regard, we believe that the firing patterns –among which the more relevant ones to mention are the *tonic* and the *bursty* patterns– are a consequence of the variation in time of the firing rate. Therefore, in the upcoming stages of this research, we will further investigate the possible causes of these changes, as well as the synchrony.

Finally, as one of the main goals, the model, should allow us to predict the effects that transcranial magnetic stimulation applied over the motor cortex would have on the patient, in different stages of the disease. This is possible by forcing the firing rate in the motor cortex to be at a certain level that should produce changes in the firing rates and patterns downstream in the topology, especially in the basal ganglia structures.

9.4. Methodology # 1:

9.4.1. General Context

Neural networks –also referred to as *neural circuits*– are sets of structural and functional connections established between neurons of diverse types from different regions in both the central and

peripheral nervous systems. In the human brain, each network is responsible for a particular group of biological functions regulated by the synaptic activity between neighbor neural subpopulations. In neurology of movement disorders, conditions such as Parkinson's disease (PD) and Dystonia require a deep understanding of the alterations of the neural activity of the motor circuits, including –but not limited to– physiological variables, activity patterns, progression of the disease, and underlying mechanisms behind the symptoms. This comprehension allows for the development of more and better treatments for such conditions, as well as the possibility of early diagnosis and evaluation of their evolution. However, the observation of neural activity is challenging because of the limitations of the current electrophysiology technologies. Some of these technologies are extremely inaccurate for the observation of neural activity at a cellular level, such as *electroencephalography* (EEG) or *magnetoencephalography* (MEG), while others are extremely invasive such as the case of *local field potential* (LFP). Even more, identifying an overall behavior in a neural circuit from the individual behavior and localized measurements by subpopulation is not an easy task, especially when the circuit changes in time as a consequence of the progression of the disease. These are the main reasons why explaining the underlying mechanisms that produce PD symptoms under conditions of low dopaminergic activity in the *basal ganglia* has been particularly complex so far with the existing approaches. These difficulties are valid –in a general manner– for circuits that involve cortical subpopulations, but especially for those including deep brain structures with limited physical access for signal capture and parameter extraction (e.g. the basal ganglia).

For many years, Parkinson's disease (PD) has captured the attention of the scientific community in search of key factors at different stages that can reveal how to make an early diagnosis, predict its progression, and develop better treatments and therapies for the symptoms. The literature is extensive reporting correlations found between altered firing rates and firing patterns of neurons in several regions, at rest, and the development of PD symptoms such as tremors, muscular stiffness, slow

movement (bradykinesia), and balance problems, among others [34], [49]–[54]. These alterations, despite being particularly higher in neural subpopulations directly connected to the dopaminergic pathways (i.e. the *putamen* and *caudate nucleus* of the *striatum* (*STR*) in primates, and *dorsolateral* and *dorsomedial striatum* in rodents), have an impact on the activity of other subpopulations downstream of the circuit. This includes the *motor cortex (CTX)* but also deeper brain structures such as the *globus pallidus internus and externus* (*GPi and GPe*), the *subthalamic nucleus (STN)*, and the *ventral lateral nucleus of the thalamus (VL)*, showing altered states when the dopaminergic activity is significantly reduced in the *Substantia Nigra pars Compacta* (*SNc*). Other publications affirm the existence of a connection between the synchrony of the neural spikes and the erratic response of the motor system in PD and Dystonia [34], [51], [55], [56] under the same circumstances at the *SNc*.

Despite all these correlations between PD symptoms and altered firing rates and synchrony are well documented in the literature –based on in-vivo and in-vitro human and animal work– the underlaying mechanisms leading to the onset of symptoms are not well understood yet, the reason why researchers are using modern techniques of simulation for the study of such complex scenarios.

The exploration of novel bioengineering approaches for neuromodeling of brain circuits has the potential to reveal aspects in the circuit dynamics of these networks that might not otherwise be easily observed from the classical neuroscience perspective. While computational neural networks are widely used nowadays to simulate the interaction of different subpopulations and evaluate their outcomes, their complexity implies the simulation of hundreds to thousands of neurons to approximate a reliable result. In addition, most of these solutions (especially those based on *deep neural networks, [DNN]*) have unknown intermediate stages between the inputs and the outputs, acting as a "*black box*" for the analyzers, which take them away from a real physical interpretation of the mechanisms in between and the temporal evolution of the disease.

This article presents a novel approach for modeling the *Basal Ganglia-Thalamocortical Circuit (BGTCC)* (the complex neural network where PD originates) in its entire progression –for the first time to our knowledge– from a healthy state to a full parkinsonian condition, throughout the patient's life. The model departs from the oscillatory nature of the neural activity at the synapses and creates a mathematical representation of the firing rates at every subpopulation of the circuit as a function of the firing rates of neighbor regions interconnected. Similarly, the model predicts the synchrony of the spikes at each region with calculations based on the probability that the neurons of a subpopulation fire simultaneously as a consequence of a common input.

Our model has been created in a state-space representation throughout the normalized patient's timeline, showing the temporal evolution of the disease with predictions of the future stages. The representation converts a Multiple Input-Multiple Output problem (MIMO) into a Single Input-Multiple Output system (SIMO) by using referential data published in the scientific literature. These data have been used as temporal boundary conditions of the system, with the initial conditions given by the firing rates of healthy subjects and the final conditions given by rates of parkinsonian patients. We have also included a representation of the dopaminergic activity in the *Substantia Nigra Pars Compacta (SNc)* as a temporal numerical vector acting as the only independent variable from which the entire system depends.

The computational model allows for the evaluation of the progression of the disease from the healthy to the fully-developed parkinsonian condition in terms of the mathematical solution that satisfy both ends of the problem. This constitutes a first validation method in itself when a match in the firing rates is verified, as well as in the behavior of the synchrony and firing patterns. The model has also been evaluated under parameters that simulate deep brain stimulation (DBS) applied in the basal ganglia and transcranial magnetic stimulation (TMS) over the motor cortex to observe the neural

response by subpopulation. The results of the DBS simulations compared to reported results for real DBS patients constitutes our second method of validation of the model, showing its efficacy to predict the effects of different types of neurostimulation method. The TMS results cannot be compared against previous studies because the literature does not report clear attempts at TMS for PD with highlightable outcomes. However, these results constitute our first predictions of what a TMS-based therapy would be for PD, complimentary or not to the existing DBS neuromodulation therapies and drug-based therapies.

Other results were also extracted and analyzed such as the typical spike plots and raster plots commonly studied by neuroscientists, which allow them to observe the neural activity by subpopulation in a more natural manner.

Finally, a new hypothesis that would explain the underlaying mechanisms behind the symptoms in presence of altered firing rates and patterns has arisen from the analytical results of our mathematical model and their physical interpretation in the context of PD.

9.4.2. The Oscillatory Nature of the BGTCC

The *integrate-and-fire neuron model* is likely the most well-known approach that explains the dynamics of neural activity. It shows how the membrane potential grows with respect to the potential outside the soma until reaching a threshold that leads the neuron to fire [57]–[60]. In a real synapse, the exchange of neurotransmitters between the pre-synaptic and the post-synaptic neurons determines the regulation of the ionic charge inside the soma. Each neurotransmitter is responsible for a specific action of opening or closing ionic channels through the cell membrane, which results in the migration of groups of ions, from the extra-cellular environment into the soma and vice versa. The nature of the neurotransmitter is associated with the type of ion that is moving through the cell membrane and, in

consequence, with the increase or decrease of the inner potential of the soma with respect to the extra cellular potential.

A circuital representation of a neuron that is consistent with the *integrate-and-fire model* is shown in Fig. 6-a, corresponding to the also well-known Hodgkin–Huxley model [57], [61], [62]. This model has a direct correspondence with the actual mechanism inside the neuron since it describes the growth of the inner potential of the soma as the charge of an equivalent capacitance (C_m) representing the neural membrane. The ionic currents in this model are represented by arrangements of equivalent voltage sources and conductances by type of ionic channel (i.e. E_{Na} and g_{Na} for sodium and E_k and g_k for potassium, respectively) as well as a general leakage conductance (g_L) and leakage source of potential (E_L).
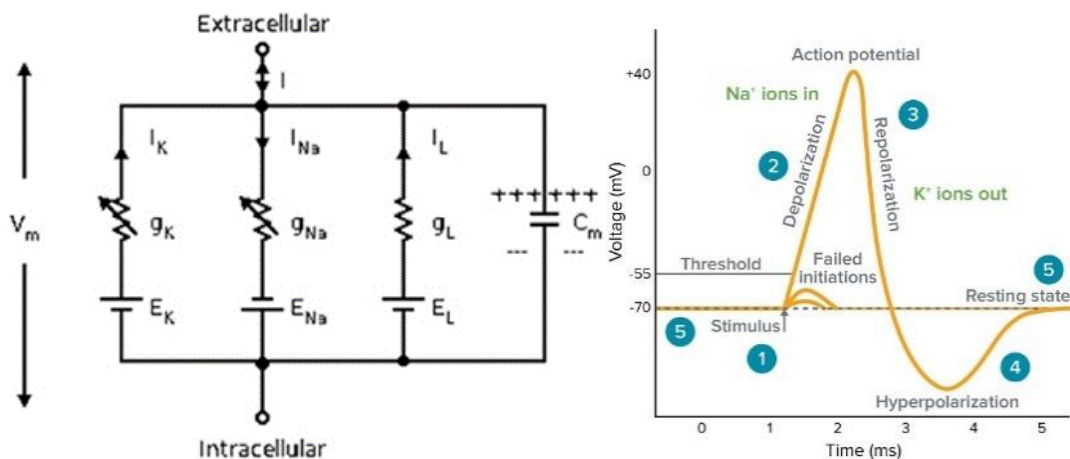
Figure 6 – a) Hodgkin-Huxley model [61]. b) Action potential time diagram [62].

The *integrate-and-fire model* is a simplified but still useful representation of how ionic currents moving through the cell membrane contribute to changing the electric potential at the *soma*. The potential grows until reaching the threshold necessary to initiate an action potential, which typically occurs at -55mV [63], [64]. After exceeding the threshold, the neuron shows a sudden release of energy increasing the potential –usually up to a depolarization voltage of 40mV– when it is said that the neuron "fires". Immediately after, the neural impulse initiates its propagation downstream through the axon, which will produce again a reduction in the potential inside the *soma*. This reduction follows a

42

decreasing exponential waveform that falls below its resting potential, often located at -70mV. The final stage takes place when a damping ripple reaches a hyperpolarization peak of (on average) -90mV, to rise back to the resting potential [63] (see Fig. 6-b).

The membrane potential grows with the relative difference of ionic charges coming inside and out of the soma. Since new ionic exchanges occur every time an incoming spike arrives from a pre-synaptic cell, it is possible to say that the instantaneous membrane potential will be a function of the number of ions present inside and outside the cell at one specific instant. Moreover, different types of ions contribute with distinct equivalent charges, which may be either positive or negative, depending on the nature of the synaptic connection and neurotransmitter –i.e. excitatory or inhibitory- and the specific stage in the action potential cycle. Figure 6 shows a timing diagram that illustrates the progression of the action potential for a neuron with purely excitatory pre-synaptic stimuli. Notice how the change of net ionic charge after each incoming spike on the left side corresponds to a change in the inner potential of the soma on the right.

But knowing the exact amount and type of ions present in the *soma* at one specific instant is such a complex task that does not seem to be practical to intend obtaining an analytical expression for the instantaneous potential or predict the spikes as a function of these variables (especially for all the neurons of every neural subpopulation in a circuit). In Fig. 7, assuming that each of the three rows of net ionic change corresponds to the individual contribution of three pre-synaptic neurons of neighbor regions with different firing rates, it is easy to understand how the net increase of the inner potential occurs at the same rates as the incoming spikes at the synapse. This illustrates the oscillatory characteristic of the pre-synaptic stimuli that determines the also oscillatory behavior of the post-synaptic spikes.

The previously mentioned oscillatory nature of the synaptic activity and neural spikes at rest makes it possible to represent firing rates for different neurons –measured in spikes per second– as frequency values in hertz (Hz). The firing rate is the typical pace of occurrence at which neurons of the same type and region produce their spikes. In general, its frequency will determine a quasi-invariant behavior in which –no matter what the function that describes the membrane potential growth in one cycle is– it will be repeated with minor variations right at the next cycle, showing its periodicity. Notice that the terms "quasi-invariant" and "minor variations" have been intentionally included to denote the unavoidable stochastic characteristic of variables associated with the frequency such as the firing rate itself, but also the phase and the synchrony between neurons of the same population, also considered in this work.
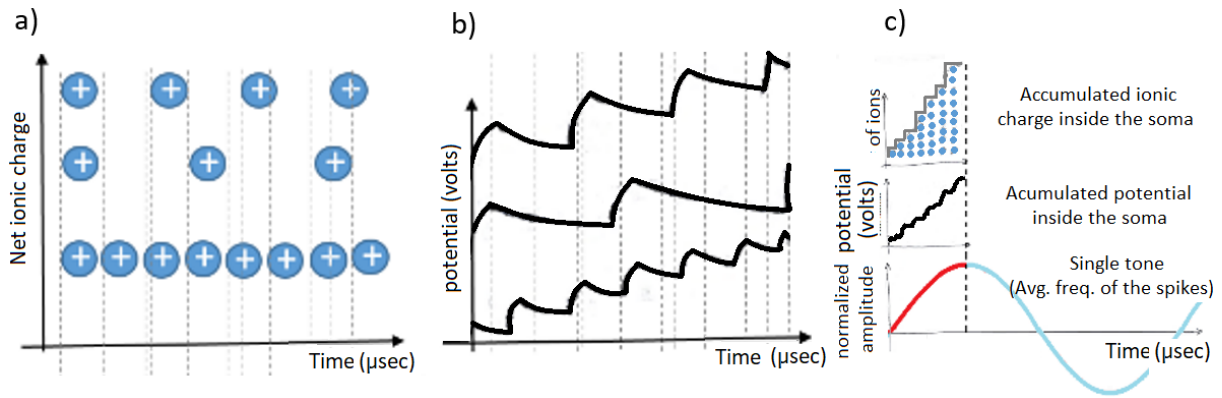
Figure 7 – a) Net change of ionic charge given by each incoming pre-synaptic spike; b) change in the net membrane potential as a consequence of the ionic charge changes.

In our model, a single tone (sinusoid of a certain frequency) represents the period elapsed from spike to spike, seen as the time difference existent from peak to peak, regardless of the amplitude. All parts of the sinusoidal waveform between peaks represent the phase of potential increase from the previous spike to the next one, being the spikes located exactly at the peaks of the sinusoid. The sinusoidal waveform *per se* does not correspond to the pseudo-random waveform of the increasing membrane potential but characterizes well the periodic nature of the phenomena. This characterization is valid, not only for one neuron but is taken as the average behavior of all the neurons of a specific

neural sub-population. This way, we represent both the spikes (signals) and the circuit formed by the neural subpopulations (system) as an oscillatory network with a direct correspondence between new mathematical variables (frequencies) and their physical interpretation as incoming/outgoing firing rates. We have named this correspondence *"the oscillatory nature of the Basal Ganglia-Thalamocortical Circuit (BGTCC)"*.

9.4.3. Average Frequency

In order to determine an analytical expression that describes the relationship between pre-synaptic and post-synaptic firing rates, we take into consideration the oscillatory nature of the signals and the system by stating that any combination of periodic signals in the input will lead to an also periodic signal in the output. Therefore, since these pre-synaptic spikes reach from different neighbor regions, the outgoing frequencies from one particular neural subpopulation must be a function of the frequencies present in the input.

Consider the diagram shown in Fig. 8 where the synapse between five or more neurons is represented. Each neuron is assumed to belong to a different neighbor region in the neural circuit topology. Observe that the incoming spikes from the pre-synaptic neurons have firing rates at frequencies $f_1, f_2, f_3, f_4 \cdots f_n$, being f_n the frequency that represents the n_{th} neighbor region interconnected. Based on this scenario, we departed from the hypothesis that a linear combination of periodic inputs should produce an analytical expression for the output frequency. For this, we considered the fact that every group of pre-synaptic connections coming from a neural subpopulation has a certain number of connections to a neighbor region, out of the total of incoming connections in such region. This means that the contributions of each neighbor region to the output of another region under study will be given by a weighted average of the incoming frequencies, considering the synaptic weights of each region

into another as the coefficients of the linear combination. Consequently, Eq. (1) characterizes the *weighted average of frequencies* for a region as a function of the inputs.
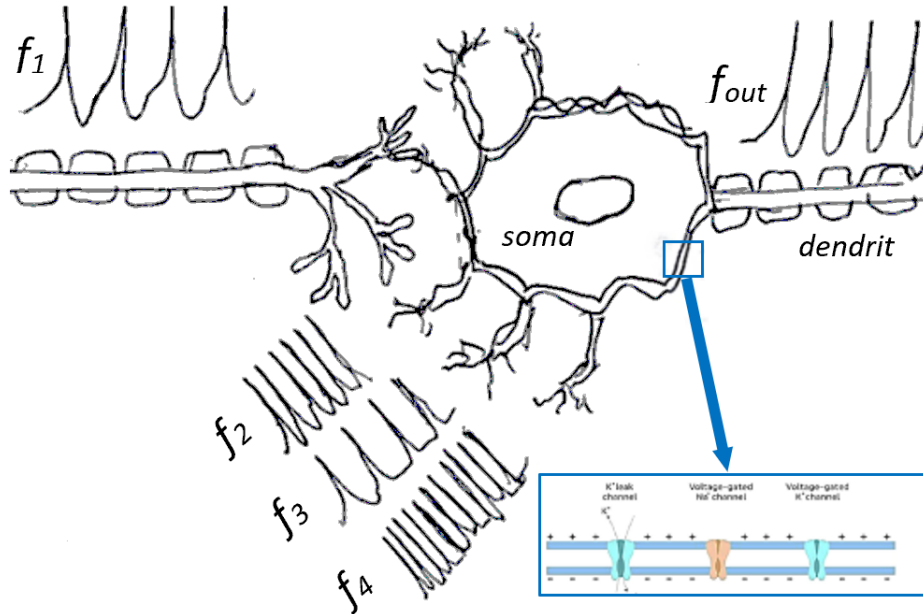
Figure 8 – Detail of the synapsis between five or more neurons. f_1, f_2, f_3, f_4 are the frequencies of the pre-synaptic spikes. f_{out} represents the frequency in the output -dendrite. * Detail of the ionic channels and ion distributions inside and out of the neural membrane.

$$f_{Avg} = w_1 \cdot f_1 + w_2 \cdot f_2 + w_3 \cdot f_3 + \cdots w_n \cdot f_n \tag{1}$$

In Eq. 1, each frequency represents the average firing rate of an entire subpopulation of neurons that is part of the neural network under study (the BGTCC in this case), and not the mere firing rate of a single neuron, as it would occur in conventional computational approaches of neural networks and fuzzy logic networks.

9.4.4. Membrane constant and low-frequency approximation

The accuracy of prediction of the firing rate requires a close look at the factors that intervene in the inter-spike duration (period). The first approach for the period of the *membrane potential growth* is given by the multiplicative inverse of the *weighted average of frequencies* in Eq. 1, to be adjusted through a scale factor (C_{reg}) explained later on in this text (Eq. 2).

$$T_{pot\_grw} = \frac{1}{C_{reg}} \cdot \frac{1}{f_{Avg}} = \frac{1}{C_{reg} \cdot [w_1 \cdot f_1 + w_2 \cdot f_2 + w_3 \cdot f_3 + \cdots w_n \cdot f_n]} \tag{2}$$

Rigorously speaking, the entire inter-spike period should also consider the depolarization period, as well as the repolarization and refractory periods that form the action potential. For practical purposes, the waveform of the action potential can be approximated as the combination of a unitary impulse –Dirac delta– representing an almost instantaneous potential growth and negligible depolarization period, followed by a decreasing exponential function that lasts the sum of the repolarization and refractory periods.
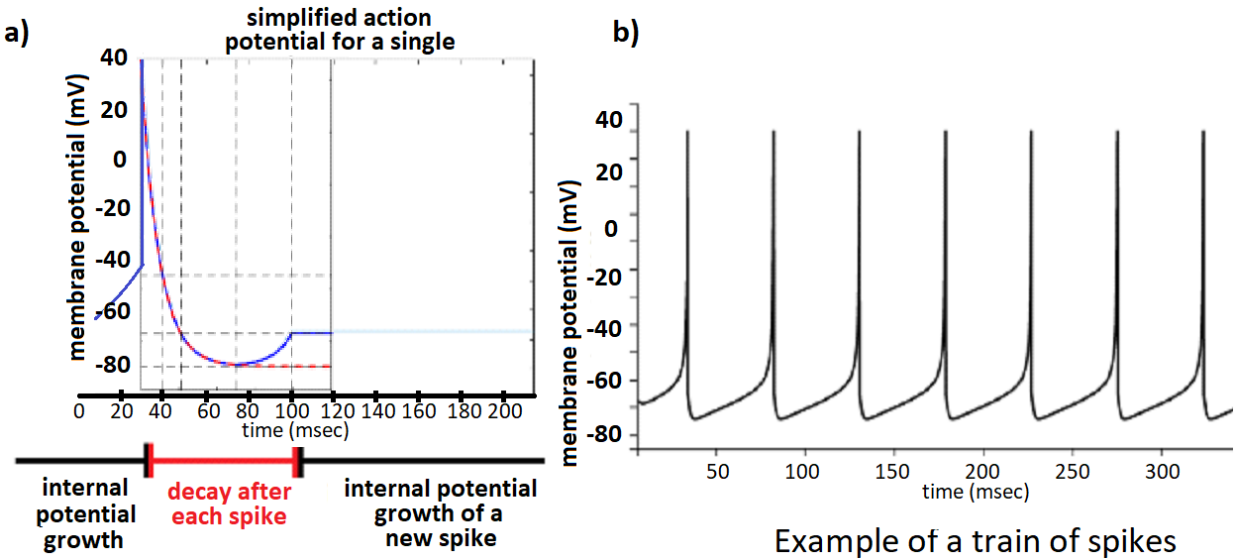
Figure 9 – a) Approximation of the neural spike waveform; b) General appearance of a train of spikes.

Being generic, we will say that the duration of this decay, named *decay period of the spike*, will last k times the membrane constant (τ_m), being k another physiological constant that varies depending on the type of neuron. The constant k determines how fast or slow neurons can repolarize their membrane to the resting potential and is related to the different conductances of the ionic channels by type of neuron. The product of the constant k and the membrane constant τ_m leads to Eq. 3, similar to the time constant in an RC circuit.

$$T_{decay} = k \cdot \tau_m \qquad (3)$$

Now, the complete period of a train of spikes (Fig. 9-b) will be the sum of the *potential growth period* and the *decay period*.

$$T_{spikes} = T_{pot\_grw} + T_{decay}, \qquad (4)$$

$$T_{spikes} = \frac{1}{C_{reg} \cdot [w_1 \cdot f_1 + w_2 \cdot f_2 + w_3 \cdot f_3 + \cdots w_n \cdot f_n]} + [k \cdot \tau_m], \qquad (5)$$

and the frequency of the train of spikes becomes

$$f_{spikes} = \frac{1}{T_{spikes}} = \frac{1}{\left[C_{reg} \cdot \frac{1}{(w_1 \cdot f_1 + w_2 \cdot f_2 + w_3 \cdot f_3 + \cdots w_n \cdot f_n)} \right] + [k \cdot \tau_m]}, \qquad (6)$$

The literature is extensive reporting membrane constants (τm) for different types of neurons that are one or two orders of magnitude smaller than the fundamental period of their spikes (see the Boolean expression below) [32], [35], [38], [39], [65]–[68].

$$(\tau_1 \ll T_1) \, \& \, (\tau_2 \ll T_2) \, \& \, (\tau_3 \ll T_3) \, \& \, \dots (\tau_n \ll T_n) \qquad (7)$$

This is the case for all the neurons present in the BGTCC, for which we can ensure that, at a low frequency, the *potential growth period* is significantly longer than the *decay period*, being this last one negligible for the calculation of the spike period. This is perceptible at the denominator in Eq. 6 that tends to the value given by the first (left) term within brackets when $k \cdot \tau_m$ is significantly smaller than T_{pot_grw}.

Finally, the low-frequency approximation for the firing rate of the outgoing spikes is shown in Eq. (8). This constitutes an analytical expression in which f_{spikes} is, for the first time to our knowledge, expressed as a function of the incoming firing rates at the synapse and the corresponding synaptic weights by neighbor region.

$$f_{spikes} = C_{reg} \cdot [w_1 \cdot f_1 + w_2 \cdot f_2 + w_3 \cdot f_3 + \cdots w_n \cdot f_n] \qquad (8)$$

Going back to the meaning of C_{reg}, we have introduced this scaling factor by region to guarantee a match between the calculated values of f_{spikes} –obtained from the *weighted average of incoming frequencies*– and the actual firing rate values of different neural subpopulations in real subjects of study reported in the literature (Fig. 10). The mere *weighted average of incoming frequencies* by itself does not necessarily coincide with the outgoing frequency. This occurs because in each neural sub-population different factors such as the type of neurotransmitters at the synapse and the type of pre-synaptic and post-synaptic neurons lead to different magnitudes of incoming and outgoing ionic flows through the membrane after each incoming spike. Hence, the rate of growth of the inner potential differs from the one predicted by the *weighted average* and needs to be adjusted for each scenario because the period and firing rate of the output are affected by the type of synapse through a faster or slower growth of such potential. In simple words, this means that each type of synapse in the BGTCC is a sub-system in itself that depends on the regions interconnected through it. Each sub-system needs then to be characterized for the particular operating conditions that vary from subject to subject (*inter-subject variations*), and from the healthy to the full-parkinsonian condition (*intra-subject variations*), as explained later.
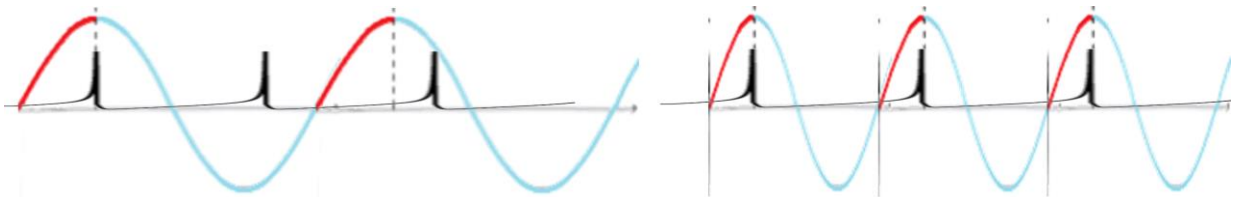
Figure 10 – Effect of the frequency scaling factor (C_{reg}) in the output frequency. The calculated *weighted average of the incoming frequencies* (left side) is scaled up/down through C_{reg} to match the exact firing rate observed in one specific neural subpopulation.

9.4.5. The Firing Rate Model for the Characterization of PD

9.4.5.1. Network topology and nomenclature

The first step for the design of our model has been the definition of a well-accepted topology for the *Basal Ganglia-Thalamocotrical Circuit* (BGTCC) in both healthy and parkinsonian conditions. Figure 11, shows both cases including the following neural subpopulations and nomenclature: motor cortex (*CTX*); differentiated D1 and D2 dopaminergic receptors located at the *caudate-putamen* [dorsal striatum] (*STRD1* and *STRD2*, respectively); *Substantia Nigra Pars Compacta* (SNc); *Globus Pallidus internus* and *externus* (*GPi* and *GPe*), the *subthalamic nucleus* (*STN*), and the *ventral lateral nucleus of the thalamus* (*VL*).
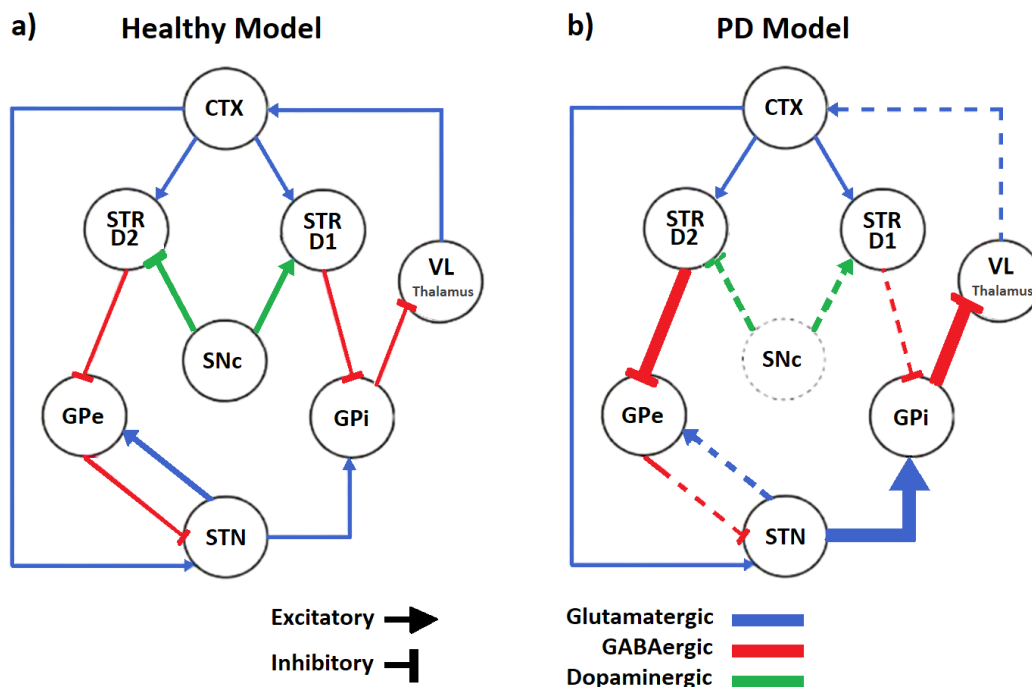
Figure 11 – Network topologies for the BGTCC in a) a healthy subject and b) a parkinsonian patient.

As is well known in the field of movement disorders neurology, there exist two different motor pathways in the BGTCC that control the activity at the GPi. The direct pathway starts with excitatory *dopaminergic* connections from the SNc to the D1 receptors at the *striatum*, which leads to an inhibitory action of these neurons over the GPi using GABA neurotransmitters at the synapse. The

indirect pathway inhibits instead the activity of the D2 receptors at the *striatum* through the release of dopamine from the *SNc*. Then, the D2 receptors inhibit the activity at the GPe and these neurons inhibit the spikes at the STN, all using *GABAergic* connections. The STN finally excites the GPi through *glutamatergic* connections, contrarily to the direct pathway. This explains the potential of different nuclei such as GPe, GPi, STN, and *Thalamus* to be stimulated, aiming to regulate the neural rhythms in the *motor cortex* using the feedback link from the *Thalamus*.

On the other hand, the parkinsonian model is characterized by a moderate to high decrease in the activity of the *dopaminergic pathways* from the *SNc* to the STRD1 and STRD2 receptors (Fig. 11-b). This ends up decreasing the direct inhibitory effect of the STRD1 neurons over the GPi and increasing the inhibitory effect over it through the indirect pathway.

9.4.5.2. Initial time-independent model. Learning from a failed approach.

Provided with an expression that relates incoming and outgoing firing rates in a neural population (Eq. 8), our next natural step was to create a mathematical representation of the system including all the subpopulations and establishing the connections that describe both the healthy and the parkinsonian model of the BGTCC. Equation 8 led us to obtain a time-independent system of equations formed by 7 regions and 7 expressions. However, the healthy and the parkinsonian conditions are significantly different and the healthy model shows different firing rates and parameters than those used in the parkinsonian model, leading to doubling the number of regions and expressions to 14. No additional equations were added for the firing rate at the SNc since its influence would be treated indirectly through a constant for the parkinsonian model to be called *Active Cell Ratio (ACR)* that expresses the decreased levels of dopamine delivered to the *striatum* (explained later in the text).

In Eq. 8 we can identify the input and output frequencies as variables, whereas the scaling factor C_{reg} and synaptic weights w_i are considered parameters since (although unknown) they should not vary

in time with the progression of the disease. Another of our considerations in the model is that neurons in all the subpopulations of the BGTCC should also have incoming connections from other regions/subpopulations outside the circuit, though in smaller ratios. These connections from outer subpopulations were named *rest-of-brain (RoB) connections*, defined for each of the 7 subpopulations of the BGTCC (excluding SNc) [69], [70]. This added the problem of 7 additional unknown synaptic weights (parameters) and 7 more firing rates (variables) to be found.

In our first approach, all the synaptic weights were also treated as variables because they were originally unknown. We made use of 8 known referential firing rates under healthy conditions and 5 known referential firing rates under parkinsonian conditions extracted from the literature. This aspect is better explained in the next section. Two additional parkinsonian firing rates were also unknown (f_{CTX} and f_{SNc}). Finally, the first model obtained was a linear but highly coupled system of equations with 44 unknowns and only 14 equations, making the system unsolvable by analytical methods (Eq. 9 to 22).

The first attempt at solving the mathematical problem led us to define the system in MATLAB software (R2020) using matrix notation and the *fsolve* function. The solver was configured to use the Levenberg–Marquardt algorithm also referred to as the *damped least-squares method*. Both the maximum number of iterations and function evaluation were set to 1×10^{20}. The method of solution consisted of the minimization of the error between the calculated output firing rate for each region (based on Eq.8) and referential values of such firing rates extracted from the literature (see next section). Each run made use of a "*seed",* a unique vector of initial values for the iterations that was randomly generated using a mean and a standard deviation for each variable. This assures diversity of resolution paths which should all converge to a unique solution. The stopping criterion was an error tolerance of 1×10^{-80}, or the maximum number of iterations (first thing to occur).

Healthy Sub-model:
Referential values: $f_{oh_{CTX}} = 5Hz$; $f_{oh_{SNc}} = 2Hz$; $f_{oh_{STRD1}} = 1Hz$; $f_{oh_{STRD2}} = 1Hz$
$f_{oh_{GPe}} = 70Hz$; $f_{oh_{GPi}} = 70Hz$; $f_{oh_{STN}} = 20Hz$; $f_{oh_{VL}} = 18Hz$

$$f_{oh_{CTX}} = C_{CTX} \cdot \left(w_{1(VL-CTX)} \cdot f_{oh_{VL}} + w_{RoB_{CTX}} \cdot f_{RoB_{h_{CTX}}} \right) \tag{9}$$

$$f_{oh_{STRD1}} = C_{STRD1} \cdot \left(w_{1(CTX-STRD1)} \cdot f_{oh_{CTX}} + w_{2(SNc-STRD1)} \cdot f_{oh_{SNc}} + w_{RoB_{STRD1}} \cdot f_{RoB_{h_{STRD1}}} \right) \tag{10}$$

$$f_{oh_{STRD2}} = C_{STRD2} \cdot \left(w_{1(CTX-STRD2)} \cdot f_{oh_{CTX}} + w_{2(SNc-STRD2)} \cdot f_{oh_{SNc}} + w_{RoB_{STRD2}} \cdot f_{RoB_{h_{STRD2}}} \right) \tag{11}$$

$$f_{oh_{GPe}} = C_{GPe} \cdot \left(w_{1(STRD2-GPe)} \cdot f_{oh_{STRD2}} + w_{2(STN-GPe)} \cdot f_{oh_{STN}} + w_{RoB_{GPe}} \cdot f_{RoB_{h_{GPe}}} \right) \tag{12}$$

$$f_{oh_{GPi}} = C_{GPi} \cdot \left(w_{1(STRD1-GPi)} \cdot f_{oh_{STRD1}} + w_{2(STN-GPi)} \cdot f_{oh_{STN}} + w_{RoB_{GPi}} \cdot f_{RoB_{h_{GPi}}} \right) \tag{13}$$

$$f_{oh_{STN}} = C_{STN} \cdot \left(w_{1(CTX-STN)} \cdot f_{oh_{CTX}} + w_{2(GPe-STN)} \cdot f_{oh_{GPe}} + w_{RoB_{STN}} \cdot f_{RoB_{h_{STN}}} \right) \tag{14}$$

$$f_{oh_{VL}} = C_{STN} \cdot \left(w_{1(GPi-VL)} \cdot f_{oh_{GPi}} + w_{RoB_{VL}} \cdot f_{RoB_{h_{VL}}} \right) \tag{15}$$

Parkinsonian Sub-model:
Referential values: $f_{op_{CTX}} = unknown$; $f_{op_{SNc}} = unknown$; $f_{op_{STRD1}} = 10Hz$;
$f_{op_{STRD2}} = 10Hz$; $f_{op_{GPe}} = 60Hz$; $f_{op_{GPi}} = 90Hz$; $f_{op_{STN}} = 40Hz$; $f_{op_{VL}} = unknown$

$$f_{op_{CTX}} = C_{CTX} \cdot \left(w_{1(VL-CTX)} \cdot f_{op_{VL}} + w_{RoB_{CTX}} \cdot f_{RoB_{p_{CTX}}} \right) \tag{16}$$

$$f_{op_{STRD1}} = C_{STRD1} \cdot \left(w_{1(CTX-STRD1)} \cdot f_{op_{CTX}} + w_{2(SNc-STRD1)} \cdot f_{op_{SNc}} + w_{RoB_{STRD1}} \cdot f_{RoB_{p_{STRD1}}} \right) \tag{17}$$

$$f_{op_{STRD2}} = C_{STRD2} \cdot \left(w_{1(CTX-STRD2)} \cdot f_{op_{CTX}} + ACR \cdot w_{2(SNc-STRD2)} \cdot f_{op_{SNc}} + w_{RoB_{STRD2}} \cdot f_{RoB_{p_{STRD2}}} \right) \tag{18}$$

$$f_{op_{GPe}} = C_{GPe} \cdot \left(w_{1(STRD2-GPe)} \cdot f_{op_{STRD2}} + ACR \cdot w_{2(STN-GPe)} \cdot f_{op_{STN}} + w_{RoB_{GPe}} \cdot f_{RoB_{p_{GPe}}} \right) \tag{19}$$

$$f_{op_{GPi}} = C_{GPi} \cdot \left(w_{1(STRD1-GPi)} \cdot f_{op_{STRD1}} + w_{2(STN-GPi)} \cdot f_{op_{STN}} + w_{RoB_{GPi}} \cdot f_{RoB_{p_{GPi}}} \right) \tag{20}$$

$$f_{op_{STN}} = C_{STN} \cdot \left(w_{1(CTX-STN)} \cdot f_{op_{CTX}} + w_{2(GPe-STN)} \cdot f_{op_{GPe}} + w_{RoB_{STN}} \cdot f_{RoB_{p_{STN}}} \right) \tag{21}$$

$$f_{op_{VL}} = C_{STN} \cdot \left(w_{1(GPi-VL)} \cdot f_{op_{GPi}} + w_{RoB_{VL}} \cdot f_{RoB_{p_{VL}}} \right) \tag{22}$$

After numerous initial evaluations, we noticed that the algorithm always ended with the maximum number of iterations (increased the maximum several times up to the one above indicated) and not due to the tolerance. Moreover, increasing the tolerance was not an option since the final error would be quite large. However, we also observed that most of the firing rates tended to decrease the error significantly, whereas some others were still significantly far from convergence. At this point, we were able to conclude that the system was not compatible as it was presented, and **we hypothesized that** ***one or more factors must change over time within the system to make it compatible with both the*** ***healthy and the parkinsonian conditions***. **This change would be related to the variation of the**

activity levels in the dopaminergic pathways from the SNc to the striatum, making the model a time-dependent system.

Despite the lack of convergence and incompatibility of the first model, the results left us halfway in the search for unknown parameters such as the synaptic weights and scaling factors. This allowed us to perform a statistical analysis of the outcomes to obtain new seeds, closer to the real parameters for our next model.

III-c. Referential values for the time-independent model and temporal boundary conditions for a new time-dependent approach

Firing rates are probably one of those variables to be included in any human neural model that shows more variation from one individual to another. Studying firing rates in healthy human subjects is difficult because of the constraints of the existing electrophysiology technology that requires inserting invasive probes in the cortex, and deeper brain structures, to perform extracellular or intracellular recording for the capture of action potentials (*e.g. Local Field Potential [LFP] or in vivo patch-clamp recording)* [71], [72]. However, the literature compiles information about referential firing rates of healthy subjects in different nuclei that have been extracted from in-vitro studies of human neurons, non-invasive electrophysiological recordings of healthy subjects (*e.g.*, EEG), and even from in-vivo animal studies of species proximate to humans (primates).

Conversely, data from parkinsonian patients are more abundant and easier to find since many publications report firing rates and firing patterns extracted from patients with DBS probes implanted. Once the conditions of PD patients justify surgery, DBS probes are used for LFP across the *basal ganglia*, *motor cortex*, *striatum,* and *thalamus* depending on their trajectories. In addition, firing rates from primates with induced parkinsonism are also available for reference.

With base on this available data, we have extracted a set of values for the referential firing rates we required for both the healthy and the parkinsonian sub-models. This data is summarized in Table I with their correspondent sources [66], [73]–[81].

The *referential firing rate*s have been used as "*know values"* in the timeless system of equations of the first modeling approach to look for the parameter of the system (treated as variables) that satisfy such values. Nonetheless, once formulated the hypothesis of the system changing in time as a consequence of a decrease in the dopaminergic levels, we reformulated our model to make it a temporal progression model (see *time-dependent modeling* in section 8.4.5.4.).

In the temporal progression model, our referential firing rates were taken as temporal boundary conditions. Hence, the values for healthy subjects were considered as the initial (healthy) conditions whereas the referential firing rates for PD patients were designated as the final (full parkinsonian) condition.

Table I – Referential firing rates for healthy human subjects and advanced PD patients [66], [73]–[81]

Nucleus	Firing Rate (spikes/sec) Healthy condition	Firing Rate (spikes/sec) Advanced PD
CTX	5 Hz	unknown
STRD1	1 Hz	10 Hz
STRD2	1 Hz	10 Hz
SNc	2 Hz	unknown
GPe	70 Hz	60 Hz
GPi	70 Hz	90 Hz
STN	20 Hz	40 Hz
VL	18 Hz	unknown

9.4.5.3. Synaptic weights and scaling factors

The synaptic weights are values that represent the abundance of incoming synaptic connections in a region from its neighbor neurons. In the context of this paper, it will be defined as the ratio between the number of incoming synaptic connections from a neighbor region over the total incoming connections in the post-synaptic region. Since they denote ratios, the synaptic weights can be expressed as a value between zero and one but also in percentage terms.

Obtaining the synaptic weights was an even more difficult task to carry out than the extraction of the firing rates since the first ones are parameters not directly measurable. Thousands to millions of incoming and outgoing synaptic connections to or from a neural population make it impossible for scientists to count them all experimentally. Hence, the best choice is the performance of indirect estimations through neural activity. However, due to the same technical difficulties found for the firing rates associated with a constraint with the current electrophysiology technology, correlating the neural activity of neighbor subpopulations to extract the synaptic weights out of it seems also a challenging task. Performing literature research about the synaptic weights, we were able to find very few values for the model [32], [79], [82] and some of them might not be fully reliable due to the level of uncertainty involved in the methods of extraction. Therefore, for more accuracy, we chose to treat the synaptic weights as variables of our system and extract their values by mathematical deduction. For this, we used the referential firing rates in the initial time-independent model first and then in the temporal progression model *time-dependent model* in section 8.4.5.4.).

With the time-independent model, we first performed 10 runs of the program until its end with the stop criteria explained in the previous section. This led us to obtain 10 points per region for the synaptic weights of each subpopulation. The next step was the creation and adjustment of a normal curve for each of the subpopulations, extracting the mean (μ_{w_i}) and standard deviation (σ_{w_i}) of the synaptic

weights by region. Then, curve outliers were removed to obtain adjusted curves with a standard deviation equal to or smaller than 0.01 (variations of ±1% in the synaptic weights around the new mean). This first approach allowed us to obtain good approximations for what the final values of all the synaptic weights would be later, but still not the final values due to the lack of convergence. In some cases where after several iterations the values stagnated, the partial results of this analysis ended up being significantly close to the final values obtained through the boundary conditions (explained later in this section).
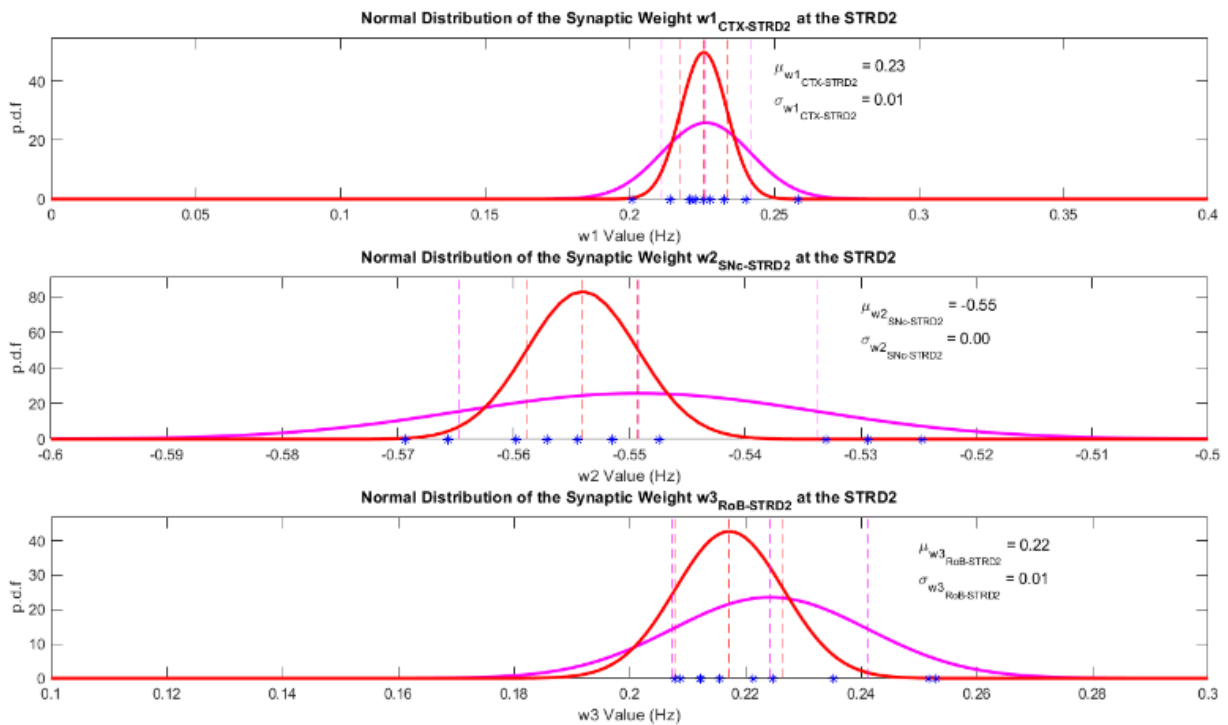
Figure 12 – Example of the normal curves of adjustment for 10 runs of the time-independent model at the subpopulation of D2 receptor cells of the striatum.

In Fig. 12, an example of the synaptic weights calculated for the STRD2 subpopulation is shown. This includes the incoming connections from CTX and SNc, according to the diagram in Fig. 11, and also the synaptic weight for connections from the rest-of-brain (RoB).

In our model, we have included the RoB synaptic weights because we recognize the role that other connections –from neurons not belonging to neighbor subpopulations within the BGTCC– may have

in the dynamics of the BGTCC itself. This does not necessarily mean that neurons that are not part of the BGTCC have an active role in the regulation of motor functions or malfunction of the motor circuits, but we believe that they might define a basal level for some populations in their firing rates at rest. This is reflected in the final additive term in all the equations from Eq. 9 to Eq. 22, where the product $w_{RoB} \cdot f_{RoB}$ by region must be a constant.

One substantial change introduced in the time-dependent model in state-space representation is that we have made the product $w_{RoB} \cdot f_{RoB}$ constant and identical for both the healthy and the parkinsonian conditions per region. This condition (different from the time-independent model) is based on our presumption that this basal level should not vary significantly in time as a consequence of the progression of the disease because most of its contributors come from regions outside the BGTCC.

In our model, the RoB synaptic weights include the synaptic weights of the self-connections (from a neural subpopulation to itself) [82]–[86]. This means that a w_{RoB} term will consider all other synaptic connections for subpopulations that do not strictly come from a neighbor subpopulation within the BGTCC. When designing the model, we could have chosen to use two separate synaptic weights and firing rates for the self-connections and connections from outside the BGTCC $(w_{RoB} \cdot f_{RoB} = w_{out\_BGTCC} \cdot f_{out\_BGTCC} + w_{self} \cdot f_{elf})$ but this would add an additional level of complexity to the system and number of variables that are not necessary at this point for firing rate predictions. However, this shows the ability of this model and nomenclature to discretionally integrate or separate nuclei in as many sub-nuclei as is convenient for the analysis. Finally, another reason to include the self-connections in the w_{RoB} term is that we believe that they play a fundamental role in the spike synchrony by region, as it will be shown later on in this text.

The calculation of the synaptic weights finally reached a more accurate method once we changed the approach to a time-dependent model. In the time-independent model, we were seeking to find the synaptic weight values from the general solution of a system that was unable to converge due to the incompatibility of the healthy and parkinsonian sub-models without the consideration of the changing nature of the system in time. Contrarily, the time-dependent approach would permit us to use the temporal boundary conditions to restrict the solution of the synaptic weights to the only compliance of the initial and final conditions for one subpopulation. For expressions with two synaptic weights (for instance, those for the CTX and VL nuclei) the use of the healthy and parkinsonian equations would lead to a determinate compatible system with two equations, two unknowns and a direct solution (e.g Eq. 9 & 16 and Eq. 15 & 22). In this scenario, the cancellation of the $w_{RoB} \cdot f_{RoB}$ term from the subtraction of both equations, and the clearance of w_{RoB} from the healthy equation lead to the following expressions for w_1 and w_{RoB}.

$$w_1' = \frac{fo_p - fo_h}{f1_p - f1_h} \tag{23}$$

$$w_{RoB}' = \frac{fo_h - w_1' \cdot f1_h}{f_{RoB}} \tag{24}$$

In Eq. 23 and 24, w_1' and w_{RoB}' are the scaled versions of the synaptic weights w_1 and w_{RoB}, which are finally found using the scaling factor C_{reg} by region as follows:

$$w_1' = C_{reg} \cdot w_1 \tag{25}$$

$$w_{RoB}' = C_{reg} \cdot w_{RoB} \tag{26}$$

But the values of Creg are also unknown. To find them we depart from the fact that the modules of all the synaptic weights of a region must sum the unit. Therefore, taking modulus on both sides and adding Eq. 25 and 26 we obtain the scaling factors as shown in Eq. 27.

$$C_{reg} = w_1' + w_{RoB}' \tag{27}$$

Finally, the synaptic weights w_1 and w_{RoB} are obtained normalizing the scaled versions of them with Eq. 25 and 26.

For expressions with three synaptic weights, Eq. 10 to 14 and 17 to 21 one additional temporal condition and equation would be needed. Having three unknowns and two equations, the system is indeterminate and admits infinite solutions since one of the three synaptic weights becomes a parameter. In this case, we have analyzed the predictions of the synaptic weights previously obtained from the time-independent system and used the synaptic weight closest to the convergence (out of the three for each equation) as the parameter. This way the synaptic weight problem becomes a compatible two-unknown, two-equation system again and is solved as it was previously described.

The synaptic weights not only describe the ratios of the synaptic connections, but also the nature of it. According to our explanation in section II, excitatory connections in our topology (Fig. 11) have a positive sign in the synaptic weight, whereas inhibitory connections are negative.

Using the previously described method, we finally solved the problem of 24 unknown synaptic weights and 7 unknown scaling factors for our time-dependent model by using the temporal boundary conditions of healthy and full parkinsonian states. The calculated values are shown in Table II. Paradoxically, these values are considered time-invariant and identical for both the healthy and the parkinsonian condition, and the progression in time will depend on other factors.

Table II – Synaptic Weights

Region	Cr_{eg}	W_1	W_2	W_{RoB}
CTX	2.1743	0.57	0	-0.43
STRD2	3.8513	0.2397	-0.5692	0.1911
STRD1	3.0917	0.5822	0.3234	-0.0943
SNc	1.0000	1	0	0
GPe	10.1521	-0.6567	0.2463	0.0971
GPi	5.0995	-0.4358	0.3922	0.172
STN	4.8681	0.4108	-0.2054	0.3837
VL	1.5189	-0.6505	0.0395	0.31

9.4.5.4. Time-dependent modeling of the BGTCC.

After the results and incompatibility of the healthy and parkinsonian sub-models in the time-independent approach, we concluded that the best modeling for Parkinson's disease over the BGTCC would be through a time-dependent representation. We also hypothesized that something within the system must be changing in time to make the system compatible with the two temporal boundary conditions, but not simultaneously. Strictly speaking, we will say that under the new approach the BGTCC will be a time-invariant system (fixed synaptic weights, scaling factors, and RoB firing rates) but time-dependent with respect to factors varying over the development of the disease (variables). Such factors are, in principle, the firing rates of the different neural subpopulations, but this approach will be changed later.

Considering the BGTCC a linear time-invariant (LTI) system, we were able to make use of all the properties of such types of systems, including access to matrix representation and algebraic manipulation. Then, we introduced the state space representation, an approach in which the system

depends on the current and past states of the unknowns (called state variables), represented by a first-order system of differential equations to be solved by explicit numerical methods.

Going backward in its deduction, we started with the final representation of the system of difference equations in a discrete domain to then understand the actual behavior of neurons in the continuous domain, depending on the temporal derivatives of the variable of interests. The model starts reconfiguring the system in Eq. 9 to 22 making it a function of the discretized time for each instant "*n*". Then, we would say that <u>all values of outgoing firing rates at the current instant (*n*)</u> for each of the neural subpopulations in the BGTCC <u>are functions of the firing rates</u> of the neighbors involved according to the topology <u>at the immediately previous instant (at *n-1*)</u>.

In our state-space model, each variable is expressed as a vector, a succession of values representing the progression of the variable in time.

9.4.5.5. Active Cell Ratio at the SNc

Departing from a system with multiple inputs and outputs (firing rates) from which we need to know its progression in time, we needed to reduce the number of independent variables for better controllability. In Parkinson's disease, the well-known origin of the alterations is the decrease of the activity in the dopaminergic pathways as a consequence of the death of the dopaminergic neurons in the *substantia nigra pars compacta (SNc)*. In the time-independent model, we included the term ACR (*Active Cell Ratio)* to parametrize the level of dopaminergic activity from the SNc to the striatum. Originally, we were expecting to find a value for this term that math the full parkinsonian condition, but we understood later that in the time-dependent model we should consider the ACR as an independent variable instead of a parameter.

Active Cell Ratio (ACR) is a concept that we have introduced to refer to the proportion (from 0 to 1) of active neurons in a neural subregion, out of the total original population in a healthy and normal condition. By "active" we mean, not only alive neurons but also neurons actually firing. Then, the ratio of both dead neurons and inactive neurons to the total may be expressed with the ACR concept. Nevertheless, ACR could also be used to refer to (for example) the induced state of total or partial transient inactivity of a neural subpopulation under medication. In this text, the ARC will be often referred to in percentage terms as $ACR_\%$.

In the time-dependent model, we defined ACR of the SNc subpopulation as a vector in time that represents the variation of the dopaminergic activity in the patient's normalized timeline, throughout his/her entire life. For this, we have selected the error function complement (erfc) as the waveform that we believe better represents a moderate transition from 1 (100% of activity) to 0 (0%). The *erfc* has a soft transition at the beginning and the end of the curve, and its biggest rate of change is found in the middle. Figure 13 shows the ACR function programmed in MATLAB for the SNc, with its correspondent time derivative underneath. For this particular example, we have set the maximum rate of change to be at the 60% of the patient's normalized timeline, but it could be discretionally located at any point to simulate the development of PD at any age.
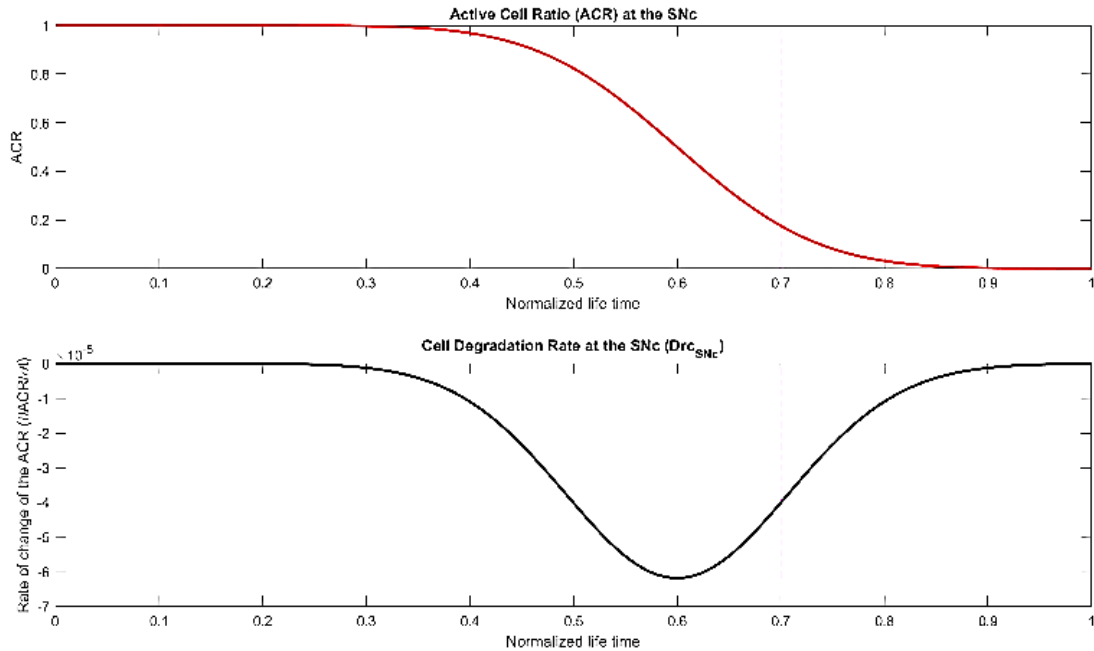
Figure 13 – *Active Cell Ratio (ACR)* vector at the *SNc* with maximum slope simulated at 60% of the patient's life.

III-e-2. State-space representation

We departed from the time-independent model by stating that in a time-dependent representation present states of the outputs in each of the subpopulations must be a function of their past states, as a consequence of the causality of the system. In order to observe a detailed progression of the states on a time scale with small incremental timesteps, we made all the outputs in the present discrete timestep [n] dependent on the outputs in the previous timestep [n-1], as shown in Eq. 28 to 34. Notice that in this state-space representation we have only 8 variables, 7 of which are dependent with the ACR being the only independent variable. With this representation, we have converted the problem of a *multiple input-multiple output (MIMO) system* into a more simple and solvable *single input-multiple output system (SIMO)*.

In the system presented above, each of the neural subpopulations is differentiated with one color, showing to the left side the present outputs for each of them and to the right side the relationship of dependence with the immediately previous stages. The levels of dopamine and progression of the disease are represented through the variation of the ACR vector with a constant firing rate for the

neurons at the *substantia nigra (SNc)*. This permits the activity at the D1 and D2 receptors to vary to observe the projections downstream through the rest of the system a few iterations later.

State-space representation of the firing rate model:

Initial (healthy) conditions: $\quad f_{oh_{CTX}} = 5Hz$; $f_{oh_{SNc}} = 2Hz$; $f_{oh_{STRD1}} = 1Hz$; $f_{oh_{STRD2}} = 1Hz$; $\quad f_{oh_{GPe}} = 70Hz$; $f_{oh_{GPi}} = 70Hz$; $f_{oh_{STN}} = 20Hz$

Final (parkinsonian) conditions: $f_{op_{CTX}} = unknown$; $f_{op_{SNc}} = 2Hz$; $f_{op_{STRD1}} = 10Hz$; $f_{op_{STRD2}} = 10Hz$; $f_{op_{GPe}} = 60Hz$; $f_{op_{GPi}} = 90Hz$; $f_{op_{STN}} = 40Hz$

$$f_{oh_{CTX_{[n]}}} = C_{CTX} \cdot \left(w_{1(VL-CTX)} \cdot f_{oh_{VL_{[n-1]}}} + w_{RoB\,CTX} \cdot f_{RoB\,h_{CTX}} \right) \tag{28}$$

$$f_{oh_{STRD1_{[n]}}} = C_{STRD1} \cdot \left(w_{1(CTX-STRD1)} \cdot f_{oh_{CTX_{[n-1]}}} + w_{2(SNc-STRD1)} \cdot ACR_{[n-1]} \cdot f_{oh_{SNc_{[n-1]}}} + w_{RoB\,STRD1} \cdot f_{RoB\,h_{STRD1}} \right) \tag{29}$$

$$f_{oh_{STRD2_{[n]}}} = C_{STRD2} \cdot \left(w_{1(CTX-STRD2)} \cdot f_{oh_{CTX_{[n-1]}}} + w_{2(SNc-STRD2)} \cdot ACR_{[n-1]} \cdot f_{oh_{SNc_{[n-1]}}} + w_{RoB\,STRD2} \cdot f_{RoB\,h_{STRD2}} \right) \tag{30}$$

$$f_{oh_{GPe_{[n]}}} = C_{GPe} \cdot \left(w_{1(STRD2-GPe)} \cdot f_{oh_{STRD2_{[n-1]}}} + w_{2(STN-GPe)} \cdot f_{oh_{STN_{[n-1]}}} + w_{RoB\,GPe} \cdot f_{RoB\,h_{GPe}} \right) \tag{31}$$

$$f_{oh_{GPi_{[n]}}} = C_{GPi} \cdot \left(w_{1(STRD1-GPi)} \cdot f_{oh_{STRD1_{[n-1]}}} + w_{2(STN-GPi)} \cdot f_{oh_{STN_{[n-1]}}} + w_{RoB\,GPi} \cdot f_{RoB\,h_{GPi}} \right) \tag{32}$$

$$f_{oh_{STN_{[n]}}} = C_{STN} \cdot \left(w_{1(CTX-STN)} \cdot f_{oh_{CTX_{[n-1]}}} + w_{2(GPe-STN)} \cdot f_{oh_{GPe_{[n-1]}}} + w_{RoB\,STN_{[n-1]}} \cdot f_{RoB\,h_{STN}} \right) \tag{33}$$

$$f_{oh_{VL_{[n]}}} = C_{STN} \cdot \left(w_{1(GPi-VL)} \cdot f_{oh_{GPi}} + w_{RoB\,VL} \cdot f_{RoB\,h_{VL}} \right) \tag{34}$$

9.4.5.6. The Role of Burstiness: A Hypothesis Derived from the Firing Rate Model

The first set of simulations showed results of divergence for all the firing rates in each of the subpopulations. The divergence was observed as a continuous and uninterrupted increase in the firing rate curves that tended to infinity. This is a physically impossible result that revealed –from a mathematical point of view and for the first time to our knowledge– that **a control mechanism must exist to avoid such divergence within the BGTCC**, and that such mechanism should be unveiled through appropriate time-dependent modeling. Many real physical systems in nature exhibit stable

mathematical behaviors **oscillating around a value**, preventing them from divergence. This would lead the system to a new condition of pseudo-stability around a new mean. Hence, we evaluated the behavior of the network by introducing hypothetical **control mechanisms that we believe there exist in neurons of certain subpopulations to regulate the firing rates in abnormal conditions**.

Our first attempt at looking for the location of the predicted regulatory mechanism was by obtaining an analytical expression that provides the outgoing firing rate with variations proportional to the error with respect to reference values. We believe that such references are the healthy firing rates (initial conditions) for neurons in certain subpopulations in the BGTCC. The error for any deviation from these values would have to be proportional and of an opposite sign to introduce compensation to the system a few iterations later.

$$f_{out_{comp_{[n]}}} = f_{reg_{[n-1]}} \cdot k \cdot \left(\frac{f_{ref_h} - f_{reg_{[n-1]}}}{f_{ref_h}} \right) \tag{35}$$

Equation 35 represents our best presumption for what a natural compensation function would be, based on the error with respect to a reference. $f_{out_{comp[n]}}$ would be the present compensated firing rate per region and $f_{reg[n-1]}$ represents the previous firing rate at the output of a region or subpopulation at the instant [n-1], given by Eq. 28 to 34. f_{ref_h} is the referential firing rate for a healthy state of such a subpopulation. Finally, the factor "k" is a constant of proportionality that indicates the level of compensatory action in a subpopulation per unit error.

If our hypothesis was correct, the results would have to match the temporal boundary conditions, reveal the location(s) of the control mechanism, and explain how this mechanism is manifested in reality.

9.4.6. Modeling the Synchrony in PD

The synchrony of the spikes in a neural subpopulation is another topic of great interest for the scientific community studying PD. Important pathological variations are widely reported in the literature for advanced stages of the disease, characterized by a notably elevated synchrony in the basal ganglia sub-nuclei, especially at the GPe [54], [56], [65], [87]–[90].

Based on the previously explained dependence of the firing rate outputs in neural subpopulations with respect to their inputs, we believe that the synchrony in such subpopulations may be explained by a similar mechanism with different variables. Since the neural spike is produced after the membrane potential exceeds a certain threshold, we paid special attention to what the last pre-synaptic contribution could have been the instant right before the spike. Then, we see different possibilities. For instance, for a neural subpopulation sharing pre-synaptic connections with two neighbor regions we have three potential sources of the last pre-synaptic contribution. Two of them could be neighbor regions, but the third one could be the rest-of-brain connections (RoB), which –in the case of our model– include the self-connections.

The location in time of a neural spike (phase) by subpopulation can be modeled as a random variable (variate) with a Gaussian probability density function, a mean value, and a standard deviation. Then, we can say that **the probability that a neuron fires triggered by a specific neural subpopulation that provided the last pre-synaptic contribution will be the probability that the phase of such pre-synaptic neuron leads to the phases of the other one or two types of pre-synaptic spikes**. Moreover, if the variate represents the phase of each neuron in a subpopulation, with a probability to fire at a particular phase point in a complete period (from $-\pi$ to π), then such probability will represent the ratio of neurons in the post-synaptic subpopulation firing simultaneously, as a consequence of such last pre-synaptic spikes arriving before the rest.

On the other hand, we believe that, differently than what is observed in any healthy neural subpopulation in the BGTCC with notorious asynchrony, the connections represented by the rest-of-brain connections (RoB) are highly synchronous, especially if we consider that part of them include the self-connections coming from the same subpopulation.
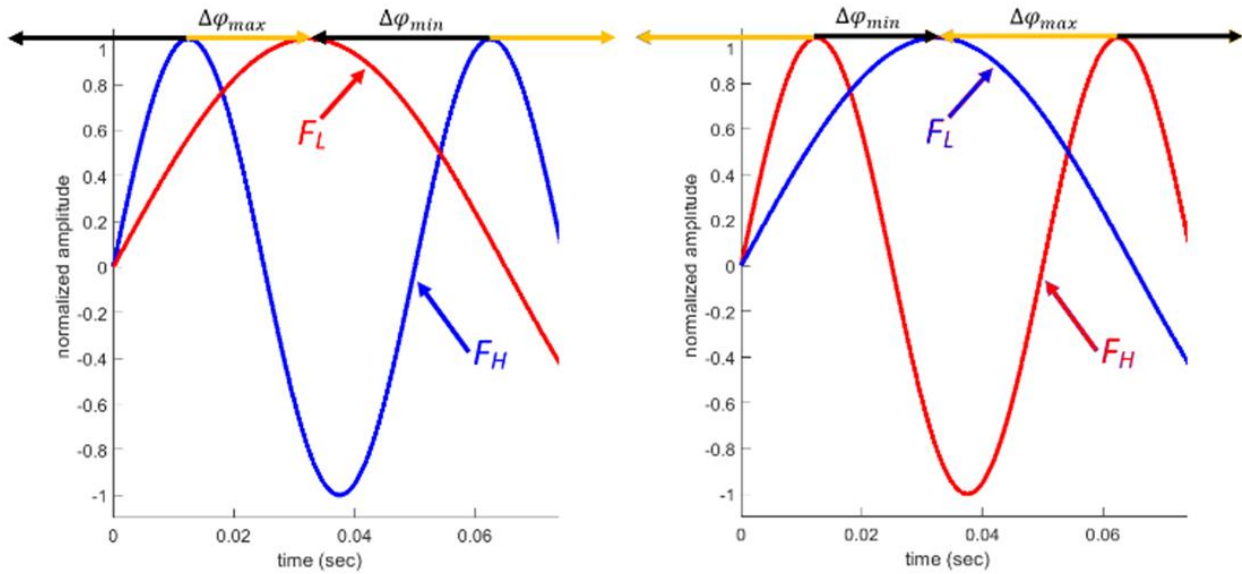
Figure 14 – Referential plot of the phase leading and lagging relation between the sinusoidal versions of the RoB spikes and a neighbor region. a) Case in which $f_{RoB} = f_H \geq f_{reg} = f_L$; b) case in which $f_{RoB} = f_L \leq f_{reg} = f_H$.

9.4.6.1. Sub-Hypothesis of the Synchrony Mechanism

Based on the heretofore mentioned, we hypothesize that the synchrony levels in the BGTCC are given by the probability that the neurons in a subpopulation fire as a consequence of the last spikes provided by a common source, likely from the rest-of-brain (RoB) connections. In other words, we believe that the probability that the phases of the RoB spikes lead the phases of the neighboring presynaptic spikes determines the ratio in which these last spikes, presumably highly synchronized, are the last to arrive and trigger the postsynaptic neurons, almost simultaneously (Fig. 14).

For the calculation of the probabilities, we departed from the assumption that all the variates that represent the phases at the different nuclei (φ_{reg}) have a mean value equal to zero ($\mu_\varphi = 0$), and a standard variation equal to pi ($\sigma_\varphi = \pi$). Under this assumption, any healthy subpopulation has a

theoretical range of variation of the phases from $-\infty$ to ∞, but a practical range between $-\pi$ to π within which they are more likely to fire.

State-space representation of the synchrony model:

Initial (healthy) conditions: $\quad \sigma_{\varphi_{hCTX}} = \pi; \quad \sigma_{\varphi_{hSNc}} = 0 \; ; \; \sigma_{\varphi_{hSTRD1}} = \pi \; ; \; \sigma_{\varphi_{hSTRD2}} = \pi$

$$\sigma_{\varphi_{hGPe}} = \pi \; ; \; \sigma_{\varphi_{hGPi}} = \pi \; ; \; \sigma_{\varphi_{hSTN}} = \pi$$

Final (parkinsonian) conditions: unknown

$$\sigma_{\varphi_{CTX_{[n]}}} = C_{CTX} \cdot \left(w_{1(VL-CTX)} \cdot \sigma_{\varphi_{VL_{[n-1]}}} + w_{RoB\,CTX} \cdot \sigma_{\varphi_{RoB\,CTX}} \right) \tag{36}$$

$$\sigma_{\varphi_{STRD2_{[n]}}} = C_{STRD2} \cdot \left(w_{1(CTX-STRD2)} \cdot \sigma_{\varphi_{CTX_{[n-1]}}} + w_{2(SNc-STRD2)} \cdot ACR_{[n-1]} \cdot \sigma_{\varphi_{SNc_{[n-1]}}} + w_{RoB_{STRD2}} \cdot \sigma_{\varphi RoB_{STRD2}} \right) \tag{37}$$

$$\sigma_{\varphi_{STRD1_{[n]}}} = C_{STRD1} \cdot \left(w_{1(CTX-STRD1)} \cdot \sigma_{\varphi_{CTX_{[n-1]}}} + w_{2(SNc-STRD1)} \cdot ACR_{[n-1]} \cdot \sigma_{\varphi_{SNc_{[n-1]}}} + w_{RoB_{STRD1}} \cdot \sigma_{\varphi RoB_{STRD1}} \right) \tag{38}$$

$$\sigma_{\varphi_{Gpe_{[n]}}} = C_{GPe} \cdot \left(w_{1(STRD2-GPe)} \cdot \sigma_{\varphi_{STRD2_{[n-1]}}} + w_{2(STN-GPe)} \cdot \sigma_{\varphi_{STN_{[n-1]}}} + w_{RoB_{GPe}} \cdot \sigma_{\varphi RoB_{GPe}} \right) \tag{39}$$

$$\sigma_{\varphi_{GPi_{[n]}}} = C_{GPi} \cdot \left(w_{1(STRD1-GPi)} \cdot \sigma_{\varphi_{STRD1_{[n-1]}}} + w_{2(STN-GPi)} \cdot \sigma_{\varphi_{STN_{[n-1]}}} + w_{RoB_{GPi}} \cdot \sigma_{\varphi RoB_{GPi}} \right) \tag{40}$$

$$\sigma_{\varphi_{STN_{[n]}}} = C_{STN} \cdot \left(w_{1(CTX-STN)} \cdot \sigma_{\varphi_{CTX_{[n-1]}}} + w_{2(GPe-STN)} \cdot f_{oh_{GPe_{[n-1]}}} + w_{RoB_{STN[n-1]}} \cdot \sigma_{\varphi RoB_{STN}} \right) \tag{41}$$

$$\sigma_{\varphi_{VL_{[n]}}} = C_{STN} \cdot \left(w_{1(GPi-VL)} \cdot \sigma_{\varphi_{GPi_{[n-1]}}} + w_{RoB_{VL}} \cdot \sigma_{\varphi RoB_{VL}} \right) \tag{42}$$

As shown for the firing rates, phases as random variables should respond to the same time-dependent state-space model expressed as a linear combination of the inputs using the synaptic weights as coefficients. The reason is that the variability and randomness of each of the inputs should contribute to the variability and randomness of the outputs in the same ratios as the synaptic weights. Therefore, we have built the synchrony model similar to the firing rate model, replacing these deterministic frequency variables with the also deterministic standard deviation of the phase (σ_φ) [see Eq. 36 to 42].

The plots of the standard deviation vector (σ_φ) are shown in Fig. 15. Notice how σ_φ has a behavior similar to the firing rates. On the healthy side (left) a fixed value is shown in each of the subpopulations, whereas on the parkinsonian side (right) an oscillating response is observed.
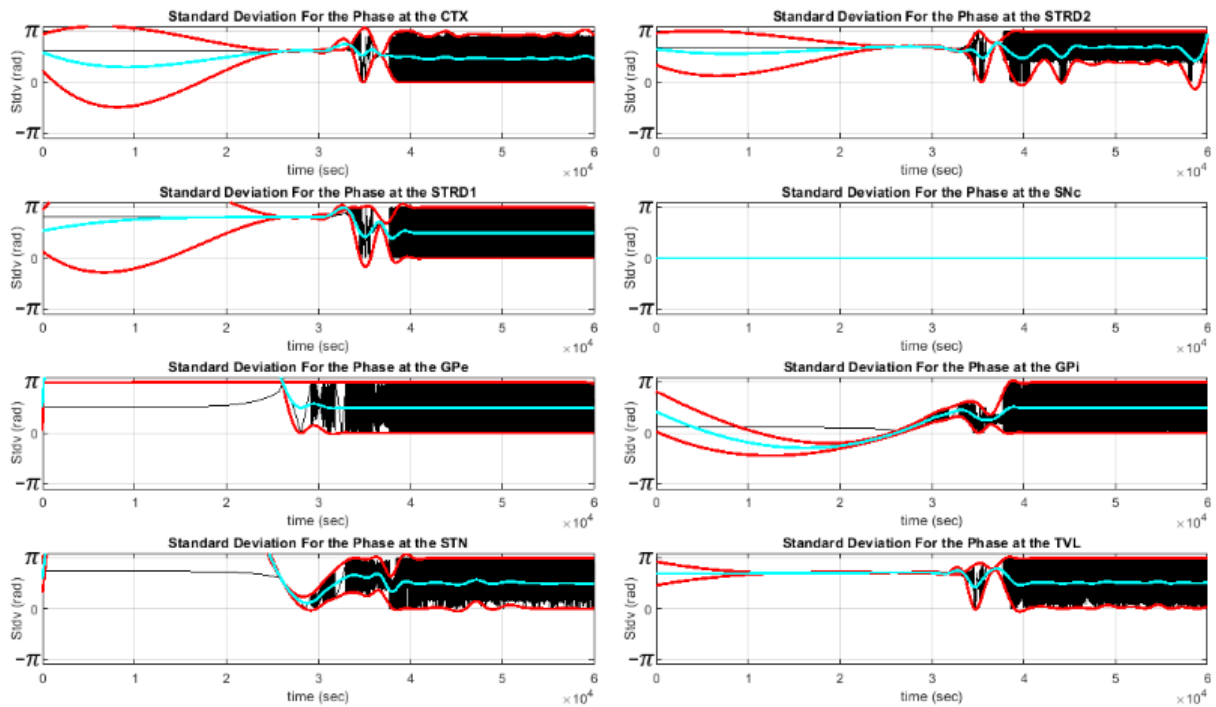
Figure 15 – Results of the simulation of the standard deviation in time with the evolution of PD. Notice how the standard deviation increases in the parkinsonian side for all the BGTCC nuclei, leading to a bigger randomness in the phase of the spikes, which will have an impact in the level of synchrony.

9.4.6.2. Synchrony Calculation

The calculation starts by determining the probabilities that the phase of the RoB spikes is ahead of the phases of the neighbor regions 1 and 2 for each subpopulation. This is done by using a referential scenario with all the spikes coinciding at the instant t = 0 of the analysis. Then, we estimate the range of maximum variation that the location of the spike (phase) can tolerate before the phases of the RoB connection lag behind the spikes of the other two regions.

The range of phase variation tolerable for each neuron of the post-synaptic subpopulation to fire synchronously is calculated using equations 44 and 46 (upper limit) and 45 and 48 (lower limit). f_{RoB} and f_{nr} are the firing rates of the rest-of-brain connections and neighbor regions of each subpopulation in which the synchrony is calculated, with T_{RoB} and T_{nr} being their periods. The value "N" is defined as the integer quotient between f_{RoB} and f_{nr}, with the biggest of them in the numerator.

If $f_{RoB} \geq f_{nr}$:

$$N = \frac{f_{RoB}}{f_{nr}} \tag{43}$$

$$\Delta\varphi_{max} = 2 \cdot \pi \cdot \left(\frac{T_{nr} - N \cdot T_{RoB}}{T_{nr}}\right) \tag{44}$$

$$\Delta\varphi_{min} = 2 \cdot \pi \cdot \left(\frac{(N+1) \cdot T_{RoB} - T_{nr}}{T_{nr}}\right) \tag{45}$$

If $f_{RoB} \leq f_{nr}$:

$$N = \frac{f_{nr}}{f_{RoB}} \tag{46}$$

$$\Delta\varphi_{max} = 2 \cdot \pi \cdot \left(\frac{T_{RoB} - N \cdot T_{nr}}{T_{RoB}}\right) \tag{47}$$

$$\Delta\varphi_{min} = 2 \cdot \pi \cdot \left(\frac{(N+1) \cdot T_{RoB} - T_{nr}}{T_{RoB}}\right) \tag{48}$$

Once $\Delta\varphi_{max}$ and $\Delta\varphi_{min}$ are determined for each combination between the RoB connections and a neighbor region, we proceed to calculate the probability that the variate *"phase"* is located within this range for each subpopulation. This was made by subtracting the cumulative gaussian probability up to the lower limit from the same probability up to the upper limit.

The syntax used for the calculation, similar to the one used in MATLAB is: *normcdf(val,μ_φ,σ_φ)*, where *"normcdf"* is the cumulative Gaussian distribution function, *"val"* is the value up to which the accumulated probability is calculated, and μ_φ and σ_φ are the mean and standard deviation of the phase. Then, the probability that the phase of RoB leads the phases of the neighbor region is given by Eq. 49, using a null mean ($\mu_\varphi = 0$) and standard deviation.
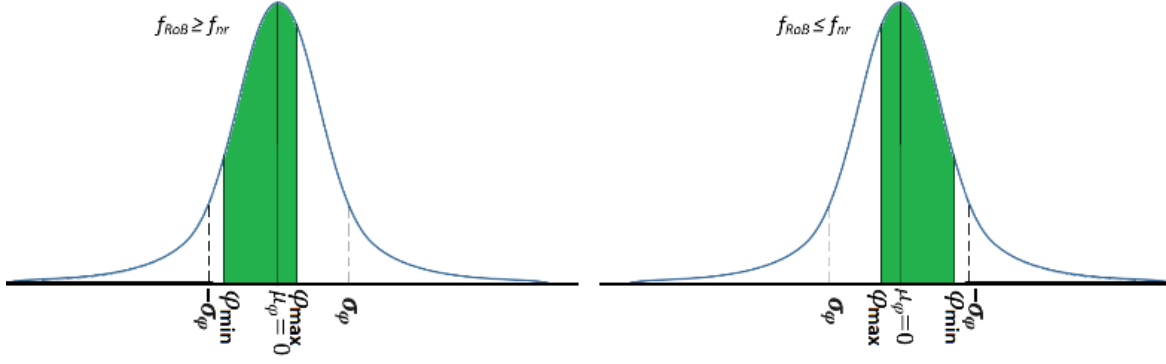
Figure 16 – Normal (Gaussian) probability distribution functions (blues curve) showing the mean and standard deviation of the variate "phase", and the values of maximum and minimum phase variation tolerable. The green area under the curve denotes the probability that the RoB spikes lead the spikes of the neighbor region. The plot on the left corresponds to cases in which $f_{RoB} \geq f_n$ whereas the one on the right side shows the case in which $f_{RoB} \leq f_{nr}$.

$$P_{Reg_1\ RoB} = normcdf\left(\Delta\varphi_{max\,Reg_1} \cdot RoB, 0, \sigma_\varphi\right) - normcdf\left(\Delta\varphi_{min\,Reg_1} \cdot RoB, 0, \sigma_\varphi\right) \quad (49)$$

Finally, using Eq. 49 we calculated the probability that the RoB spikes lead the spikes of a neighbor region 1 ($p_{[\varphi RoB \geq \varphi R1]}$), and also the spikes of a neighbor region 2 in those subpopulations in which it applies ($p_{[\varphi RoB \geq \varphi R2]}$). Thus, we say that the synchrony of the spikes (S) at an instant "n" is the joint probability of both events (Eq. 50).

$$D_{[n]} = p_{[n]_{(\varphi_{RoB} \geq \varphi_{R1})}} * p_{[n]_{(\varphi_{RoB} \geq \varphi_{R2})}} \quad (50)$$

9.4.7. Calculation of DBS and TMS Parameters

Departing from the time-dependent state-space model in Eq. 28 to 34, we calculated the stimulation frequency required in one specific nucleus to produce the *compensation frequency* in its output. For this, we considered the action of any type of neurostimulation by electrical or electromagnetic means, whose objective is to induce ionic currents in the surroundings of the target neurons. Such currents exhibit an associated time-varying electric field able to change the membrane potential in somas and axons. Then, we anticipated that, in presence of any electrical/electromagnetic stimulus with enough power at a certain frequency, such stimulation frequency should be overlapping and replace the action of the pre-synaptic spikes, totally or partially.

If the stimulation at the synapse is partial (the most likely scenario that varies as a function of the volume of influence of the stimulating *E-field*), one portion of the pre-synaptic spikes –by type– will be at the *stimulation frequency*, whereas the rest of them will be at the current firing rate of the neighbor pre-synaptic subpopulations. To simulate these ratios by type of pre-synaptic connection, we introduce three normalized *stimulation ratio coefficients* (C_1, C_2, and C_3) multiplying the synaptic weights and frequencies in the calculation of the output frequency (Eq. 51). Then, the calculation criterium for the adjustment of the coefficients was to produce an output firing rate in the target subpopulation that equals its *compensation frequency* (referential healthy value).

$$f_{o_{target}} = C_{target} \cdot \Big((C_1) \cdot w_1 \cdot f_{stim} + (C_2) \cdot w_2 \cdot f_{stim} + (C_3) \cdot w_3 \cdot f_{stim} \Big) + \cdots \atop \Big((1-C_1) \cdot w_1 \cdot f_1 + (1-C_2) \cdot w_2 \cdot f_2 + (1-C_3) \cdot w_3 \cdot f_{RoB_{target}} \Big) \tag{51}$$

$$stim_{\%target} = (C_1) \cdot w_1 + (C_2) \cdot w_2 + (C_3) \cdot w_3 \cdot f_{stim} \tag{52}$$

$$non-stim_{\%target} = (1-C_1) \cdot w_1 + (1-C_2) \cdot w_2 + (1-C_3) \cdot w_3 \tag{53}$$

Equation 50 shows the calculation of the output firing rate in the presence of a stimulation frequency (f_{stim}). Equation 52 represents the percentage of target effectively stimulated whereas Eq. 53 represents the non-stimulated target that operates at the regular pre-synaptic rates. The sub-products $C_n \cdot w_n$ and $(1 - C_n) \cdot w_n$ provide the specific synaptic weights of the contributions of each frequency component to the new modulated output. In all cases, region 3 corresponds to the RoB connections.

Since the firing rates and synaptic weights represent average normalized values within a subpopulation of neurons, the new synaptic weights multiplied by the coefficients indicate the percentages of neurons of the total subpopulation that should be stimulated with an influence in the synapse with each pre-synaptic region. But stimulating specific synaptic connections in specific neurons is not simply feasible with the current neurostimulation technology, since the area of influence

73

of any device will cover a volume of the target instead. In addition, the rest-of-brain (RoB) connections, including self-connections, are not easily identifiable. Under this scenario, a more reasonable approach seems to be one calculating a unique (common) value for C_1, C_2, and C_3 which means a percentage of the target area to be stimulated.

Based on the previously explained, we attempted to calculate the *stimulation ratio coefficients* for the *compensation frequency* at the GPi, STN, and CTX that lead to a reestablishment of the healthy firing rates in the thalamocortical feedback pathway. The results revealed that no identical values were mathematically possible for C_1, C_2, and C_3 in any of the cases, the reason why we looked for differentiated coefficients. A result of, for example, 0.5 in C_2 and zero (0) in the other two would reveal that half of the neurons of the pre-synaptic region 2 need to be stimulated, while the rest of them should be not. In practice, this is not always possible or easily reachable. The best approach for non-identical *stimulation ratio coefficients* should be then to identify the fiber tracts that connect one neighbor region to another one and stimulate the pre-synaptic axons in areas far enough from the synapses, to obtain differentiated stimulation leaving the rest of the synapses unstimulated. Contrarily to the previous case, in scenarios of identical coefficients, the best approach should be stimulating a percentage of the target region identical to the coefficient on a scale from 0 to 100.

9.5. Results

9.5.1. Transient-state results of the firing rate model

Modeling the degradation of the normal dopaminergic activity through the ACR vector (section III-d.1), we ran simulations of the system in state-space representation a total of 128 times. This quantity corresponds to the number of possible combinations of neural subpopulations that may exhibit

the hypothesized self-regulatory mechanism (from 0 to 7) out of the seven total regions (excluding the SNc). However, before the simulations, we anticipated that the highest probability of convergence would be for one or more of the 15 possible combinations between the GPe, GPi, STN, and VL. The reason is that, for these nuclei, notorious variations in the firing rates, firing patterns, and synchrony are reported in the literature in advanced stages of Parkinson's disease, which we believe is intrinsically related to the mechanism we aimed to find.

The results successfully validated our hypothesis, showing convergence for only 1 out of the 128 combinations, located precisely between the group of 15 identified with the highest probability. The successful combination had the self-regulatory mechanism present at the GPi, STN, and VL nuclei only, diverging for the rest of the cases.

Figure 17 displays the results of the firing rates by region predicted –for the first time to our knowledge– for the entire life of what an average parkinsonian patient would be. These graphs (shown in blue color) are plotted over a normalized subject's timeline to make the results generic and insensitive to the exact patient's age, focusing on the progression of the disease instead. All the plots include upper and lower envelopes (in red) that show the maximum and minimum values between which the firing rates fluctuate at the parkinsonian condition. The black plots under every blue curve show the presence –or not– of the self-regulatory mechanism we predicted. This plot can be also understood as the effort that neurons of a subpopulation do to regulate the outgoing firing rates, once the operation of the BGTCC has become unstable in advanced PD stages.
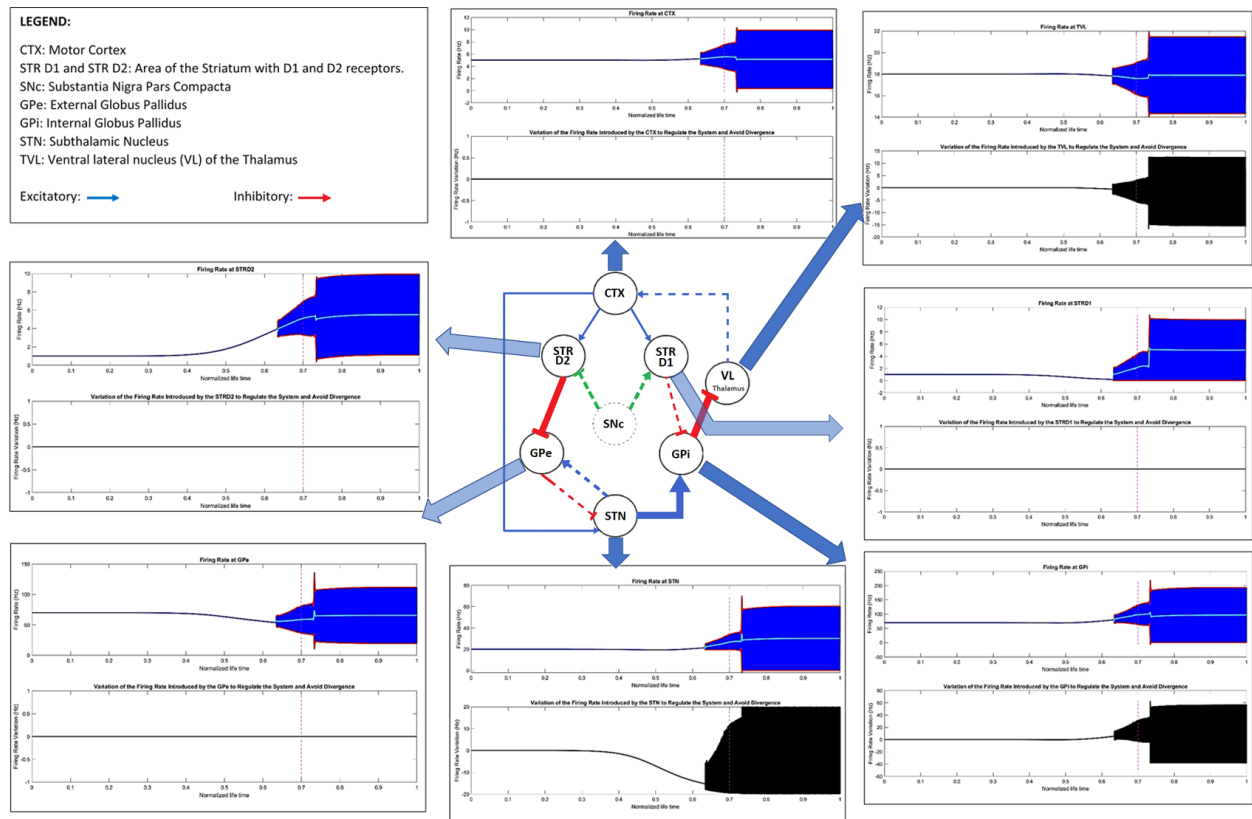
Figure 17 – Results of the firing rates for the simulated topology with the time-dependent state-space model. The firing rates are shown in blue color with the left side representing the healthy end and the right side representing the parkinsonian end. The parkinsonian sides display a transition from constant values to oscillatory curves of the firing rates in time with upper and lower envelopes in red. Notice that the trend line (cyan) in all the cases is the average between the two envelopes, showing how the average firing rate either increases or decreases from the healthy to the parkinsonian condition. Plots in black indicate the compensation/correction action that the mathematical model suggests neurons would do in each subpopulation to regulate the firing rates in their outputs, being observed only in the STN, GPi, and TVL regions.

In Fig. 17, each curve has two ends. The origin represents the healthy side, whereas the far end represents the fully-developed parkinsonian condition. Notice that the progression of all the firing rate curves has a direct relation with the progression of the dopaminergic levels represented by the ACR vector. Moreover, observing the time derivative of the ACR –which for the particular case of the *SNc* has been named *cell degradation rate (CDR)* – we can notice that there is a peak, discretionally located at 60% of the normalized timeline for this simulation.

Shortly before the CDR peak (approximately at 30% of the timeline), we start seeing an increase –or decrease– in some of the firing rates at different subpopulations. However, they still show themselves as a fixed value varying slowly in time but not fluctuating. After such a peak, once passed 60% of the timeline, we can appreciate the emergence of a new oscillatory behavior of the firing rates

and the appearance of the upper and lower envelopes. We have called this the *critical point*. Moving forward from this point, the firing rates in all the plots change from being an exact value to a fluctuating value that grows in amplitude up to a new point of *pseudo-stability*. However, the average firing rates between the envelopes show continuity with the final non-oscillating, exact firing rate value before the *critical point*.

The first major observation of the results occurs at the GPi, STN, and VL thalamus where the neurons perform regulatory actions around their reference values that introduce oscillations of the firing rates to the system with also oscillatory projections downstream in the rest of the network. This way we found that the abnormal firing rates and patterns at the cortex, responsible for a variety of PD symptoms, are a consequence of an attempt of these three regions for keeping the system stable, preventing it from divergence in advanced parkinsonian stages.

Consistent with what the classic parkinsonian model of the BGTCC indicates, and what is mostly reported in the literature for advanced parkinsonian stages, the average outgoing firing rate increases to 10 Hz from the D2 receptor at the striatum, which increases the inhibition of GPe neurons. GPe cells decrease their average firing rate to around 60 Hz, contributing to the rise of the excitatory activity at the GPi through the STN. On the other hand, receptors D1 show behavior that fluctuates between a peak firing rate close to 10 Hz and a lower limit close to 0 Hz but with a lower average firing rate than the reference because of longer silent semi-periods. The overall effect of the direct and indirect pathways increases the activity at the GPi, which is fluctuating again as a consequence of the regulatory actions but with a higher average that reaches the parkinsonian boundary condition of 90 Hz. The increased activity at the GPi ends up inhibiting even more those neurons at the ventral lateral thalamus (VL) which overexcites the motor cortex. An increased firing rate of up to almost 10 Hz peak is observed at the CTX with fluctuations that fall to 0.3 Hz, and an average of 5.1 Hz.

The second relevant observation (common to all the subpopulations) is the fact that the model shows soft and continuous transitions for the firing rates, from fixed values to oscillating values, with bigger or smaller averages. The point of transition is the *critical point* that appears shortly after the peak *CDR* and shows a remaining $ACR_\%$ close to only 40%. In the context of this simulation, the short separation between the peak CDR and the *critical point* is about 2% of the patient's life, which, for a patient with a projected life of 80 years, would be on a scale of about one and a half year. Before the critical point, neurons at the GPi, STN, and VL do not require to perform regulatory actions since the system still converges under those conditions (although to a different operation point than the one at the healthy end). Right at the *critical point*, such neurons start the regulation proportionally to the level of deviation observed in the incoming firing rates and, in consequence, in the outgoing firing rates.

The aspects explained in the previous paragraph mean that all the operation points and firing rates before the *critical point* are compatible with healthy and parkinsonian sub-models of the time-independent approach. However, after the *critical point*, the healthy and parkinsonian time-independent sub-models become incompatible because no solution satisfies both ends with a fixed firing rate. Only the time-dependent approach can cover the entire dynamic spectrum of the disease throughout the complete patient's timeline.

The results showed until this point are called *transient-state results* because they reflect the continuously changing nature of the BGTCC as a system. Contrarily to the most common conception of *transient state* associated with short-duration phenomena and *steady-state* related to long-term behaviors, in this model we will say that the progression of PD is a continuous and uninterrupted *transient state* that lasts the complete patient's life, driven by the variation of the ACR, with short periods of activity in time in which variations are not so significant (approximately invariant). For these

periods, we will say that the system shows a *quasi-steady* response, which could last a few seconds, minutes, weeks, or even months.

9.5.2. Quasi-steady state results of the firing rate model

9.5.2.1. Time scale reduction

The time vector that represents the patient's timeline was designed to have 6,000,001 double-precision points. In a normalized timescale of the patient's life, this vector goes from 0 to 1 with a $\Delta t \approx dt = 1.67 \times 10^{-7}$, equivalent to incremental steps of 0.0000167% of the patient's life. This allows the model to calculate the evolution of the system throughout the entire patient's life without the need to represent every second of it. To provide an idea of how important the time scale is in our model, if we intend to represent the life of –for example– an 80-year-old patient with an accuracy of 10,000 samples/sec without rescaling, that would imply more than 25 trillion double-precision points. That is about 188,000 GB of RAM required per each variable, and there are hundreds of intermediate variables in the system.

In order to make the model computationally feasible, we have designed it to be mathematically solved at a macro temporal scale in which we can observe the long-term transitions (transient state) presented in the previous section. Then, we would downscale such results to obtain more plots at a micro-temporal scale, in the order of one second.

The downscaling process takes place by resampling the results of the *transient-state* solution from a sampling rate of Fs = 60,000 samples/%-of-life to a new sampling rate of Fs = 10,000 samples/sec. This means a transformation ratio of 6 seconds in the micro temporal scale per each 1 % of the macro temporal scale, or 0.167 % of the normalized timeline per each second in the micro temporal scale. The downscaling implies considering all the behavior seen in a time window of 0.167% of the patient's life

in the macroscopic temporal scale (that is only about 48 days in –citing the previous example– a projected life of 80 years) to be quasi-steady and representative of what occurs in a one-second window of the micro temporal scale. This is approximately equivalent to solving the system with a time vector with a sampling rate of 10,000 samples per second for all the seconds that fit in the patient's life, no matter what the final age is. The advantage of this method is the reduction of the computational requirements in a ratio of 2.5 billion to 1, with the possibility to inspect the results on a global scale or an instantaneous spike plot scale.

The downscaling is representative and accurate because it means that, instead of solving the problem with millions of fluctuations in the output throughout decades, we solve it with very few fluctuations first to find the overall behavior, to put them back on the right scale later to find the details. The macro temporal scale provides us with important information such as the firing rate limits and trend lines, the average firing rates, and the low-frequency waveform that represents the progression of the disease in the patient's life. These values are identical to those that would be obtained if we modeled the system for every 0.1 milliseconds in the entire patient's life.

9.5.2.2. Instantaneous firing rates and spike plots

The micro-temporal scale provides us with information about what the instantaneous variations of the firing rates would look like in a one-second window. After the downscaling process, we obtained detailed plots of these instantaneous functions for all the neural subpopulations in BGTCC (Fig. 18).
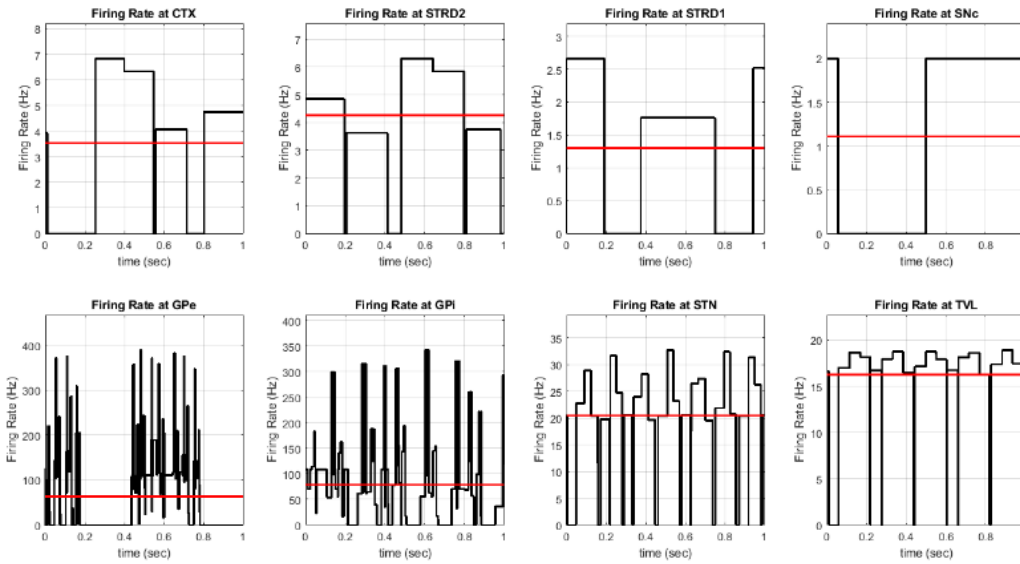
Figure 18 – Instantaneous firing rate functions for an $ACR_\%$ = 40% calculated for a 1-second time window for each subpopulation of the BGTCC. Notice how, after a certain (variable) time interval, the firing rates in the outputs vary as a consequence of either the self-regulatory effects of the same region or the downstream effects of the same mechanism in neighbor regions.

The next step was building concatenated signals of 1 second with sinusoidal functions (cosines) at the frequencies indicated in the instantaneous firing rate plots. These plots have each of the peaks located at the point where the spikes would be (Fig. 19).
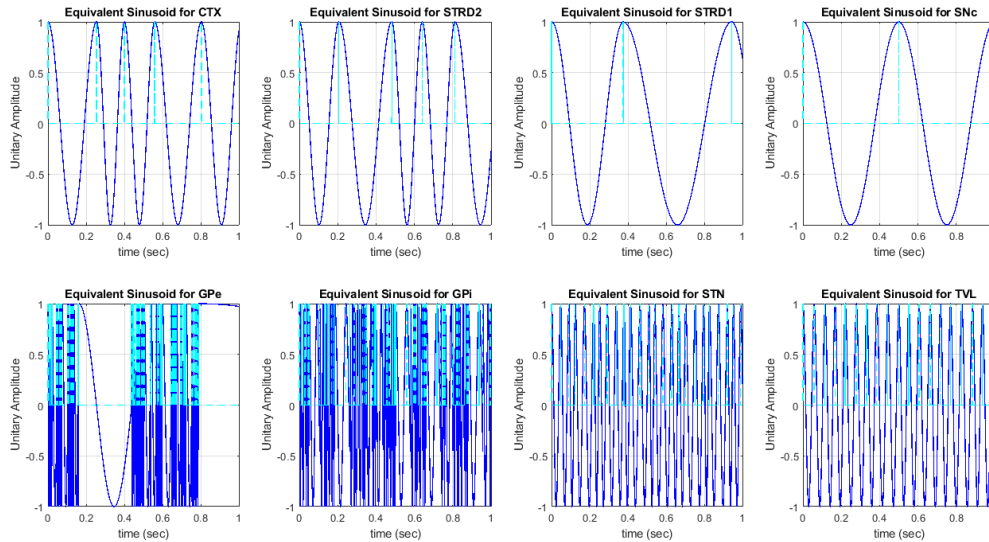
Figure 19 – Process of conversion of the instantaneous firing rates in Fig. 18 to intermediate sinusoidal waveforms of varying frequency accordingly. The location of the peaks represents the point where the spikes would be located.
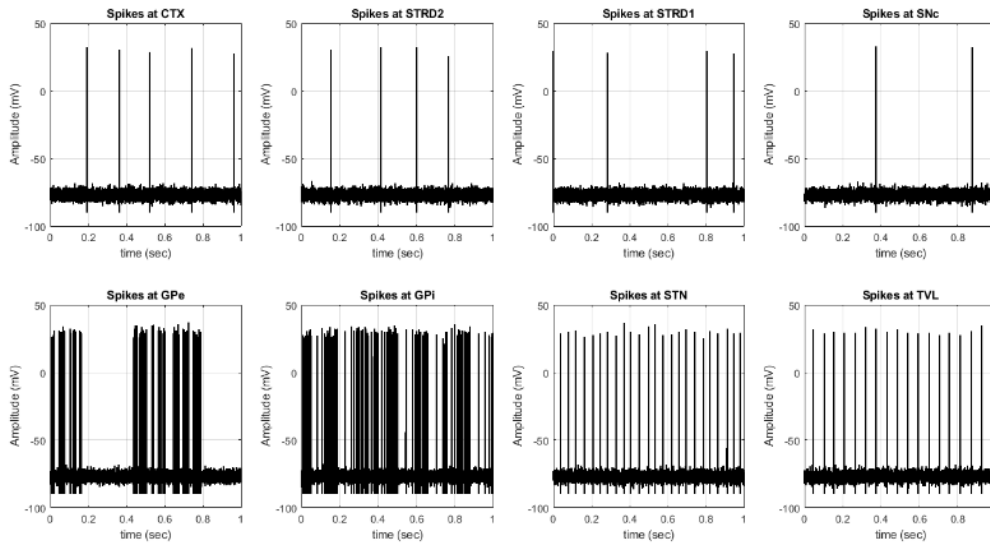
Figure 20 – Spike plots for every region at the BGTCC for an *ACR%* of 40%. These plots were obtained from the downscaling process and instantaneous firing rate functions in Fig. 18. Notice the still tonic pattern at subpopulations such as *CTX* and striatum D1 and D2 receptors, and the burstiness at the *GPe*, *GPi,* and *STN* nuclei.

The final step was creating the spike plots from the sinusoidal waveforms, with the typical resting potential, depolarization peak, and repolarization peak indicated in section II. We also included additive white gaussian noise (AWGN) into the signals of SNR = 30 dB to mimic the real appearance of the train of spikes.

9.5.2.3. Discussion of the results of the time-dependent firing rate model

The time-dependent model revealed –from a mathematical point of view– underlying mechanisms that connect PD symptoms with abnormal firing rates in advanced stages of the disease. From the results, we conclude that the divergence at the parkinsonian brain is a trend because there is only one point of stability, which is the healthy condition. The divergence of the system before the correction of the model led us to understand that the abnormal firing rates in PD are the natural response of the basal ganglia-thalamocortical circuit to degraded operation conditions related to low levels of activity at the dopaminergic pathways. According to the results, this abnormal activity is stable up to an *ACR%* of 50 % approximately, a point at which the *cell degradation ratio* (*CDR*) is maximum. Shortly after that, the low *ACR* turns the system unstable, and the system tends to divergence at all times.

The sudden increase or decrease of the instantaneous firing rate has been identified as the mechanism of neurons at the *GPi*, *STN,* and *VL thalamus* to introduce corrections to their outgoing firing rates according to the current operations conditions, aiming to regulate the entire system. In our model, this was simulated through the calculation of the error between the output firing rate per region and a reference of the healthy firing rate at such a location. However, the exact manner in which this mechanism takes place inside each neuron is not well understood. We theorize that it could be associated with neurons activating internal mechanisms triggered by out-of-range output firing rates that lead them to delay or accelerate their firings through the control of different ionic gates in the membrane. Another possibility is that, instead of being triggered by the own output firing rate, it could be triggered by the out-of-range incoming firing rates at the synapse. In any case, either of the possibilities leads to one of the most well-known and reported behaviors in advanced parkinsonian stages, which is *burstiness*.

Our model showed that the *burstiness* is, in subpopulations such as *GPi*, *STN,* and *VL thalamus*, the mechanism used by neurons to regulate the firing rates in their own regions, but also downstream. This action prevents the system from diverging physically in frequency and provides it with a new state of "*pseudo-stability*" characterized by fluctuations of the firing rates and a mean value instead of a fixed value as in the healthy stage. In other cases, such as in *GPe*, the *burstiness* is not a cause but an effect of the projection of the burstiness of neighbor regions downstream trying to regulate the system.

It is important to highlight that the effects of the parkinsonian stage at the motor cortex (CTX) are better understood once we consider the self-regulatory mechanisms previously explained. All the projections of the bursty nuclei in PD converge at the VL thalamus, the reason why we observe a significant fluctuation in the firing rate at the CTX, under a state of overexcitation from the VL nucleus.

This is a key factor to understand how to plan new treatments based on neuromodulation or drug delivery, by observing the activity at the basal ganglia and their projections to the cortex.

9.5.2.4. Results of the Synchrony Model

The calculation of the synchrony vector has been performed with Eq. 36 to 50 for every instant in the normalized patient's timeline. The results by subpopulation for an $ACR_\% = 40\%$ are shown in Fig.21.
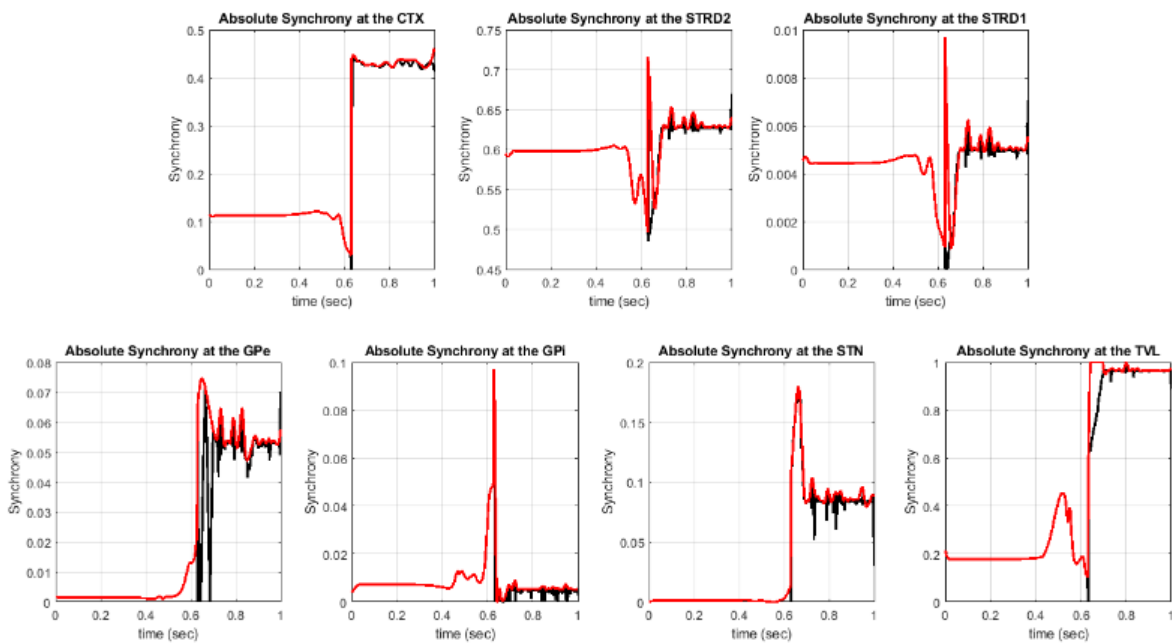
Figure 21 – Synchrony function plots for each of the subpopulations in the BGTCC. Notice the sudden increase in the synchrony after 0.6 in the x-axis (location of the CDR peak in this simulated scenario).

In Fig. 21 we observe increased synchrony in the thalamus (VL) and different sub-nuclei of the basal ganglia (GPe, GPi, and STN) in advanced PD stages ($ACR_\% < 50\%$), as has been widely reported in the literature [54], [56], [65], [87]–[90]. Contrarily to the behavior of the firing rates, the synchrony manifests abrupt transitions from low to high values in all the subpopulations, instead of a soft progression. Another important observation is that such transition occurs at the CDR peak, before the critical point for the firing rates. This indicates that *synchrony* has the potential to be used as an early

indicator of the development of PD since it will be manifested even before appreciable variations in the firing rates.

9.5.2.4.1. Raster plots

Based on the synchrony plots, we defined 100 neurons per sub-population and generated the calculation of the firing instants. The synchrony indicates how many of the 100 neurons fire at the same time exactly over the referential period (reciprocal of the firing rate). For the rest of them, the location was calculated by adding to the referential period a value obtained randomly using a gaussian distribution with a null mean, and the standard deviation previously calculated at each instant. This guarantees that a fraction of the neurons will fire simultaneously and the rest of them randomly around such referential point. This constitutes the inverse method to the typical experimental calculation of the synchrony in an experiment with a certain population of neurons being monitored.
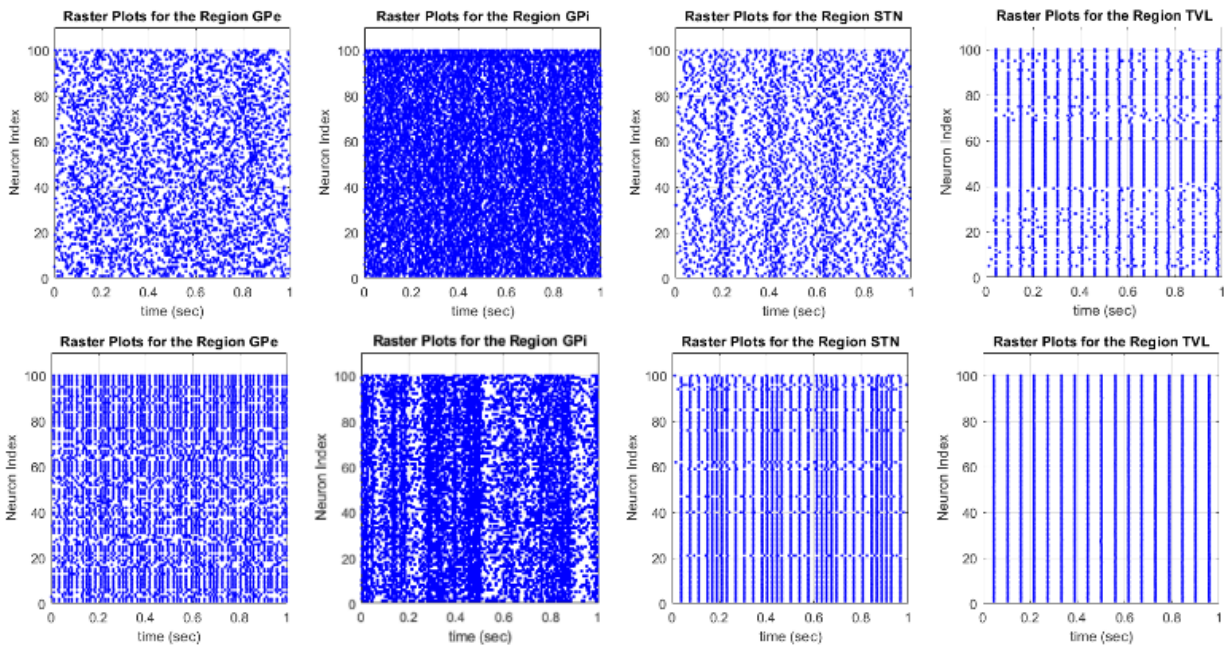
Figure 22 – Raster plots for GPe, GPi, STN and VL thalamus with $ACR_\%=100\%$ (above) and $ACR_\%=20\%$ (below). The GPe, GPi, STN, and VL nuclei show prominent synchrony in the parkinsonian state as predicted.

Figure 22 shows a comparison between the raster plots predicted in the basal ganglia nuclei and VL thalamus at a healthy state ($ACR_\%=100\%$ at $t = 0.2$) and a full parkinsonian state ($ACR_\%=40\%$ at

t = 0.8). Notice how the synchrony in the advanced PD state has increased significantly as a consequence of the increase in the standard deviations of the phases at this point, which makes neurons more likely to fire triggered by the RoB connections.

9.5.3. Determination of neurostimulation parameters

After the development of the model, we were interested in evaluating the ability of the system to extract stimulation parameters for different neurostimulation techniques such as *deep brain stimulation (DBS)* and *transcranial magnetic stimulation (TMS)*. For this, we made observations on multiple simulations forcing the firing rate of one nucleus at a time (target) between the GPi, STN, and CTX to be at a fixed value. This was carried out by modifying the firing rate vector of the target manually, reassigning the fixed value after each iteration during the computing process. Multiple simulations were performed until we observed satisfactory reestablishment of the firing rate at the motor cortex (CTX).

The results in all the simulations revealed that **the most effective stimulation to stop the firing rate oscillations in the BGTCC occurs when the firing rate of the mentioned target is reestablished to the healthy (initial) value**. It is important to clarify that this firing rate –to be called *compensation frequency*– corresponds to the frequency of the spikes that should be reestablished in the target, and not the stimulation frequency required to produce such spikes with any neurostimulation method, which is explained in details in the next section.

The importance of the results lies in the fact that, although the operative conditions in the advanced parkinsonian state have changed with respect to the healthy state, the STN, GPe, and GPi have a strong influence on the regulation of the cortical firing rate through VL-CTX feedback pathway. For this reason, reestablishing the firing rate originally present in the healthy state is as effective as the proximity of the target nuclei to the mentioned pathway.

9.5.3.1. Resulting DBS and TMS Stimulation Parameters

Using Eq. 51 to 53 we calculated the stimulation parameter for DBS applied to STN and GPi and TMS applied to the cortex. The results are shown in Table III.

The results of the parameter calculation show three different scenarios. The first scenario (TMS at the motor cortex) presents identical coefficients, meaning that the entire region needs to be stimulated with a 75 Hz pulse rate. The target should be those cortical neurons with projections to the D1 and D2 receptors in the striatum and those connected to the subthalamic nucleus (STN). The second case (DBS at the STN) requires the stimulation of around 50% of the axons coming from the motor cortex to the STN region. The third scenario is the most complex since it presents uneven non-null coefficients (different from cases 1 and 2). In this case, the stimulation of 93% of the neurons in the GPi, and 100% of the pre-synaptic axons coming from the STRD1 and STN will allow leaving 6.24% of the RoB connections unstimulated.

The stimulation parameters –which include the *stimulation frequency* (f_{stim}) and the *stimulation ratio coefficients*– allow us to understand the specific type of stimulation that is required per nucleus and where to stimulate. The practical usability depends on the specific type of neuromodulation technology and its ability to focally stimulate small target areas of neurons (somas) and/or presynaptic axons.

Table III – Calculated DBS and TMS Stimulation Parameters

Region	f_{stim}	C_1	C_2	C_3	$C_1 \cdot w_1$	$C_2 \cdot w_2$	$C_3 \cdot w_3$	Stim%	Non-stim%
CTX (TMS)	75 Hz	1	1	1	0.57	0	0.43	100%	0%
								Reduction to practice: stimulation of 100% of cortical neurons connected to STRD1, STRD2, and STN.	
STN (DBS)	140 Hz	0	0.5030	0	0	-0.1033	0	10.33%	89,67 %
								Reduction to practice: 50.3% of all the axons from the CTX need to be stimulated.	
GPi (DBS)	175 Hz	1	1	0.6324	-0.4358	0.3922	0.1087	93.76 %	6.24 %
								Reduction to practice: 93.76% of the neurons in the GPi with outputs connected to the VL thalamus and 100% of the axons from STRD1 and STN need to be stimulated.	

Currently, finding the correct stimulation point requires in practice that neurosurgeons and neurologists carefully manipulate the tip of the DBS probe, and voltages in four independent terminals on it, once the probe is implanted within the basal ganglia. This is done with the *implantable pulse generator* (IPG) turned on and tuned to frequencies and voltages tested to be effective in the past.

From the results of the model and parameter calculations for DBS, we understand that the maneuver of manipulation of the probe and voltages performed by the neurosurgeon has the effect of

finding -from a practical standpoint- the stimulation with the exact coefficients for the particular condition. Therefore, the use of the proposed model and methodology would permit better planning of the surgery, identifying routes and locations for the best stimulation of neurons and axons. It would also permit the definition of the IPG voltages and parameters in a more precise manner according to the condition and develop more and better technologies based on non-invasive alternatives such as TMS.

9.5.4. Validation of the Model and Parameter Calculation Method Through TMS and DBS Simulations

Because of the restrictions in the current technology to extract firing rates and patterns from all BGTCC nuclei in healthy human subjects and PD patients, especially in a non-invasive manner, experimental validation of the model with patient-specific parameters is not possible yet. While our team works on new alternatives to perform further experimental validations, other three types of validation methods were applied to the model here developed.

The first validation of the model was obtained through the match found between the average parkinsonian boundary conditions and the predicted outputs of the simulation for an $ACR_\% \leq 20$ %. The average firing rates from the literature for fully-developed PD states coincided in all cases with either the maximum or minimum values simulated for the firing rates, or their average values. Similar results were obtained for the firing patterns and burstiness of the neural activity in the GPe, GPi, STN, and VL thalamus, demonstrating to be significantly more bursty and synchronous that in a healthy state, as the literature reports [31], [34], [37], [53], [66], [70], [73], [76], [81]. The second validation was the finding of calculated stimulation frequencies for DBS in the STN and GPi that are located within the practical range of implementation in clinical DBS protocols (typically between 130 and 185

Hz) [91]–[95]. The third validation was made by using the stimulation parameters calculated for both DBS and TMS, expecting to observe if the behaviors were those predicted with the stabilization of the firing rates at the GPi, VL, and CTX with the *compensation frequency*.

The results of the simulation of DBS in the GPi are shown in Fig. 23-a. The stimulation parameters are indicated in Table III. The green arrow indicates the time interval in which DBS was simulated at the GPi. The *compensation frequency* obtained in this interval was the healthy firing rate for the GPi (60 Hz) –as predicted– with no oscillations. Similarly, the results show a zero-effort compensatory curve segment (orange arrow) for neurons at the GPi during the stimulation window, which stopped the burstiness in the basal ganglia and recovered the tonic pattern in the motor cortex. The downstream effect includes a reestablished firing rate at the VL thalamus similar to the one present in the healthy state, and zero-effort compensatory curves at this nucleus, as well as in the STN and GPi. All these changes after the stimulation of the GPi permitted to reestablish the firing rate in the cortex during the DBS window to exactly at 5 Hz, as in the healthy state.

Besides the firing rate outcomes, the results of the simulation of DBS in the GPi show a significantly decreased synchrony in the GPe, GPi, VL thalamus, and the motor cortex (CTX) [see Fig.23-b]. According to our model, in advanced PD states, the standard deviation of the phase of the spikes decreases for the RoB connections and increases for all the nuclei in the BGTCC. Therefore, the probability that the RoB spikes lead the rest of the spikes is high. Nevertheless, with the stimulation at the GPi, the standard deviation of the phase decreased close to zero due to the synchrony of the stimulation pulses. This reduced also the standard deviations downstream in the other nuclei restoring an asynchrony similar to the healthy state.
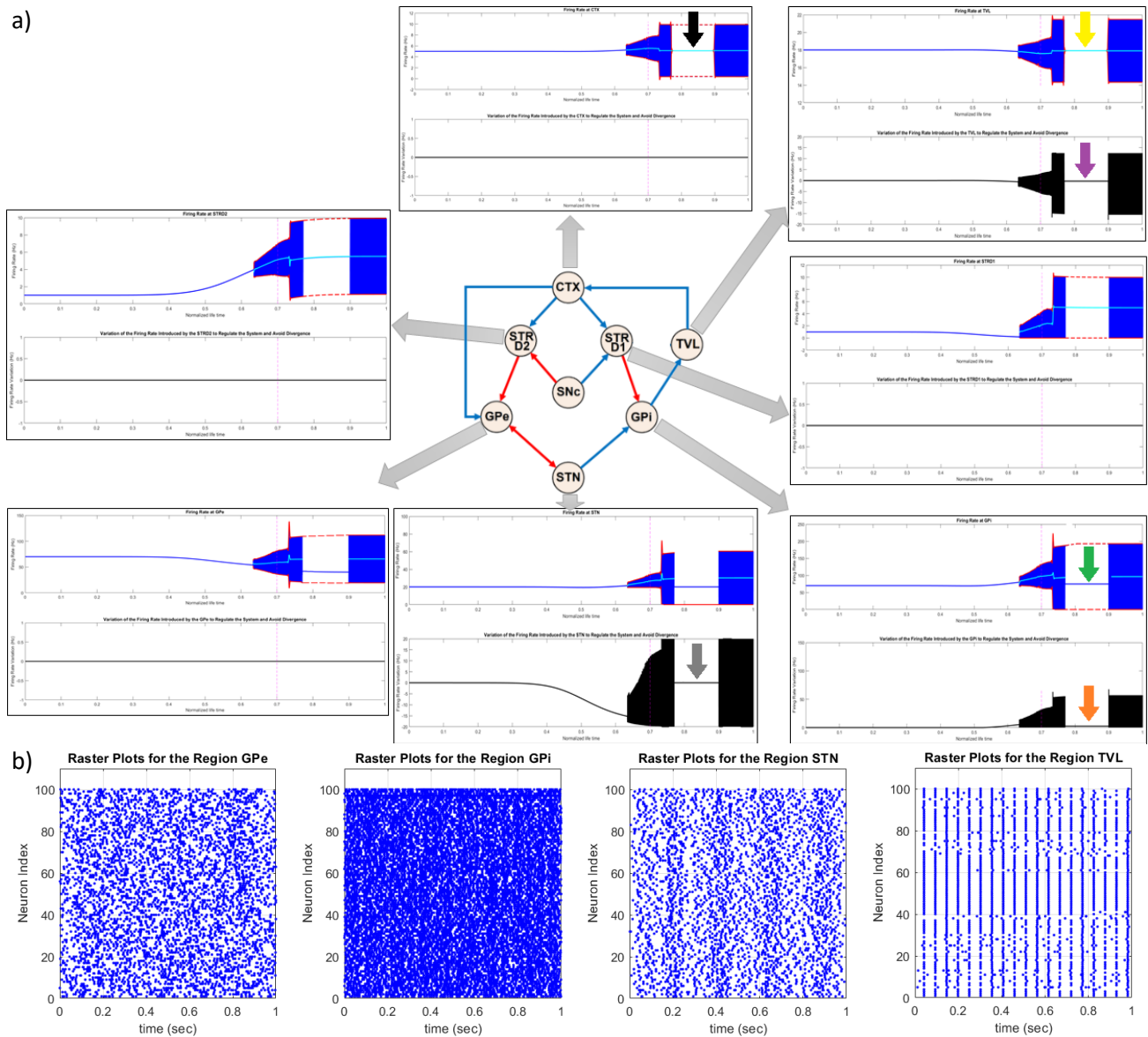
Figure 23 – a) Results of the simulation of DBS applied to the GPi. The green arrow indicates the interval in which a *compensation frequency* is forced at the GPi, which should be the output frequency of the target region while DBS is applied. The green, yellow, and black arrows show the reestablishment of the healthy firing rates through the thalamocortical feedback pathway for GPi, VL, and CTX, respectively. The dark gray, orange, and purple arrows indicate the halt in the oscillatory compensation mechanism in STN, GPi, and thalamus during the same DBS window. b) Results of the raster plots obtained for the (from left to right) GPe, GPi, STN and VL thalamus during DBS of 175 Hz in the GPi. Notice how the asynchrony has been partially reestablished compared to the advance PD state with ACR = 0.2.

The results of the simulation of TMS applied to the cortex are shown in Fig. 24. Notice how the

frequency of the motor cortex is reestablished as a consequence of the stimulation. However, no

stimulation parameter was optimal for the reestablishment of the operation at the GPi and the

thalamocortical feedback pathway. This is because the feedback loop from the VL thalamus prevents

establishing a unique operational point from the cortex to restore the firing pattern in the lowest part of

91

the BGTCC without fluctuations. In other words, TMS recovered values of average firing rates at all the nuclei but failed to produce a fixed value of frequency as in the healthy state. This suggests that TMS could act better for the upper part of the BGTCC where it has a better area of influence than in the basal ganglia. This also means that TMS could be used for combined treatment with DMS, regulating cortical and subcortical nuclei at the same time.
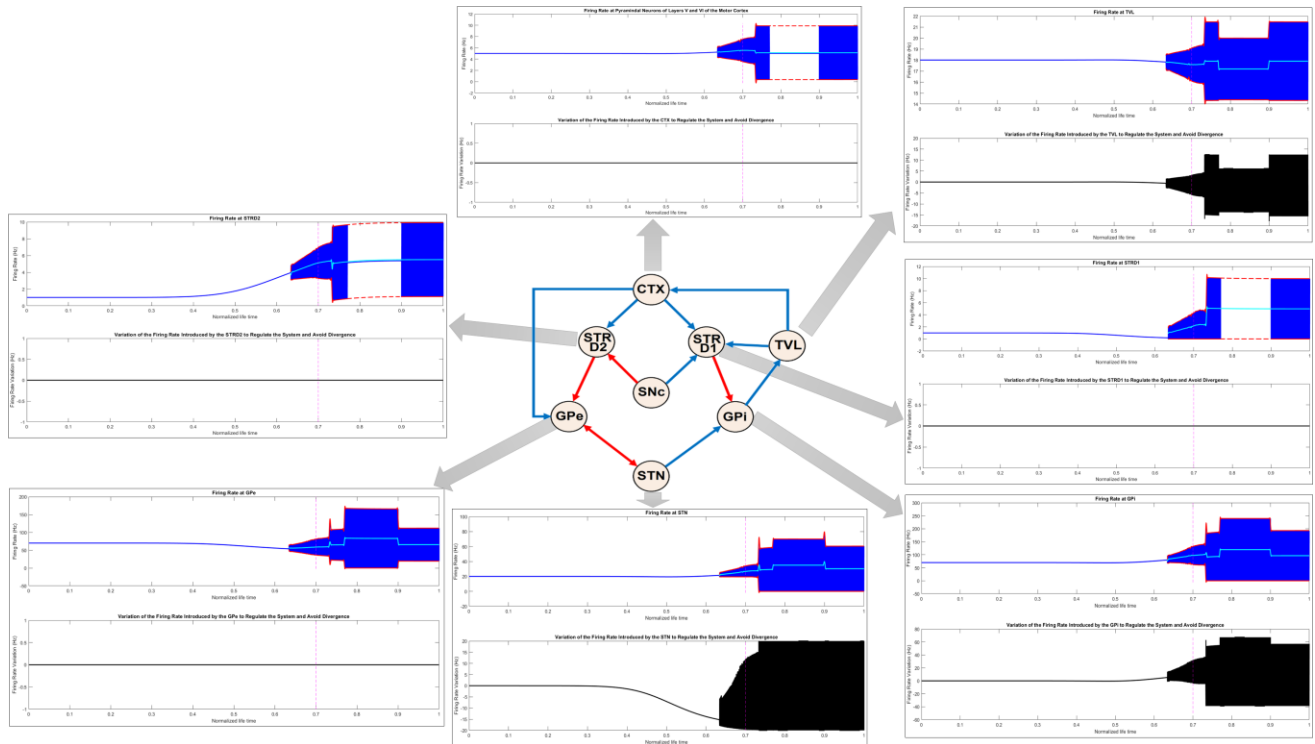
Figure 24 – Results of the simulation of TMS applied to the CTX. Notice how, during the TMS window, nuclei such as GPe, GPi, STN and Vl thalamus do not recover fix firing rate operation. The average values tend to the healthy values (compensation frequency), but the oscillation cannot stop since the regulation in the cortex do not suffice with the parameters tested to have enough influence in nuclei where the compensatory mechanism takes place (GPi, STN an VL).

9.6. Conclusion

The firing rate and synchrony sub-models in state-space representation proved to be an effective, functional, and computationally efficient approach to analyze the BGTCC with revealing results of the progression of PD. For the first time to our knowledge, the complete progression of PD is simulated with a varying resolution from one second to the complete patient's life. Our results suggest from a mathematical point of view that burstiness in PD is the self-regulatory mechanism that takes place at the GPi, STN, and VL to compensate for the instability in the frequency of the system caused by the dopamine depletion. We also suggested what we believe is the mechanism that explains changes in synchrony in the development of the disease with results that match reports in the literature of low synchrony in healthy subjects and high synchrony in advanced PD patients. The oscillatory model of the BGTCC also showed its suitability for the evaluation of neuromodulation treatments such as DBS, TMS, and others, and its feasibility to develop new treatments based on neuromodulation methods and/or drug therapy.

9.7. Summary of Advantages of the Model

9.7.1. From a Neurology Point of View.

- For the first time to our knowledge, the model allows for the simulation of PD <u>throughout the entire patient's normalized timeline</u> as a function of the dopamine levels.

- Dopamine depletion is simulated through a temporal vector called *Active Cell Ratio (ACR)* which represents the percentage of neurons actively firing over the original (healthy) subpopulation in the SNc. The ACR is taken as the only independent variable of the model, and the progression of PD is observed as a function of it.

- The model permits to see firing rate plots with a healthy and a parkinsonian side, as well as spike plots in which patterns of tonic firing and burstiness are observed.

- The model allows observing the progression of firing rates and synchrony in PD on a macro-temporal scale of the entire patient's life, as well as on a micro-temporal scale as small as one second.

- Theoretically, all kinds of existing neuromodulation methods based on electric/electromagnetic means can be simulated and tested, and their stimulation parameters can be calculated. The stimulation parameters include the *stimulation frequency* and *stimulation ratio coefficients*. These coefficients are used to determine where and how to stimulate a combination of complete neurons and pre-synaptic axons to obtain a compensatory effect in the desired nuclei.

- Early-stage indicators of the development of PD can be identified and studied with this model and plan how to treat the symptoms based on neuromodulation and drug delivery.

- The ACR factor could be used, not only to indicate the level of activity of neurons in the SNc but also to evaluate scenarios in other nuclei when a certain drug is administrated to increase/decrease their activity.

- Novel neuromodulation methods and protocols can be developed and evaluated in the model before being put into practice, predicting the effects that they should produce.

- Patient-specific models could be developed in the future to study the condition of subjects with an accurate prediction of the evolution of the disease and the more appropriate treatment to alleviate symptoms.

9.7.2. From a Mathematical/Computational Point of View.

- The model solves the incompatibility of the healthy and parkinsonian time-independent model.

- The problem of the multiple variables (more than 40) representing unknown synaptic weights and firing rates is solved by using both deterministic and statistical methods, obtaining values that math the healthy and parkinsonian boundary conditions.

- The system is converted from a multiple-input multiple-output (MIMO) system to a parametric single-input multiple-output (MIMO).

- The model provides a computational saving of RAM in a ratio of 2.5 billion to 1. This makes it possible to simulate the complete progression in the patients' timeline that would not be otherwise possible with computational neural network approaches.

- The nature of the system, being an analytical model, provides the user with the ability to inspect, manipulate and evaluate values and behaviors at intermediate states of the computing, differently from the limitations provided by conventional computational neural networks.

9.8. Summary of Relevant Findings

- The firing rate in advanced PD states demonstrated to become unstable, being a natural tendency of the system to diverge (increase indefinitely) in frequency.

- We found that the natural response of the BGTCC to such a tendency in advanced PD states seems to be a compensatory effect in some neural subpopulations. We demonstrated mathematically that the STN, GPi, and VL thalamus are such nuclei and there is enough evidence from the results to believe that they are the only ones responsible for the regulation of the complete network.

- We found, from a mathematical standpoint, that such a compensatory mechanism must be responsible for instantaneous increases and decreases in the firing rates to produce a new pseudo-stability that stabilizes the firing rates. The firing rates oscillate then around a new mean in these compensatory

nuclei and the same oscillatory behavior is observed in the firing rates of the rest of the BGTCC as a consequence.

- We understood that the burstiness in advanced pathological PD states must be the mentioned regulatory mechanism. In other words, the model revealed that the burstiness exists in PD as a natural response of the BGTCC to new operation conditions after dopamine depletion. Under these conditions, only a new oscillatory pseudo-stability is possible in frequency, leading to a combination of low-frequency, silent, and high-frequency bursty periods.

- We hypothesized that the synchrony in spikes of the same neural subpopulation is given by the probability that the neurons fire as a consequence of a last highly-synchronized common pre-synaptic input that we named rest-of-brain connections. This group of connections should come from regions different than the pre-synaptic neighbors (outside the BGTCC) and should also include the self-connection of each subpopulation.

- Based on the results, we concluded that the elevated synchrony in the GPe, GPi, STN, and VL thalamus of PD patients should be a function of an increased standard deviation of random phases with low values in healthy subjects. The dopamine depletion should also affect the randomness of the phases as it modifies the firing rates in the evolution of PD, which explains the progression of synchrony in time, leading to severe PD symptoms.

- Although the synchrony model demonstrated to match the reported behaviors for both healthy and parkinsonian states, we believe this particular sub-model requires more study seeking experimental evidence of the behavior here described.

9.9. Future Work

Future work is in progress to create non-invasive TMS technology that will allow validating the model experimentally in rats. We are also working on methods to convert this technique into patient-specific models to be used in treatment planning, diagnostic, and early indicators studies.

10. **Chapter II: Innovative Methods for Transcranial Magnetic Stimulation at High Frequency**

10.1. Problem # 2:

Current technologies in transcranial magnetic stimulation work in a relatively well-defined range of frequencies, usually up to 3 kHz [40]–[42]. Although this is not a strict value, the restriction is mainly imposed by the typical physiological response of neurons to induced time-varying E-fields and current densities during TMS, at frequencies below this limit.

Rigorously speaking, there is no theoretical restriction for the frequency of an electromagnetic pulse to produce an interaction with the ionic species of the extracellular environment of neurons. However, for a neuron to be induced to fire, the duration of the stimulating pulse should be long enough to allow the membrane potential to grow up to the depolarization threshold [96]–[98]. This means that low frequencies –whose periods are longer– give the neuron enough time to reach the threshold, whereas the small periods of high frequencies do not permit this to occur. This aspect appears by itself to reduce the frequency requirements to the minimum possible.

Despite the heretofore mentioned, another important reason forces designers to contrarily make the frequency in TMS as high as possible. According to *Faraday's Law of induction*, the resulting electric field, obtained from the variation in time of an applied magnetic field, is a direct function of the time derivative of its magnetic flux density (*B*). This implies that the higher the frequency of *B*, the higher the resulting time derivative and, therefore, the *E-field* magnitude. Consequently, the definition of a suitable frequency of operation in TMS is a tradeoff between a low value that makes the membrane depolarization possible and a reasonably high value for an adequate *E-field* strength. An appropriate value of frequency of TMS pulses is typically between 2 kHz and 3 kHz in practice.

From a parametric analysis of a typical TMS coil, it is easy to understand that there is a direct dependence between the size of the coil and the frequency. The lower the frequency of operation, the lower the impedance of the coil, which needs to be compensated with more turns to produce the

required magnetic field and *E-field* magnitude in the target. In addition, with the typical frequencies in TMS, very high intensities of current are needed through the conductors that form the coil, usually in the order of a few kilo amperes (kA). This forces the conductors to use the biggest cross-sectional area possible for power dissipation, again, increasing the size of the coil significantly.

When a high focality of the electric field is sought, the size of the TMS coil becomes a critical problem. Many published works in the field show efforts to obtain focal coils based on the manipulation of the geometry (shape), having the same restrictions in terms of current intensity, power dissipation, number of turns, and size. In this respect, the use of high frequency in TMS is desirable, and would be highly attractive in the field as it would permit:

    a) To reduce the size of the coils.

    b) To decrease the current intensity and power requirements in general for TMS stimulators.

    c) To increase the focality on small targets.

    d) To improve the penetration depth for deep TMS applications.

Questionably, the use of high frequency is not possible with the current conception of the TMS technology, likely because the operation frequency is perceived as a parameter that must meet the physiological requirements for neuron stimulation, instead of being conceptualized as a means for energy transfer. However, some efforts have been made to introduce high frequency to some neuromodulation methods. Such is the case of the recently introduced temporal interference (TI), a technique in which high-frequency components are applied through electrodes to obtain a superposition of signals inside the brain tissue. The temporal interference produces envelope modulation, a type of modulation that generates a low-frequency component in the envelope of the resulting signal that neurons can detect. This was demonstrated by Grossman *et al* in [99] and constitutes our starting point

to propose operation at even higher frequencies. Grossman and his co-authors worked for the first time demonstrating the response of neurons to envelopes, but their work was made with electrodes (*transcranial alternating current stimulation, tACS*) and not with *transcranial magnetic stimulation* (TMS). This work is much more challenging because of the implication of working with coils of high impedance at high frequency.

Another high-frequency neurostimulation work relevant to mention as a background was made by Xin *et al* in [100]. They study for the first time the possibility of temporal interference at TMS through simulations with moderate frequency (5.01 kHz). Although their results were pioneering in the area, they claim in their work that the main limitation of the technology is the considerably high current and frequency, with limitations in the thermal management in the hardware.

An additional problem related to the frequency is found in clinical settings, when patients manifest their discomfort in TMS sessions, due to the loud and annoying sound caused by the pulse of current in the coil. In this respect, although the use of frequency components out of the audible range has been theorized [41], [101], [102], once more, the constraint of the frequency (under the premise that it needs to directly stimulate the neuron, with a limited pulse duration) prevent researchers from using significantly higher frequencies and alternative neuromodulation methods.

10.2. Hypothesis # 2:

High-frequency modulated current, used with appropriate neuromodulation techniques, permits the frequency shifting of the stimulation energy out of the current TMS band, and its final recovery inside the brain, with soundless and effective neural stimulation. Similarly, it allows using smaller coil

sizes, lower power requirements, higher focality, and greater penetration depths, compared to those used by current TMS technology.

10.3. Rationale # 2:

Transcranial magnetic stimulation (TMS) is based on the application of time-varying magnetic fields from outside the head, to induce an electric field over the cortical surface of the patient. According to the Maxwell-Faraday equation in vector form (1), which describes Faraday's Law of Induction, the magnitude and spatial variation of the E-field are functions of the variation rate of the magnetic flux density.

$$\nabla \times \vec{E} = -\frac{\partial B}{\partial t} \tag{54}$$

In its complex form, Eq. (54) can be re-written as in (55), indicating that the time derivative of B can be seen as a *frequency dependence* in steady-state.

$$\nabla \times \vec{E} = j\omega\vec{B} \tag{55}$$

On the other hand, the integral form of (54) is shown in Eq. (56).

$$\oint \vec{E} \cdot dl = \iint_{s} \vec{B} \cdot ds \tag{56}$$

Developing (3) for a regular solenoid of a circular cross-section of radius r, where a constant and homogeneous distribution of the B-field is assumed, it is possible to demonstrate that:

$$2\pi \cdot r \cdot |E| = \pi \cdot r^{2} \cdot \omega \cdot |B| \tag{57}$$

Finally, replacing ω by $2\pi \cdot f$ and simplifying, we have:

$$|E| = \pi \cdot r \cdot f \cdot |B| \tag{58}$$

Equation (5) demonstrates how the frequency would be a key factor for the increase of the magnitude of the electric field without increasing the magnetic flux density (B). This would allow decreasing significantly the current required to produce such magnetic flux density in the TMS coil. However, the use of high frequency (f), as explained before, would not permit neurons to be directly stimulated, because of the low-pass behavior they exhibit, the reason why this option has been disregarded in the field so far.

After an analytical inspection of the expressions (1) to (5), we observed that the frequency variable "f" –and its equivalent angular frequency "ω"– are the result of the time derivative of the sinusoidal waveform of the B-field. Therefore, for a B-field of the form "$A \cdot Cos(2 \cdot \pi \cdot f \cdot t)$", the term "$2 \cdot \pi \cdot f$" in the argument will multiply the magnitude "A" when the time derivative $-\partial B/\partial t$ is calculated in (1). But, again, at this point, the stimulating frequency is possible to be only in the range $f \leq 3$ kHz for the neurons to be able to respond.

From the communication theory, we know that –as a variable– the frequency is part of the channel encoding required to send a message through a transmission medium. Such message could be in its original range of frequencies (baseband), or in a higher/shifted range of frequencies that make it more appropriate for its transmission (modulated). In the telecommunications area, modulation techniques are used to reduce the power of transmission, the size of the antennas, and obtain multichannel access to the medium, among other advantages. In the Biomagnetics Laboratory, we are convinced that we can use similar techniques of analog modulations –originally conceived for communication purposes– to produce better technology for transcranial stimulation (TMS) with increased performance and reduced technical requirements.

10.3.1. High-Frequency Amplitude Modulation

Going back to the waveform of the magnetic flux density (*B*), assume that the operating frequency is intentionally selected to be out of the TMS range (i.e., ≥ 3kHz), in a frequency tone that we will call *carrier frequency, "f_c"* (see Fig. 25 a-b). This will automatically make the induced *E*-field ineffective to stimulate the neurons. Now, assume that we can multiply this *carrier* tone by a different tone of unitary amplitude, and frequency within the TMS range (i.e., ≤ 3kHz). We will call this second component "*message frequency*" (*f_m*) or "stimulating tone" (Fig. 25 c-d). Expression (6) contains this product as shown next.

$$B_{(t)} = [A_m \cdot \cos(2\pi \cdot f_m \cdot t)] \times [A_c \cdot \cos(2\pi \cdot f_c \cdot t)] \tag{59}$$

where A_c is the amplitude is the carrier tone. For the example represented in Fig. 25: $f_m = 1$ kHz, $f_m = 10$ kHz, $A_m = 1$ and $A_c = 5$.

Now, we say that the amplitude of the high-frequency *carrier tone* is modulated by the low-frequency *stimulating tone*. This means that the envelope formed by the peaks of the resulting *high-frequency product signal* will vary following the waveform of the *stimulating tone* (Fig. 25-e).

In other words, the *amplitude-modulated signal* implicitly contains the waveform of the *stimulated tone* (*f_m*), in a version of higher frequency (*f_c*), meaning that the stimulating tone has been shifted in frequency. In Fig. 25-f it is observed the frequency shifting of the AM signal obtained with the *Fast Fourier Transform (FFT)*, showing two sidebands (single tones shown as deltas), located at $f_c - f_m$ and $f_c + f_m$ (9 kHz and 11 kHz, respectively for this example). An additional tone at the *carrier frequency f_c* (10kHz) is also observed as part of the AM modulation process, to provide the signal with more power.
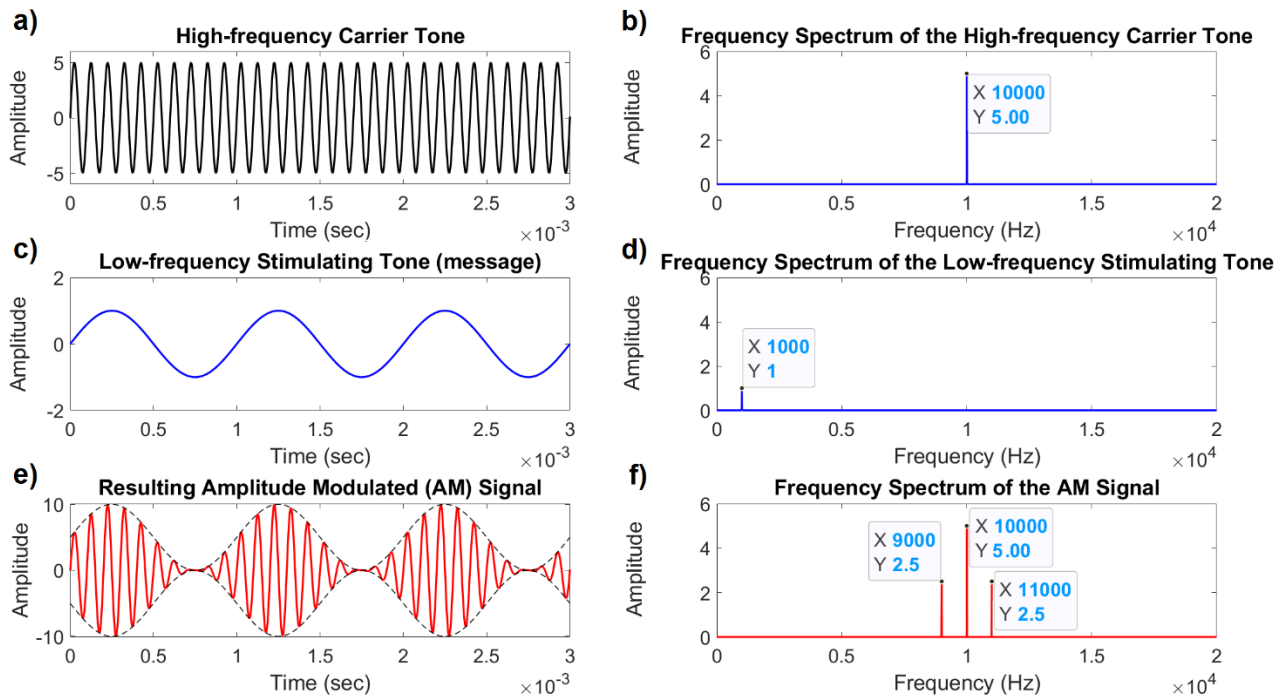
Figure 25 – Amplitude modulation process. On the left side, the signal in the time domain. On the right side, their frequency spectra calculated with the *Fast Fourier Transform (FFT)*.

At this point, we can observe through the amplitudes of the deltas, how the power/energy content (depending on whether the pulse is repetitive or not) of an amplitude-modulated signal is shifted in frequency to occupy a bandwidth of $BW = 2 \cdot f_m$. This will occur over a frequency band between $f_c - f_m$ and $f_c + f_m$, which clearly shows that, if the AM signal represented the induced *E*-field with TMS, it would be applied as an *out-of-band/modulated* signal to the brain tissue, which would not directly stimulate the neurons. However, it would contain the original stimulating tone and energy to be recovered back to the baseband through different methods to be tested.

10.3.2. Theory of the Demodulation Process and Stimulation Baseband Recovery

Because of the lack of reference in the literature about this specific novel topic, our main uncertainty before the design of the new high-frequency neurostimulator was how the neurons would

respond to the presence of an amplitude-modulated *E-field*. For this, we have theorized three (3) possible response mechanisms, each of which leads to a different method for the demodulation and recovery of the stimulating tone over the brain tissue. Hence, during the design process, we needed to provide the stimulator with the ability to operate under all these three scenarios.

10.3.2.1. Sub-hypothesis # 1 about the neuron response to the Modulated E-field

The first sub-hypothesis of the neural response to the AM/DSM E-field states that, although the symmetry between the upper and lower envelopes, neurons would respond to only one of them, acting as a voltage follower with a rectifier diode.

Name of the demodulation method: Auto-demodulation based on the natural envelope-detection behavior of the neuron membrane.

Rationale: We depart considering the voltage-triggered ionic channels in the neuronal membrane and the inertial characteristic of the ionic species, whose mass would prevent them from being suddenly accelerated/deaccelerated at high frequencies (Fig. 26 a and b). These are two possible causes for the ionic currents to flow in just one direction at high frequency. Based on this, we believe that neurons could exhibit the behavior of a rectifier to the high-frequency amplitude modulated waveform of the *E*-field around them (Fig. 26-c). This behavior, in addition to the low-pass filter characteristic of the neural membrane, would make neurons act as a natural envelope-detector circuit that would auto-demodulate any amplitude modulated signal, recovering the stimulating envelope within the TMS frequency range.
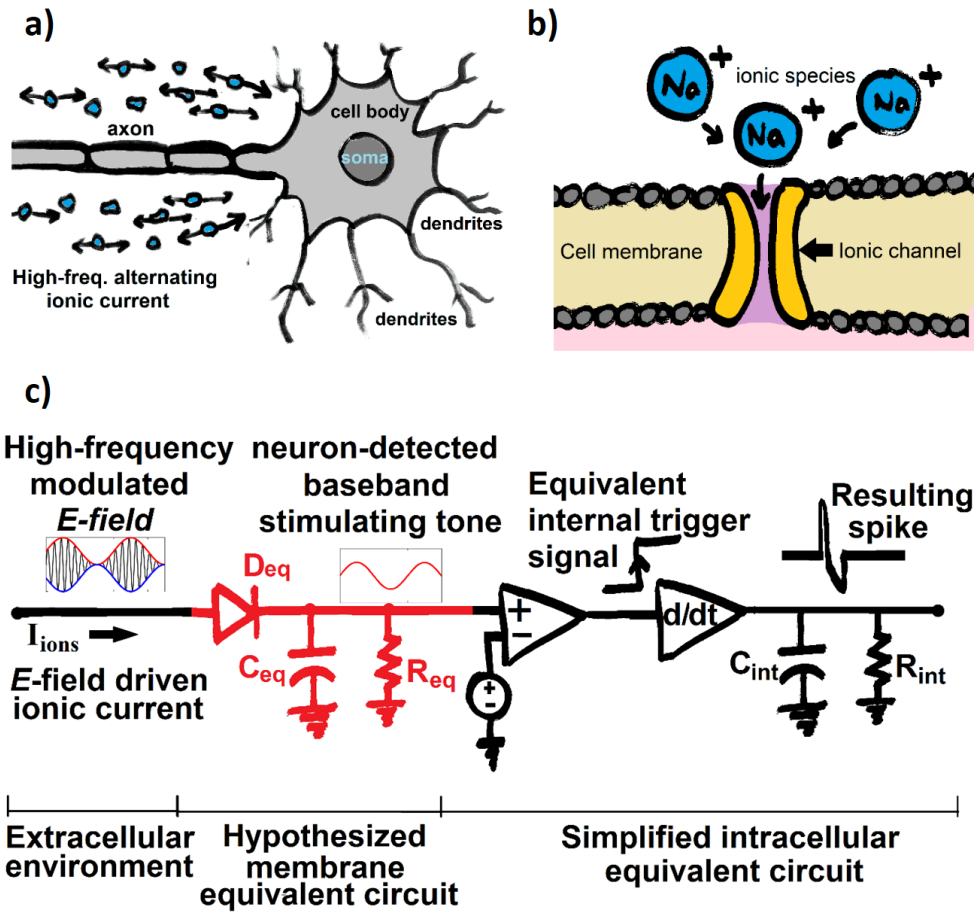
Figure 26 – a) Representation of the neural extracellular environment with ionic currents flowing around. b) Representation of the neuron membrane and the Na+ ion motion through it. c) Equivalent circuit diagram of the envelope-detection behavior with rectifier neuron membrane hypothesized for the neurons at high frequency.

10.3.2.2. Sub-hypothesis # 2 about the neuron response to the Modulated E-field

Because of the symmetry between the upper and lower envelope of the AM/DSB signal, neurons would try to respond to both of them, observing a null average *E*-field.

Name of the demodulation method: Induced asymmetry of the amplitude modulated signal.

Rationale: If the amplitude modulated signal is rectified from the pulse generator or made asymmetric concerning their envelopes by adding a DC offset, neurons would respond to the average electric field, which should have a waveform identical to the upper envelope, being the lower one a constant equal to zero (Fig. 27).
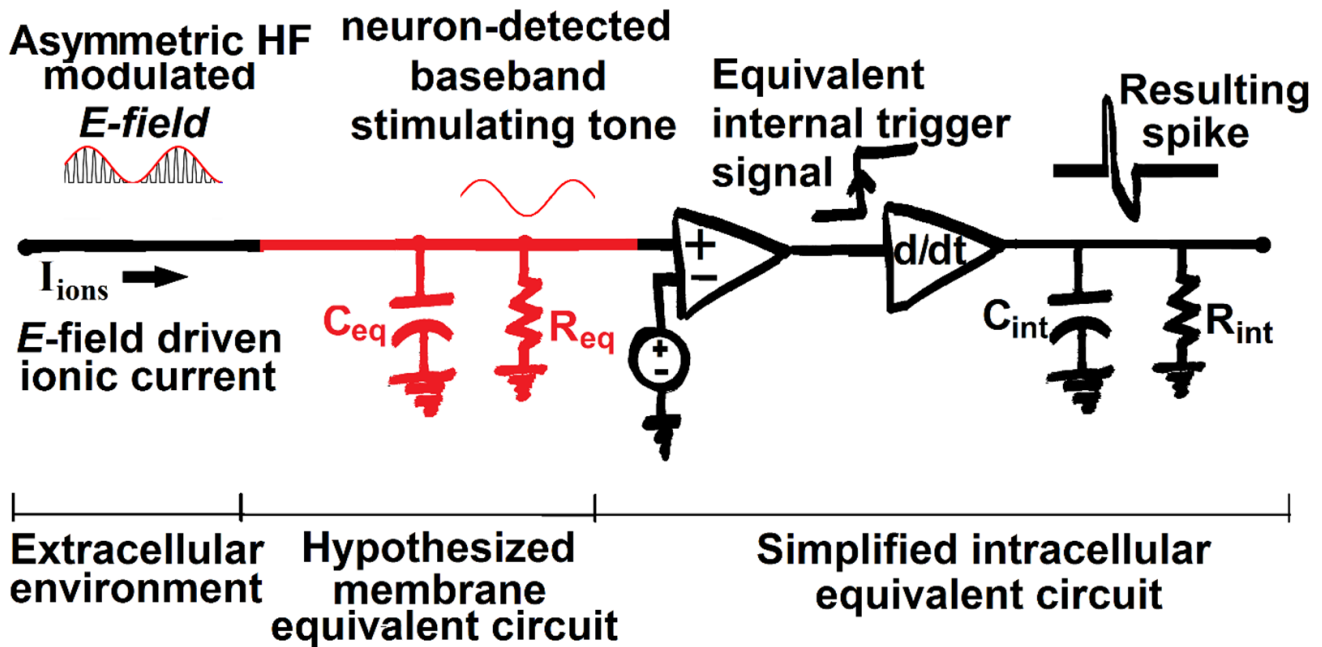
Figure 27 – Equivalent circuit diagram of the sampling-and-hold behavior (with no rectifier) hypothesized for the neurons at high frequency. It is theorized that the neurons can detect the low-frequency envelope from an asymmetric (circuit-rectified) AM signal.

10.3.2.3. Sub-hypothesis # 3 about the neuron response to the Modulated E-field

Because of the high frequency, neurons would not able to follow any of the envelopes and detect them.

Name of the demodulation method: Induced demodulation with superposition of a secondary induced E-field.

Rationale: If the neurons do not respond to any of the previous methods, then the demodulation would be induced by applying an additional E-field from a secondary coil, with a sinusoidal (non-modulated) waveform at the frequency of the carrier (Fig. 28). This would produce two new frequency components located at the frequencies of f_m (frequency of the message) and $2f_c$ (twice the carrier frequency). The last one ($2f_c$) would be a modulated high-frequency component and would be ignored by the neurons, according to the assumptions of this scenario. The first component (f_m) would be the

original baseband *stimulating tone* recovered from the envelope, to which the neurons should respond if the *E-field* magnitude is above the firing threshold.
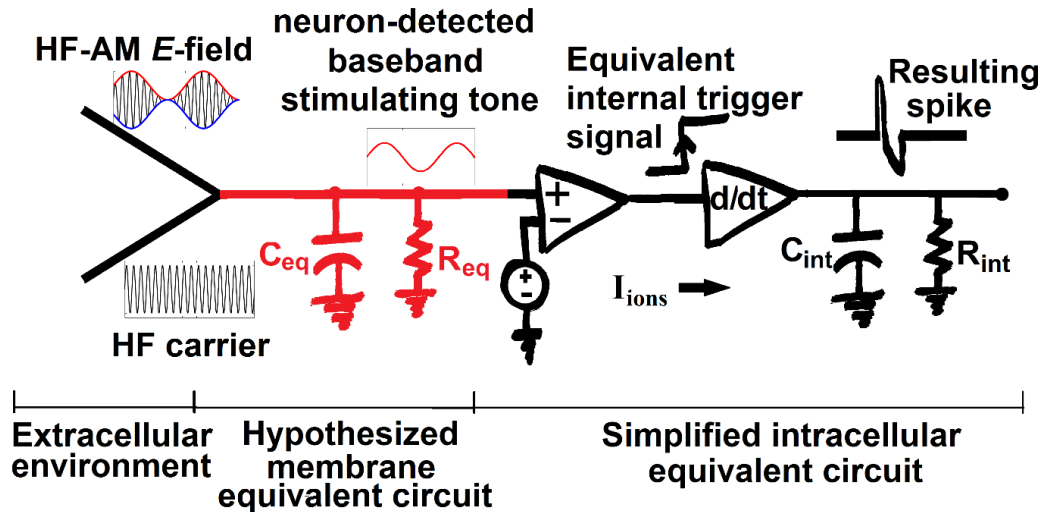
Figure 28 – Same equivalent circuit as in Fig. 27, with two induced (modulated and non-modulated) E-fields. For this case, it is theorized that the neurons are not able to detect the low-frequency envelope by themselves. Therefore, induced demodulation is enforced when the E-fields of the AM signal and the non-modulated carrier overlaps in a constructive interference over the brain tissue.

10.4. Methodology # 2:

10.4.1. Analytical Derivation of the HF Neurostimulation Method for TMS using AM/DSB Modulation.

In the first stage, we conceptualized the high-frequency neuromodulation method and obtained analytical expressions that allow us to explain the dependencies of the electric field in the target on different variables. For this, we departed from the expression of the amplitude modulated voltage that would be obtained in the stimulator terminals and obtained the expressions for the electric current and magnetic flux density in a solenoidal coil of a given inductance (L). The coil includes a ferromagnetic core of AISI 1010 carbon steel (studied in the third objective) including the non-linear characteristic of its *magnetic flux density vs magnetic field* (B-H) curve. Then, we calculated the electric field in the target, whose waveform would be similar to the modulated output voltage in the stimulator terminals with the low-frequency stimulating tone in the envelope. Finally, we calculated the amplitude of the

recovered envelope to determine the magnitude of the *E*-field that would be seen by neurons. This magnitude should exceed the stimulation threshold of neurons in the motor cortex, which is assumed to be 100 V/m, according to what is reported in the scientific literature [4]–[8].

10.4.1.1. Voltage in the Coil:

Defining the voltage in the terminals of the stimulator as a high-frequency carrier of amplitude A_c and frequency f_c, modulated in amplitude by a message (stimulating tone) of amplitude m and frequency f_m, we have:

$$V_{AM} = A_c.\cos(2 \cdot \pi \cdot f_c \cdot t) \cdot [1 + m \cdot \cos(2 \cdot \pi \cdot f_m \cdot t)] \tag{60}$$

which can be demonstrated is equivalent to:

$$V_{AM} = A_c \cdot \cos(2 \cdot \pi \cdot f_c \cdot t) + \frac{A_c \cdot m}{2} \cdot \cos(2 \cdot \pi \cdot [f_c - f_m] \cdot t) + \frac{A_c \cdot m}{2} \cdot \cos(2 \cdot \pi \cdot [f_c + f_m] \cdot t) \tag{61}$$

In (2) it is observed the summation of three tones seen in the frequency domain as Dirac Delta functions at the frequencies of f_c, $f_c - f_m$, and $f_c + f_m$. The first tone is the *carrier* signal, whereas the other two are called *sidebands*. Because $f_c \gg f_m$, Eq. 61 demonstrates the frequency shifting of the energy from the low-frequency stimulating tone to high frequencies around f_c.

10.4.1.2. Current in the Coil:

Now, the current in the coil will be:

$$I_L = \frac{1}{L} \cdot \int V_L \cdot dt \tag{62}$$

In steady-state, Eq. 62 is equivalent to the complex form:

$$I_L = -\boldsymbol{j} \cdot \frac{1}{\omega \cdot L} \cdot V_L, \tag{63}$$

with $\omega = 2 \cdot \pi \cdot f$, being f the frequency of each tone present in the signal. The imaginary number $\boldsymbol{j}$ indicates a change of phase in the waveform of $+90°$ (lagging angle of the current with respect to the voltage).

Then, the final expression for the current in the coil will be:

$$I_L = \frac{A_c}{\omega_c \cdot L} \cdot \sin(2 \cdot \pi \cdot f_c \cdot t) + \frac{1}{2} \cdot \frac{A_c \cdot m}{\omega_{LSB} \cdot L} \cdot \sin(2 \cdot \pi \cdot f_{LSB} \cdot t) + \frac{1}{2} \cdot \frac{A_c \cdot m}{\omega_{LSB} \cdot L} \cdot \sin(2 \cdot \pi \cdot f_{USB} \cdot t), \tag{64}$$

where $f_{LSB} = f_c - f_m$ is the frequency of the *lower sideband*, $f_{USB} = f_c + f_m$ is the frequency of the *upper sideband*, and ω_{LSB} and ω_{USB} are their equivalent angular frequencies.

10.4.1.3. Magnetic Field in the Coil:

For the calculation of the analytical expression of the magnetic flux density (B) in the coil, we depart from its relationship with the magnetic field intensity (H) through the magnetic permittivity of the core material (μ), as follows.

$$B = \mu \cdot H \tag{65}$$

Once more, the magnetic permittivity μ is the product of the magnetic permeability of the vacuum ($\mu_o = 4\pi \times 10^{-7} \frac{H}{m}$) and the relative permittivity of the core material (μ_r) in our case, AISI 1010 carbon steel. Nevertheless, the ratio between B and H in Eq. 65 is not constant along the entire domain of H, the reason why we have used the typical B-H curve for AISI 1010 carbon steel to calculate the

magnetic flux density (see Fig. 29). Then, the magnetic permittivity, instead of being a constant, will

be a function of H (*i.e.*, $\mu_{(H)}$).

Now, the magnetic field intensity (H) can be written as a function of the current (I_L) circulating

through the coil. Then, the resulting magnetic flux density (B) will be:

$$B = \mu_{(H)} \cdot \frac{N \cdot I_L}{l},$$ (66)

where N is the number of turns in the coil, l is its length (height), and I_L is the modulated current

defined in Eq. 64.
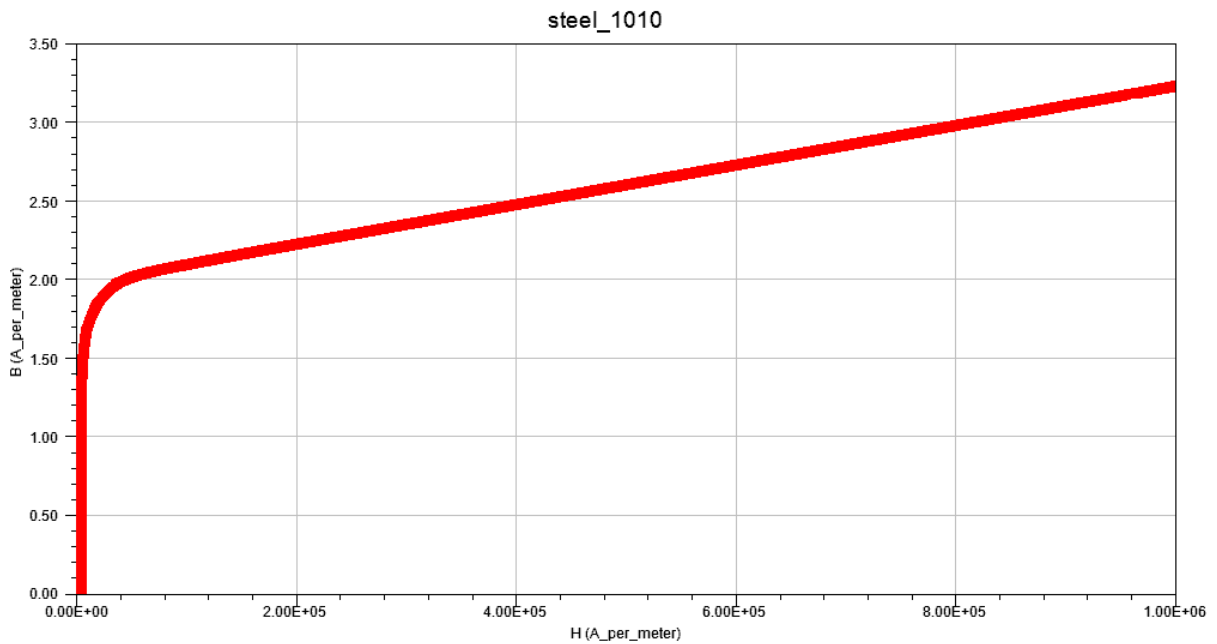
Figure 29 – B-H curve for AISI 1010 carbon steel, showing a linear region of fix slope in the beginning, and then a saturation point at approximately 2 T.

10.4.1.4. Electric Field in the Coil:

Departing from the Maxwell-Faraday equation that describes Faraday's induction law,

we have:

$$\nabla \times \vec{E} = -\frac{\partial \vec{B}}{\partial t} \tag{67}$$

This expression indicates that the electric field –and particularly its spatial variation– is a consequence of the variation in time of the magnetic field, expressed as the rate of change of its magnetic flux density B. In its integral form, this expression is equivalent to:

$$\oint_l \vec{E} \cdot dl = -\int_A \frac{\partial \vec{B}}{\partial t} \cdot dA, \tag{68}$$

which is equivalent to:

$$\oint_l \vec{E} \cdot dl = -\frac{\partial}{\partial t} \int_A \vec{B} \cdot dA \tag{69}$$

But the surface integral of the flux density in an area gives us the net magnetic flux Φ. Then, eq. (69) becomes:

$$\oint_l \vec{E} \cdot dl = -\frac{\partial \Phi}{\partial t} \tag{70}$$

Assuming a homogeneous distribution of the resulting magnetic flux density, that does not vary with the radius in its area of influence in a transversal plane below the coil, B becomes a constant in Eq. 69. Then, the flux will be the product of the flux density B by the area A:

$$\oint_l \vec{E} \cdot dl = -\frac{\partial \vec{B} \cdot A}{\partial t} \tag{71}$$

On the other hand, with a homogeneous distribution of B in an area of radius r, the E-field leaves the line integral and the expression becomes:

$$\vec{E} \cdot l = -A \cdot \frac{\partial \vec{B}}{\partial t} \tag{72}$$

In (72), l and A are the length and area of the region influenced by the homogeneous magnetic field. Assuming a circular profile coming from a solenoid of circular shape and core, Eq. (72) becomes:

$$\vec{E} \cdot 2 \cdot \pi \cdot r = -\pi \cdot r^2 \cdot \frac{\partial \vec{B}}{\partial t} \tag{73}$$

which is finally simplified to:

$$\vec{E} = -\frac{1}{2} \cdot r \cdot \frac{\partial \vec{B}}{\partial t} \tag{74}$$

Now, an alternative expression for Eq. 74 in its complex form is:

$$\vec{E} = -\boldsymbol{j} \cdot \frac{1}{2} \cdot r \cdot \omega \cdot \vec{B} \tag{75}$$

Once more, the imaginary number $\boldsymbol{j}$ indicates a change of phase, which with the negative sign results in a shifting of -90° in the waveform (leading angle with respect to the E-field).

Finally, taking modulus in both terms, and replacing ω by $2\pi f$, the expression 75 can be simplified to:

$$\boldsymbol{|E| = \pi \cdot r \cdot f \cdot |B|} \tag{76}$$

At this point, with equations (60), (64), (66), and (76), we have the analytical expressions that define the system modulated in amplitude up to the electric field right at the core-air interface.

Assume that $\alpha_{B(z)}$ is the attenuation factor (in m^{-1}) that describes the reduction of magnetic flux density (B), as a consequence of the spreading in the z-direction. Then, Eq. (76) is redefined as:

$$\left|E_{(z)}\right| = \pi \cdot r \cdot f \cdot |B| \cdot e^{-\alpha \cdot z} \tag{77}$$

Now, let $H_{n(f)}$ be the transfer function that describes the neuron response to frequency as a low-pass filter. Then, the magnitude of the E-field seen by the neurons ($|E_{n(z)}|$) at a depth "z" will be:

$$\left|E_{n(z)}\right| = \pi \cdot r \cdot f \cdot |B| \cdot e^{-\alpha \cdot z} \cdot H_{n(f)} \tag{78}$$

Finally, the stimulating tone recovered from the envelope of the E-field seen by the neurons is:

$$\left|E_{n(z,f_m)}\right| = \pi \cdot r \cdot f_c \cdot |B| \cdot e^{-\alpha \cdot z} \cdot \frac{m}{2} \cdot H_{n(f_m)} \tag{79}$$

In the eq. (79), the term $\frac{m}{2}$ applies for auto-demodulation (envelope-follower behavior) of the neurons with either balanced or unbalanced envelope. However, if the demodulation method needs to be *enforced demodulation* with a secondary coil and a single carrier tone of amplitude A_{C2}, the term $\frac{m}{2}$ must be multiplied by $\frac{A_{c2}}{2}$.

10.4.2. MATLAB Simulations of the HF Neurostimulation Method for TMS using AM/DSB Modulation

In a second stage, we developed end-to-end simulations of the entire neurostimulation process, using MATLAB software (The MathWorks, Inc.). On it, we used the analytical expressions derived in the previous section to generate time-domain plots, as well as frequency-domain analyzes using *Fast Fourier Transform* (*FFT*). The MATLAB simulations allowed us to dynamically vary important parameters of the system, such as currents, frequencies, and radiuses, among others, which permitted us to adjust design parameters for the physical neuromodulator equipment that would be built in the next stage. Both the analytical results and simulation results would allow us to verify the feasibility to reach an *E*-field magnitude in the target of 100V/m with the neurostimulator that would be manufactured later.

The simulation process started by defining the parameters of the stimulation coil such as the number of turns and geometric dimensions, inductance, resistance, core material, and relative magnetic permeability of it. Then, we defined the voltage in the stimulator terminals as an AM/DSB signal of a certain amplitude. This amplitude is a value that we would actively manipulate before any new execution of the algorithm to find the necessary voltage to produce a 100 V/m E-field.

When applied to the coil, the waveform of the current is the integral of the voltage. This produces an associated time-varying magnetic field of the same waveform as the current. Finally, the time-varying magnetic field induces an electric field that will have the same waveform as the voltage.

The inductor simulated was a 20-turn, 4-layer coil with a height of 10 mm and an outer diameter of 15 mm. The core material used was a cylinder of AISI 1010 steel with a diameter of 3 mm and a height of 10 mm. The stimulation tone used was 1.5 kHz. The carrier frequency used was 25.5 kHz.

The electric field was calculated in a circular area of the same diameter as the one in the core, both immediately below the coil and 4.25 mm away. This last distance would represent the distance from the top of the scalp to the pyramidal neurons of layers 5/6 in the primary and secondary motor cortex. The first calculation was for the modulated induced electric field at the mentioned two distances. This *E*-field still has the stimulation energy shifted out of the TMS baseband. The second calculation was made for the demodulated *E*-field seen by the target neurons as a consequence of the superposition of the modulated signal and the non-modulated carrier. All the calculations follow the mathematical expression obtained in the analytical deduction previously explained.

The recovery process of the low-frequency tone has been represented in this case by a 2nd order low-pass filter of cut-off frequency $f_{cn} = 6.5$ Hz. The cut-off frequency was calculated as $f_{cn} = 1/(2 \cdot \pi \cdot \tau_n)$, where $\tau_n = 24.49$ ms is the typical decay constant of the cell membrane for pyramidal neurons of layers 5/6 in the motor cortex [68]. This *low-pass filter behavior* is intrinsic to the neuron and independent of the method of demodulation that results to be effective.

Our main concern during the design process was the attenuation that the magnetic flux density undergoes in the typical depth between the top of the scalp and the pyramidal neurons of layers 5/6 in the motor cortex. This depth is typically 4.25 mm. According to simulations presented in Chapter 3, and experimental results we obtained with coils at

25.5 kHz with AISI 1010 core, the expected attenuation in the mentioned distance is in the order of 50%, which we used to calculate E and B at the target.

10.4.3. Process of Design and Construction of the High-Frequency Neurostimulator and Coils

The third stage has been the design and manufacture of the customized high-frequency neurostimulator based on AM/DSB modulations, as well as the TMS coils required to perform proofs of concepts and measurements. These devices have been designed with the characteristics defined in the previous analysis and simulation stages.

10.4.3.1. Initial Design and Prototyping

In this stage, all the signal generation, treatment, and filtering stages of the circuitry were fully designed and tested. In Fig. 30, a general view of the original circuit diagram is shown, along with images of the circuit prototype built on a 6-column breadboard. The power source used has been set as a 3 terminal dual output of $\pm 12V$ + ground. The current consumption at this stage was only 90 mA. In Fig. 30-c it is possible to observe a set of knobs (potentiometers) used for the adjustments of different parameters such as bias voltage of the message (DC level), envelope balance, maximum amplitude, and modulation index.

Fig.31 shows the preliminary results of the obtained amplitude modulated voltage in the output of the stimulator. As observed in Fig. 31-a-e, the modulation index can be varied

to be in full modulation (modulation index m = 1), under modulated (m < 1), or over modulated (m > 1). Since the modulation index m is designed to vary in a range from 0 to 1 (0 to 100%), this parameter will be used to control the final amplitude of the stimulating tone, seen by the neurons during experimental work, according to Eq. 79.

Fig. 31-f and g show the frequency spectrum of the AM signal in Fig. 31-a, where is observed the presence of the carrier tone and the sidebands at the frequency of f_c = 25.5Khz, f_c - f_m = 24Khz, and f_c + f_m = 27Khz, with amplitudes of 19 dB, 10 dB, and 10 dB, respectively.

The last part of the prototyping stage was the design of a power electronic stage that consisted of the implementation of an H-bridge with pulse with modulation (PWM) on it. This would permit the conversion of the continuous modulated voltage waveform into a signal between logic 0's and logic 1's, allowing the power transistors to operate in the cut/saturation mode. This is a very important part of the system since, without it, it would
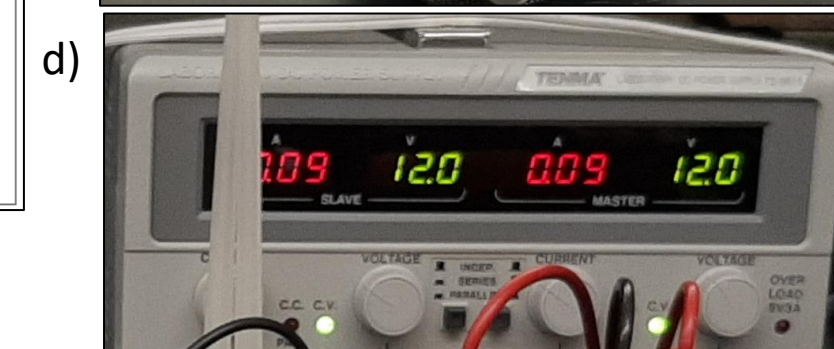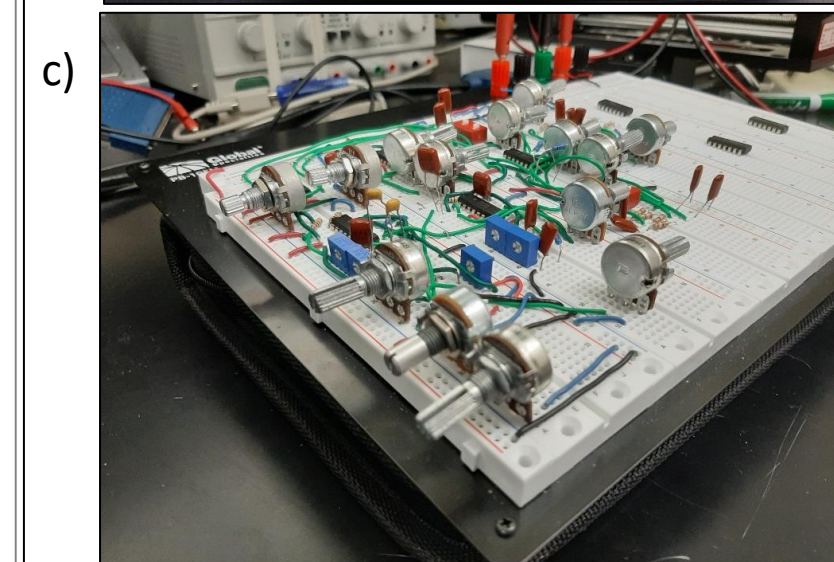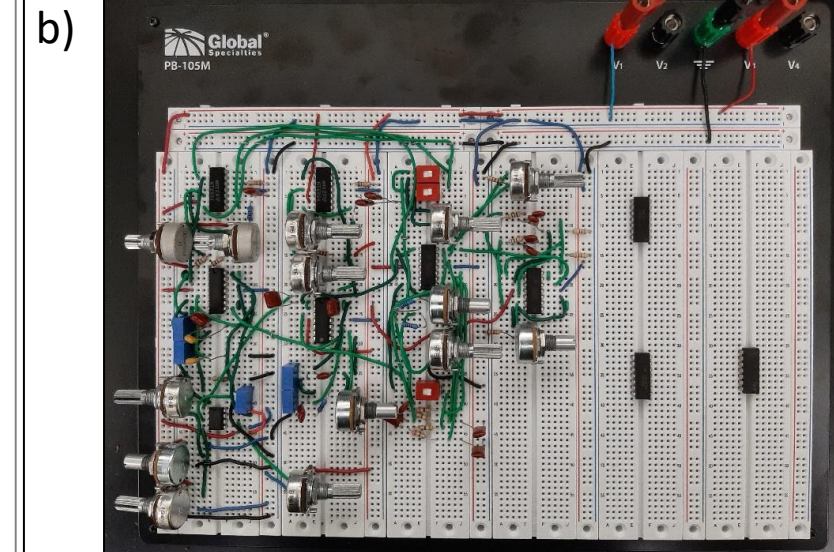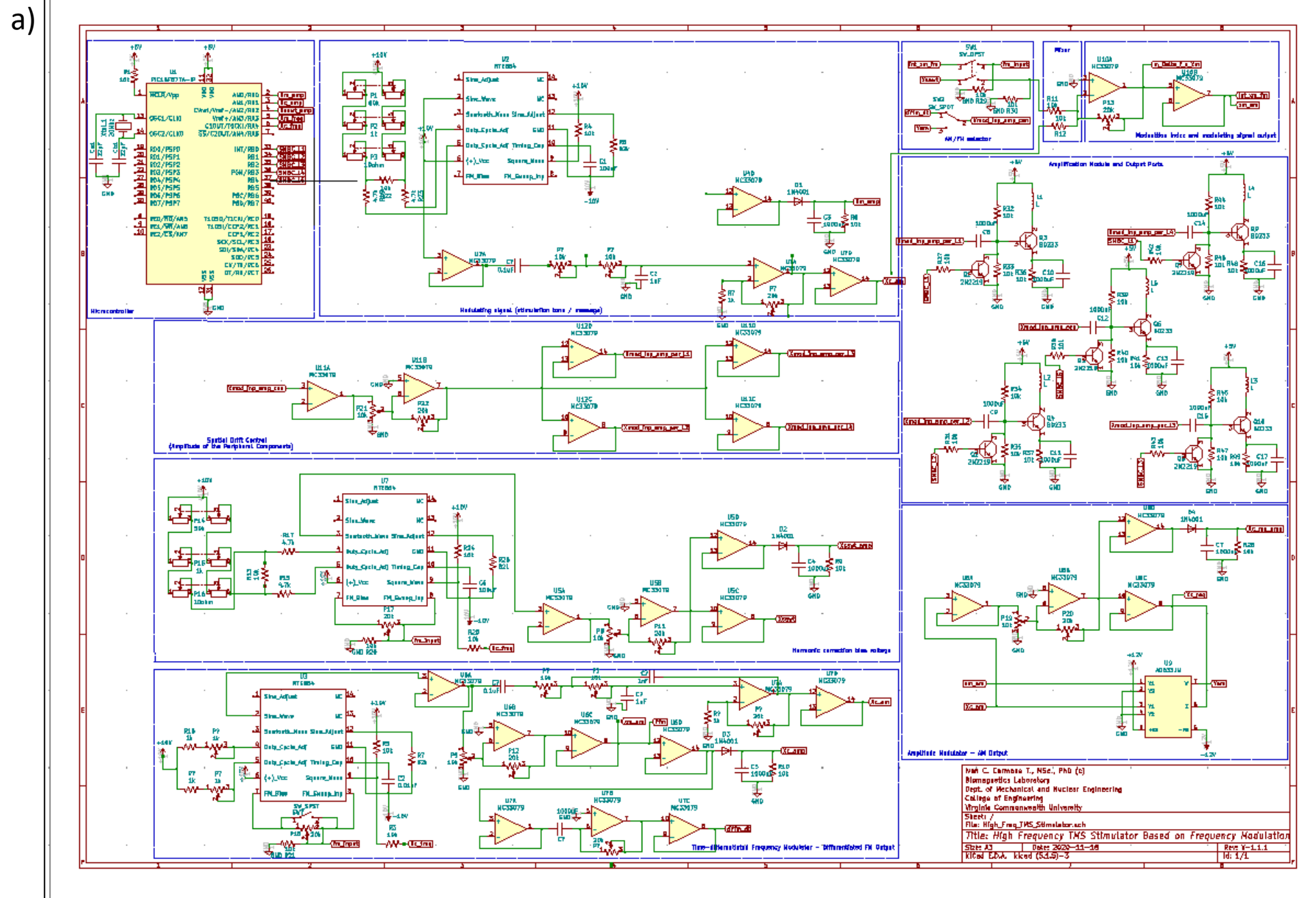
Figure 30– a) Circuit diagram of the designed high-frequency modulator based on AM (1st version). b-c) Circuit prototype built on a breadboard (front view (b) and isometric view (c)). d) Currents and voltages in the DC power source. At this stage, the circuit only needs the final stage of current amplification (coil terminals) to be completed.
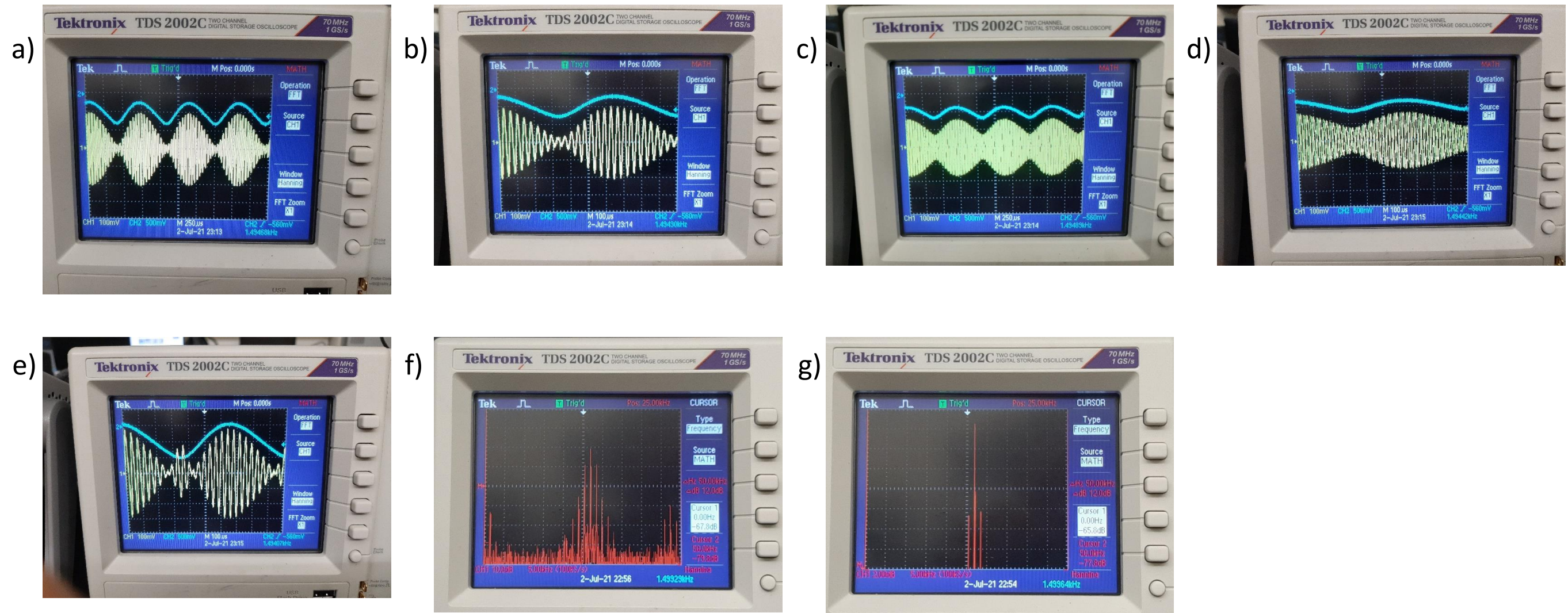
Figure 31 – a-b) General and detailed view of an amplitude modulated (AM) signal with modulation index m = 1, generated by the stimulator in its prototype stage. c-d) General and detailed view of an AM signal with modulation index m < 1. e) Detailed view of an AM signal with modulation index m = 1. f-g) General and detailed view of the frequency spectrum of the signal in figures a-e.

not be otherwise possible to deliver a significantly large current intensity to the coil due to the large power dissipation in the switching devices.

The switches selected for this stage were power MOSFETs model IXFB210N30P3 of the manufacturer IXYS, which are rated for 300 volts of drain-source voltage (V_{DSS}), 210 A of forward current at 25 C, and up to 550 A for pulsed (peak) non-repetitive current.

To operate the MOSFETs it was necessary to design trigger cards able to isolate the control circuit from the power electronics circuit. This is due to the need to keep separate ground domains that avoid damage to the low-voltage components getting coupled from the H-bridge that would be fed by high-voltage.

10.4.3.2. Printed Circuit Board Versions and Final Prototype

In order to provide the equipment with the biggest stability possible during its operation, and a safe transfer of it to experimental facilities, we designed the printed circuit board (PCB) versions of the entire circuitry. During this process, we were able to obtain the final diagrams for all the modules of the circuit explained next.

10.4.3.2.1. Signal Generation Module (SGM)

This module is responsible for the generation of both the low-frequency stimulating tone and the high-frequency carrier, as well as the resulting modulated signal based on the mix of them (Fig. 32). Both signals are obtained using a *precision waveform generator integrated circuit*, model NTE864 of the manufacturer NTE DEVICES. This circuit is an oscillator able to produce sinusoidal, square, and triangular waveforms with adjustable frequency. The SGM

was designed with knobs for the adjustment of both the stimulation frequency and the carrier frequency. Although a wide operational range was permitted, we selected 1.5 kHz as the stimulation frequency to be generated and a carrier frequency of 17 times such value, that is, 25.5 kHz. This ratio would assure an adequate sampling of the stimulating waveform and, therefore, the integrity of the modulated and demodulated frequency spectra.
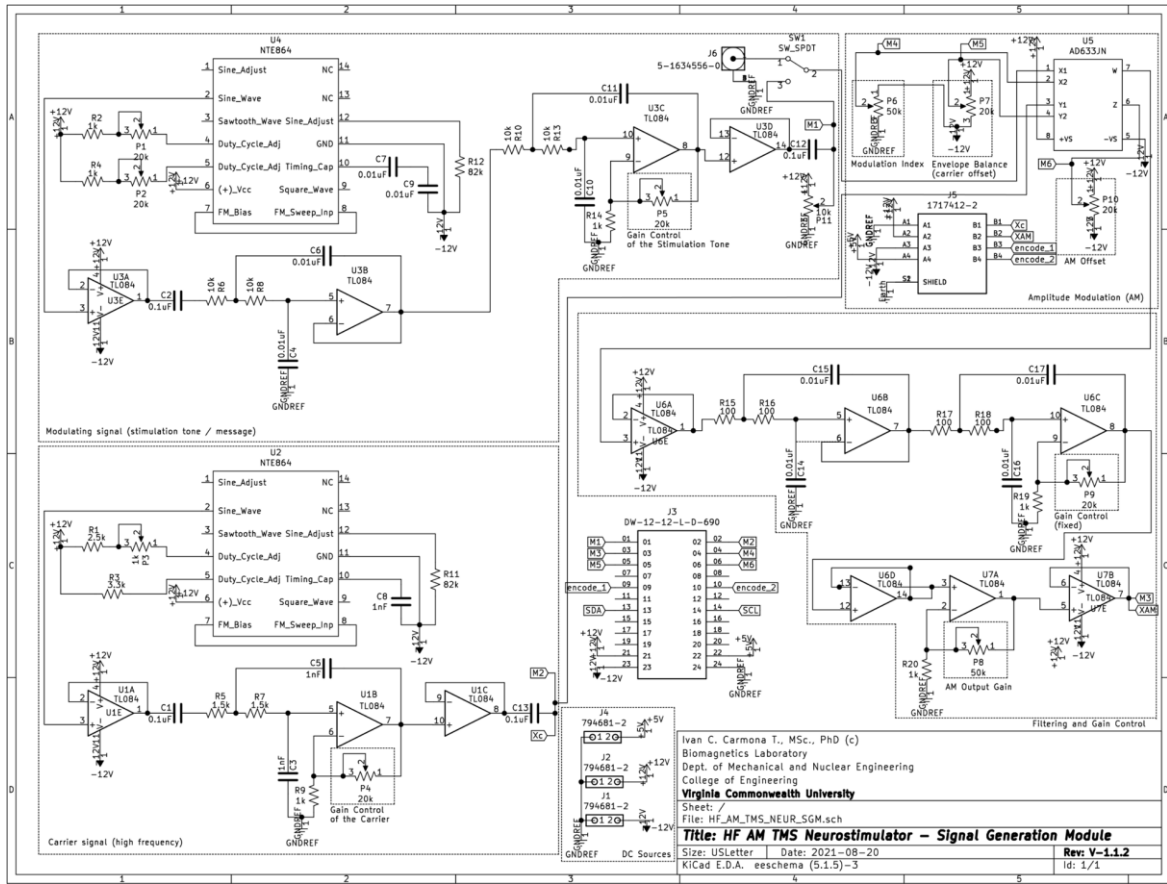
Figure 32 – Circuit diagram of the *signal generation module (SGM)*. Notice the presence of two signal generation modules whose outputs are preconditioned through operational amplifiers to be delivered to the mixer AD633JN. Then, the output is filtered and delivered to the *power electronic module (PEM)* in the point tagged as XAM.

The main purpose of the module is the generation of the AM/DSB-SC signal. For this, we have selected an integrated mixer model AD633JNZ of the manufacturer ANALOG DEVICES. This device allows independent control of the AC input levels in both the message side and the carrier side, as well as the control of the DC level in each of them. With this, it

is possible to manipulate the modulation index (*m*), the envelope balance (symmetry), and the offset of the output. The output of the SGM is then filtered with a 2nd order low-pass filter in Butterworth configuration with a cut-off frequency of 156 kHz. This cut-off value ensures a wide range of operation of the equipment if we decide to increase the carrier later. Finally, the filtered signal is delivered to the next stage called *power generation module (PCM)* through a non-inverting amplifier and a high-impedance decoupling stage.

10.4.3.2.2. Power Electronic Module

The purpose of the *power electronic module, PEM,* (Fig. 33) is to provide the modulated signal with the necessary power (current and voltage) to be delivered to the coil and produce a magnetic field of the expected values. For this, we are using the power transistors of the MOSFET type described in the prototyping section. In order to control the H-bridge, the module needs to generate an equivalent single-channel PWM signal that modulates the AM/DSB signal over an even higher PWM carrier frequency. The carrier frequency selected is 331.5 kHz, namely 13 times the AM/DBS carrier frequency. This means that the output frequency will be the stimulated tone modulated over the envelope of the AM/DSB carrier at 25.5 kHz, re-modulated over a 331.5 kHz PWM carrier.

Using logic gates, the next step splits the single-channel PWM signal and creates a two-channel PWM signal, each channel with the opposite logic levels of the other one.

In a different circuit section, the AM/DSB carrier is used to generate a square version of it that is then negated to produce two channels of opposite Boolean logic. Then, the periods are extended using arrangements of diodes, capacitors, and transistors to enlarge the *off-state*

semi-periods and shorten the *on*-state semi-periods in both signals. This strategy creates

periods of no conduction for any of the transistors that are called *dead times*, with a value that

has been set to 1 μsec.
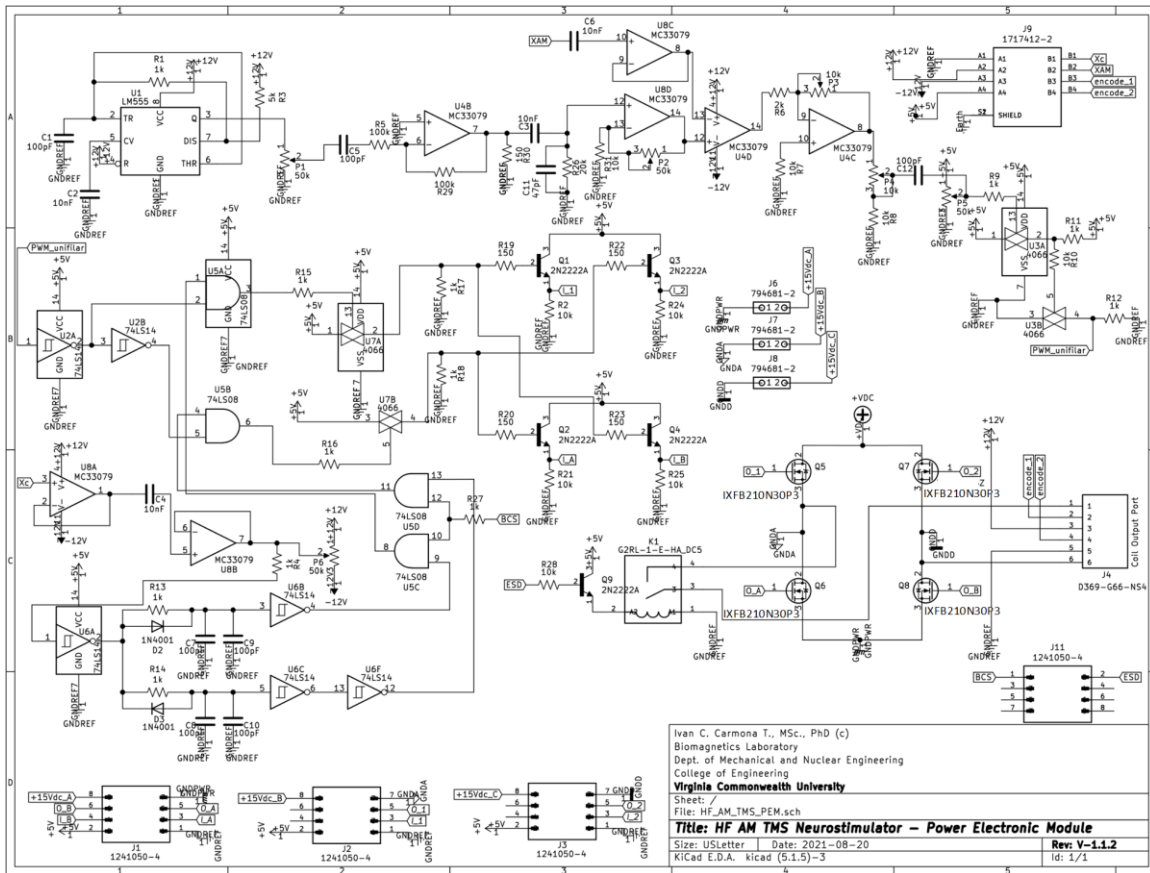
Figure 33 – Circuit diagram of the *power electronic module (PEM)*. The input identified as XAM comes from the SGM with the AM/DSB modulated signal. The input with the tag Xc brings the AM/DSB carrier to PEM to create the two-channel *dead time control signal*. J1, J2, and J3 are the output ports in which the trigger cards are connected.

Finally, the two-channel *dead time control signal* is passed through AND gates along

with the two-channel PWM signal. This creates the final two-channel PWM signal version

that prevents the H-bridge from short circuiting during overlapping periods. The PWM

signals in PEM are finally delivered to trigger cards that will isolate the control/signal

generation stage from the power electronics stage (H-bridge).

In total, two PEM were manufactured. One of them modulates in PWM the AM/DSB modulated signal, whereas the other one modulates also in PWM the non-modulated AM/DSB carrier.

10.4.3.2.3. Power MOSFET Trigger Controller Cards

The trigger card (Fig. 34) is connected to PEM through three 8-pin ports that contain, on the one side, +5Vcc and GND_ref (referential low-power stage ground) connections and the PWM inputs in 5V logic levels. On the other side, they have isolated +15Vcc with respect to a floating ground that is called GND_pwr for the lower part of the H-bridge and GND_A and GND_D for the mid part of the H-bridge where the coil terminals are located.

Each trigger card has been made of four (4) individual 10 A MOSFET drivers, model 1EDI60N12AF of the manufacturer INFINEON. The drivers provide the low power control/ signal generation stage and the power electronic stage with an input-output optical isolation of up to 1.2 kV. The maximum switching frequency of the driver is 4 MHz and its rated output is 10 A.

The trigger cards were one of the most problematic components to design in this equipment. At least 6 months were invested in replacing this card for new versions with new chips until we obtained the necessary stability in operation. The problems occurring are summarized in a set of transients generated by the inductance of the coil, the parasitic inductance and capacitances in the wires and PCBs, and the intrinsic capacitances drain-source, drain-gate, and gate-source of the power MOSFETs. This was continuously generating undesired underdamped high-frequency oscillations (around 2 MHz) in the voltage and current of the coil. Such transients were generating also undesired AC transient

currents that were being coupled to the MOSFET drivers through the +15Vcc power supplies and through the intrinsic capacitances of the power MOSFETs. These transient currents were causing repeated failures of the trigger cards, having the driver chips overheated and damaged after a few seconds of operation at voltages beyond +20Vcc in the H-bridge.

The transient problems were finally solved by adding RC snubber circuits. These are passive dissipators whose function is to damp the undesired transients as much as possible. As another measure, we set independent +15Vcc power supplies for the left and right ends of the lower side of the H-bridge. They were originally connected to the same power supply in what apparently was the right design logic since they share the same ground connections. However, we eventually noticed that the shared power supply was acting as a low-impedance AC path for transients to couple from one end to the other one. This was a hidden problem most of the time until careful inspection of the process was performed to draw such conclusions.
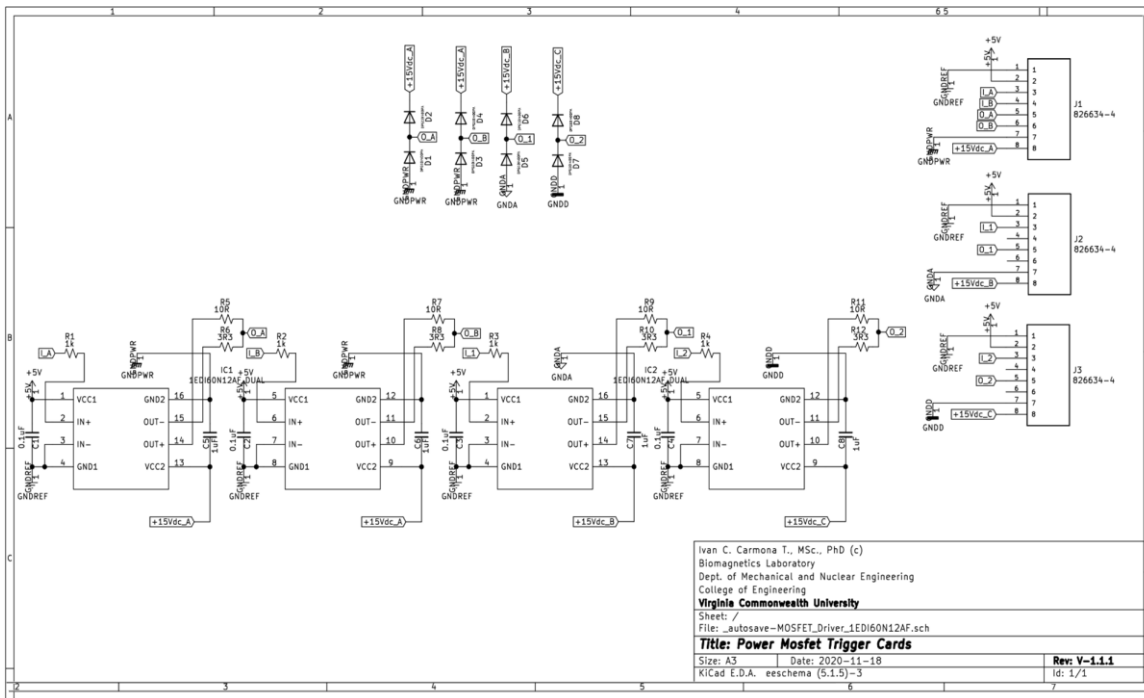
Figure 34 – Circuit diagram of the *power MOSFET trigger cards*. The card has been designed to be pin-compatible with the output of PEM. The clamping diodes in the upper part help to stabilize the voltage in the gate that may course overcurrent in each of the drivers.

We also connected 10 ohms 5 W resistors in all the +15Vcc power supplies to prevent instabilities in the switching outputs and included fast recovery diodes in clamping configuration to the gate of the power MOSFET to prevent this voltage from fluctuating above +15Vcc and below the GND reference.

After applying all these changes in time, we finally obtained a stable operation at any voltage in the H-bridge.

10.4.3.2.4. Trigger Signal Generator Card

The PEM has been designed to be externally triggered by a square signal of a certain duration. That duration determines the interval in which the two-channel PWM signal is delivered to the *power MOSFET trigger controller cards* and, therefore, the duration and repetition rate of the output modulated pulses. If a single pulse is delivered in the input of the *power MOSFET trigger controller card*, a unique modulated pulse will be delivered in the output, and if the input is a train of pulses, the same pattern will be obtained in the output. This is a very useful characteristic that permits the equipment to reproduce any protocol set in any commercial pulse generator or stimulator in which parameters such as pulse width, inter-pulse spacing, number of intra-burst pulses, and inter-burst repetition rate can be configured.

In order to generate such input signal, the *trigger signal generator card* (Fig. 35) needs to produce such pulses either manually triggered or received from external equipment. The manually triggered signal is released by pressing and releasing a push button located in the

front panel of the equipment. This button initiates a chain of events that ends with the release of a single pulse in the output of a duration of 667 µsec (the reciprocal of the 1.5 kHz stimulating tone). The signal is released in phase with the stimulating tone, for which a zero-cross detector circuit is included.

When the push button is not pressed, the signal may come from external equipment through an OR gate that shares a connection with the manually triggered signal branch and the external input branch. This allows the equipment to be triggered in both modes. The external input enters the equipment through a female BCN-type coaxial connector with high input impedance. The circuit diagram of the *trigger signal generator card* is shown next.
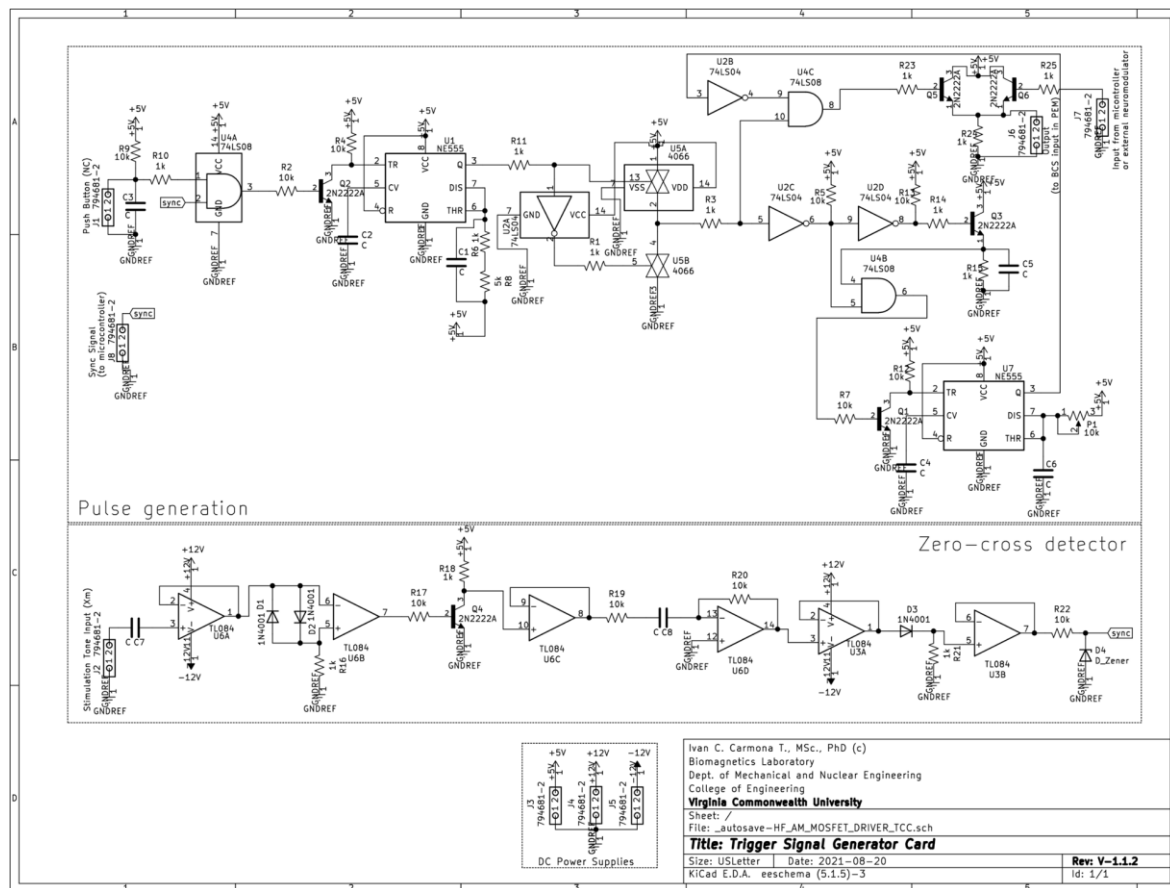
Figure 35 – Circuit diagram of the Trigger Signal Generator Card. The input signal may originate from the push button (J1) in phase with the referential stimulating tone (J2) or from an external equipment through the input J7.

10.4.3.2.5. H-Bridge and Main DC Power Supply

The H-bridge (Fig. 36) is a sub-part in the *power electronic module* (PEM), in charge of driving the high current circulating through the coil. As mentioned before, MOSFETs model IXFB210N30P3 of the manufacturer IXYS were selected, with 210 A of forward (sustained) current at, and up to 550 A for pulsed (peak) non-repetitive current. Since we expect to deliver pulses of short duration at all times (667 µsec), even with several pulses accommodated on a TMS burst we would neither exceed such sustained current nor surpass the peak current. The lower part of the bridge is the common potential reference (GND_pwr), whereas the upper part is called +VDC.
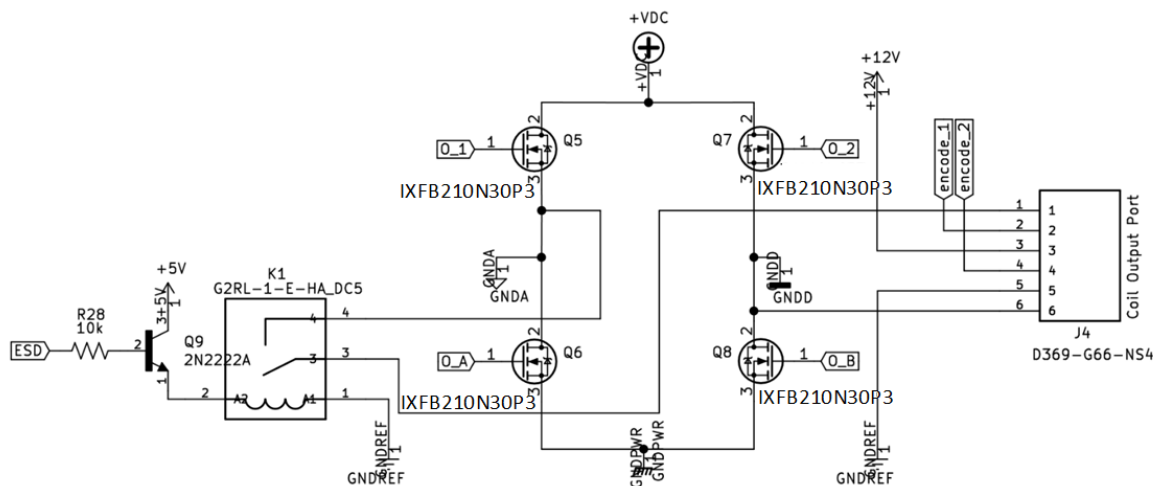
Figure 36 – Circuit diagram of the H-bridge. Notice the position of the coil (terminals 1 and 6 in the output port) connected to the mid side of the bridge (GND_A and GND_D). The PWM signals allows the alternation of the current in the coil from left to right with the activation of Q5 and Q8 and deactivation of Q6 and Q7 simultaneously. Then, in the negative semi cycles the current flows from right to left activating Q6 and Q7 and deactivating Q5 and Q8. A severe short may occur if Q5 and Q6 are activated simultaneously of Q7 and Q8, but the careful selection dead times made in PEM prevents it.

+VDC is an adjustable high-power voltage supply made with a bridge rectifier of 4 A of rated current, and a 27,000 µF, 200 V electrolytic capacitor. The AC input to the bridge rectifier comes from a VARIAC (variable AC transformer) with an adjusting wheel to control the AC voltage in the output. This VARIAC is at the same time connected to an insulation

transformer. The variation of the AC level in the VARIAC produces a certain DC level in +VDC with a big capacity to deliver a high current intensity due to the large capacitance.

10.4.3.2.6. Stimulating TMS Coils

In order to test the stimulator, two customized TMS coils were designed and built for both the modulated AM/DSB signal and the non-modulated carrier. This design has a close relation to all the aspects studied in Chapter 3, especially with those related to the coils in the SVEVM work. However. This time we have built only two out of the seven coils that would be necessary for the implementation of SVEVM because it would imply also the construction of five additional PEM cards. Since this work was beyond the scope and required too many resources and significant time, we decided to operate with two coils, equivalent to one petal, and the central coil of the *figure-of-flower coil* (see Chapter 3).

The coils were designed to operate with a ferromagnetic core made of AISI 1010 carbon steel, whose electromagnetic properties were previously described. The cylindrical shape of the cores has dimensions of 10 mm in height and 3 mm in diameter. No tip sharpening was made at this point since we determined that tips act as a flux concentrator at the expense of greater attenuation once it leaves the tip-air interface (see Chapter 3). Instead. We chose to use a flat tip to operate the coil at the saturation point. Preliminary simulations allowed us to understand that a saturated cylindrical core produces a more homogeneous distribution of the magnetic flux density underneath, which is more beneficial for a higher magnetic field.

Each coil counts 20 turns in a high of 10 mm, formed by 4 layers of 5 turns each. The inner radius is the same as the radius of the core, this is, 1.5 mm. The external radius is 5.5

mm for a total diameter of 11 mm. The coils were made tight with a heat shrink material and an overlapping factor close to the unit. The wire used for the windings was a 1 mm diameter insulated copper wire.

Regarding the cabling, long wires of 1 meter each were used with a gage of 12 AWG. This provides the coils with maneuverability at the time of use. Since each coil has two wires this adds additional parasitic resistance and inductance to the system. Then, the values were measured to be able to perform calculations with accuracy. The parameters measured on each coil are shown in Table IV. They were obtained using an RLC meter.

Table IV – Inductance and Resistance Measures in the Customized TMS Coils

COIL 1	Value	Unit	Description
R1dc	1.00E-02	Ω	DC resistance of coil # 1
R1_10kHz	4.60E-02	Ω	AC resistance of coil # 1 measured at 10 kHz
L1_10kHz	4.42E-06	H	Inductance of coil # 1 measured at 10 kHz
COIL 2	Value	Unit	Description
R2_dc	1.00E-02	Ω	DC resistance of coil # 2
R2_10kHz	5.80E-02	Ω	AC resistance of coil # 2 measured at 10 kHz
L2_10kHz	5.34E-06	H	Inductance of coil # 2 measured at 10 kHz
Wire	Value	Unit	Description
Rw	8.00E-03	Ω	Joint AC resistance of the 2 cables measured at 10 kHz
Lw_10kHz	1.24E-06	H	Joint parasitic inductance of the cables measured at 10 kHz

10.4.4. Measurement Procedures

In order to determine the intensity of the current flowing through the coils, the voltage drop across the coils, the generated magnetic field and magnetic flux density at the bottom of the coil (and a few millimeters away from it), and the induced electric field, we developed the following methodology.

10.4.4.1. Coil Current Measurement

We connected a shunt resistor of 0.00117 Ω in series with each of the TMS coils to determine the current through it. The voltage drop in the shunt resistor divided by the resistance value gives the amplitude of the loop current, which is the same that crosses the coil. Since in the resistor shunt resistor voltage and current are in phase, the waveform of the voltage drop will be exactly the time waveform of the current.

We set the equipment to operate at 40 V at +VDC in the H-bridge. Then, we triggered single pulses and registered the current waveform in the oscilloscope through the shunt resistor.

Using the math menu of the oscilloscope, we observed the frequency spectrum of the current through the coil obtained with an FFT of the time domain waveform. This allowed us to evaluate specific frequency components that otherwise would not be possible to separate in the time domain. Using the 5 kHz spectrum (5 kHz/div) we observed the amplitude of the current at the carrier frequency, which is registered in decibel volts (dBv) with respect to the average noise floor. Converting backward we obtained the voltage drop in the shunt resistor and finally the current at such frequency. This method applies to both the measurement of the modulated current and the non-modulated carrier current.

10.4.4.2. Coil Voltage Calculation (indirect measurement from the current)

The next step was the calculation of the voltage drop in the coil with Eq. 80. This was made using the measured current and coil parameters (resistances and inductances, including the parasitic values).

$$V_{coil} = 2 \cdot \pi \cdot f_c \cdot L_{coil} \cdot I_{coil(f_c)} \qquad (80)$$

The result represents the AC voltage drop in the coil terminals at the frequency of the AM/DSB carrier. This value is expected to be significantly larger than the DC voltage in the H-bridge (+VDC) due to the impedance of the coil at such a high frequency.

10.4.4.3. Magnetic Flux Density Calculation (indirect measurement from the current)

The next step after determining the voltage drop is the calculation of the net flux linkage (Φ) and the magnetic flux per turn (Ψ).

$$\Phi = N \cdot \Psi \qquad (81)$$

$$\Phi = L \cdot I = \frac{V}{\omega_c} \qquad (82)$$

Combining Eq. 81 and 82 we have.

$$\Psi = \frac{V}{N \cdot \omega_c} \qquad (83)$$

Finally, the magnetic flux link per turn (Ψ) is divided by the area of the flux section (which is assumed to be the same as the magnetic core), to obtain the magnetic flux density (B).

$$B = \frac{\Psi}{\pi \cdot r_{core}^2} \qquad (84)$$

If the value of the magnetic flux density is smaller than the magnetic saturation, the calculated value is the actual B in the core. If the magnetic flux density exceeds the saturation

point, then the coil core is operating at the saturation point and the actual value is given by the B-H curve.

10.4.4.4. Electric Field Calculation (indirect measurement from the current)

The calculation of the electric field is made from the expression in Eq. 76. Recalling, we have.

$$|E| = \pi \cdot r \cdot f \cdot |B| \tag{85}$$

Since the E-field needs to be calculated both below the coil and 4.25 mm away from it (coil-target distance for pyramidal neurons in layers 5/6), we use a decreasing exponential term as a function of the coil-target distance "z" with an attenuation factor β in m^{-1}.

$$|E| = \pi \cdot r \cdot f \cdot |B| \cdot e^{-\beta \cdot z} \tag{86}$$

10.4.4.5. Stimulation protocol for future animal experimentation based on the high-frequency neurostimulator.

Because of the complexity of the performance of animal work, which depends on resources external to the Biomagnetics Laboratory not completely available at the time of presentation of the results, the scope of this dissertation extends only to the demonstration of the operation of the technology of neurostimulation created, which includes: the frequency shifting of the stimulating energy out of the TMS range and audible range, the calculation of

the overall gain factor operating at high frequency, and the demonstration of the recovery of the stimulating baseband through superposition of signals. Although animal experimentation will be out of the scope of this dissertation, we have prepared a detailed explanation from a bioengineering standpoint of how the stimulation would work during the real test on animals. This will help the operators to understand the application of the modulated stimulating signal and the non-modulated carrier necessary for the recovery of the TMS baseband within the brain tissue.

The main objective of an animal test would be the finding of experimental evidence that shows that the neurons will respond to the envelope of the modulated signal. As explained before, this is an aspect that depends on the behavior of neurons in presence of a high-frequency amplitude modulated signal. Recalling what was shown at the beginning of this chapter, we have three sub-hypotheses. Sub-hypothesis # 1: neurons will act as an envelope follower circuit seen only one of the envelopes. Sub-hypothesis # 2: neurons will see a null average E-field due to the symmetry of the envelopes, for which we would need to induce asymmetry with a DC level. Sub-hypothesis # 3: none of these behaviors are demonstrated and demodulation with a non-modulated carrier is required.

For the first test scenario, the voltage waveform would be an original (non-modified) amplitude modulated signal. The objective of this test is to verify the theorized envelope-follower behavior of the neurons in the primary motor cortex (M1) and the predicted auto-demodulation process.

If the first scenario does not show effective stimulation of the M1 region in the rat, in a second test scenario a rectified version of the AM voltage would be used, with a DC-level

added (balance control). This test aims to verify the theorized sampling-and-hold behavior of the neurons in the presence of a high-frequency asymmetric amplitude modulated signal.

The first and second stimulation scenarios are shown in Fig. 37.
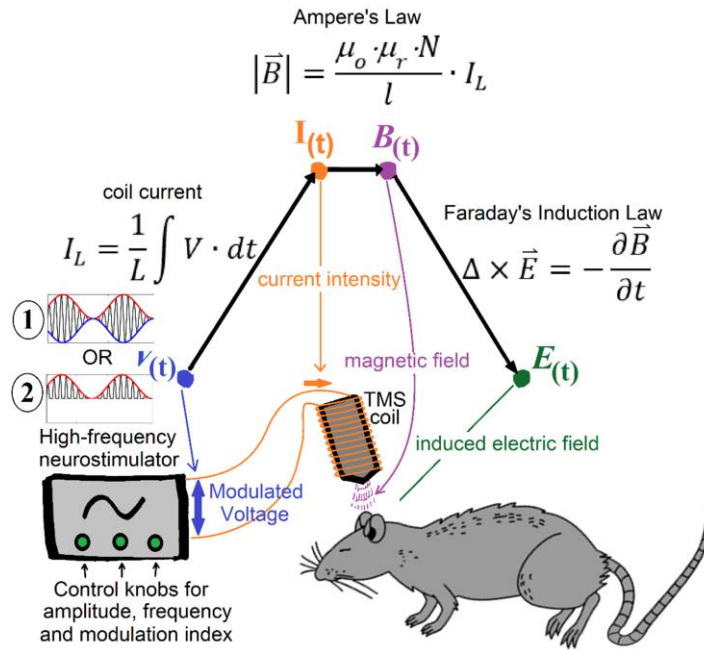
Figure 37 – Experiment setup for cases 1 and 2 with symmetric and asymmetric incoming amplitude modulated voltage. Notice how the energy flows from the stimulator, first as an applied voltage (V), then as the resulting current through the coil (I), later as a current-driven magnetic field with a flux density (B), and finally as an induced *E*-field in the brain tissue. In the trapezoid diagram, the variables in the bottom base ($V_{(t)}$ and $E_{(t)}$) share the same waveform of an amplitude modulated/double-sideband (AM/DSB) signal (symmetric or not), whereas the variables in the top base ($I_{(t)}$ and $B_{(t)}$) have the waveform of the integral of an AM/DSB signal.

If none of the two first scenarios succeed in producing effective stimulation, a third scenario will be required, including an additional coil in the setup (Fig. 38). The first coil will drive an amplitude-modulated voltage, as in the first scenario, whereas the second coil will only drive the carrier (non-modulated) signal. The two coils should be placed in a position that guarantees the intersection of the magnetic flux lines right in the target. We expect this technique produces the superposition of the modulated and non-modulated tone, which will allow recovering the baseband. This baseband tone should be able to finally stimulate the targeted neurons.
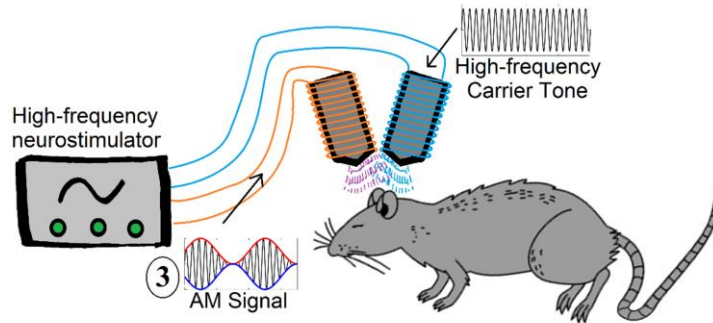
Figure 38 – Experiment setup for case 3 with two coils and two applied voltages. On the first coil, a symmetric amplitude modulated voltage is applied, whereas, in the second coil, the high-frequency non-modulated carrier is used alone. Notice how the energy flows from the stimulator, first as an applied voltage (V), then as the resulting current through the coil (I), later as a current-driven magnetic field with a flux density (*B*), and finally as an induced *E*-field in the brain tissue.

If none of the above-described scenarios succeeds in stimulating the M1 region, the conclusion would be negative results for the attempt of stimulating neurons with high frequency, at least for the magnitude of the magnetic field provided.

10.5. Results # 2:

10.5.1. Results of the MATLAB Simulation of the HF Neurostimulator

The simulations were made using similar values of coil inductance as well as the same modulation scheme as those used in the physical stimulator, to make the predictions comparable to experimental results.

Through the simulation, we have sought the values of voltage, current, and magnetic field that would be necessary for the coil to obtain an electric field of 100 V/m in the core-air interface first and 4.25 mm away (target distance) later.

The first results show that, for an *E*-field around 100 V/m right below the coil, the peak amplitude of the amplitude-modulated voltage waveform needs to be 40 V (see Fig. 39, plot #1). This means an amplitude of 22.22 V at 25.5 kHz for the carrier, and 11.11 V at 24 kHz

and 27 kHz for the lower and upper sidebands, respectively. Notice in the lower subplot in plot #1 how the spectrum of magnitudes within the typical TMS range (up to 3.5 kHz) is empty. This means that all the energy of the stimulating signal (originally located at 1.5 kHz) has been shifted to the sidebands, out of both the TMS range (≤ 3kHz) and audible range (0-20 kHz).
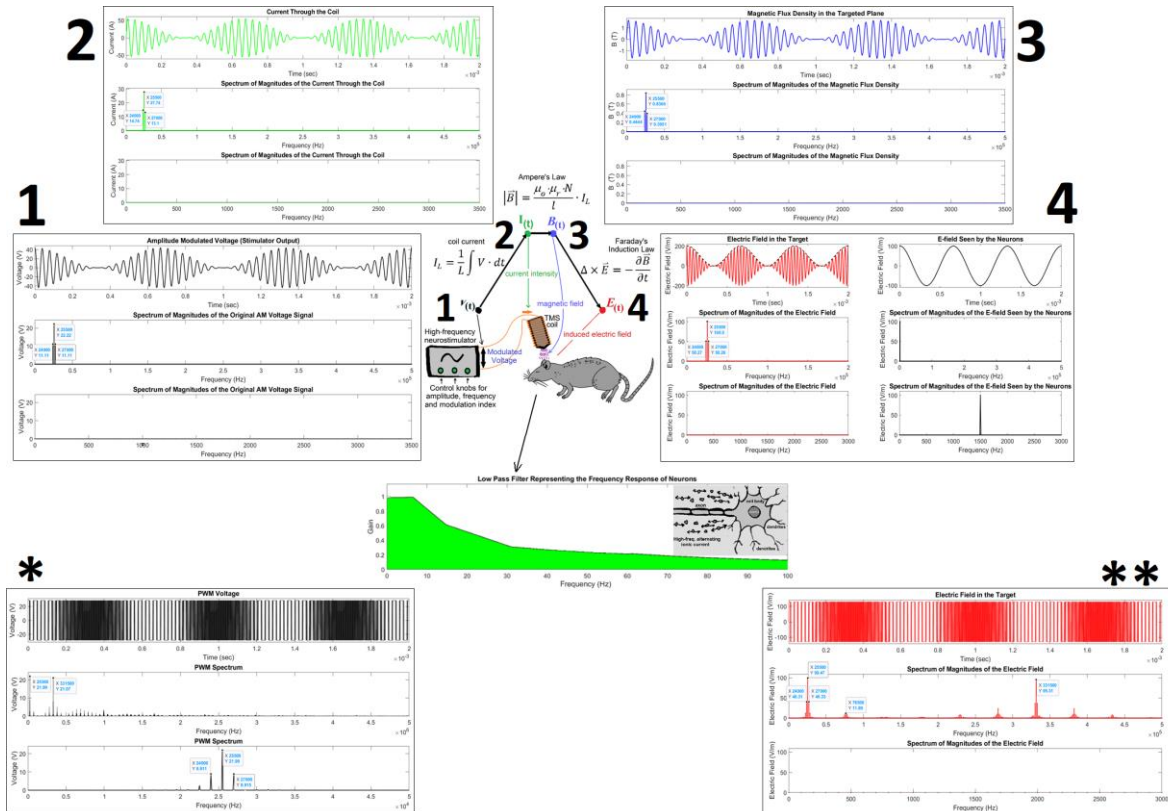
Figure 39 – Signal diagram of the high-frequency stimulation with amplitude-modulated voltage and   E-field. Notice how the E-field seen by neurons is the result of an envelope follower behavior of the neural membrane to recover the low-frequency component from the modulated E-field in the target.

Immediately after in the diagram (subplot # 2) we observe the results for the requirements of current intensity. The waveform, although similar in appearance, is the integral of the voltage waveform. The peak value of the envelope needs to be 50 A, which seen in the frequency spectrum of magnitudes means a carrier amplitude of 27.74 A, and lower and upper sidebands of 14.74 A and 13.1 A, respectively. This is the waveform, values, and frequency

distribution that our simulation results predicted for the current that needs to circulate through the coil to reach 100 V/m in the core-air interface.

Sub-plot # 3 shows the waveform of the magnetic flux density (*B*) which is identical to the current. The peak value of the modulated waveform reaches 1.67 T, which is relatively close to the saturation point of the AISI 1010 carbon steel ($\cong$ 2T). The frequency distribution is almost 0.84 T for the carrier frequency component, 0.44 T for the lower sideband, and almost 0.4 T for the upper side band. At this point, the magnetic flux can grow 0.33 T only before reaching saturation, which needs to be considered for the compensation of the attenuation (explained later in this chapter).

Finally, the resulting electric field (*E*-field) at the core-air interface has a carrier amplitude of 100.5 V/m and sidebands of 50.27 V/m. The peak amplitude of the envelope is 100.4 V/m at 1.5 kHz. According to the literature, this *E*-field should be enough to stimulate neurons of the primary motor cortex. However, this is the *E*-field at the core-air interface, and the attenuation that the magnetic flux undergoes still needs to be considered.

In Chapter 3 we calculated attenuation curves for magnetic cores as a function of the geometry in the tip through simulations. Since we are using a flat tip, which demonstrated to undergo the smallest attenuation, we estimated the attenuation as the following expression.

$$A = e^{-\beta \cdot z} \text{ , with } \beta = 167.67 \tag{87}$$

In Eq. 87, "*z*" is the vertical distance from the end of the core to the point of inspection of the field. Then, calculating for $z = 4.25$ mm, which is the distance between the top of the scalp and pyramidal neurons of layers 5/6 of the motor cortex, we obtained that the expected attenuation at such depth is $A_{(4.25\ mm)} = 0.4924$, which is equivalent to -3.07 dB.

Since the system is linear for the frequency band of interest (around 25.5 kHz) while the core is not saturated, then the current needs to be increased by 3.07 dB, this is, multiplied by a factor of ≈ 2. This increase then needs to be applied to the voltage, resulting in the following final required values.

Table V – Results of the Prediction of *V, I, B* and *E* for the HF Neurostimulator Based on the MATLAB Model

Variable	Variable	Value	Unit
V_{coil}	AM peak voltage	88.89	V
$V_{carrier}$	Carrier peak voltage	44.44	V
+VDC	DC voltage required at the H-bridge to produce the same continuous AM voltage waveform with PWM	50.92	V
I_{coil}	AM peak current	110.9	A
$I_{carrier}$	Carrier peak current	55.48	A
B_{peak_tip}	Peak AM magnetic flux density at the air-core interface (tip)	2 (saturated)	T
$B_{carrier\_tip}$	Carrier peak magnetic flux density at the air-core interface (tip)	1.42	T
E_{peak_tip}	AM *E*-field at the air core interface (tip)	402.1	V/m
$E_{carrier\_tip}$	Carrier peak voltage *E*-field at the air core interface (tip)	170.9	V/m
$E_{1.5kHz\_tip}$	Resulting 1.5KHz-*E*-field component at the air-core interface (tip)	200.8	V/m
B_{peak_target}	Peak AM magnetic flux density 4.25 mm below the tip (target)	0.9849	T
$B_{carrier\_target}$	Peak carrier magnetic flux density 4.25 mm below the tip (target)	0.70	T
E_{peak_target}	Resulting AM *E*-field 4.25 mm below the tip (target)	198.03	V/m
$E_{carrier\_target}$	Resulting carrier *E*-field 4.25 mm below the tip (target)	84.17	V/m
$E_{1.5kHz\_target}$	**Resulting 1.5KHz-*E*-field component below the tip (target)**	**98.89**	**V/m**

The results of the MATLAB simulation showed, from an analytical point of view, that the use of the high-frequency neuromodulation scheme based on AM/DSB modulation should be effective in producing the necessary electric field in the envelope to stimulate pyramidal neurons in layers 5/6 of the motor cortex. The method can theoretically achieve the required 100 V/m set as the referential threshold of stimulation at a depth of 4.25 mm with a potential between +VDC and GND_PWR of 50.92 volts in the H-bridge.

10.5.2. Experimental Results with the HF Neurostimulation Equipment Built

10.5.2.1. Voltage, current, magnetic field, and electric field results.

We start this subsection by showing the results of the waveform of current obtained through an insulated probe in the oscilloscope on a 20X scale. Since they are in series, the shunt resistor (0.00117Ω) allowed us to observe the current through the coil, downscaled 0.0017 times.

The elevated electromagnetic noise due to the high-frequency switching makes the waveform in the time domain unclear to be easily distinguishable as in the simulation (Fig.40). However, when the same signal is observed in the frequency domain (Fig. 41), its observation becomes simpler. Using the FFT function in the math menu of the oscilloscope, we observe the frequency spectrum of the signal as follows.
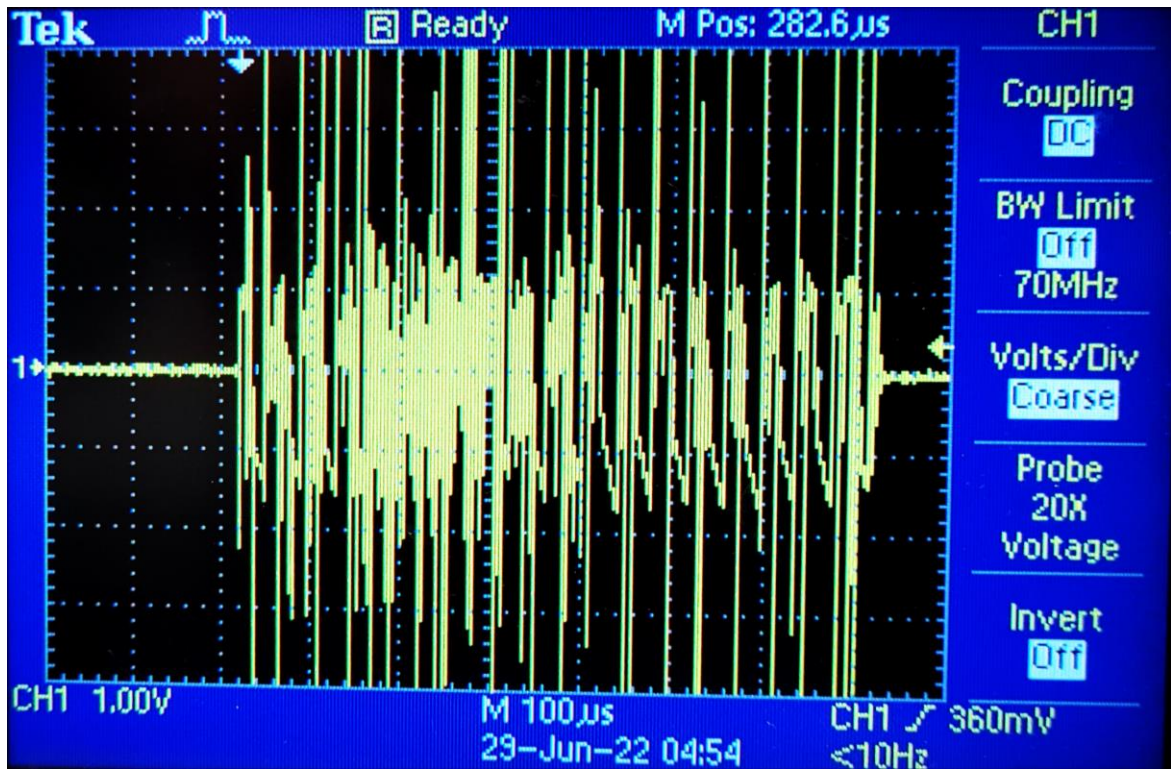
Figure 40 – Voltage waveform in the shunt resistor as a method to measure the current flowing through the TMS coil. Notice the high-frequency switching noise that can be separated from the signal in the frequency domain.
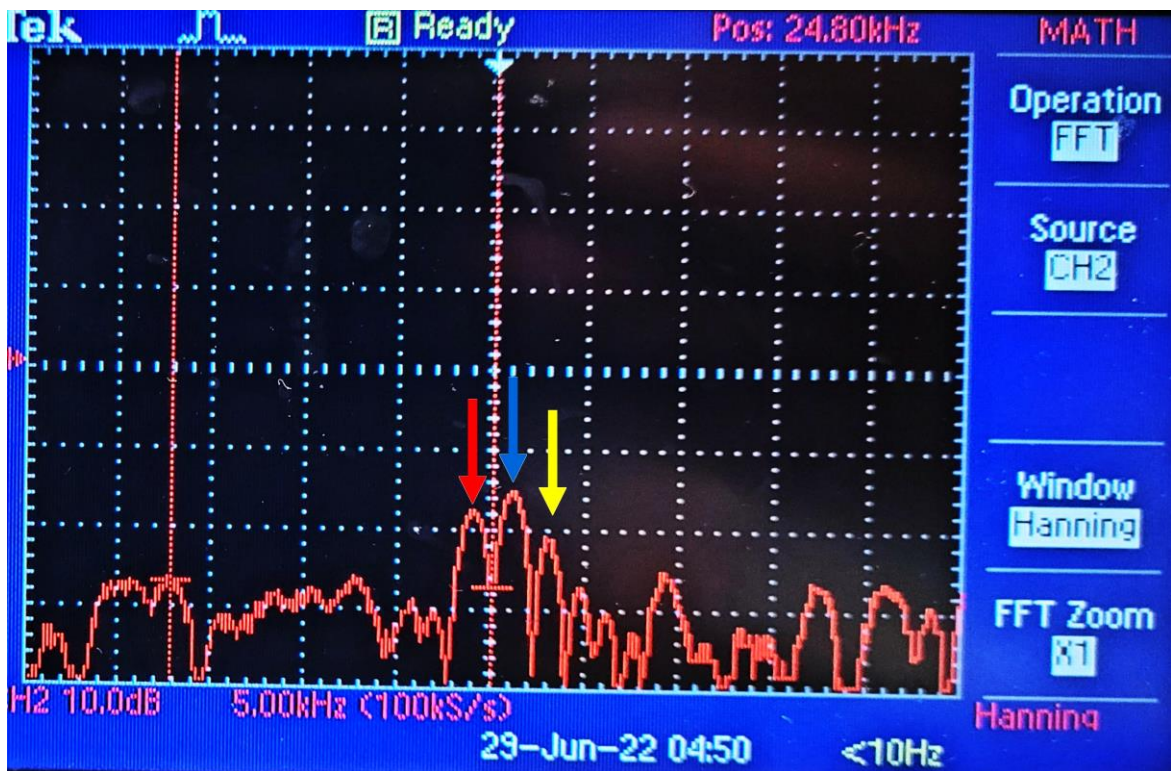
Figure 41 – Frequency spectrum of the waveform of current seen as a voltage drop in the shunt resistor. Amplitudes are expressed in dBV. The blue arrow indicates the location of the carrier at 26 kHz (deviation of 0.5 Hz from the theoretical value). The red and yellow arrows indicate the location of the lower and upper sidebands (24 kHz and 28 kHz). The calculation of values of current require the conversion from dB to volts and then the division by 0.0117.

As observed in the picture, the magnitude of the carrier is exactly 10 dB bigger than the average magnitude of the noise floor. The, being 10 dB the net voltage of the carrier in the shunt resistor we calculated the current. The calculation revealed that the current at the frequency of the carrier (26 kHz) is 270.26 Arms, equivalent to 382.23 A.

With the current calculated we found the voltage, flux linkage, magnetic field, magnetic flux density, and electric field at the frequency of the carrier. The resulting values are shown in Table VI for +VDC = 40 V, and the adjustment to reach 100 V/m in the target is shown in Table VII.

Table VI – Results of the Direct and Indirect Measurement of *V*, *I*, *B* and *E*

over the Prototype of HF Neurostimulator (peak values)

Variable	Variable	Value	Unit
$I_{carrier}$	Current at the frequency of the carrier	382.23	A
$V_{carrier}$	Voltage at the frequency of the carrier	327.04	V
+VDC	DC voltage required at the H-bridge to produce the same AM voltage waveform with PWM	40	V
$\lambda_{carrier}$	Flux linkage at the frequency of the carrier	2.04E-03	Wb
$H_{carrier}$	Magnetic field at the frequency of the carrier	764,467.71	A/m
$B_{carrier}$	Magnetic flux density at the frequency of the carrier (saturated). The B-H curve was used to consider the saturation	2.1091	T
$E_{carrier\_tip}$	Electric field at the air core interface (tip)	390.86	V/m
$E_{carrier\_target}$	Electric field 4.25 mm below the tip (target)	167.37	V/m
E_{stim}	*Electric field of the envelope (baseband stimulation E-field) at z = 4.25 mm*	83.68	V/m

Table VII – Results after the adjustment of the voltage in the H-bridge to reach the 100 V/m in the target.

Variable	Variable	Value	Unit
$I_{carrier}$	Current at the frequency of the carrier	456.75	A
$V_{carrier}$	Voltage at the frequency of the carrier	390.80	V
+VDC	DC voltage required at the H-bridge to produce the same AM voltage waveform with PWM	47.80	V
$\lambda_{carrier}$	Flux linkage at the frequency of the carrier	2.44E-3	Wb
$H_{carrier}$	Magnetic field at the frequency of the carrier	913,506.26	A/m
$B_{carrier}$	Magnetic flux density at the frequency of the carrier (saturated). The B-H curve was used to consider the saturation	2.1	T
$E_{carrier\_tip}$	Electric field at the air core interface (tip)	467.06	V/m
$E_{carrier\_target}$	Electric field at the carrier frequency 4.25 mm below the tip (target)	200	V/m
E_{stim}	*Electric field of the envelope (baseband stimulation E-field) at z = 4.25 mm*	100	V/m

Notice that the value of electric field in the target is 100 V at 4.25 mm from the core tip. This indicates our success in attempting to reach the stimulation threshold in the target.

It is important to mention that during the operation of the stimulator we observed a similar value of current at the frequency of the carrier in the range between 20 and 40 volts in the H-bridge (+VDC). The no apparent variation of this current is evidence that the core material is saturated magnetically, and that the additional increase in voltage is translated into additional frequency components as a result of the distortion of the waveform. Therefore, the net current increases after crossing the saturation threshold, but the component at the frequency of the carrier remains virtually steady.

10.5.2.2.Stimulating Pulse Sound Power Results

In contrast to the loud noise produced by commercial TMS equipment and experimental equipment within the TMS range (around 140 dB) [103], our stimulation registered a maximum value of 45 dB at 40 V in the H-bridge. This is comparable and very similar to the sound produced by pressing a key on a computer keyboard. With voltages lower than 40 V, the sound power was comparable to the background noise in a room with standard air conditioning and ventilation system. Therefore, the sound click was imperceptible, turning the stimulation virtually noiseless. The dB measurements were performed using the app *Sound Meter* from the manufacturer *Pony, Inc*.

10.6. Discussion of the Results

Our experimental results, obtained from measurements over the high-frequency neurostimulator prototype, demonstrated that the electric field exceeds the 100 V/m threshold for the targeted depth, i.e. 4.25 mm below the coil. The computational predictions were accurate in calculating the required voltage and magnetic field to obtain the desired electric field in the target. However, we found a discrepancy between the predicted and the actual current in the coils. This discrepancy was due to the magnetic saturation inside the ferromagnetic core, which increases the current with the inverse ratio between the predicted increase of the magnetic flux density (B_{linear}) if the core was completely linear and the actual value of magnetic flux density (B_{real}), i.e. (B_{real}/B_{linear}). After the saturation point, any attempt of the system at increasing the magnetic flux density results instead in an increase of the current, while the magnetic density remains increasing slowly. The B_{real}/B_{linear} factor was estimated to be 8.48. This confirmed that our coils are operating at the saturation point at 2.1 T at the frequency of the carrier.

The resulting electric field measured at the core-air interface was 200 V/m and the attenuation for a depth of 4.25 mm was 0.4924. This is with a voltage in the H-bridge equal to 47.80 Vdc, similar to the 50.92 Vdc originally predicted computationally. Therefore, the electric field at the depth of the target was 100 V/m.

10.7. Conclusion

The proposed high-frequency neurostimulation method for TMS based on AM/DBS modulation proved to be effective in shifting the stimulating energy outside the commercial TMS band and audible range. The measured electric field in the core-air interface was 167.37, whereas the electric field in the target was 83.68 V/m. This value represents the amplitude of the low-frequency stimulating tone in the envelope. Our results indicate using two different methods that increasing the voltage in the H-bridge to almost 50 volts will allow reaching an electric field of 100 V/m in the target, as expected.

The operation showed to be minimally sonorous at 40 Vdc in the H-bridge and completely soundless at 20 Vdc. This is because our results were obtained with significant saturation in the core at 40 Vdc, but showed an almost identical magnitude of current at 20 Vdc. Therefore, the indirect measurement of the induced electric field is the same, at least in this range of saturation.

10.8. Summary of Advantages of the HF Neuromodulation Method

The invention consists of a novel *neuromodulator* equipment that uses –for the first time to our knowledge– modulation techniques (AM/DSB-SC, ASK, and FM) at high frequency

(tens of kHz) for _transcranial magnetic stimulation_ (TMS). The method modulates a low-frequency stimulation signal (X_s) –located within the stimulable range for neurons– over a high-frequency carrier (X_c) –located out of the _commercial TMS frequency range_– to generate a _frequency shifting_ that takes the stimulating energy out of the _stimulable baseband_. This aims to exploit the capabilities of operating non-invasive TMS coils with elevated -dB/dt and frequency, leading to:

- Reduction of |B| and, therefore, of the necessary current in the TMS coils to produce the required |E|.

- Reduction of the power dissipation in TMS coils as a function of the reduced TMS currents.

- Possibility of unrestricted repetitive TMS (rTMS) because of the reduced power dissipation in coils

- Reduction of the size of the existing TMS coils (r).

- Increase of the focality and penetration depth through smaller coils.

- Noiseless TMS equipment and therapies.

- Hardware reduction in the power electronic requirements compared to existing technology.

- Reduction in the size of the equipment and increase of portability.

11. Chapter III: Development of Novel TMS Coils and Methods.
    Focal Stimulation of Deep and Narrow Brain Targets

11.1. Problem # 3:

The focal stimulation of the primary and secondary motor cortex (M1 and M2 regions) in rats is one of the long-term goals pursued by our research team since it would allow us to investigate the connections of cortical neurons with deep brain structures such as the basal ganglia and thalamus. These results would enable concluding about those same connections in the human brain, considering the anatomical similarities existing between these two species. In addition, the stimulation of the M1 and M2 regions would permit evaluating the effects of novel experimental non-invasive therapies for several neurological conditions such as Parkinson's disease.

The main challenge of stimulating the motor cortex in experimental animals like rats is that, given their small size, along with a limited focality of the currently available TMS equipment (coils and stimulators), the existing technology tends to overstimulate non-targeted regions in the surroundings of the target area. Sometimes, such overstimulation extends across the entire rodent body, defining the stimulation as "poorly-focal" or "non-focal". Something similar occurs in the human brain with the overstimulation of unintended areas, when the size of the target is smaller than the stimulated area that the TMS-coil can produce.

One of the main problems of low focal stimulation with TMS in experimental environments is the restrictions it implies for the correct identification of the neural connections –and their projections– in a network. Moreover, poorly focal stimulation produces unwanted stimulation of other non-intended areas (with their associated side effects in the individual under study), making TMS non-suitable for certain applications with the current technology.

On the other hand, most of the existing commercial TMS coils are based on air-core configurations, which somehow restricts the levels of magnetic flux density reachable with current intensities of a few kA. Very few studies in the TMS area include the use of ferromagnetic cores as an attempt to increase the focality of the E-field. From our literature research, we have observed much more attempts to increase the focality by modifying the coil's shape and geometry (still with an air core), with no apparent correlation or analysis of the role that different variables and parameters play in the focality.

11.2. Hypothesis # 3:

The use of <u>ferromagnetic cores in new customized TMS-coil designs</u> based on the correct <u>parametric analysis</u> of the relevant variables involved, allows reaching an increased and controlled focality of the electric field, to precisely stimulate narrow areas within the brain cortex in rats (as small as a few mm^2), as a proof of the potential to achieve the same focality in humans.

11.3. Rationale # 3:

Ferromagnetic materials exhibit significantly better magnetic properties than air as a core material for magnetic applications. A moderate-to-high *relative magnetic permeability*[3]*(μ_r)*, hundreds to several thousand times bigger than air's, combined with relatively high *saturation*

---

[3] The r*elative magnetic permeability* (μ_r) is the property that every material has to enable the flow of magnetic field lines through it, to create a certain level of *magnetic flux density* (*B*) in values per unit area. It relates the current-dependent *magnetic field intensity* (*H*) with the obtained *magnetic flux density* (*B*) over the material, and is a multiple of the referential *magnetic permeability of the vacuum* (μ_o = $4\pi\times10^{-7}$ H/m). The total magnetic permeability of the material will be defined then as $\mu = \mu_o \cdot \mu_r$.

magnetization[4] (M_{sat}) values, make ferromagnetic materials suitable candidates for TMS applications where an increased magnetic flux density is required.

In the initial stages of this research, we found that the main restriction in the use of ferromagnetic cores in coils intended to be focal is given by the presence of multiple media (materials) along the circulation path of the magnetic field. In devices such as transformers and toroidal coils, where the close path of the magnetic core guarantees a never-changing material in the cross-sectional area, this is not a problem, since the magnetic permeability is approximately constant along the entire path.

Different from what occurs in closed-core coils, in solenoidal coils –or arrangements of them in which the magnetic core ends on each side of the winding– there is a sudden change in the magnetic path. In TMS implementations, the *relative magnetic permeability* of the medium changes from the *ferromagnetic core* to the *air gap* below the coil. In some other cases, the change occurs directly to the biological tissues inside the head, when no air gap is left below the coil. In any case, the relative gain obtained in the magnetic flux density with the use of ferromagnetic cores is lost in a rapid decay, as a consequence of the abrupt change of medium. This turns the use of ferromagnetic materials ineffective after a few millimeters of separation (depth) between the coil and the target, including the multiple layers of biological tissue into the specimen's head, down to the brain cortex.

---

[4] The *saturation magnetization* (*M*) is the maximum value of magnetic moment per unit volume in a material, which is a direct indicator of the maximum *magnetic flux density* it can reach. Beyond this saturation point, an increase in the magnetic field does not necessarily manifest a significant (appreciable) increase in the magnetic flux density (B), since the slope of the *B-H* curve turns out extremely low (almost horizontal).

Based on the aforementioned, we believe this is the main reason why, within the still-emerging TMS area, the use of ferromagnetic core has been underrated to date as an effective alternative to increase the focality of the electric field.

Nevertheless, one of our main findings in the initial stages of this work shows that taking into consideration the abrupt decay of the *B-field*, and a typical (sometimes variant) top-of-the-scalp to brain distance for each species, there is a still useful range in which the effect of the selected magnetic core boosts the local magnetic flux density in the target. These results, compared to those obtained with no core (air) under the same conditions, reveal that the magnetic material would play a fundamental role in the achievable levels of *B-field*, with still manageable current intensities, under the right set of parameters. Therefore, one of the main goals in the upcoming stages should be to perform a parametric analysis that quantifies the levels of dependence of the magnetic flux density and penetration depth of the E-field on parameters such as the magnetic permeability, current intensity, focal distance, coil dimensions, among others.

Another improvement that the use of ferromagnetic materials introduces is the possibility to design coils of smaller size, compared to those needed for air-cored coils (no core). Moreover, for an air-cored coil to achieve the same B-field levels as a ferromagnetic-core coil of the same size in the tip (and a few millimeters away), it would need a significantly higher current intensity. This, along with the requirements of power dissipation in the wire (proportional to the cross-sectional area of the conductor), results in significantly bigger sizes for air-cored coils, as opposed to the required reduction in size for a higher focality that ferromagnetic core coils can provide.

Finally, yet importantly, the use of ferromagnetic cores allows the implementation of tip-sharpening as a technique to shape the magnetic flux density distribution right below the tip, and a few millimeters away.

11.4. Methodology # 3:

11.4.1. Part 1: Parametric Analysis in the Use of Ferromagnetic Cores and Tip-Sharpening for TMS Coils

For the first stage of work in this objective, we performed finite element simulation of a customized solenoidal coil in the shape of a truncated cone made of 67 turns, with a ferromagnetic material as a core with different shapes. The coil was designed with a wire of 1 mm in diameter, 200 mm in height, 20 mm in diameter at the bottom, and 5.71 degrees of opening angle. These values match those of an existing coil of the same characteristics, previously built in our lab for experimental work. The simulations were performed using ANSYS Maxwell 3D software. We included a cylindrical core made of MnZn ferrite, with a height of 174.4 mm, a radius of 18 mm, and tip sharpening in a conical shape with opening angles of 60°, 120°, and 180° (flat profile). The stimulating current was a sinusoidal pulse of 5 kA (peak) at 2500 Hz. The purpose of this initial work has been to explore the behavior of the magnetic field in the core-air interface and identify all the dependences of the magnetic flux density on parameters that modify its patterns of spreading and attenuation as spatial functions.

11.4.1.1. Finite Element Analysis

To obtain the distribution of the magnetic flux density (B) and the influence of a selected core, 3 finite element simulations were conducted with tip-sharpening variation, using a fixed opening angle and number of turns for the body of a conical coil. Details on the configuration and methodology are explained next.

11.4.1.1.1. Geometry Simulation

All the simulations contain 3 main bodies.

a) The coil: Simulated of standard copper for windings with properties extracted from the ANSYS MAXWELL materials database. The number of turns was fixed at 67, with a height of 200 mm and a wire width of 1 mm. The opening angle for the body is 5.71 degrees from the axial axis, forming a truncated cone of 20 mm and 60 mm in diameter in the circumferences between the bottom and the top. These dimensions match an existing coil in our laboratory for future experimental work (Fig. 42).

b) The core material: Represented as a cylinder with the same height as the coil and 174.4 mm in diameter that perfectly fits inside the coil. This volume was configured with a ferromagnetic material of customized properties, described in the next section.

c) The container volume: Common for all of the simulations, it was configured in the shape of a rectangular box filling the surroundings of the coil and the core. The material used for the volume was air of standard properties from the ANSYS database. The dimensions of the air box are 7 mm × 7mm (W × D), with a height that extends 10 mm above the top of the coil and 10mm below the lowest end of the core, with or without a tip.

155

The geometries were designed using SolidWorks and imported as ".SLDPRT" files to ANSYS Maxwell.
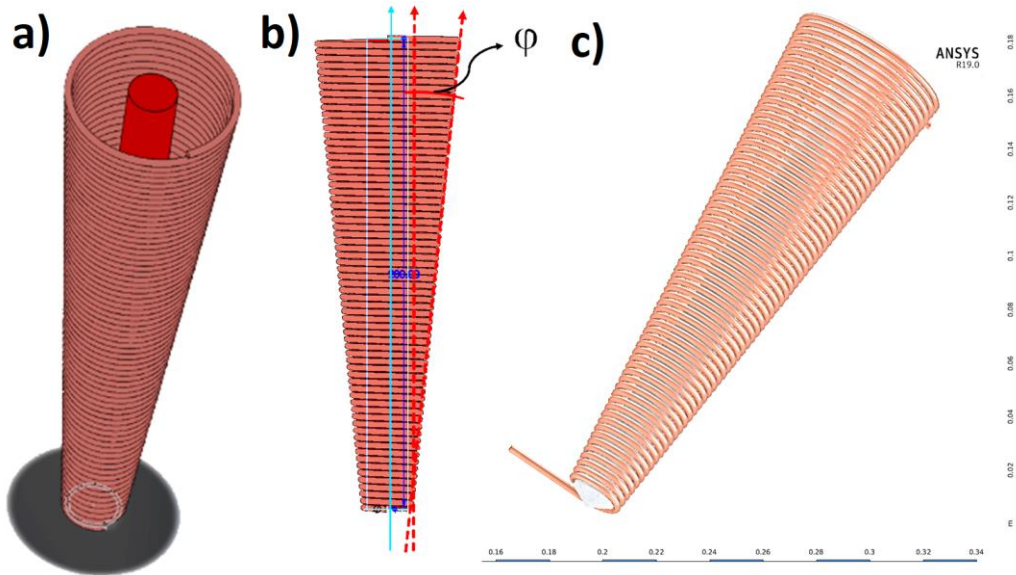
Figure 42 – Simulated conical coil with MnZn ferrite core. a) isometric view. b) Front view with opening angle.
c) Isometric view of the coil with a core with 120° of tip sharpening.

11.4.1.1.2. Core Material

The ferromagnetic material used for these simulations was MnZn Ferrite with initial relative magnetic permeability (μ_i) of 2200 at 1mT. The whole B-H curve up to 1200 A/m is shown in Fig. 43-a, extracted from the datasheet of the commercial product PC90 of the manufacturer TDK[104]. The module of the magnetic permeability is shown in Fig. 43-B, which remains constant for low-frequency values.
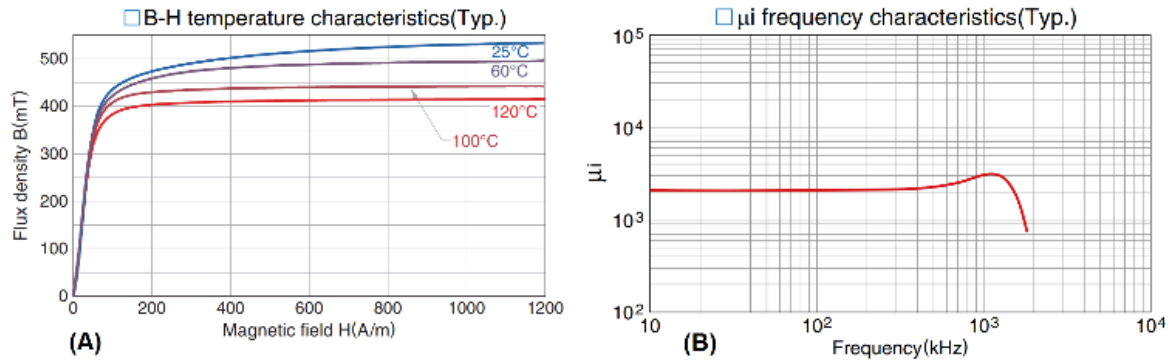
Figure 43 – Magnetic properties of the PC90 MnZn Ferrite. A) B-H curve at different temperatures. B) Module of the Complex Magnetic Permeability vs. frequency

11.4.1.1.3. Electric Current Set Up

The simulations use 1000 Adc from the bottom to the top to produce a magnetostatic analysis that reveals the outgoing flux lines. Due to the approximately invariant behavior of the complex permeability for the MnZn ferrite within the typical range of application of TMS (typically up to 3.5 kHz) [105][42][106], frequency effects over the magnetic properties and losses are not considered. This part of the work studies instead the impact of geometric parameters in the distribution of the magnetic flux density (*B*) towards the increase of the focality, regardless of energy losses.

11.4.1.2. Simulated Cases

Three cases were simulated to determine the influence of the tip-sharpening in the magnetic flux distribution at the targeted area. All of them used the same conical coil previously described, only varying the opening angle of the tip as follows: a) ferromagnetic cylindrical core (f.c.c.) with non-sharpened tip (180 degrees of opening angle), b) moderately sharpened f.c.c. (120 degrees) and c) highly sharpened f.c.c. (60 degrees). Figure 44 shows an example of each of the geometries for the three cases of tip sharpening.
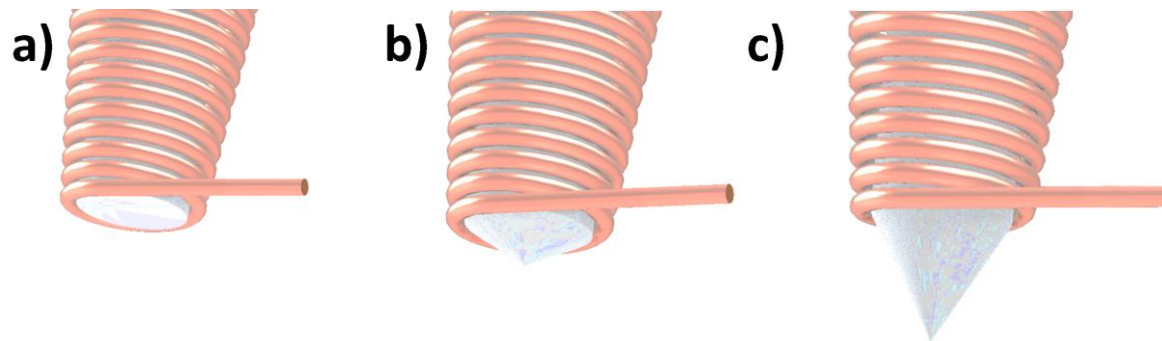
Figure 44 – Cases simulated for different degrees of tip sharpening in the core. a) 180 degrees (flat tip); b) 120 degrees; c) 60 degrees.

For all the cases, the magnetic flux density distribution was obtained both in an X-Z vertical plane and in an X-Y front plane. This would allow us to obtain the behavior of the magnetic flux density as a function of the tip sharpening.

11.4.2. Part 2: Development of a highly focal TMS coil for narrow targets in small experimental animals. The Quintuple AISI 1010 Core Coil

Based on the acquired knowledge of the first group of simulations, concerning the spreading and attenuation of the *B-field* in conical coils, in a second project we tested at least twenty (20) different configurations of coils, including: solenoidal straight, conical, and elliptical coils; figure-of-eight coils; and arrangements of coils of different geometries. This set of simulations allowed us to understand how the spreading of both the magnetic field and the current density affect the induced E-field during TMS, in volumes below the cortical surface, and how the induced currents interact to create an E-field profile when arrangements of coils are used.

To evaluate different configurations of TMS coils designed to achieve highly focused stimulation, we performed recurrent simulations using finite element modeling on ANSYS Electronics Desktop (Maxwell 3D). Each modeled coil is a dual-winding solenoid of elliptical top-view cross-section with a ferromagnetic core of the same shape (Fig.45). In the early stages of this work we predicted required magnetic flux densities of above 2 T per solenoid, in order to induce E-fields of around 100V/m with reasonable dB/dt (defined by the typical range of TMS frequencies, up to 3.5kHz). Then, we conducted preliminary research looking for cost-effective ferromagnetic materials with saturation magnetization (M) over 2 T, significantly high relative permeability –in order to reduce power requirements– and relative ease for machining or future additive manufacturing processes. This way we found the AISI 1010 low-carbon steel to be an appropriate material for our ferromagnetic cores, having an $M \cong 2$ T with a magnetic flux intensity (H) of 4×10^4 A/m, an initial relative permeability of μ_r=667.75 and standardized for relatively low complexity machining, given the low carbon composition. All the reference parameters for this material were extracted from the SysLibrary of ANSYS.

The parameters of the coil are: wire diameter = 1mm; turns = 50 (2x25); height = 25.4mm; core cross section: semi-mayor axis = 10.6mm, semi-minor axis = 2.8mm.
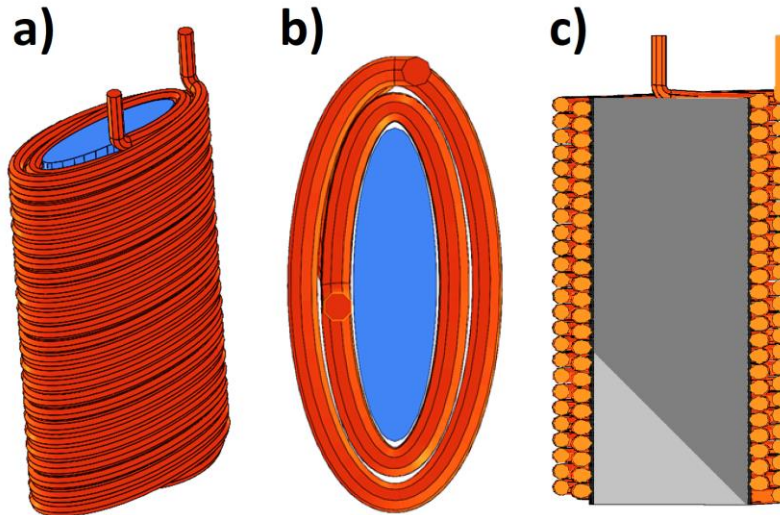
Figure 45 – Dual solenoid of elliptical shape with AISI 1010 carbon steel core. a) Isometric view; b) top view c) internal view (V-shape profile in dark gray and complement for flat profile in light gray).

Fig. 46 shows the B-H curve of the core material, whereas the electric and magnetic properties of the simulated materials for the coils are in Table VIII.
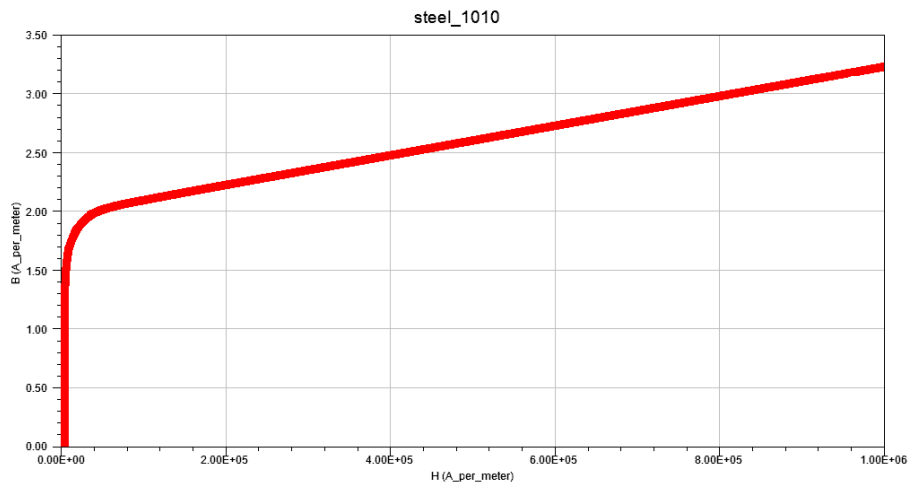
Figure 46 – B-H curve for AISI 1010 carbon steel, showing a linear region of fix slope in the beginning, and then a saturation point at approximately 2 T.

Table VIII – Electromagnetic Properties of the Coil

Material	Electrical Conductivity (σ) [S/m]	Relative Electric Permittivity (ε_r)	Relative Magnetic Permeability (μ_r)
Copper	5.8E7	1	0.999991
1010 Steel	2.0E6	1	667.75 (peak)
Air	0	1.0006	1.0000004

Departing from the basic geometry in Fig. 45, we have built the coil arrays shown in Fig. 47 a and b. The initial configuration is made of two elliptical dual-winding solenoids placed in pairs, vertically standing on orthogonal axes over the plane z = 0mm (using the lowest point of the coils as reference). This setup was repeated with and without a magnetic core (replaced by air), and then with a V-profile tip, sharpened toward the centroid of the array. The results of this part would be used to create the final configuration of five solenoids (Fig. 47-b), explained later in this chapter.
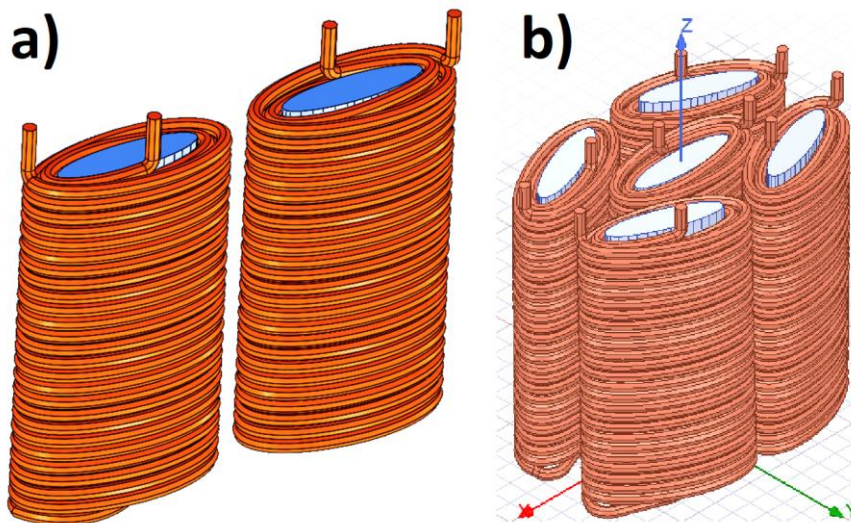
Figure 47 – Double array of elliptical dual solenoids (AISI 1010 carbon steel or air core in blue). b) Final quintuple array of dual solenoids.

To accurately predict the induced E-field that would be obtained in practical implementations, we identified the location of the pyramidal neurons of layers V and VI (Fig. 48-a) in the M1 region of the motor cortex, using the rat brain atlas [107], [108] in stereotaxic coordinates.

Figure 48 – a) Depth by layer in the rat brain cortex * [109], [110] b) Thickness by layer in the rat head ** [109]

In order to accurately determine the depth of stimulation, the thickness of the scalp, skull, and connective tissue layers (Fig. 48-b) were considered for the rat head [109].

The relative coordinates of the targeted cortical region[110] with respect to the bregma (reference point for stereotaxis on the rat skull) [111], [112] were: ML=3mm, AP=2mm, and DV=2mm.

Fig. 49-a-d illustrates the targeted point in the corresponding coronal, sagittal and horizontal planes. The desired stimulated region needs to be restricted to a radius of ~0.56 mm around the target point (red dot in Fig. 49). Given the reduced scale, this highlights how

small the dimensions of the target and its surroundings are, as well as the difficulty to obtain a focal stimulation.

Using a 3D surface model of the rat brain, we extracted a simpler spherical approximation of the rat head with a diameter of 30.00 mm (blue sphere in Fig.49-a), extended from the target to the closest point in the head surface.
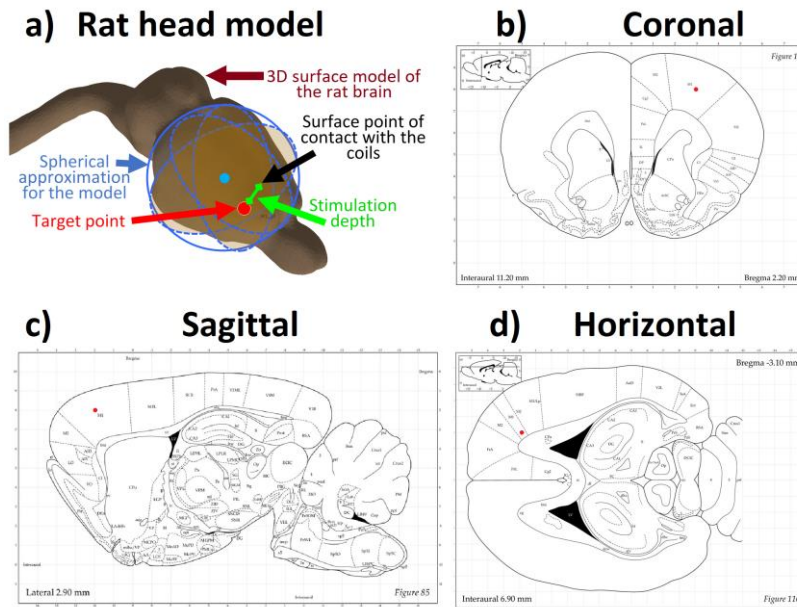
Figure 49 – a) Rat head and brain 3D models. Stereotaxic coordinates in the Rat Brain Atlas. b) Coronal plane c) Sagittal plane d) Horizontal plane.

Subsequently, we built a spherical head model (Fig. 50 a and b) with the same curvature of the section, adding layers of tissue with thickness and electromagnetic properties similar to those present in an adult rat head (Fig. 48 and Table IX).

In order to simplify the complex calculations of the E-field in relatively thin layers, our head model merged these layers with the thicker contiguous layers of highest proximity in electromagnetic properties. The result is the simplified four-layers rat head model in Fig. 50 and Table IX.
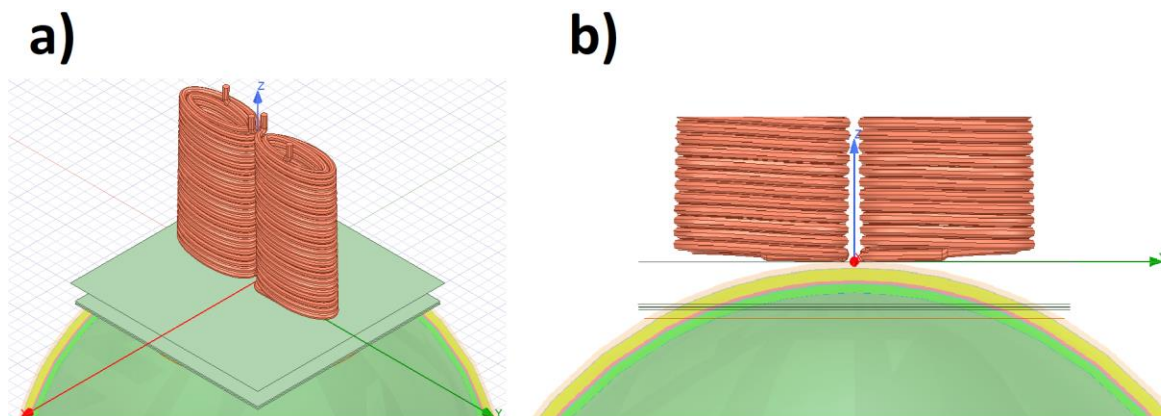
Figure 50 – Spherical model, coils and planes. a) Isometry. b) Front.

Table IX – Electromagnetic Properties of the Head Model

Actual Layer in theRat Head	Layer in the Simplified Head Model	Thickness (µm)	Electrical Conductivity (σ) [S/m]	Relative Electric Permittivity (εr)	Relative Magnetic Permeability (µr)
Scalp	Scalp	500	0.17	12000	≈ 1
Periosteum		100	Approximated to the same as the scalp		
Skull	Skull	1000	0.01	800	≈ 1
Dura mater		300	Approximated to the same as the skull		
Arachnoid	Cerebrospinal Fluid (CSF)	75	1.654	6000	≈ 1
Sub-arachn. S.		750	Approximated to the same as the CSF		
Pia Mater	Brain cortex	25	Approximated to the same as the GM		
Gray Matter (GM)		--	0.276	12000	≈ 1

For the evaluation of the ability of the coil to focally stimulate the M1 and, analogously, the M2 region, we have created three secant planes (Fig. 50) at depths of 3.75, 4.00, and 4.25 mm –the same depths as the targeted pyramidal neurons– in which we have obtained the distributions for the magnitudes of the E-fields and B-field.

The simulations have been configured in a transient state, using a single biphasic pulse of current of cosine waveform, with a peak amplitude of 5kA. The frequency of the pulse is

2500Hz (within the typical TMS range [42], [105], [106]) and the duration is one period (400µs).

In the meshing process, we have chosen a non-adaptative initial grid, provided by ANSYS Maxwell 3D for transient solutions, applied to all geometries. After generating tetrahedral elements of varying sizes, we carefully refined the mesh in all the layers of our head-brain model to ensure a high resolution around a target of about 1 mm in diameter. Then, we restricted the average element size (RMS edge length) in these layers to 1mm, obtaining minimum element sizes of 0.3842mm. This means a resolution of about 15.64 elements/mm^2 in the target (most sensitive region), which is high enough to observe variation patterns and gradients in the fields. For the rest of the elements, we have assured average element sizes no bigger than 1.05mm for the coils, 2.07mm for the cores, and 1.32mm for the air enclosure. For more details, please see supplementary data.

The previous setup was repeated for recurrent simulations with air core, as well as with planar-faced and V-shaped AISI 1010 carbon steel cores. Then, different configurations were obtained by varying the relative position of the 2 and 5 coils with respect to the center.

11.4.3. Part 3: Development of a Space-Varying E-field Vector Modulation for Spatial and Temporal Control of the Electric Field

11.4.3.1. Theoretical Approach

We started with the idea of using a fixed configuration of solenoids to create a coverage area over a target plane where a moving focal *E*-field can be obtained. With the appropriate geometric arrangement, this is possible by a mere change of polarization on each solenoid,

leading to constructive and destructive interferences in the magnetic flux density (*B*-field) and induced current densities. These interferences aim to produce cold and hot spots in the *E*-field magnitude distribution that we can move at will. Previous attempts at producing electric fields electronically controlled are shown in the literature [20], [113], [114]. The most relevant technology so far is *multilocus TMS (mTMS)* [114], a variant of TMS that used multiple coils overlapped to produce superposition of the induced electric fields. TMS has proven to be effective and currently has the attention of part of the TMS community. However, one of the main drawbacks is the low focality for narrow targets, due to the significantly large size of the coils.

In [115] we demonstrated high controllability of the point of maximum *E*-field using the approach of *the path of the highest current density*. In that work, we used identical polarization in each of the five solenoids of the QCC coil with single sinusoidal pulses of current of 10 kA at 2.5 kHz. This allowed us to restrict the spreading of the magnetic flux lines below the central coil to keep them aligned with its longitudinal axis. The result was a path of increased current density along the central axis, which also raised the associated *E*-field in the target as expected. Such results made us aware of the potentiality of this technique to also control the location of the induced *E*-field at will if we were able to manipulate the coil currents independently.

Using seven solenoids of two layers of 25 turns for each petal, with a height of 25.4 mm (1 inch) and cylindrical magnetic cores of similar height and radius of 0.5 mm, we built the configuration shown in Fig. 51. Then, we labeled each double solenoid with a number (Fig. 51-a) and identified 25 probable stimulation zones in a hexagonal coverage area (Fig. 51-b).

The stimulation zones are separated into five (5) different groups, according to the type of polarization required for the expected *E*-field. The green zones with capital letters are designed to stimulate the areas between two consecutive petals (*e.g.,* solenoids 1 and 6). This pattern is obtained using opposite currents in the two solenoids (phase-shifting of 180°).
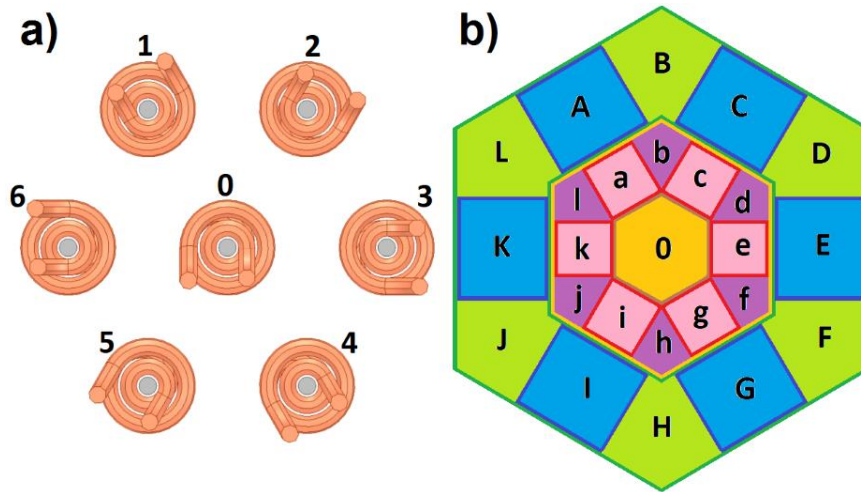
Figure 51 – a) Figure-of-Flower Coil (FFC) of 6 petals. b) Stimulation zones.

This type of polarization is similar to the one in a standard figure-of-eight coil (FEC), but with reduced size and specific location in the target plane. The pink zones with lowercase letters will be stimulated using the same method between the central coil and any of the petals (*e.g.,* coils 0 and 6).

The pink and green zones provide stimulation to almost half of the coverage area with the simple and direct polarization of the two closest coils. However, the blue, yellow, and purple zones are more difficult to stimulate directly since they are located either below a solenoid or between three adjacent solenoids. At these zones, the hotspot of the *E*-field can be produced neither with the polarization of the coil on top nor with the polarization of two consecutive coils. To solve this, we carried out computer-based models of the FFC that allowed us to obtain the necessary polarization configurations to stimulate such areas, based on time-averaged *E*-fields. Finally, the operation of the SVEVM was tested over realistic

anatomically accurate human and rat head models. This demonstrated the feasibility of the coil (FFC) and the method (SVEVM) to focally stimulate moving targets over small cortical areas in both clinical trials and research environments.

11.4.3.2.Methods

Using ANSYS Maxwell 3D software we first performed finite element simulations over a heterogeneous spherical rat head model with differentiated tissue layers. The model, shown in Fig. 52 includes the thickness and electromagnetic properties of the scalp, skull, cerebrospinal fluid (CSF), and gray and white matter (GM & WM) (Table IX).

Table X – Properties and Parameters of the FFC and FEC

Coil	Material	Location	ε_r	σ (S/m)	μ_r	Description
FCC	AISI 1010 Low Carbon Steel	Core	1	2×10^6	See B-H curve below	Cylindrical shape. Diameter = 1 mm Height = 25.4 mm
	Copper	Winding	1	5.8×10^7	0.999991	2 layers $\times$ 25 turns Wire diameter = 1 mm
	Air	Surrounding volume	1.0006	0	1.0000004	Filling the enclosure that surrounds the entire model
FEC	Copper	Winding	1	5.8×10^7	0.999991	Inner Diam. = 52 mm, Outer Diam. = 88 mm, Height = 7 mm N° of Turns = 2x10, Cross sectional area = 7$\times$1 mm
	Air	Surrounding volume	1.0006	0	1.0000004	Filling the core and the enclosure that surrounds the entire model
Source: ANSYS Maxwell Library						

An FFC of six petals was simulated over the spherical model (Fig. 52). Each solenoid was built according to the characteristics shown in Table X. All the simulations were carried out using the *Eddy Current solver* for sinusoidal currents at 100 kHz.

Published works have reported the use of envelope modulation with two tones at intermediate frequencies (a few kHz) to produce a low-frequency stimulation component of *E*-field (around 10 Hz) [99], [116], [117].

We have investigated the use of high frequency in TMS to exploit the capabilities of a higher -dB/dt, among other advantages. This would allow reducing the size of the coils and pursuing higher focalities and penetration depths as it is required in the field. Although our study of TMS at high frequency is in the publication process, an additional study on the feasibility to obtain oriented E-field with vector techniques was needed. For this reason, all the simulations in the present work are performed at 100 kHz, increasing the –dB/dt in a range up to 100 times compared to the typical TMS range (1-3 kHz).
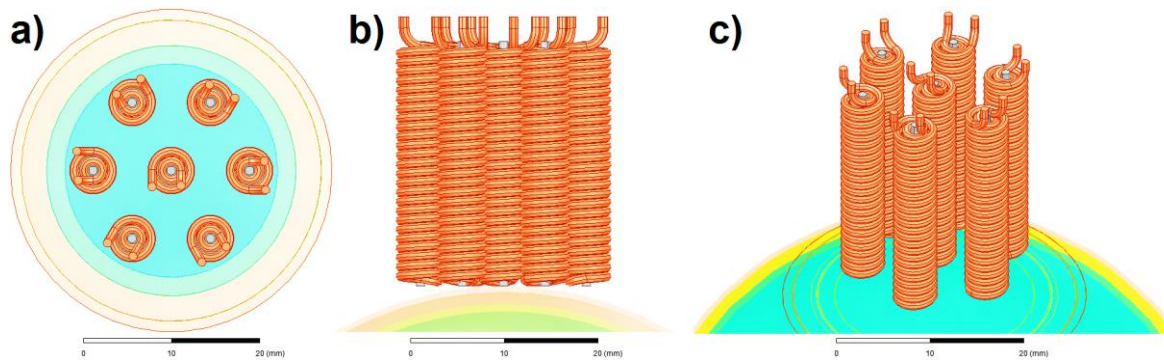
Figure 52 – FFC over the multi-layer spherical rat head. a) Top view; b) front view and detail of the different tissue layers; c) isometric view.

The configuration mentioned above allowed us to explore the different possible combinations when polarizing the solenoids independently in the FFC. These combinations rely on changes in amplitude and phase to vary the interference patterns and, therefore, the resulting *E*-field. Although changes in frequency can also be managed, due to the extensive

scope they are not included in this paper. However, this is currently included in our upcoming publications.

The first simulated pattern was obtained with the polarization of petals 1 and 6 with amplitudes of 5kA in each solenoid and 0 A in the rest of them (turned off). This enabled us to verify the predicted hotspot of E-field magnitude over the zone "L", applicable to all other green zones with the polarization of the correspondent petals. A second scenario was prepared to test the location of the stimulating point in zone "a", representative of the same case for all the pink zones. This scenario required amplitudes of 5kA in petal "1" and -5kA (phase shifting of 180°) for the body or central coil (coil "0").

The third scenario simulated aimed to stimulate zone "l", demonstrative of the method to stimulate any of the purple zones. For this case, we polarized petals 1 and 6 with 2.5 kA and the body (coil 0) with 5kA. With this, we obtain stimulation of the zone with a stripe pattern parallel to the direction formed by the petals. Alternatively, for the purple zone we ran four more simulations with 3.5kA in the central coil and -3.5kA (phase shifting of 180°) in all the petals but one, which was left off. The petals turned off in each simulation were 6, 5, 4, and 3. With the E-field magnitudes calculated for each sub-case (polarization mode), we exported the data to MATLAB using 24-bit .bmp files. Then, using a graphic method that considers the directions of the E-field vectors, we computed the resulting scalar field of magnitudes through a weighted sum of each polarization mode with a similar contribution (25% each). The sum represents the time-averaged E-field seen at the target plane after switching from one polarization mode to another, in consecutive periods of the sinusoidal waveform at 100 kHz. This allowed us to obtain a hotspot at zone "b" based on the constructive interference at this location, and colder zones of E-field in the surroundings.

The fourth pattern attempted was the one necessary to stimulate blue zones below the petals. For zone "K" we tried this pattern polarizing the petal 6 with -3kA and the petal 3 and central coil with 3kA. All other solenoids were turned off. The result showed the maximum *E*-field magnitude biased toward coil 6 as expected, due to the increased *B*-field to the right side of the zones "0" and "E". However, the *E*-field never reached the center below the coil 6 focally. After several other combinations, we concluded that the best method to stimulate blue zones is by adding a second layer of six petals, radially aligned with the existing ones. This would permit stimulating these zones polarizing two petals in a radial line. However, this would also require six additional ports in the power electronics of the stimulator, with the associated difficulty and costs. For this reason, it is convenient to assess the idea of an FCC of six petals with no coverage of the blue zones instead.

Finally, a fifth scenario was tested for the stimulation of the zone "0", with the polarization of the coils 6 and 3 with 5kA and -5kA, respectively. We originally expected a similar pattern of high *E*-field in the center as in any FEC, but due to the separation of the solenoid, the focality was too poor. We finally tried an alternative configuration polarizing coils 1, 5, and 6 with 5kA and coils 2, 3, and 4 with -5kA, resulting in a lengthier and thinner vertical polarization strip than the one obtained with coils 6 and 3. To reduce the overstimulation of unwanted zones we have combined this pattern in time with the same pattern rotated 60 degrees counterclockwise, with the polarization of the correspondent petals for it. This finally produced a pattern with the maximum right below the central solenoid.

For the assessment of the SVEVM with the FFC over real specimens, we prepared two final sets of simulations over realistic head models, repeating the patterns of stimulation obtained over the spherical model. The first simulation included an anatomically accurate rat

head model obtained from a combination of CT scans and MRI images [118]. The second set of simulations was carried out over an MRI-based realistic human head model obtained from an adult healthy human subject, similar to the one we used in [119]. In both models, the scalp, skull, CSF, GM, and WM, were differentiated assigning their correspondent electromagnetic properties according to [119] and [118], and Tables XI and XII.

Table XI – Properties of the Spherical Rat Head Model and the Anatomically Accurate Rat Head Model

Layer	ε_r	σ (S/m)	μ_r	Thickness for the spherical model (mm)	Description
Skin (scalp)	12000	0.465	≈1	0.6	Merging scalp and periosteum
Skull	800	0.010	≈1	1.3	Merging skull and dura matter
CSF	6000	1.654	≈1	0.825	Merging Arachnoid and sub-arachnoid
Brain cortex (Avg. GM & WM)	12000	0.27	≈1	Radius = 35 mm	Measured from the center to the cortex to follow the curvature of the brain

Table XII – Properties of the Realistic Human Head Model

Layer	ε_r	σ (S/m)	μ_r	Description
Skin (scalp)	12000	0.465	≈1	Merging scalp and periosteum
Skull	800	0.010	≈1	Merging skull and dura matter
Cerebrospinal Fluid (CSF)	6000	1.654	≈1	Merging Arachnoid and sub-arachnoid
Gray Matter (GM)	12000	0.42	≈1	
White Matter (WM)	12000	0.22	≈1	Measured from the center to the cortex to follow the brain curvature

11.4.1. Part 4: Design of a novel focality measurement methodology

During the literature research and simulations for our coil design, we became aware of a set of limitations in current methodologies for *focality* calculation. While most of the existing definitions of *focality* are based on the estimation of the stimulated area (in surface units), they do not consider the overstimulation of the surrounding tissues. This is a critical aspect when we intend a coil to be focal since it should consider the side effects caused by the overstimulation of untargeted areas. Another common observation in published works is the use of the term "focality" without describing a focal point, focal distance, or target. By definition, these concepts are intrinsically related, and we believe they should be reported together to express the specific conditions of operation of the coil when the measurement is done.

In order to quantify the suitability of a coil to stimulate a target region focally, we have defined a weight function that satisfies the following requirements; a) Need to quantify the focality in a continuous normalized scale from zero (0 = non-focal) to one (1 = fully focal), alternatively representable in percentage terms. b) Need to grow towards the unity from each side of the curve, with a soft peak, being continuous and fully differentiable in its entire domain. c) The roll-off factor from the peak to each of the sides should be high enough to benefit only scenarios of high overlap between the stimulated area (A_s) and the target area (A_t), and rapidly decrease in cases of low overlap or overstimulation of non-targeted areas.

$$AES\_erfc_{d_n} = erfc(2.5 \cdot d_n) \times erfc(-2.5 \cdot d_n) \tag{88}$$

Equation (2) shows the proposed function with the previously described characteristics, which we have named "*Adjusted Even Symmetry Error Function Complement*" or *AES-erfc*

(Fig. 53-a). Notice that the x-axis in Fig. 53-a contains the values of a normalized dimension (d_n) related to the level of overlap between the targeted area (A_t) and stimulated area (A_s), defined as "*focality form factor*" (Eq. 89).

$$d_n = \frac{A_s - A_t}{A_t} \quad , \quad \forall \, 0 \leq A_s \leq A_t \tag{89}$$

The y-axis in Fig. 53-a shows the *normalized weight* assigned to such levels of overlap, termed "*specific focality*" (*sf*).

Since the *AES-erfc* is a symmetric function, it becomes zero by the right side at infinity. However, on the left side it is restricted to a minimum of $sf = 8.1374 \times 10^{-4}$, where it should be zero when $d_n = -1$ (no area stimulated). This means an error of 0.0814% in the *AES-erfc* at *this point* (Fig. 53-b).
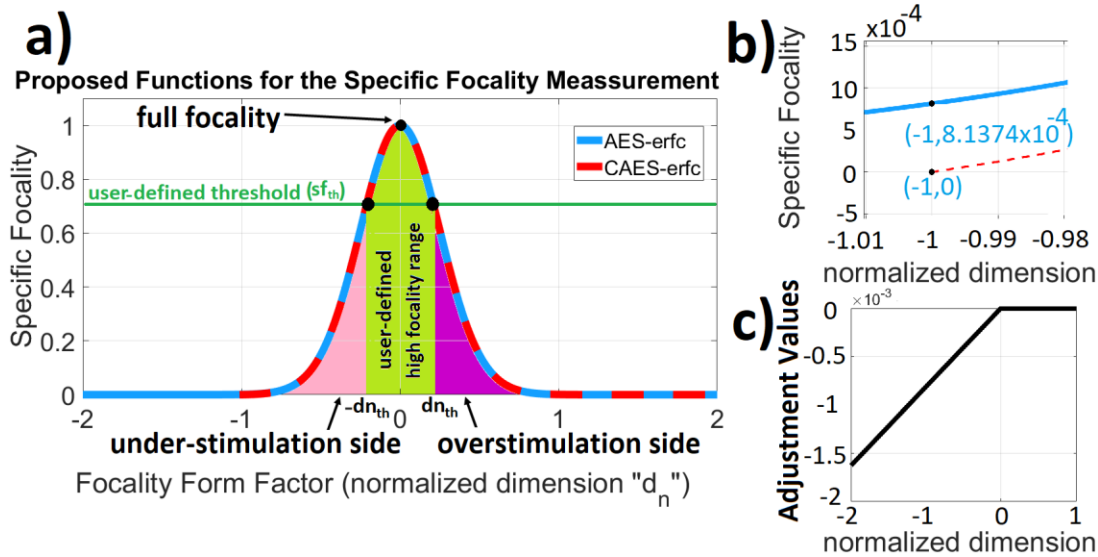
Figure 53 – a) AES-erfc and CAES-erfc plots. b) Error at dn=-1 for AES-erfc (blue) and correction for CAES-erfc (dashed red). c) Adjustment function.

Though the error is minimal, in order to keep the accuracy we have calculated a correction term that makes the specific focality -and its error- zero at $d_n = -1$ (Fig. 53-b).

The correction term is given by Eq. 90 (see Fig. 53-c), where "U" is the Heaviside function introduced to make the expression valid only up to $d_n = 0$.

$$ct = [erfc(-2.5) \times erfc(2.5)] \cdot d_n .* U(-dn) \tag{90}$$

Now, the specific focality is given by the new "Corrected-Adjusted Even Symmetry Error Function Complement" or CAES-erfc, defined as:

$$sf = erfc(2.5 \cdot d_n) \times erfc(-2.5 \cdot d_n) + ct_{(d_n)} \tag{91}$$

AES-erfc and C*AES-erfc* can be used discretionally. C*AES-erfc* allows accurate results in focality quantification for comparisons of coils, whereas *AES-erfc* is better for rapid estimations where a minor error is acceptable. Hence, C*AES-erfc* is considered in this text for *sf* calculations.

Based on the range of d_n using CAES-erfc, Fig. 53-a allows to identify scenarios of under-stimulation ($-1 \leq d_n \leq 0$), focal stimulation ($d_n = 0$), overstimulation ($d_n \geq 0$) or no stimulation ($d_n = -1$). Moreover, the user may define a flexible criterion for what "full" or "high" focality would be for a particular application. This criterion may be based on either a *specific focality threshold* (*sf_{th}*) or a *focality form factor threshold* (*dn_{th}*).
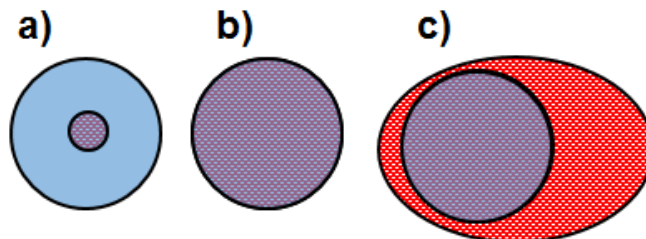
Figure 54 – Scenarios of a) under-stimulation; b) focal stimulation and c) overstimulation. Target areas in blue, stimulated areas in red and focally stimulated areas (intersection) in purple.

Eq. 88 to 91 should be used only when the *stimulated area* totally covers the *target area* in one piece, or vice versa (Fig. 54). However, because of the *lack of homogeneity*, most of the cases in TMS result in *stimulated areas* that cover both *targeted* and *non-targeted* areas. This leads to more complex scenarios of *partially focal stimulation* of the target with potential overstimulation of the non-targeted areas in the surroundings (Fig. 55).
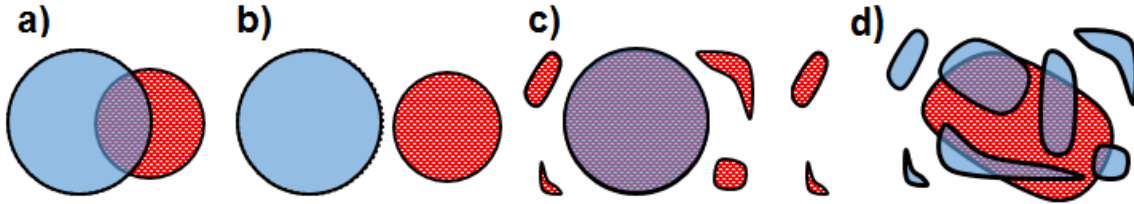
Figure 55 – Scenarios of a) partially (low) focal stimulation with moderate overstimulation of the adjacent region; b) non-focal stimulation (very high overstimulation outside the target); c) High focal stimulation with moderate overstimulation outside; d) High focal stimulation of multiple target segments with moderate overstimulation of the surroundings. Target area/segments in blue, stimulated areas in red and focally stimulated areas (intersection) in purple.

Since combined scenarios of partial focality in the target with overstimulation of adjacent areas are more likely, the *focality form factor* needs to be redefined in two separate parts.

a) The first part calculates a defined *focal stimulation factor* (ψ). This is the ratio between the focally stimulated areas inside one or multiple target segments in a plane (A_{focal}), and the total area of such target segments (A_t), according to Eq. 92.

$$\psi = \frac{\Sigma(A_t - A_{focal})}{\Sigma A_t} \tag{92}$$

b) The second part, called *overstimulation factor* of the adjacent areas (χ), is calculated as the ratio between the sum of all the existing overstimulated areas (or segments) outside the target ($A_{overstim}$) and the total area of the target segments (A_t) in Eq. 93.

$$\chi = \frac{\Sigma A_{overstim}}{\Sigma A_t} \tag{93}$$

Now, the *focality form factor* can be redefined as a complex value (d_{nc}) that takes into account both the focal behavior in the target and the overstimulation characteristic in the surroundings. These behaviors are simultaneously expressed in the orthogonal real and imaginary axes of the complex plane, to create a *complex focality diagram* (Fig. 56), according to Eq. 94.

$$d_{nc} = \psi + j\chi \tag{94}$$

Notice from Eq. 92 to 94 that, when the overstimulated areas are null and there is only one segment of the target area, Eq. 89 and 94 are of identical modulus and opposite signs. This change of sign was intentionally inserted in Eq. 92 to restrict the *complex focality diagrams* to the first quadrant of the complex plane. The *complex focality form factor* (d_{nc}) indicates at all times the specific scenario of focal stimulation of the target, and adjacent overstimulation for each coil configuration (Fig. 56).
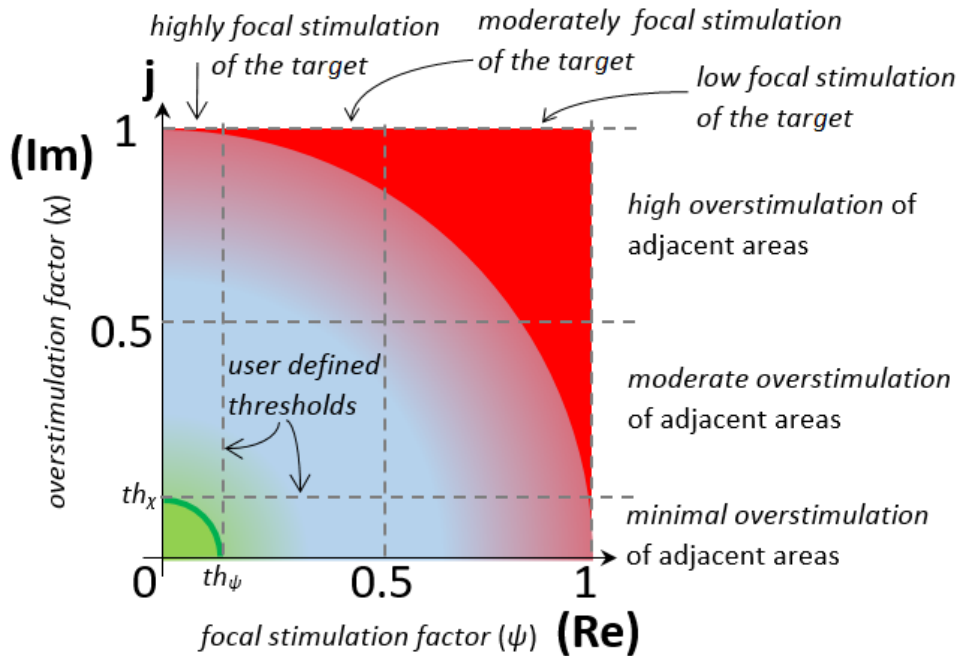
Figure 56 – *Complex Focality Diagram.* First quadrant of the complex plane showing the components of the *complex focality form factor.* The user-defined thresholds for the focal stimulation factor (th_ψ) and the overstimulation factor (th_χ) determine the tolerances for what is considered to be the zone of highly focal stimulation of the target with minimal overstimulation of adjacent areas (green zone).

When the stimulated area is smaller and completely located inside the target area (Fig. 54-a), the focality form factor (d_n) is negative. Then, its equivalent *complex focality form factor* (d_{nc}) will be positive, purely real, and of the same modulus as d_n. Contrarily, when the stimulated area is equal to or bigger than the target (Fig. 54 b and c) and completely overlaps it, the focality form factor (d_n) is positive (including the zero). In that case, its equivalent *complex focality form factor* (d_{nc}) will be a positive purely imaginary quantity of the same modulus. These conversions are shown in (9) and (10).

$$d_{nc} = -d_n \tag{95}$$

$$d_{nc} = \boldsymbol{j}d_n \tag{96}$$

Eq. 95 and 96 are used to obtain the *complex focality form factor* and the *complex focality diagram* (Fig. 56) only for cases in Fig. 54. However, for all other cases (e.g. those in Fig. 55), the *complex focality form factor* will result in non-null real and imaginary parts. Therefore, Eq. 92 to 94 represent the general equations to be used in any case to obtain the *complex focality form factor* and *diagram.*

Now, we redefine the calculation of the *specific focality* as a function of the *modulus of the complex focality form factor* ($|d_{nc}|$). Then, for all cases, the focality of the coil can be assessed using Eq. 97, obtained by replacing d_n with $|d_{nc}|$ in (2) or (3). The domain of Eq. 97 (possible values for $|d_{nc}|$) will be from zero to infinity, and its range all the possible values of AES-erfc or CAES-erfc to the left of the peak of full focality. Negative values of the semi-axis of abscises are not part of the domain when $|d_{nc}|$ is used as an argument in (2) or (3).

$$sf_S = erfc(2.5 \cdot |d_n|) \times erfc(-2.5 \cdot |d_n|) \tag{97}$$

11.4.1.1.1. Specific Focality in Thin Target Areas

a) The *surface specific focality* (*sf$_S$*) of the E-field over thin targets within a volume was calculated following the next steps.

b) Define the planes with the target areas to be stimulated.

c) Plot the modulus of E-field (|E|) for each plane of interest.

d) Define an E-field stimulation threshold.

e) Using a color map, identify the edges of the segments of the stimulated area with E-field above the threshold.

f) For segments of the stimulated area with regular geometry (e.g. circle, square, etc.), calculate the surface (As) directly. If irregular, simplify it to the closest regular shape(s) possible.

g) Find the complex focality form factor with Eq. 92 to 94, the specific focality (11), and the complex focality diagram.

11.4.1.1.2. Specific Focality in a Target Volume (sf$_V$)

The *volumetric specific focality (sf$_V$)* of the E-field was obtained from the recurrent calculation of the *surface specific focality (sf$_S$)* over consecutive secant planes. The target was divided into multiple trapezoidal sections of different cross-sectional areas and variable heights to cover the entire volume.

$$sf_{VF} = \frac{1}{V_t} \cdot \sum_{n=1}^{N} \left[\left(\frac{sfs_{(zn)} + sfs_{(zn+1)}}{2} \right) \cdot \left(\frac{At_{(zn)} + At_{(zn+1)}}{2} \cdot |z_{n+1} - z_n| \right) \right] \quad (98)$$

Eq. 98 calculates the *volumetric sf as* the summation of the products between a) the average *surface specific focality* of the two planes that define a trapezoidal section, and b) the average volume of the section, normalized with respect to the total volume of the target. Similar to the *surface specific focality*, the *volumetric specific focality* provides dimensionless values.

11.4.1.1.3. Nomenclature

Equation (13) shows the proposed nomenclature for its general use in results of the *specific focality of the E-field* for TMS coils.

$$ {}_{th}^{z}\, \Psi_{X_E}\, {}_{A_S}^{A_t} \tag{99} $$

The nomenclature in (13) allows expressing the *specific focality* in a unique symbol with four parameters. a) The focal distance (z) represents the separation between the lower point of the coil and the target plane. In volumes, the distance is considered up to the mid-depth of the target volume. b) The stimulation threshold (th), expresses the minimum admissible percentage of the E-field in the stimulated region, with respect to its maximum. c) The *target area* (A_t), which is the area intended to be stimulated. d) The stimulated area (A_s) is the resulting area of the stimulated surface. When reporting *volumetric specific focality*, A_t and A_s should be replaced by their volumetric equivalences V_t and V_s. Sub-index X should be also substituted for "V" for *volumetric* and "S" for *surface sf*.

11.5. Results and Conclusions # 3:

11.5.1. Part 1: Parametric Analysis in the Use of Ferromagnetic Cores and Tip Sharpening for TMS Coils

11.5.1.1. Results

Using the configuration of the conical coil shown in Fig. 42, we tested the effects of the tip sharpening of a ferromagnetic core of MnZn ferrite, with tip angles of 60°, 120°, and 180° (flat tip) [Fig. 54 a-c]. Fig. 54 d-f show how the biggest concentration of magnetic flux lines occurs with the tip of 60°, which is consistent with the magnitude profiles of the B-field in Fig. 54 g-i.

The results in Fig. 55-a show how the optimal angle of tip sharpening for a good trade-off between a low spreading and a high peak magnetic flux density is 60°. On the other hand, Fig. 55-b demonstrates how after the sudden change of means at the core-air interface, there is an abrupt increase in the magnetic flux density to produce an accentuated decay in the curve. Once more, the tip sharpening of 60° proved to be the best trade-off between a desired low decay rate with respect to the distance and relatively high values of B-field magnitude.

a)   b)   c)

d)   e)   f)
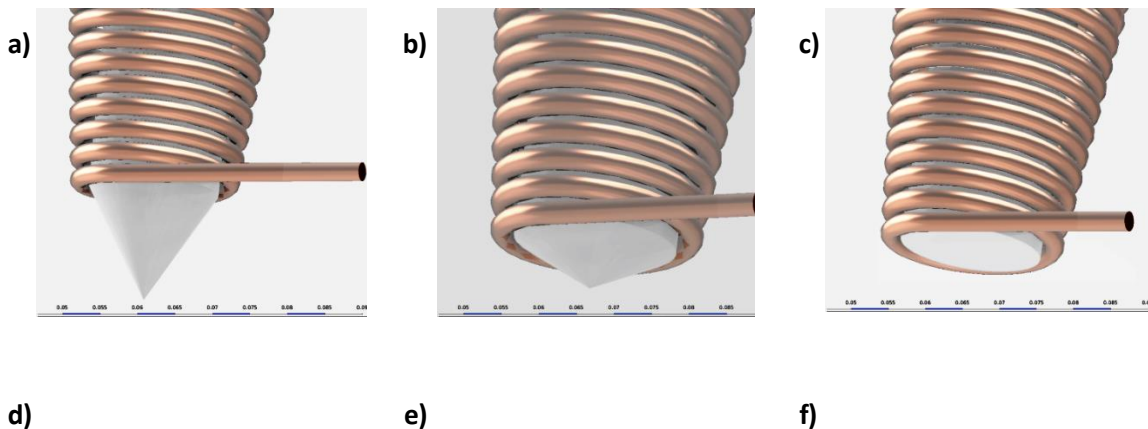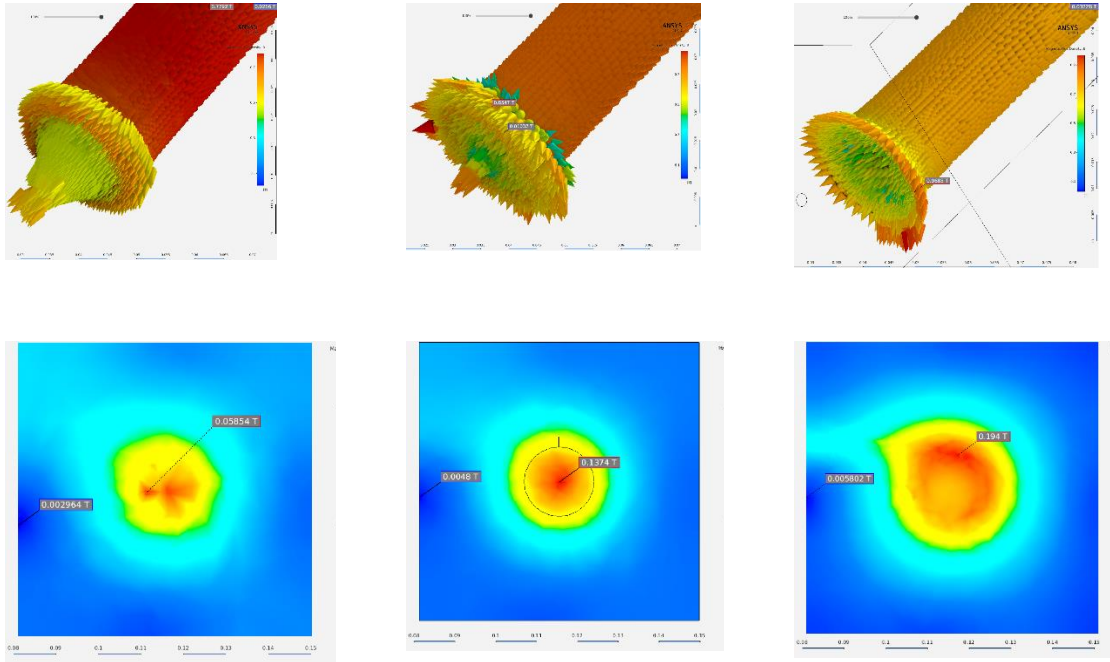
Figure 57 – a-c) Tip sharpening with opening angles of 60°, 120°, and 180° (flat). d-f) Vector field representing the magnetic flux density for cases a) to c). h-j) Magnitude of the magnetic flux density in the plane z = -4.25 mm (typical scalp-brain distance up to neurons of the layer V/VI of the motor cortex in rats). Notice the trade-off between the size of the coverage area and the maximum magnitude of B.
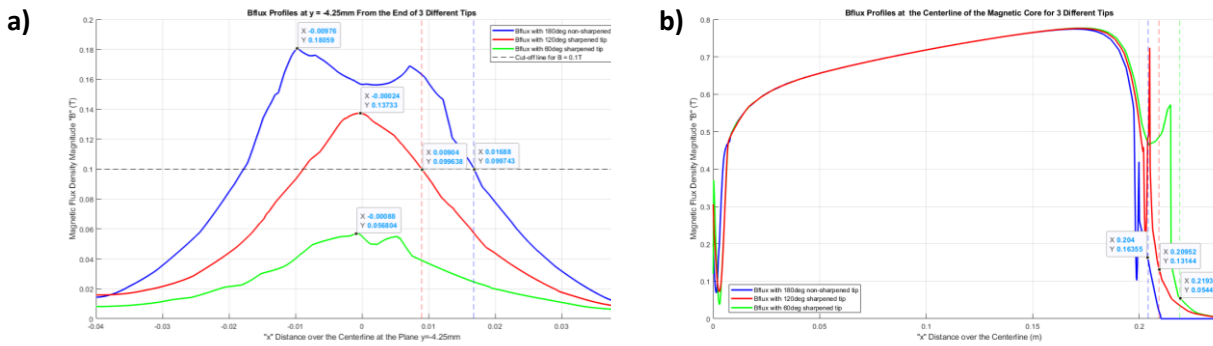
Figure 58 – a) Spreading of the magnetic flux density at the intersection of the planes y = 0 and z = -4.25 mm. b) Magnetic flux density distribution along the "z" (vertical) axis of the coil.

11.5.1.2. Conclusions

The simulations demonstrated that the use of sharpened ferromagnetic cores allows for increasing the flux density in the near neighborhood of the tip, which is useful if the targeted plane is close enough. However, the decay of B in the Z-direction becomes more abrupt, depending on the tip length and how much of it exceeds the coil.

Right after a peak (just at the tip of the core) a rapid decay starts until reaching the original curve without tip-sharpening. In consequence, different core materials can increase the saturation point, but this does not increase the flux density significantly outside the vicinity of the tip (1 or 2 mm away). However, the effect in the energy distribution -and thus in the focality- would still be notable. The attenuation/decay also changes the focality in each of the successive planes from the tip and increases the standard deviation of the magnetic flux lines following a normal distribution because of the dispersion of the flux.

The use of ferrites increases the flux density in a useful manner in the vicinity of the tip, determines the attenuation behavior, and has a direct influence on the focality with more dependence on the tip-sharpening than the relative permeability.

The tip with 120 degrees of opening angle proved to be the one with the best focality (more than 75%) measured at 4.25mm from the tip with a threshold of 30% of the maximum magnetic flux density. This value is bigger than those obtained for the cases of 180.

With calculated magnitudes of above 0.6 T in the vicinity of the tip and over 0.1 T at 4.25 mm, using a current of 1000 A, the MnZn ferrite demonstrated to be a good candidate for some TMS application of small penetration depth. However, considering the attenuation, other materials with higher magnetization points could also be studied in future stages.

11.5.2. Part 2: Development of a highly focal TMS coil for narrow targets in small experimental animals. The Quintuple AISI 1010 Core Coil

11.5.2.1. Results

The first group of simulations with two elliptical solenoids (Fig. 47-a) shows the effect of the relative position of the coils on the distribution of the magnetic flux density (B) and the electric field (E) over the plane z=0.

As observed in Fig. 59-i, when placed close to each other (Fig. 47-a), the coils generate two hotspots of the E-field, as a consequence of the same distribution for J, indicating a high concentration of charges associated with induced currents toward the center.

This is a highly focal behavior of the E-field induced at the surface of the coil. We have termed this referential current density distribution at z=0 "nucleation of charges" (Fig. 59-i).

On the other hand, the analysis in consecutive secant planes below z=0 reveals how the initial distributions of B, E, and J change as a function of the depth. This is due to both the dispersion of the magnetic flux lines (shown as a decrease of B, in Fig. 59 a-h), and the dispersion of the charges associated with the induced currents (and E) from the nucleation point, which tend to repel each other and spread out (Fig. 59 i-p).
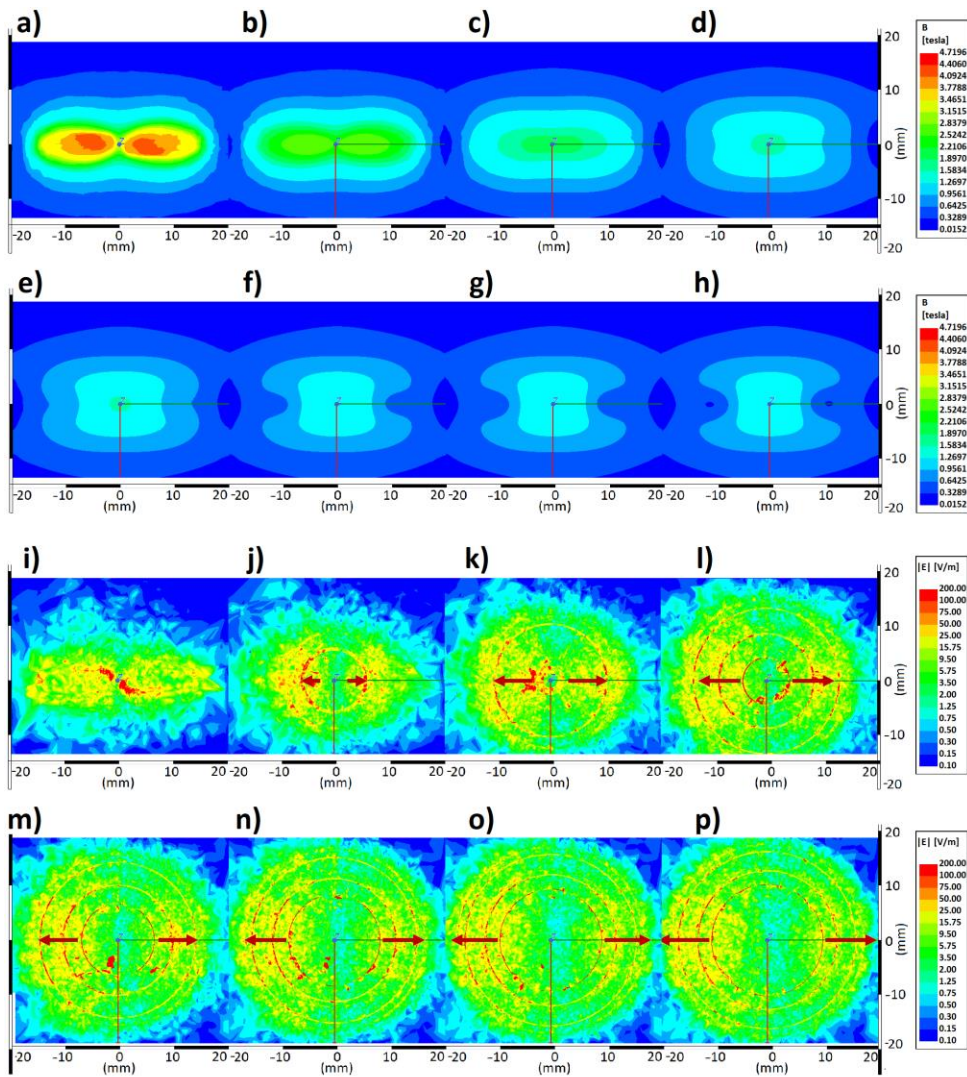
Figure 59 – |B| at depths of a) 0.0, b) 1.0, c) 2.0, d)2.5, e) 3.0, f) 3.75, g) 4.0 and h) 4.25 mm. |E| at depths of i) 0.0, j) 1.0, k) 2.0, l)2.5, m) 3.0, n) 3.75, o) 4.0 and p) 4.25 mm. The red arrows show the component in the XY plane of directional vector of maximum current density (propagation of charges associated with the induced currents).

As seen in Fig. 59 i-p, the spatial displacement of the two hotspots occurs from the nucleation points, in opposite directions in every XY plane and towards the negative direction of the z-axis. We have called the resulting directions "paths of highest current density". Then, we understand that the maximum electric field in the target will be obtained as long as this path intersects the target area.

Another relevant result observed is the role of the ferromagnetic core in the nucleation of the charges associated with the induced currents, and therefore, in the path of highest

conduction current density (J). Fig. 60 shows how the E-field (as a consequence of the current density distribution) tends to be more evenly distributed with a flat-face AISI 1010 steel core (Fig. 60-e), becomes higher towards the center with no core (Fig. 60-d), and even higher with a V-shaped AISI 1010 steel core (Fig. 60-f) at the plane z=0. This is consistent when we compare the associated distributions of B in the same plane (Fig. 60 a-c).
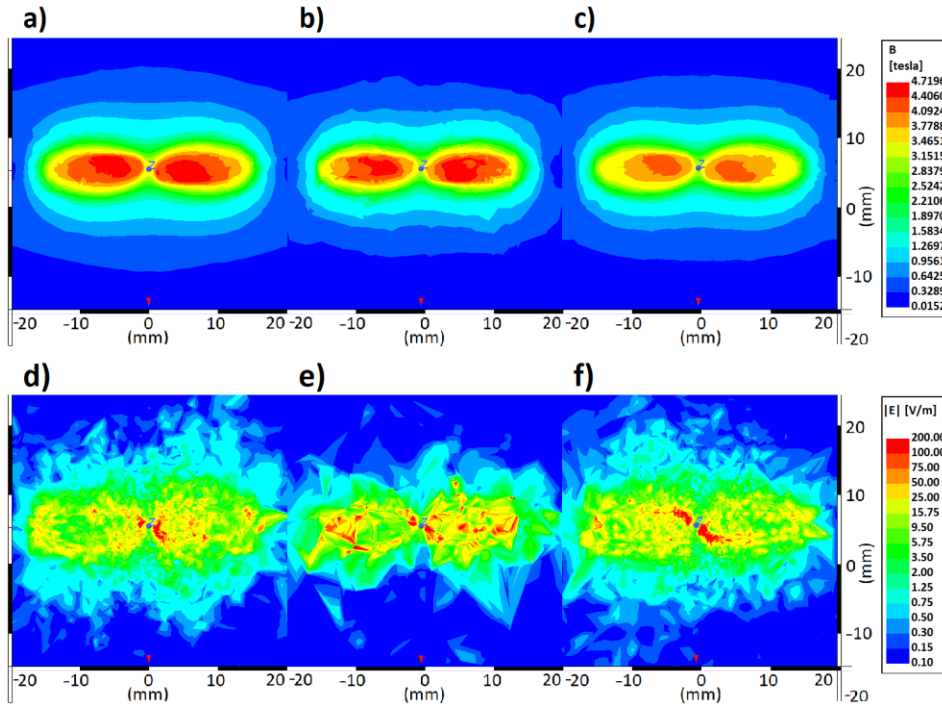
Figure 60 – B-field for a) air core; b) flat surface AISI 1010 steel core; c) V-shape AISI 1010 steel core. E-field for d) air core; e) flat surface AISI 1010 steel core. f) V-shape AISI 1010 steel core.

Having understood the mechanisms of nucleation of charges associated with the induced currents right below the coil, and the formation of the path of the highest current density, we have changed the configuration to the quintuple array of dual solenoids in Fig. 61-a. The new coil is an arrangement of four elliptical dual solenoids, making a parallelogram from the top view, with an extra dual solenoid in the center (Fig. 61-b).
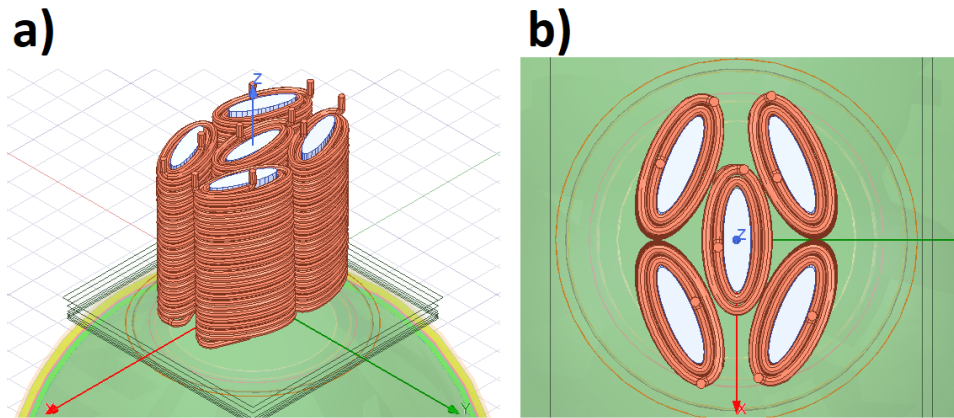
Figure 61 – Quintuple arrangement of elliptical solenoids and planes. a) Isometric view. b) Top view.

For this simulation, we have kept the same previously described waveform, duration, and frequency of the pulse of current, and set the peak amplitude to 10kA. The resulting inductance -calculated during the simulation- is 1.9 mH for each coil, with a power factor angle Φ_{PF}=72 deg.

The objective of this configuration has been to restrict, as much as possible, the dispersion and migration of the charges associated with the currents induced by the coil in the middle (Fig. 62-a) to zones of lower charge densities. This restriction is imposed by the quadruple arrangement of peripheral solenoids (Fig. 62-b) which generate four nuclei of charges associated with the induced currents in the surroundings. Being of the same sign, the peripheral charges repel the charges induced by the fifth coil in the center such that this last group is forced to propagate vertically along the z-axis. We have termed this deliberately restricted direction of propagation (Fig. 62-c) "oriented central path of highest current density".
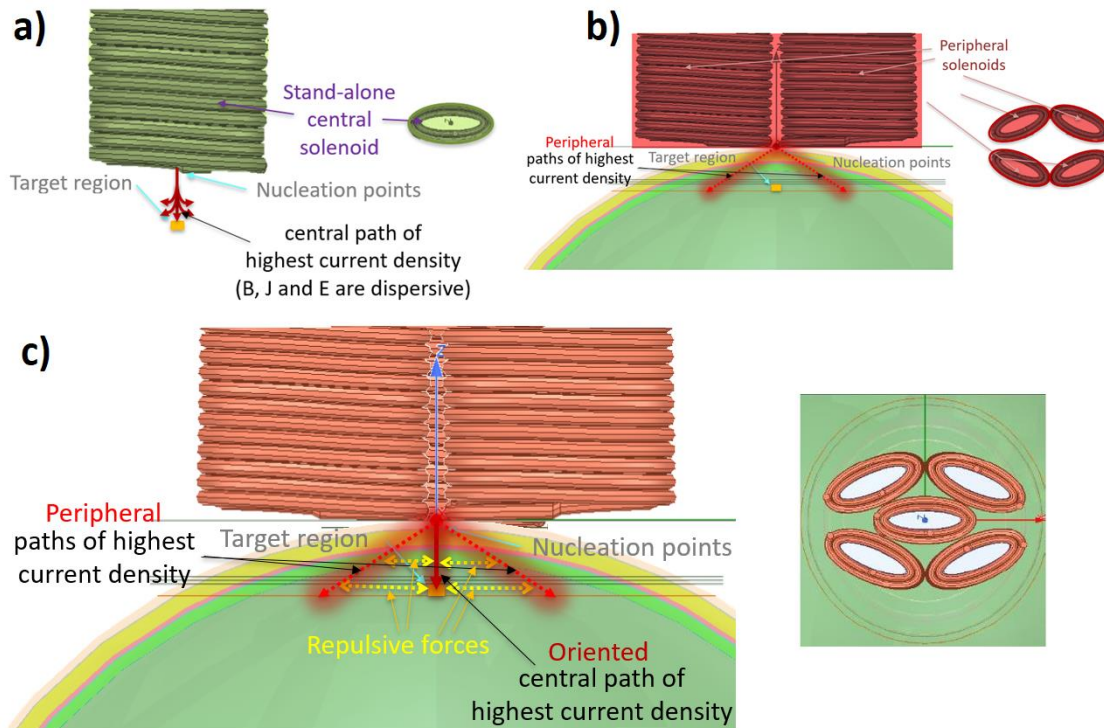
Figure 62 – a) Stand-alone central solenoid. b) Quadruple arrangement of peripheral solenoids. c) Oriented control of J and E with the quintuple arrangement of elliptical solenoids.

Eventually, after a certain depth, the dispersion of the peripheral charges allows the central charges to spread out. However, the restriction will provide the central charges the chance to reach the target in a still relatively compact group, with an associated high current density.
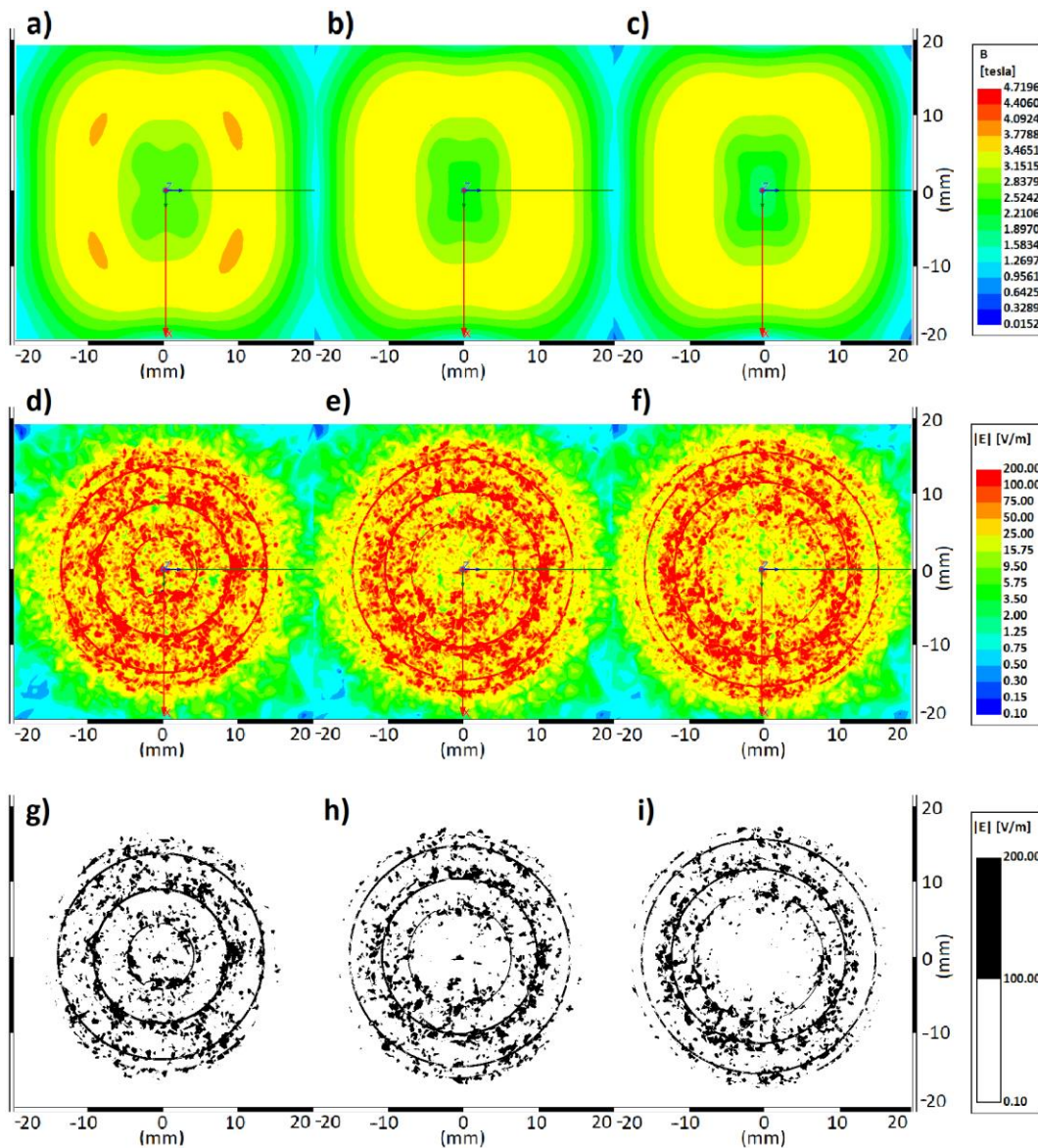
Figure 63 – a-c) |B| at z= 3.75, 4.00 and 4.25mm. d-f) |E| at the same depths. g-i) Point exceeding a threshold of 100V/m.

In this way, we have confined the path of the central group of charges associated with the induced currents to point and pass through the target point, increasing the E-field on it. We have named this technique "oriented control of the electric field based on the directional vector of highest current density".

On the other hand, the propagation of peripheral charges will occur outwards in a dispersive manner, which will form a conical pattern to be called "peripheral path of the

highest current density". This path, though unoriented, is still necessary to provide control over the central path.

Fig. 63 presents the results for the planes z=-3.75, -4.00, and -4.25 mm, showing the magnetic flux density distribution (Fig. 63 a-c) and the correspondent E-field (Fig. 63 d-i). Notice in the E-field plots how the group of peripheral charges (rearranged in ring-shaped red dot clouds) still prevents the scattering of the central group of charges at these depths, allowing them to penetrate -still together- up to the target. In consequence, the associated E-field is higher in the middle and lower in the outer area due to the dispersion.

11.5.2.2. Conclusion

The designed quintuple AISI 1010 carbon steel core coil of dual solenoids demonstrated to be able to stimulate the M1 sub-region in the rat brain, without appreciable encroachment on the surrounding regions. The key aspect of the novel design is the obtained oriented control of the E-field, based on the control of the directional vector of the central path of the highest current density. This path crosses consecutive secant planes in a straight line, from the nucleation point to the target.

The oriented control consists of the prediction of the trajectories of all the paths of highest current densities, and their placement such that at least one of them points and passes through the target point, with acceptable low dispersion, ensuring clearance in the surroundings.

The novel coil showed an effective induced E-field at the targeted point, within the spherical rat head model, above the typical neuron stimulating threshold defined around 100V/m [1], [2], [120]–[122]. These values were observed at least over the planes z=-3.75

and z=-4.00 mm, deep enough to reach the layers V and VI of the M1 and M2 regions in the rat brain. The approximate stimulated area is $1mm^2$ with cleared surrounding areas at the targeted planes with |E| below the stimulation threshold.

It is important to note that, since the propagation of the induced peripheral currents has a radial characteristic, and given the circular nature of the induced E-fields in TMS -defined by the Maxwell-Faraday's Law- there might exist more halos of E-field with magnitudes above the threshold. However, it is possible to configure the system to make these halos to be outside the perimeter that defines either an established clearance area or the entire specimen's brain. This will depend on the specific geometry of the specimen's head and brain, dimensions of the coil, and specific parameters of stimulation. Therefore, the use of this coil should always be subjected to a previous study of the conditions to assure minimization of undesired adjacent stimulation.

For a peak amplitude of 10kA, the energy dissipated in the quintuple AISI 1010 core coil was calculated as 208.9 mJ per pulse of current. This means a very low and safe energy dissipation over the coil for non-repetitive (single pulse) TMS, in this case for pathway identification in neural networks. This would also allow an equivalent maximum power dissipation of 208.9mW/pulse in repetitive TMS, with an interlock window of at least 1 sec. For repetitive TMS (r-TMS), though, the number of consecutive pulses and duration of the interlock may be adjusted, keeping a compromise between the generated real power and the capacity of the coil to effectively dissipate it. This will prevent a temperature rise that causes damage to the device in r-TMS, which is not a concern for the purpose of this work. Similarly, the calculated energy dissipated within the brain tissue, in a volume of $1mm^3$ over the targeted planes, is 1.10 nJ. The very small energy dissipated and short duration of the single pulse of

400 µs make the temperature rising negligible and represent evidence of the safety of the designed device to perform non-repetitive TMS in rodents. This is consistent with reports in the literature showing negligible temperature variation in the brain during TMS[40]. Future work in progress is aiming to further reduce the dissipated power and improve the thermal response of the coil in r-TMS, using pulse shaping and neuromodulation techniques.

Although the rat head model has been considered of isotropic and homogeneous electromagnetic properties, this might not be the exact case in a real specimen. The complexities in the microscopic structure of tissues such as the brain cortex and the skull bones create tiny localized unbalances in the current densities and electric fields, at a microscopic scale, that is challenging to predict. From a macroscopic engineering point of view, though, the fluxes and densities implicitly reflect these microscopic inhomogeneities - or anisotropies- in averaged values per unit area, reported in the literature by type of tissue. Then, we understand that, as long as we can provide stimulation to the targeted neurons with an average E-field above the threshold for enough time (one period in this case), a big proportion of the neurons located in this area will fire at the same time, after the induced pulse of current, despite the microscopic inhomogeneities or anisotropies.

Until this point, we have shown that the designed coil is able to induce manageable localized E-fields above 100 V/m, over a spherical model with the typical conductivities for the rat brain cortex. This predicts high effectiveness in in-vivo implementations -even with inhomogeneous or anisotropic properties- given the adaptative capacity of the coil to provide focal stimulation. This capacity is based on the oriented control of the E-field, with even or differentiated modulation in each independent solenoid. Future work is planned at the Biomagnetics Laboratory to test the new device over rat head phantoms, using previously

developed technology in our lab for human head phantoms[123], [124]. This way we will accurately evaluate the role that the actual rat brain anatomy plays in the final distribution of the E-field. Similarly, work in progress seeks to increase the suitability of the coil for rTMS and reduce overstimulation using high μ_r shielding materials.

11.5.3. Part 3: Development of a Space-Varying E-field Vector Modulation for Spatial and Temporal Control of the Electric Field

11.5.3.1. Results

The set of results for the simulations over our spherical head model can be separated into two different groups. The first group, to be called *direct patterns of stimulation*, is formed by the polarization patterns of the different solenoids to stimulate green, pink and purple zones in Fig. 51-b. Fig. 64 shows the magnitudes of the *B*-field (a-c) and *E*-field (d-f) obtained for these three cases. These *B*-field magnitudes were possible to obtain because of the use of ferromagnetic cores of AISI 1010, which increased the flux density in a smaller area. In addition, the use of currents at 100 kHz allowed exploiting a *-dB/dt 33* times bigger than a typical 3 kHz TMS baseband signal. With this, we were able to reach the necessary *E*-field magnitude around a stimulation threshold of 100 V/m with a smaller coil. These two factors permitted a reduction in the size of the coils in a ratio of 20:1, from the typical average diameter of commercial coils of 100mm to only 5 mm.

Notice in Fig. 64-f that the direction of the *E*-field in the purple zone "l" is parallel to the direction of the two coils polarized in the same direction (1 and 6), out of the three in use

at a specific time. This direction could be changed at will by switching the two coils with the same polarization.
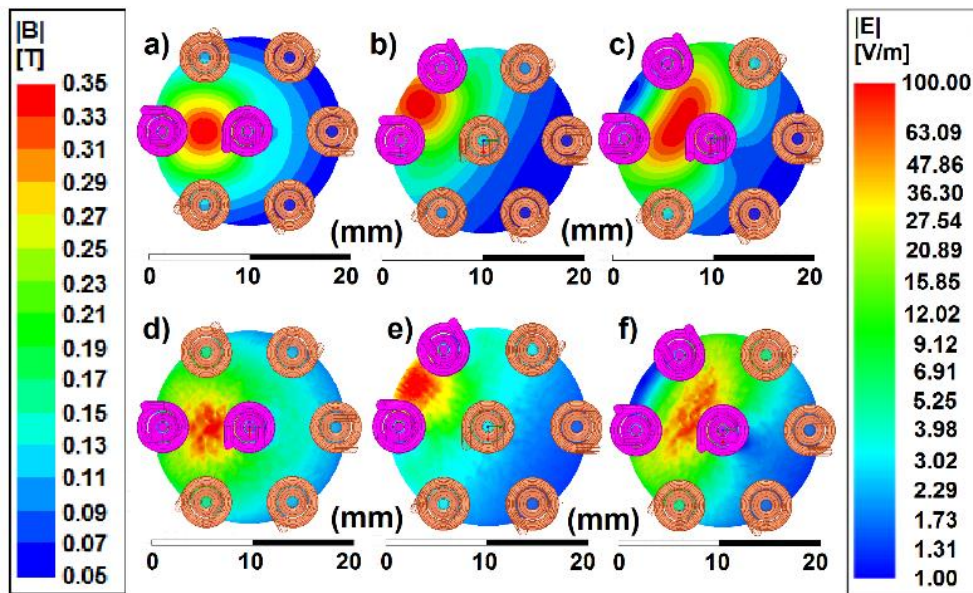
Figure 64 – B-field (a-c) and E-field patterns (d-f) for zones "k", "L" and "l".

The second group of results shows polarization patterns of the coils switched in time to produce average *E*-field patterns covering two or more contiguous zones. Such is the case of the pattern shown in Fig. 65 a-e). With a polarization of all the solenoids with 5 kA, except coil # 6 which is left off, it is possible to obtain the instantaneous U-shape pattern in Fig. 65a. The pattern shows the highest *E*-field in the consecutive pink and purple areas "b" to "h", by the right side. This corresponds to the path of the highest current density in the plane of inspection, as observed in Fig. 65-f. Figures 65 b-d show the same pattern in Fig. 65-a rotated 60 degrees counterclockwise. This pattern results from the switching of the coil in the off state every 10 µs, period of the sinusoidal current. Since the *E*-field vectors rotate always in the same direction but with a variable location of the maximum, the inference pattern is constructive at all times, though time-averaged. Then, the maximum appears over the zone "b", as a result of the time-averaged constructive interferences. This is another way to stimulate purple zones with dynamic control of |*E*| through the switching periods.

A different pattern of time-averaged destructive interference is obtained in Fig. 65 g-i. Fig. 65-g shows a bow-shape pattern of E-field magnitude with the polarization of coils 0, 2, 3, 4, and 5 with 2.76 kA (same phase). Fig. 65-h shows the magnitudes for the stimulation of the pink zone "k" with *E*-field vectors in the opposite direction (upwards) to those in Fig.65-g (downwards). This is obtained with 5 and -5 kA in coils 6 and 0. The result is similar to the bow-shape pattern but with the *E*-field in zone "k" significantly attenuated. The configuration is particularly useful for the simultaneous stimulation of symmetrical targets in the left and right lobes of the rat brain.

Finally, the pattern in Fig. 65-j was obtained polarizing coils 1 and 5 with 5kA and 2 and 4 with -5kA. The same pattern rotated 60° was also obtained (Fig. 64-k). The averaged result is shown in Fig. 64-l, stimulating the zone "0" below the central coil.
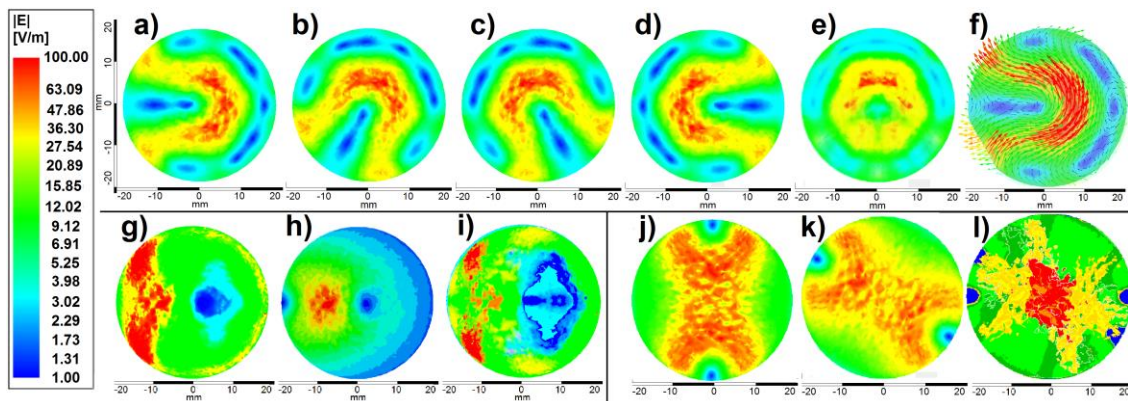
Figure 65 – a to d) U-shape *E*-fields rotated 60 deg. every 10 µs, e) Average *E*-field with a peak in zone "b". f) *E*-field vectors of pattern in "a". g) Bow-shape *E*-field pattern. h) *E*-field in zone "k". i) Average *E*-field between g and h. j-k) Patterns for zone 0 rotated 60°. l) Average *E*-field at zone 0.

Regarding the performance of SVEVM over our anatomically accurate rat head model, the results in Fig. 66 show the effect of the three (3) direct patterns –previously analyzed over the spherical model– in the stimulation of different areas of the brain cortex. As observed, in comparison with the FEC (Fig. 62-a) the combination of FFC with SVEVM shows, not only a more focal stimulation but also the possibility to move the stimulation hotspot within the

coverage area (Fig. 62-b). This characteristic minimizes the overstimulation of non-targeted areas, as it enables the simultaneous stimulation of multiple targets in the rat brain with a fixed coil.

The two time-averaged patterns were also tested resulting in the right "U" and "bow" patterns with attenuation in the center.

The magnitudes showed values around 100 V/m at the cortex (GM) as predicted with the spherical rat heat model.
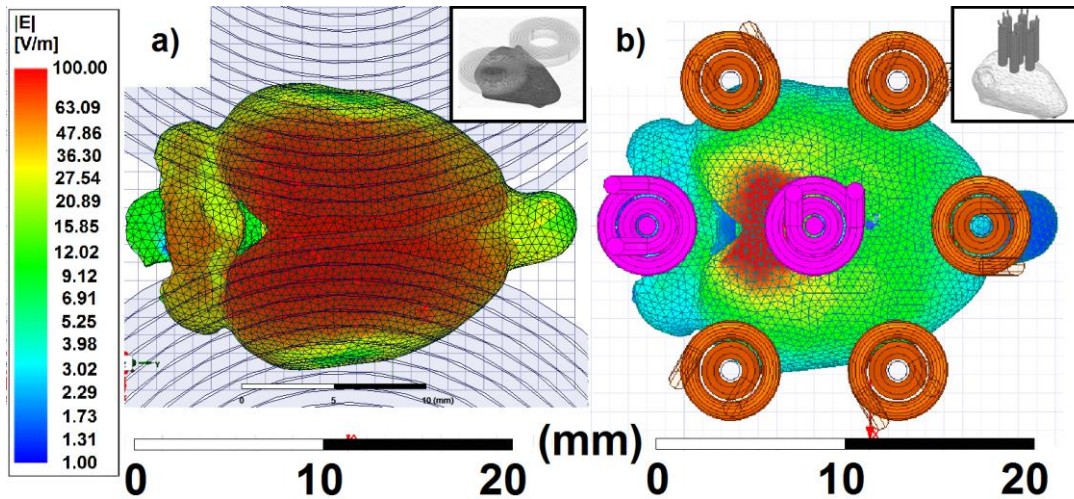
Figure 66 – a) Induce E-fields over the rat head model with a) FEC and b) FFC.

In the human head model, the simulation required an adjustment in the coil currents due to the bigger scalp-to-cortex distance compared to the rat. In our rat model, this distance was 2.75 mm, whereas in the human model it was 13.5 mm (approximately five times bigger). The distance was compensated with two times the number of turns previously used, winding with two parallel wires of half the original diameter. The increase of current has a quadratic effect in the –E-field magnitude because of the surface integral of the magnetic flux density in the target area, according to the Maxwell–Faraday equation. This, added to a conductivity of the human GM bigger than the conductivity of GM in rats, results in an adequate compensation factor close to 5.

The adjustment has made the FFC and the SVEVM suitable for use in humans, as observed in Fig. 67. On the left (Fig.6a), the stimulation pattern of an FEC is shown, where the *First Dorsal Interosseous* (FDI) region of the primary motor cortex is targeted. Notice the big overstimulation of the surrounding tissue which shows the poor focality of this coil for small targets. On the right (Fig. 67-b), the focal stimulation of the FFC demonstrates an increased focality and very low overstimulation of the same target compared to FEC, reaching the threshold of 100 V/m.

The direct patterns of stimulation of the green, pink, purple and yellow zones were also verified, as well as the time-averaged *E*-field patterns, demonstrating their feasibility in the human cortex with SVEVM.

It is important to highlight that the driving of currents in the order of 5 kA in the FFC is possible with few consecutive or single stimulation pulses and not with long repetitive bursts. The calculated energy per pulse of current at 5 kA was 104.45 mJ, meaning a very low energy dissipation of 104.45 mW/pulse if interlock windows ≥ 1 second are left between repetitions.
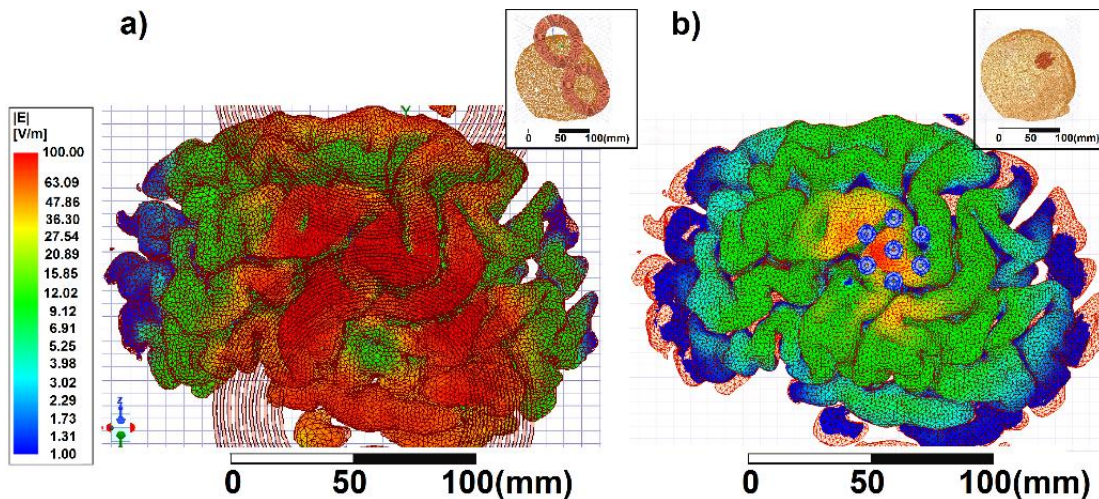
Figure 67 – a) Comparison of the induce E-fields over the primary motor cortex (M1) using the realistic human head model with a) FEC and b) FFC.

11.5.3.2. Conclusions

The patterns in all the simulations demonstrated the high spatial controllability of the *E*-field, possible with the combined use of FFC and SVEVM. This allowed defining a specific location of the hotspot of stimulation, which demonstrated the suitability of the method for the control of the stimulation point and temporal sequence of multisite stimulation at will.

The results over realistic human and rat head models verified the suitability of SVEVM as a proposed neuromodulation method for TMS for its use in clinical settings, as well as in research environments with experimental animals.

The achieved 100 V/m showed the relevance in the operation at high frequency to increase the *–dB/dt* in a scale that permits a reduction in the size of the coils to the small solenoids in FFC.

The FFC demonstrated a significantly increased focality in the order of 2 mm^2 compared to the FEC which has a focality of approximately 70 mm^2. This makes the FFC not only suitable for small experimental rodents but also introduces a new range of focality that allows targeting smaller areas in humans.

The use of the FFC and the SVEVM has the potential of introducing significant advantages in clinical settings and research environments. The location and temporal sequence of the *E*-field hotspot at will can be converted into stimulation coordinates to provide the operator with a more accurate control than the one obtained with the existing technology. Similarly, the technology has the potential to be used in the control of the penetration depth, as it is being investigated in our laboratory.

11.5.4. Part 4: Design of a novel focality measurement methodology

11.5.4.1. Results

For validation of the developed methodology, we have performed finite element simulations using ANSYS Maxwell 3D Software on three focal TMS coils over a realistic head model. Our model, obtained from MRI of a healthy adult subject, contains the scalp, skull, cerebrospinal fluid (CSF), brain matter, and white matter, as layers characterized by their electromagnetic properties [36], [123], [125]–[127] (see Table I).

Table XIII – Head Model Properties

Layer	ε_r	σ (S/m)	μ_r	Layer	ε_r	σ (S/m)	μ_r
Skin (scalp)	12,000	0.170	≈1	Gray Matter	12,000	0.274	≈1
Skull	800	0.010	≈1	White Matter	12,000	0.126	≈1
CSF	600	1.654	≈1	Air (outside)	1.00058	3×10^{-15}	≈1

The stimulation target is a volume in the *First Dorsal Interosseous* (FDI) region of the primary motor cortex (M1), in the left lobe of the brain. When stimulated, this region produces an involuntary thumb twitch in the subject. To define the exact volume of stimulation we obtained the intersection between the mentioned region and a cylinder of OD = 13mm and 5mm of depth, shown in purple in Fig. 68-a.
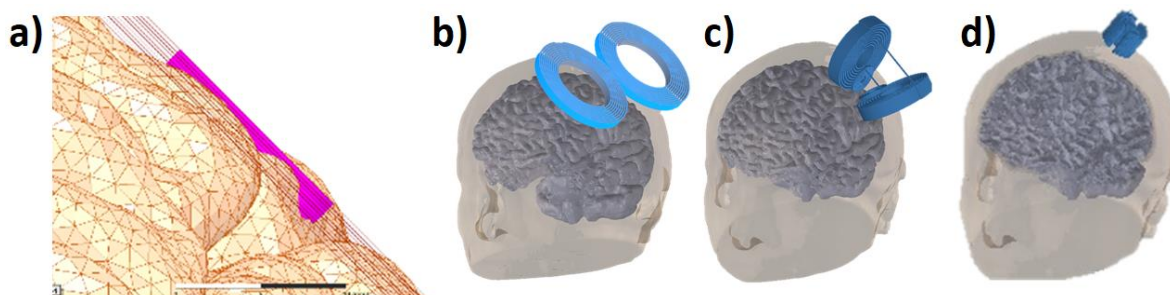
Figure 68 – Simulation setup. a) Target in the FDI region defined the purple cylinder b) Figure of eight coil (F8C); c) Quadruple butterfly coil (QBC); d) Quintuple AISI 1010 Carbon Steel Core Coil (5CC).

As shown in Fig. 68- b to d, the coils simulated were: 68-b) a Figure of Eight Coil (F8C) of 70mm of average radius; 68-c) a Quadruple Butterfly Coil (QBC) [128]–[130]; 5d) a Quintuple AISI 1010 Carbon Steel Core Coil (5CC) [115]. The main dimensions and parameters of these coils are shown in Table II.

Table XIV – Parameters of the Simulating Coils

Coil	Parameters
QBC	OD_1=70mm, OD_2=28mm, $\Phi_{1\&2}$=45°, $NT_{1\&2}$=1x9, $Xsect_1$=5×1mm , $Xsect_2$=2×1mm
F8C	ID=52mm, OD=88mm, H=7mm, NT=2x9, cross-sect=7×1mm
5CC	NT=2x25, Xsect=elliptic; semi-mayor axis = 10.6mm, semi-minor axis = 2.8mm, H=25.4mm

The stimulation current used was a single bipolar pulse of 5kA (peak value), with a sine waveform at 2.5kHz. All the coils were placed over the target region at 45° from the x-axis.

Table XV – Results of the surface *SF vs.* existing definitions

Coil	$A_{E\frac{1}{2}}$ mm²	Surface specific focality sf_S	Conclusion of the surface focality	$A_{\varepsilon E}$ mm²	Surface specific focality sf_S	Conclusion of the surface focality
F8C	189	0.4437 (44.37)%	Moderately focal target stimulation + moderate overstimulation outside	165	0.8254 (82.54%)	Focal target stimulation + low overstimulation outside
QBC	151	0.9736 (97.36%)	Highly focal target stimulation + minimal overstimulation outside	132	0.9556 (95.56%)	Very focal target stimulation + low overstimulation outside
5CC	3	0.00096 (0.096%)	Poorly focal target stimulation + minimal overstimulation outside	5	0.0016 (0.16%)	Poorly focal target stimulation + minimal overstimulation outside

For the quantification of both the *surface* and *volumetric specific focalities*, we defined eleven secant planes and obtained ten trapezoidal segments of the target volume. Then, the

surface specific focality was calculated for each plane with a threshold for the induced E-field of 100V/m. Ultimately, the *volumetric specific focality* was computed over the *target volume* for each coil, with a discretized calculation based on the (12).

Table III shows the *surface specific focalities* (sf_S) obtained for the plane z = -5mm (deepest), beside the alternative (existing) definitions of *half-value area* ($A_{E\frac{1}{2}}$) and *half-energy area* ($A_{\varepsilon E}$). Table IV summarizes the results of the volumetric specific focality (sf_V) compared to calculations of the existing half-value area ($A_{\frac{1}{2}}$) and tangential fields spread ($S_{\frac{1}{2}}$).

Table XVI – Results of the Volumetric *SF* along with existing definitions

Coil	$A_{E\frac{1}{2}}$ mm²	$S_{\frac{1}{2}}$ mm²	*Volumetric specific focality sf_V*	*Conclusion of the volumetric specific focality (sf_V)*
F8C	94.5	126.20	0.4701 (47.01%)	Moderately focal target stimulation + high overstimulation outside
QBC	75.5	100.96	0.8224 (82.24%)	Highly focal target stimulation + moderate overstimulation outside
5CC	358	477.12	6.26546E-44 (0.00%)	Non-focal target stimulation + very high overstimulation outside

From Tables XV and XIV we can observe how the defined surface specific focality and volumetric specific focality, are not only compatible with any existing definition that evaluates the average simulated area in surface units but also allow to extract additional information on the suitability of the coil to stimulate a given target region. The measure itself has quantified such suitability in percentage terms, which permitted to rank the coils for this particular application (stimulation of the FDI region). In addition, the utilized specific focality

permitted to describe the operation of the coils in terms of their scenarios of focal or under-stimulation of the target with high, moderate, low, or null overstimulation of the adjacencies.

11.5.4.2. Conclusion

The results show how the use of the *specific focality*, along with other existing definitions, enhances the amount of information that is possible to extract from the operating conditions of coils, allowing the evaluation of their suitability for a specific application.

The defined *focality form factor* (d_n) and *complex focality form factor* (d_{nc}) allowed us to measure the level of overlap between one or multiple segments of the stimulated area, with respect to one or multiple segments of the target area. This made it possible to conclude about the quality of stimulation, which includes both the precision on the target and the level of overstimulation of the adjacent areas.

The use of the proposed *AES-erfc* and *CAES-erfc* functions offers the possibility of evaluating scenarios of stimulation in normalized and percentage terms, defining the *specific focality* as a dimensionless measure. Hence, both the *surface* and the *volumetric specific focality* are useful for the assessment and comparison of coils for TMS (and other types of stimulation of biological tissues), given a stimulation threshold for the E-field.

In addition, the proposed nomenclature makes it possible to report focality values along with their parameters of *focal distance*, *stimulation threshold*, *target area,* and *stimulated area* (or their equivalences in volumes), for both evaluation and design purposes. In design tasks, the manufacturer or designer should particularly report unitary –or almost unitary-

specific focalities, with a list of all the possible/tested conditions or applications for which the coils have been designed.

Ultimately, the proposed nomenclature has the potential to be used both in research and clinical applications. This nomenclature provides the possibility to create *standards* around the *specific* focality definition for different TMS applications and stimulation environments. For that, researchers and manufacturers would need to set fixed values for specific focality parameters to be used in testing and measurement protocols described in such standards.

12. Contribution

12.1. Significance and Impact

The three specific objectives of this work have a big importance in the neuromodulation, neurostimulation, and neuromodeling areas, as they introduce new methods and techniques to overcome the existing limitations.

On the neurostimulation side, our study of ferromagnetic materials as an alternative to increase the focality of coils has demonstrated to have the potential to decrease the focally stimulated area to a surface as small as 1 mm^2, compared to the existing restriction in the order of 1 cm^2. Similarly, with the proposed QCC coil we have shown the capability to reach deeper areas with the same focality, able to stimulate the M1 and M2 regions in rats. This aspect is of significant impact on the availability of new technology that permits scientists to experiment with TMS in rats. Particularly, our results are increasing the capacity of our research team to study the neural circuits of the motor pathway in rodents and the implementation of new TMS-based treatment for some of the PD symptoms.

On the other hand, the positive verification of our hypothesis about the feasibility of neural stimulation based on high-frequency neuromodulation would introduce a big-scale change in the actual conception of neurostimulation devices. The capacity of reduction of power requirements in the electronics, noise suppression, and minimal heat dissipation in the coil is just comparable to the also increased focality and penetration depth obtained with the energy shifting technique in the frequency domain.

Finally, the disclosure of the novel neuromodeling technique based on an oscillatory model of the motor pathway would generate a change of perception with respect to the current methods based on neural networks simulating populations of thousands of individual neurons. From a computational point of view, this will reduce processing time and hardware requirements, at the time that the model perfectly manages the statistical variations in the firing rates, firing patterns, and synchrony without the simulation of individual variations. Similarly, the importance of the model relies on the possibility to find behaviors explained from a mathematical and physical point of view, that allow hypothesizing phenomena occurring at a neurological level that has not been yet identified. Such is the case of the theorized mechanism of oscillating firing rate regulation in the parkinsonian condition, and the random-phase dependency of the synchrony.

12.2. Innovation

1. The innovations in this work, explained in the previous sections, are the following:

2. The study and use of tip-sharpened ferromagnetic cores to increase the focality in stimulation, never combined –to our knowledge– in the TMS area.

3. Our developed and patented AISI 1010 Carbon Steel Core Coil with and achieved focality of 1 mm^2, published in [115].

4. The novel –also patented– mechanism of "*oriented control of the path of the highest current density and electric field*".

5. The methodology and concepts of specific focality, complex focality form factor, focal stimulation factor, overstimulation factor, and complexed focality diagram, published in [119].

6. The use of high frequency with AM as a modulation method to induce a stimulating E-field of the required magnitude, with low power requirements, soundless operation, no overheating, and increased focality and penetration depth.

7. The architecture of a novel high-frequency neurostimulator based on the developed technique.

8. The novel oscillatory model of the motor pathway for PD, also functional for other diseases and motor disorders such as dystonia.

9. The theory of the oscillatory firing rate as a consequence of a self-regulatory mechanism of the neurons at the STN, GPi, and Thalamus subpopulation. This theory stands that the mechanism exists to overcome the effects of the lack of dopamine in the parkinsonian condition, preventing the system from diverging.

13. Future Outlook

After the completion of the objectives related to the design and construction of the high-frequency neurostimulator and TMS coils of reduced size and increased focality with ferromagnetic cores, experiments with rats are designed and expected to be completed in the next few months. These experiments will allow us to conclude about the effectiveness of the neurostimulation method, as well as the envelope-following behavior of the neurons at high frequency.

Similarly, future work will seek to perform experiments to demonstrate the controllability of the *quintuple AISI 1010 core coil* (QCC) with the designed mechanism of "*oriented control of the path of the highest current density and electric field*, as well as the figure-of-flower coil (FCC) with the *space-varying E-field vector modulation.* These experiments require the construction of a version of the neurostimulator here design with five (5) and seven (7) independent coils and *power electronic modules (PEM)* that were not part of the scope due to the complexity and time constraints.

Finally, the set of experiments in rats with the new neurostimulator and coils will be extended to compare predictions of the oscillatory model of the Basal Ganglia-Thalamocortical Circuit (BGTCC), with results that can be obtained from the stimulation of the M1 and M2 regions with TMS in rats with induced PD.

14. Research Ethics

All the analytical and practical work of study, design and implementation of the developed technology has been made without experimentation neither in humans nor in experimental animals of any kind. The anatomically accurate human head and rat head models used in this work have been extracted from MRI databases of authorized access from the Biomagnetics Laboratory.

Future stages of animal experimentation may be performed out of the scope of this work with the participation of the Neurology and Neurosurgery Departments of the Virginia Commonwealth University, the McGuire Research Institute, and the Southeast Parkinson's Disease Research, Education and Clinical Center (PADRECC), the last two located at the Hunter Holmes McGuire Veterans Affairs Medical Center, in Richmond, Virginia.

All future experimentation with the neurostimulator equipment is out of the scope of this work but conceived from this stage under the compliance of all the ethical aspects related to the animal work. Such experiments are designed to be developed with the participation and approval of all the above departments/institutions, following the guidelines established in the document entitled: *"Animal Component Of Research Protocol" (ACORP), Version 4 (Protocol No. Assigned by the IACUC: 02418),* belonging to Dr. Mark Baron.

15. Publications, International Conferences, and Patents

ORIGINAL ARTICLES PUBLISHED OR IN PUBLICATION PROCESS FOR THIS RESEARCH WORK

- Low Power, Soundless Neurostimulation Using High-Frequency Modulation for TMS (IN DRAFT).

- Novel High-frequency Transcranial Magnetic Neurostimulator, Topology and Operation Modes (IN DRAFT).

- Carmona, D. Kumbhare, J. Atulasimha, M. Baron, R. Hadimani. "A Novel Modeling for Parkinson's Disease Based on the Oscillatory Nature of the Basal Ganglia Thalamocortical Circuit" (DRAFTED AND CURRENTLY UNDER REVIEW OF THE CO-AUTHORS).

- C. Carmona and R. L. Hadimani, " Space-varying E-field Vector Modulation with Multi-Core Figure-of-Flower Coil for Transcranial Magnetic Stimulation " IEEE Magnetics Letter (SUBMITTED, CURRENTLY ADDRESSING REVIEWERS' COMMENTS).

- C. Carmona, O. F. Afuwape, D. C. Jiles, and R. L. Hadimani, "Estimation of the Focality of Coils and Quality of Stimulation of Biological Tissues During Transcranial Magnetic Stimulation," in IEEE Transactions on Magnetics, doi: 10.1109/TMAG.2021.3082853.

- Carmona, D. Kumbhare, M. Baron, R. Hadimani. "Quintuple AISI 1010 carbon steel core coil for highly focused transcranial magnetic stimulation in small animals". AIP Advances. Jan 202, doi: 10.1063/9.0000219 .

OTHER PUBLISHED CO-AUTHORED ARTICLES

- C. Nimonkar, E. Knight, I. C. Carmona, and R. L. Hadimani, "Development of Anatomically Accurate Brain Model of Small Animals for Experimental Verification of Transcranial Magnetic Stimulation," in IEEE Transactions on Magnetics, vol. 58, no. 2, pp. 1-4, Feb. 2022, Art no. 5800404, doi: 10.1109/TMAG.2021.3104517.

- H. Magsood, F. Syeda, K. Holloway, I. C. Carmona, and R. L. Hadimani, "Safety Study of Combination Treatment: Deep Brain Stimulation and Transcranial Magnetic Stimulation," Front. Hum. Neurosci., vol. 14, Apr. 2020, doi: 10.3389/fnhum.2020.00123.

ORIGINAL PATENTS BASED ON THIS RESEARCH WORK

- I. Carmona, D. Kumbhare, M. Baron, R. Hadimani. "SYSTEM AND METHOD FOR MULTI-COIL STEERABLE AND SELECTIVELY FOCUSSED TRANSCRANIAL MAGNETIC STIMULATION" pending patent. Jan 15, 2021.

- I. Carmona, D. Kumbhare, M. Baron, R. Hadimani. HIGH-FREQUENCY NEUROMODULATION METHODS AND EQUIPMENT FOR TRANSCRANIAL MAGNETIC STIMULATION. Apr 26, 2022.

OTHER CO-INVENTORED PATENTS

- C. Nimonkar, E. Knight, W. Lohr, I. C. Carmona and R. L. Hadimani. INDIVIDUALIZED, ANATOMICALLY ACCURATE RAT HEAD MODEL, PHYSICAL BRAIN PHANTOM, AND FABRICATION METHODS. July 2, 2021.

CONFERENCES

- **15th Joint MMM-INTERMAG Conference 2022 (upcoming)**

  Space-varying E-field Vector Modulation with Oriented Control Using a Multi-Core Figure-of-Flower for TMS.

  New Orleans, LA December 6–9, 2021

- **4th International Brain Stimulation Conference 2021 (upcoming)**

  Innovative techniques of focal transcranial magnetic stimulation using ferromagnetic cores and oriented control of the *E*-field.

  Charleston, SC, December 6–9, 2021

- **10th International IEEE Engineering in Medicine and Biology (EMBS) Conference on Neural Engineering (NER'21) 2021**

  Focal Transcranial Magnetic Stimulation of Small Targets in the Motor Cortex with Oriented Control of the Electric Field.

  Virtual Conference May 4-6, 2021

- **IEEE INTERMAG Conference 2021**

  Estimation of the Focality of Coils and Quality of Stimulation of Biological Tissues During Transcranial Magnetic Stimulation.

  Virtual Conference Apr 26-30/2021

- **American Physics Society – March Meeting 2021**

  Methodology for Focality Homogenization in Magnetic Stimulation of Biological Tissues.

  Quintuple Carbon Steel Core Coil for Highly Focused Transcranial Magnetic Stimulation in Small Animals.

  Virtual Conference Mar 15-19, 2021

  March 15-19, 2021

- **Magnetism and Magnetic Materials Conference 2020**

  Quadruple Silicon Steel Core Coil for Highly Focused Transcranial Magnetic Stimulation in Small Animals.

  Virtual Conference Nov 2020

- **Magnetism and Magnetic Materials Conference 2020**

  Methodology for Focality Homogenization in Magnetic Stimulation of Biological Tissues.

  Virtual Conference Nov 2020

- **Magnetism and Magnetic Materials Conference 2019**

  Design and Development of a Highly Focused Coil for Transcranial Magnetic Stimulation on Small Animals.

  Las Vegas, NV Nov 2019

16. References

[1] Y. Z. Huang *et al.*, "Consensus: New methodologies for brain stimulation," *Brain Stimulation*, vol. 2, no. 1. Elsevier Inc., pp. 2–13, Jan. 01, 2009. doi: 10.1016/j.brs.2008.09.007.

[2] Y. W. Lu and M. Lu, "Comparison of induced fields in virtual human and rat heads by transcranial magnetic stimulation," *Biomed Res. Int.*, vol. 2018, 2018, doi: 10.1155/2018/5270279.

[3] S. N. Makarov, L. N. de Lara, G. M. Noetscher, and A. Nummenmaa, "Modeling Primary Fields of TMS Coils with the Fast Multipole Method," *bioRxiv*, p. 514919, Jan. 2019, doi: 10.1101/514919.

[4] M. PC, C. L, S. R, and B. PJ, "Tissue heterogeneity as a mechanism for localized neural stimulation by applied electric fields," *Phys. Med. Biol.*, vol. 52, no. 18, pp. 5603–5617, Sep. 2007, doi: 10.1088/0031-9155/52/18/009.

[5] A. Opitz, W. Legon, J. Mueller, A. Barbour, W. Paulus, and W. J. Tyler, "Is sham cTBS real cTBS? The effect on EEG dynamics," *Front. Hum. Neurosci.*, vol. 8, no. JAN, Jan. 2014, doi: 10.3389/FNHUM.2014.01043.

[6] E. Zmeykina, M. Mittner, W. Paulus, and Z. Turi, "Weak rTMS-induced electric fields produce neural entrainment in humans," *Sci. Reports 2020 101*, vol. 10, no. 1, pp. 1–16, Jul. 2020, doi: 10.1038/s41598-020-68687-8.

[7] S. R, S. S, B. PJ, and M. PC, "Determining which mechanisms lead to activation in the motor cortex: a modeling study of transcranial magnetic stimulation using realistic stimulus waveforms and sulcal geometry," *Clin. Neurophysiol.*, vol. 122, no. 4, pp. 748–758, Apr. 2011, doi: 10.1016/J.CLINPH.2010.09.022.

[8] S. H *et al.*, "Electric field-navigated transcranial magnetic stimulation for chronic tinnitus: a randomized, placebo-controlled study," *Int. J. Audiol.*, vol. 56, no. 9, pp. 692–700, Sep. 2017, doi: 10.1080/14992027.2017.1313461.

[9] P. Fitzgerald, T. Cassidy, and S. Rege, "Transcranial Magnetic Stimulation (TMS) for Depression - Review of the Evidence," *psych scene hub*, 2020. https://psychscenehub.com/psychinsights/transcranial-magnetic-stimulation-for-depression/ (accessed Jul. 12, 2021).

[10] MAGSTIM, "Image of the D70 Alpha Flat Coil." https://www.magstim.com/row-en/product/d70-flat/

[11] L. M. Koponen, J. O. Nieminen, and R. J. Ilmoniemi, "Minimum-energy coils for transcranial magnetic stimulation: Application to focal stimulation," *Brain Stimul.*, vol. 8, no. 1, pp. 124–134, Jan. 2015, doi: 10.1016/j.brs.2014.10.002.

[12] P. Rastogi, E. G. Lee, R. L. Hadimani, and D. C. Jiles, "Transcranial Magnetic Stimulation-coil

design with improved focality," *AIP Adv.*, vol. 7, no. 5, p. 056705, May 2017, doi: 10.1063/1.4973604.

[13] Y. Kawasaki *et al.*, "Quantitative assessment of the focality of a double-D coil in the human brain," *2017 32nd Gen. Assem. Sci. Symp. Int. Union Radio Sci. URSI GASS 2017*, vol. 2017-Janua, no. August, pp. 1–4, 2017, doi: 10.23919/URSIGASS.2017.8104975.

[14] S. Chang, X. Wei, Z. Zhang, J. Wang, M. Lu, and G. Yi, "Twin Coil Design Considerations for Depth and Focality in Transcranial Magnetic Stimulation," *IEEE Trans. Magn.*, vol. 54, no. 11, Nov. 2018, doi: 10.1109/TMAG.2018.2845458.

[15] L. J. Gomez, S. M. Goetz, and A. V Peterchev, "Design of transcranial magnetic stimulation coils with optimal trade-off between depth, focality, and energy," *J. Neural Eng*, vol. 15, pp. 46033–46047, 2018, doi: 10.1088/1741-2552/aac967.

[16] X. Guizhi, C. Yong, Y. Shuo, W. Mingshi, and Y. Weili, "The optimal design of magnetic coil in transcranial magnetic stimulation," *Annu. Int. Conf. IEEE Eng. Med. Biol. - Proc.*, vol. 7 VOLS, pp. 6221–6224, 2005, doi: 10.1109/IEMBS.2005.1615917.

[17] Z. De Deng, S. H. Lisanby, and A. V. Peterchev, "Electric field depth-focality tradeoff in transcranial magnetic stimulation: Simulation comparison of 50 coil designs," *Brain Stimul.*, vol. 6, no. 1, pp. 1–13, Jan. 2013, doi: 10.1016/j.brs.2012.02.005.

[18] Z.-D. Deng, S. H. Lisanby, and A. V. Peterchev, "Coil Design Considerations for Deep Transcranial Magnetic Stimulation," *Clin. Neurophysiol.*, vol. 125, no. 6, p. 1202, 2014, doi: 10.1016/J.CLINPH.2013.11.038.

[19] E. CM and D. KR, "Iron-core coils for transcranial magnetic stimulation," *J. Clin. Neurophysiol.*, vol. 19, no. 4, pp. 376–381, 2002, doi: 10.1097/00004691-200208000-00010.

[20] L. M. Koponen, J. O. Nieminen, T. P. Mutanen, M. Stenroos, and R. J. Ilmoniemi, "Coil optimisation for transcranial magnetic stimulation in realistic head geometry," 2017, doi: 10.1016/j.brs.2017.04.001.

[21] A. Thielscher and T. Kammer, "Electric field properties of two commercial figure-8 coils in TMS: calculation of focality and efficiency," 2004, doi: 10.1016/j.clinph.2004.02.019.

[22] B. J. Roth, L. G. Cohen, M. Hallett, W. Friauf, and P. J. Basser, "A theoretical calculation of the electric field induced by magnetic stimulation of a peripheral nerve," *Muscle Nerve*, vol. 13, no. 8, pp. 734–741, 1990, doi: 10.1002/mus.880130812.

[23] E. G. Lee, P. Rastogi, R. L. Hadimani, D. C. Jiles, and J. A. Camprodon, "Impact of non-brain anatomy and coil orientation on inter- and intra-subject variability in TMS at midline," *Clin. Neurophysiol.*, vol. 129, no. 9, pp. 1873–1883, Sep. 2018, doi: 10.1016/j.clinph.2018.04.749.

[24] S. D. March *et al.*, "Focused and deep brain magnetic stimulation using new coil design in mice," in *International IEEE/EMBS Conference on Neural Engineering, NER*, 2013, pp. 125–128. doi: 10.1109/NER.2013.6695887.

[25] P. Rastogi, R. L. Hadimani, and D. C. Jiles, "Investigation of Coil Designs for Transcranial Magnetic Stimulation on Mice," *IEEE Trans. Magn.*, vol. 52, no. 7, Jul. 2016, doi:

10.1109/TMAG.2015.2514064.

[26]   L. J. Crowther, R. L. Hadimani, A. G. Kanthasamy, and D. C. Jiles, "Transcranial magnetic stimulation of mouse brain using high-resolution anatomical models," in *Journal of Applied Physics*, May 2014, vol. 115, no. 17, p. 17B303. doi: 10.1063/1.4862217.

[27]   S. D. March *et al.*, "Thermal and mechanical analysis of novel transcranial magnetic stimulation coil for mice," *IEEE Trans. Magn.*, vol. 50, no. 9, Sep. 2014, doi: 10.1109/TMAG.2014.2316479.

[28]   J. Selvaraj, P. Rastogi, N. P. Gaunkar, R. L. Hadimani, and M. Mina, "Transcranial Magnetic Stimulation: Design of a Stimulator and a Focused Coil for the Application of Small Animals," *IEEE Trans. Magn.*, vol. 54, no. 11, Nov. 2018, doi: 10.1109/TMAG.2018.2846521.

[29]   Kenhub, "Basal ganglia: Direct and Indirect pathways | Kenhub." https://www.kenhub.com/en/library/anatomy/direct-and-indirect-pathways-of-the-basal-ganglia (accessed Jul. 12, 2021).

[30]   J. Knierim, "Basal Ganglia (Section 3, Chapter 4) Neuroscience Online: An Electronic Textbook for the Neurosciences. Department of Neurobiology and Anatomy - The University of Texas Medical School at Houston." https://nba.uth.tmc.edu/neuroscience/m/s3/chapter04.html (accessed Jul. 12, 2021).

[31]   A. Dovzhenok and L. L. Rubchinsky, "On the Origin of Tremor in Parkinson's Disease," *PLoS One*, vol. 7, no. 7, p. e41598, Jul. 2012, doi: 10.1371/JOURNAL.PONE.0041598.

[32]   K. Kumaravelu, D. T. Brocker, and W. M. Grill, "A biophysical model of the cortex-basal ganglia-thalamus network in the 6-OHDA lesioned rat model of Parkinson's disease," *J. Comput. Neurosci.*, vol. 40, no. 2, pp. 207–229, Apr. 2016, doi: 10.1007/s10827-016-0593-9.

[33]   T. Wichmann and M. R. Delong, "MODELS OF BASAL GANGLIA FUNCTION AND PATHOPHYSIOLOGY OF MOVEMENT DISORDERS."

[34]   D. Kumbhare, K. L. Holloway, and M. S. Baron, "Parkinsonism and dystonia are differentially induced by modulation of different territories in the basal ganglia," *Neuroscience*, 2017, doi: 10.1016/j.neuroscience.2017.03.063.

[35]   Y. Tachibana, H. Iwamuro, H. Kita, M. Takada, and A. Nambu, "Subthalamo-pallidal interactions underlying parkinsonian neuronal oscillations in the primate basal ganglia," *Eur. J. Neurosci.*, vol. 34, no. 9, pp. 1470–1484, Nov. 2011, doi: 10.1111/j.1460-9568.2011.07865.x.

[36]   J. Bahuguna, T. Tetzlaff, A. Kumar, J. H. Kotaleski, and A. Morrison, "Homologous basal ganglia network models in physiological and Parkinsonian conditions," *Front. Comput. Neurosci.*, vol. 11, p. 79, 2017, doi: 10.3389/fncom.2017.00079.

[37]   J. E. Rubin, C. C. McIntyre, R. S. Turner, and T. Wichmann, "Basal ganglia activity patterns in parkinsonism and computational modeling of their downstream effects," *Eur. J. Neurosci.*, vol. 36, no. 2, pp. 2213–2228, Jul. 2012, doi: 10.1111/j.1460-9568.2012.08108.x.

[38]   H. Bergman *et al.*, "Physiological aspects of information processing in the basal ganglia of

normal and parkinsonian primates," *Trends Neurosci.*, 1998, doi: 10.1016/S0166-2236(97)01151-X.

[39]   T. Gö Tz, U. Kraushaar, J. Rg Geiger, J. Lü, T. Berger, and P. Jonas, "Functional Properties of AMPA and NMDA Receptors Expressed in Identified Types of Basal Ganglia Neurons," 1996.

[40]   F. Syeda, K. Holloway, A. A. El-Gendy, and R. L. Hadimani, "Computational analysis of transcranial magnetic stimulation in the presence of deep brain stimulation probes," *AIP Adv.*, vol. 7, no. 5, p. 056709, May 2017, doi: 10.1063/1.4974062.

[41]   A. V. Peterchev, D. L. K. Murphy, and S. M. Goetz, "Quiet transcranial magnetic stimulation: Status and future directions," in *Proceedings of the Annual International Conference of the IEEE Engineering in Medicine and Biology Society, EMBS*, Aug. 2015, vol. 2015-Novem, pp. 226–229. doi: 10.1109/EMBC.2015.7318341.

[42]   M. Soldati, M. Mikkonen, I. Laakso, T. Murakami, Y. Ugawa, and A. Hirata, "A multi-scale computational approach based on TMS experiments for the assessment of electro-stimulation thresholds of the brain at intermediate frequencies," *Phys. Med. Biol.*, vol. 63, no. 22, Nov. 2018, doi: 10.1088/1361-6560/aae932.

[43]   T. T, J. W, M. L, and T. E, "Computational Modeling of Ultrasonic Subthalamic Nucleus Stimulation," *IEEE Trans. Biomed. Eng.*, vol. 66, no. 4, pp. 1155–1164, Apr. 2019, doi: 10.1109/TBME.2018.2869042.

[44]   J. E. Fleming, E. Dunn, and M. M. Lowery, "Simulation of Closed-Loop Deep Brain Stimulation Control Schemes for Suppression of Pathological Beta Oscillations in Parkinson's Disease," *Front. Neurosci.*, vol. 14, p. 166, Mar. 2020, doi: 10.3389/FNINS.2020.00166.

[45]   K. Butenko, C. Bahls, M. Schröder, R. Köhling, and U. van Rienen, "OSS-DBS: Open-source simulation platform for deep brain stimulation with a comprehensive automated modeling," *PLOS Comput. Biol.*, vol. 16, no. 7, p. e1008023, Jul. 2020, doi: 10.1371/JOURNAL.PCBI.1008023.

[46]   K. A. Sathi and M. K. Hosain, "Modeling and simulation of deep brain stimulation electrodes with various active contacts," *Res. Biomed. Eng. 2020 362*, vol. 36, no. 2, pp. 147–161, Apr. 2020, doi: 10.1007/S42600-020-00060-0.

[47]   M. CC and F. TJ, "Computational modeling of deep brain stimulation," *Handb. Clin. Neurol.*, vol. 116, pp. 55–61, 2013, doi: 10.1016/B978-0-444-53497-2.00005-X.

[48]   T. D. Sanger, "A Computational Model of Deep-Brain Stimulation for Acquired Dystonia in Children," *Front. Comput. Neurosci.*, vol. 12, p. 77, Sep. 2018, doi: 10.3389/FNCOM.2018.00077.

[49]   A. Singh, "Oscillatory activity in the cortico-basal ganglia-thalamic neural circuits in Parkinson's disease," *Eur. J. Neurosci.*, vol. 48, no. 8, pp. 2869–2878, Oct. 2018, doi: 10.1111/ejn.13853.

[50]   B. C. M. van Wijk *et al.*, "Subthalamic nucleus phase-amplitude coupling correlates with motor impairment in Parkinson's disease," *Clin. Neurophysiol.*, vol. 127, no. 4, pp. 2010–2019,

Apr. 2016, doi: 10.1016/j.clinph.2016.01.015.

[51]   C. Hamani, J. A. Saint-Cyr, J. Fraser, M. Kaplitt, and A. M. Lozano, "The subthalamic nucleus in the context of movement disorders," *Brain*, vol. 127, no. 1, pp. 4–20, 2004, doi: 10.1093/brain/awh029.

[52]   A. Blenkinsop, S. Anderson, and K. Gurney, "Frequency and function in the basal ganglia: the origins of beta and gamma band activity," *J. Physiol.*, vol. 595, no. 13, pp. 4525–4548, Jul. 2017, doi: 10.1113/JP273760.

[53]   C. J. Lobb, "Abnormal Bursting as a Pathophysiological Mechanism in Parkinson'sDisease," *Basal Ganglia*, vol. 3, no. 4, p. 187, Apr. 2014, doi: 10.1016/J.BAGA.2013.11.002.

[54]   M. M. McGregor and A. B. Nelson, "Circuit Mechanisms of Parkinson's Disease," *Neuron*, vol. 101, no. 6, pp. 1042–1056, Mar. 2019, doi: 10.1016/J.NEURON.2019.03.004.

[55]   H. W. Berendse and C. J. Stam, "Stage-dependent patterns of disturbed neural synchrony in Parkinson's disease," *Park. Relat. Disord.*, 2007, doi: 10.1016/S1353-8020(08)70046-4.

[56]   P. J. Uhlhaas *et al.*, "Neural synchrony in cortical networks: History, concept and current status," *Front. Integr. Neurosci.*, vol. 3, no. JUL, Jul. 2009, doi: 10.3389/neuro.07.017.2009.

[57]   M. J. Rozenberg, O. Schneegans, and P. Stoliar, "An ultra-compact leaky-integrate-and-fire model for building spiking neural networks," *Sci. Rep.*, vol. 9, no. 1, p. 11123, Jul. 2019, doi: 10.1038/s41598-019-47348-5.

[58]   C. Teeter *et al.*, "Generalized leaky integrate-and-fire models classify multiple neuron types," *Nat. Commun.*, vol. 9, no. 709, pp. 1–15, 2018, doi: 10.1038/s41467-017-02717-4.

[59]   A. N. Burkitt, "A review of the integrate-and-fire neuron model: I. Homogeneous synaptic input," *Biol Cybern*, vol. 95, pp. 1–19, 2006, doi: 10.1007/s00422-006-0068-6.

[60]   R. Jolivet, T. J. Lewis, and W. Gerstner, "Generalized integrate-and-fire models of neuronal activity approximate spike trains of a detailed model to a high degree of accuracy," *J. Neurophysiol.*, vol. 92, no. 2, pp. 959–976, Aug. 2004, doi: 10.1152/jn.00190.2004.

[61]   Z. Zhu, R. Wang, and F. Zhu, "The energy coding of a structural neural network based on the Hodgkin-Huxley model," *Front. Neurosci.*, vol. 12, no. MAR, pp. 1–16, 2018, doi: 10.3389/fnins.2018.00122.

[62]   G. Drion, T. O'Leary, J. Dethier, A. Franci, and R. Sepulchre, "Neuronal behaviors: A control perspective," *Proc. IEEE Conf. Decis. Control*, vol. 54rd IEEE, no. June 2016, pp. 1923–1944, 2015, doi: 10.1109/CDC.2015.7402491.

[63]   G. J. Kress and S. Mennerick, "Action potential initiation and propagation: Upstream influences on neurotransmission," *Neuroscience*, vol. 158, no. 1. pp. 211–222, Jan. 12, 2009. doi: 10.1016/j.neuroscience.2008.03.021.

[64]   C. H. Fry and R. I. Jabr, "The action potential and nervous conduction," *Surgery*. 2010. doi: 10.1016/j.mpsur.2009.12.001.

[65]   A. Mandali, M. Rengaswamy, V. Srinivasa Chakravarthy, and A. A. Moustafa, "A spiking Basal

Ganglia model of synchrony, exploration and decision making," *Front. Neurosci.*, vol. 9, no. MAY, p. 191, May 2015, doi: 10.3389/fnins.2015.00191.

[66]   H. Bergman, T. Wichmann, B. Karmon, and M. R. Delong, "The Primate Subthalamic Nucleus. II. Neuronal Activity in the MPTP Model of Parkinsonism," 1994.

[67]   W. Rall, "Time Constants and Electrotonic Length of Membrane Cylinders and Neurons," *Biophys. J.*, vol. 9, no. 12, p. 1483, 1969, doi: 10.1016/S0006-3495(69)86467-2.

[68]   S. Tripathy and R. Gerkin, "NeuroElectro: organizing information on cellular neurophysiology. University of British Columbia and Arizona State University. V-5.0." https://www.neuroelectro.org/

[69]   D. Joel and I. Weiner, "The connections of the primate subthalamic nucleus: indirect pathways and the open-interconnected scheme of basal ganglia-thalamocortical circuitry," *Brain Res. Rev.*, vol. 23, pp. 62–78, 1997.

[70]   T. Wichmann and M. R. DeLong, "Oscillations in the basal ganglia," *Nat. 1999 4006745*, vol. 400, no. 6745, pp. 621–622, Aug. 1999, doi: 10.1038/23148.

[71]   N. Maling and C. McIntyre, "Local Field Potential Analysis for Closed-Loop Neuromodulation," *Closed Loop Neurosci.*, pp. 67–80, Jan. 2016, doi: 10.1016/B978-0-12-802452-2.00005-6.

[72]   K. Otomo, J. Perkins, A. Kulkarni, S. Stojanovic, J. Roeper, and C. A. Paladini, "In vivo patch-clamp recordings reveal distinct subthreshold signatures and threshold dynamics of midbrain dopamine neurons," *Nat. Commun. 2020 111*, vol. 11, no. 1, pp. 1–15, Dec. 2020, doi: 10.1038/s41467-020-20041-2.

[73]   J. K. H. Tang *et al.*, "Firing rates of pallidal neurons are similar in Huntington's and Parkinson's disease patients," *Exp. brain Res.*, vol. 166, no. 2, pp. 230–236, Oct. 2005, doi: 10.1007/S00221-005-2359-X.

[74]   M. Filion and L. Tremblay, "Abnormal spontaneous activity of globus pallidus neurons in monkeys with MPTP-induced parkinsonism," *BRES 16533 Brain Res.*, vol. 547, pp. 142–157, 1991.

[75]   A. Benazzouz, S. Breit, A. Koudsie, P. Pollak, P. Krack, and A. L. Benabid, "Intraoperative microrecordings of the subthalamic nucleus in Parkinson's disease," *Mov. Disord.*, vol. 17 Suppl 3, no. SUPPL. 3, 2002, doi: 10.1002/MDS.10156.

[76]   B. D. Bennett and C. J. Wilson, "Spontaneous activity of neostriatal cholinergic interneurons in vitro," *J. Neurosci.*, vol. 19, no. 13, pp. 5586–5596, Jul. 1999, doi: 10.1523/JNEUROSCI.19-13-05586.1999.

[77]   J. Zhang, G. S. Russo, K. Mewes, D. B. Rye, and J. L. Vitek, "Lesions in monkey globus pallidus externus exacerbate parkinsonian symptoms," *Exp. Neurol.*, vol. 199, no. 2, pp. 446–453, Jun. 2006, doi: 10.1016/J.EXPNEUROL.2006.01.006.

[78]   M. Magnin, A. Morel, and D. Jeanmonod, "Single-unit analysis of the pallidum, thalamus and subthalamic nucleus in parkinsonian patients," *Neuroscience*, vol. 96, no. 3, pp. 549–564, Mar. 2000, doi: 10.1016/S0306-4522(99)00583-7.

[79] T. Heida, R. Moroney, E. Marani, and K. G. Usunoff, "Modeling and simulation of deep brain stimulation in Parkinson's disease," pp. 62–120, Mar. 2009, doi: 10.4018/978-1-60566-280-0.CH003.

[80] H. Kita, A. Nambu, K. Kaneda, Y. Tachibana, and M. Takada, "Role of ionotropic glutamatergic and GABAergic inputs on the firing activity of neurons in the external pallidum in awake monkeys," *J. Neurophysiol.*, vol. 92, no. 5, pp. 3069–3084, Nov. 2004, doi: 10.1152/JN.00346.2004.

[81] F. Syeda and N. Engineering, "Development of Novel Models to Study Deep Brain Effects of Cortical Transcranial Magnetic Stimulation," 2018.

[82] L. Logiaco, L. F. Abbott, and S. Escola, "Thalamic control of cortical dynamics in a model of flexible motor sequencing," *Cell Rep.*, vol. 35, no. 9, p. 109090, Jun. 2021, doi: 10.1016/J.CELREP.2021.109090.

[83] A. Nair, A. Razi, S. Gregory, R. B. Rutledge, G. Rees, and S. J. Tabrizi, "Imbalanced basal ganglia connectivity is associated with motor deficits and apathy in Huntington's disease," *Brain*, vol. 145, no. 3, p. 991, Mar. 2022, doi: 10.1093/BRAIN/AWAB367.

[84] P. Chen *et al.*, "Abnormal Effective Connectivity of the Anterior Forebrain Regions in Disorders of Consciousness", doi: 10.1007/s12264-018-0250-6.

[85] F. Nieuwhof *et al.*, "Cerebello-thalamic activity drives an abnormal motor network into dystonic tremor," *medRxiv*, p. 2021.11.03.21265803, Nov. 2021, doi: 10.1101/2021.11.03.21265803.

[86] D. Bernal-Casas, H. J. Lee, A. J. Weitz, and J. H. Lee, "Studying brain circuit function with dynamic causal modeling for optogenetic fMRI," *Neuron*, vol. 93, no. 3, p. 522, Feb. 2017, doi: 10.1016/J.NEURON.2016.12.035.

[87] C. Liu *et al.*, "Neural Network-Based Closed-Loop Deep Brain Stimulation for Modulation of Pathological Oscillation in Parkinson's Disease," *IEEE Access*, vol. 8, pp. 161067–161079, 2020, doi: 10.1109/ACCESS.2020.3020429.

[88] B. C. Schwab, T. Heida, Y. Zhao, E. Marani, S. A. van Gils, and R. J. A. van Wezel, "Synchrony in Parkinson's disease: Importance of intrinsic properties of the external globus pallidus," *Front. Syst. Neurosci.*, vol. 7, no. OCT, p. 60, Oct. 2013, doi: 10.3389/FNSYS.2013.00060/BIBTEX.

[89] N. C. Swann, C. De Hemptinne, A. R. Aron, J. L. Ostrem, R. T. Knight, and P. A. Starr, "Elevated Synchrony in Parkinson's Disease Detected with Electroencephalography," *Ann. Neurol.*, vol. 78, no. 5, p. 742, Nov. 2015, doi: 10.1002/ANA.24507.

[90] J. A. Goldberg, T. Boraud, S. Maraton, S. N. Haber, E. Vaadia, and H. Bergman, "Enhanced synchrony among primary motor cortex neurons in the 1-methyl-4-phenyl-1,2,3,6-tetrahydropyridine primate model of Parkinson's disease," *J. Neurosci.*, vol. 22, no. 11, pp. 4639–4653, Jun. 2002, doi: 10.1523/JNEUROSCI.22-11-04639.2002.

[91] M. Paap *et al.*, "Deep brain stimulation by optimized stimulators in a phenotypic model of dystonia: Effects of different frequencies," *Neurobiol. Dis.*, vol. 147, p. 105163, Jan. 2021, doi:

10.1016/J.NBD.2020.105163.

[92]   H. Yu, K. Takahashi, L. Bloom, S. D. Quaynor, and T. Xie, "Effect of Deep Brain Stimulation on Swallowing Function: A Systematic Review," *Front. Neurol.*, vol. 11, Jul. 2020, doi: 10.3389/FNEUR.2020.00547.

[93]   C. J. Hartmann, S. Fliegen, S. J. Groiss, L. Wojtecki, and A. Schnitzler, "An update on best practice of deep brain stimulation in Parkinson's disease.," *Ther. Adv. Neurol. Disord.*, vol. 12, p. 1756286419838096, Mar. 2019, doi: 10.1177/1756286419838096.

[94]   D. Su *et al.*, "Frequency-dependent effects of subthalamic deep brain stimulation on motor symptoms in Parkinson's disease: a meta-analysis of controlled trials," *Sci. Rep.*, vol. 8, no. 1, Dec. 2018, doi: 10.1038/S41598-018-32161-3.

[95]   J. A. Karl, B. Ouyang, and L. Verhagen Metman, "A Novel Dual-Frequency Deep Brain Stimulation Paradigm for Parkinson's Disease," *Neurol. Ther.*, vol. 8, no. 2, pp. 483–489, Dec. 2019, doi: 10.1007/S40120-019-0140-5/TABLES/2.

[96]   B. D, L. J, and P. D, "Strength-duration relationship for extracellular neural stimulation: numerical and analytical models," *J. Neurophysiol.*, vol. 104, no. 4, pp. 2236–2248, Oct. 2010, doi: 10.1152/JN.00343.2010.

[97]   H. Bostock, "The strength-duration relationship for excitation of myelinated nerve: computed dependence on membrane parameters.," *J. Physiol.*, vol. 341, no. 1, p. 59, Aug. 1983, doi: 10.1113/JPHYSIOL.1983.SP014792.

[98]   C. J. Anderson, D. N. Anderson, S. M. Pulst, C. R. Butson, and A. D. Dorval, "Neural Selectivity, Efficiency, and Dose Equivalence in Deep Brain Stimulation through Pulse Width Tuning and Segmented Electrodes," *bioRxiv*, p. 613133, Apr. 2019, doi: 10.1101/613133.

[99]   N. Grossman *et al.*, "Noninvasive Deep Brain Stimulation via Temporally Interfering Electric Fields," *Cell*, vol. 169, no. 6, pp. 1029-1041.e16, 2017, doi: 10.1016/j.cell.2017.05.024.

[100]   C. Wang *et al.*, "Magnetically Induced Temporal Interference for Focal and Deep-Brain Stimulation," *Front. Hum. Neurosci. | www.frontiersin.org*, vol. 15, p. 693207, 2021, doi: 10.3389/fnhum.2021.693207.

[101]   K. LM, G. SM, T. DL, and P. AV, "Sound comparison of seven TMS coils at matched stimulation strength," *Brain Stimul.*, vol. 13, no. 3, pp. 873–880, May 2020, doi: 10.1016/J.BRS.2020.03.004.

[102]   C. Liu, H. Ding, X. Fang, Z. He, and Z. Wang, "Noise analysis and active noise control strategy of transcranial magnetic stimulation device," *AIP Adv.*, vol. 9, no. 8, p. 085010, Aug. 2019, doi: 10.1063/1.5115522.

[103]   P. AV, M. DL, and G. SM, "Quiet transcranial magnetic stimulation: Status and future directions," *Annu. Int. Conf. IEEE Eng. Med. Biol. Soc. IEEE Eng. Med. Biol. Soc. Annu. Int. Conf.*, vol. 2015, pp. 226–229, Nov. 2015, doi: 10.1109/EMBC.2015.7318341.

[104]   TDK, "Mn-Zn Ferrite - Material Characteristics," 2019. [Online]. Available: https://product.tdk.com/info/en/catalog/datasheets/ferrite_mn-

zn_material_characteristics_en.pdf

[105] I. P. de Sousa, C. R. H. Barbosa, and E. C. Monteiro, "Safe exposure distances for transcranial magnetic stimulation based on computer simulations," *PeerJ*, vol. 2018, no. 6, 2018, doi: 10.7717/peerj.5034.

[106] A. Zolj, "Electrically Small Dipole Antenna Probe for Quasi- static Electric Field Measurements," 2018.

[107] M. Gaidica, "Rat Brain Atlas." http://labs.gaidi.ca/rat-brain-atlas/ (accessed Oct. 12, 2020).

[108] George Paxinos and Charles Watson, "The Rat Brain in Stereotaxic Coordinates - 6th Edition," Feb. 2007. https://www.elsevier.com/books/the-rat-brain-in-stereotaxic-coordinates/paxinos/978-0-12-374121-9 (accessed Oct. 12, 2020).

[109] U. Gimsa *et al.*, "Optimizing a rodent model of parkinson's disease for exploring the effects and mechanisms of deep brain stimulation," *Parkinson's Disease*. 2011. doi: 10.4061/2011/414682.

[110] M. Alaverdashvili, M. J. Hackett, I. J. Pickering, and P. G. Paterson, "Laminar-specific distribution of zinc: Evidence for presence of layer IV in forelimb motor cortex in the rat," *Neuroimage*, vol. 103, pp. 502–510, Dec. 2014, doi: 10.1016/j.neuroimage.2014.08.046.

[111] X. Li, M. Aggarwal, J. Hsu, H. Jiang, and S. Mori, "AtlasGuide: Software for stereotaxic guidance using 3D CT/MRI hybrid atlases of developing mouse brains," *J. Neurosci. Methods*, vol. 220, no. 1, pp. 75–84, Oct. 2013, doi: 10.1016/j.jneumeth.2013.08.017.

[112] K. Fox, S. Greenhill, and A. de Haan, "Barrel Cortex as a Model System for Understanding the Molecular, Structural, and Functional Basis of Cortical Plasticity," in *Handbook of Behavioral Neuroscience*, vol. 28, Elsevier B.V., 2019, pp. 189–212. doi: 10.1016/B978-0-12-812028-6.00010-0.

[113] S. Ueno, T. Tashiro, and K. Harada, "Localized stimulation of neural tissues in the brain by means of a paired configuration of time-varying magnetic fields," *J. Appl. Phys.*, vol. 64, no. 10, pp. 5862–5864, 1988, doi: 10.1063/1.342181.

[114] J. O. Nieminen *et al.*, "Multi-locus transcranial magnetic stimulation system for electronically targeted brain stimulation," *bioRxiv*, p. 2021.09.20.461045, Sep. 2021, doi: 10.1101/2021.09.20.461045.

[115] I. C. Carmona, D. Kumbhare, M. S. Baron, and R. L. Hadimani, "Quintuple AISI 1010 carbon steel core coil for highly focused transcranial magnetic stimulation in small animals," *AIP Adv.*, vol. 11, no. 2, p. 025210, Feb. 2021, doi: 10.1063/9.0000219.

[116] Q. Xiao, Z. Zhong, X. Lai, and H. Qin, "A multiple modulation synthesis method with high spatial resolution for noninvasive neurostimulation," *PLoS One*, vol. 14, no. 6, Jun. 2019, doi: 10.1371/journal.pone.0218293.

[117] J. W. Middleton, A. Longtin, J. Benda, and L. Maler, "The cellular basis for parallel neural transmission of a high-frequency stimulus and its low-frequency envelope," *Proc. Natl. Acad. Sci. U. S. A.*, vol. 103, no. 39, pp. 14596–14601, Sep. 2006, doi: 10.1073/pnas.0604103103.

[118] C. Nimonkar, E. Knight, I. C. Carmona, and R. L. Hadimani, "Development of anatomically accurate brain model of small animals for experimental verification of transcranial magnetic stimulation," *IEEE Trans. Magn.*, 2021, doi: 10.1109/TMAG.2021.3104517.

[119] I. C. Carmona, O. F. Afuwape, D. C. Jiles, and R. L. Hadimani, "Estimation of the Focality of Coils and Quality of Stimulation of Biological Tissues During Transcranial Magnetic Stimulation," *IEEE Trans. Magn.*, 2021, doi: 10.1109/TMAG.2021.3082853.

[120] J. Boonzaier, P. I. Petrov, W. M. Otte, N. Smirnov, S. F. W. Neggers, and R. M. Dijkhuizen, "Design and Evaluation of a Rodent-Specific Transcranial Magnetic Stimulation Coil: An *In Silico* and *In Vivo* Validation Study," *Neuromodulation Technol. Neural Interface*, p. ner.13025, Jul. 2019, doi: 10.1111/ner.13025.

[121] R. Salvador and P. C. Miranda, "Transcranial magnetic stimulation of small animals: A modeling study of the influence of coil geometry, size and orientation," in *Proceedings of the 31st Annual International Conference of the IEEE Engineering in Medicine and Biology Society: Engineering the Future of Biomedicine, EMBC 2009*, 2009, pp. 674–677. doi: 10.1109/IEMBS.2009.5334070.

[122] K. R. Davey and M. Riehl, "Suppressing the surface field during transcranial magnetic stimulation," *IEEE Trans. Biomed. Eng.*, vol. 53, no. 2, pp. 190–194, Feb. 2006, doi: 10.1109/TBME.2005.862545.

[123] H. Magsood and R. L. Hadimani, "Development of anatomically accurate brain phantom for experimental validation of stimulation strengths during TMS," *Mater. Sci. Eng. C*, p. 111705, Nov. 2020, doi: 10.1016/j.msec.2020.111705.

[124] H. Magsood, F. Syeda, K. Holloway, I. C. Carmona, and R. L. Hadimani, "Safety Study of Combination Treatment: Deep Brain Stimulation and Transcranial Magnetic Stimulation," *Front. Hum. Neurosci.*, vol. 14, Apr. 2020, doi: 10.3389/fnhum.2020.00123.

[125] K. M. Chew, N. Seman, R. Sudirman, and C. Y. Yong, "A comparison of brain phantom relative permittivity with CST simulation library and existing research," in *Bio-Medical Materials and Engineering*, 2014, vol. 24, no. 6, pp. 2161–2167. doi: 10.3233/BME-141027.

[126] T. Wagner *et al.*, "Transcranial magnetic stimulation and brain atrophy: A computer-based human brain model study," *Exp. Brain Res.*, vol. 186, no. 4, pp. 539–550, Apr. 2008, doi: 10.1007/s00221-007-1258-8.

[127] T. Pokorny, D. Vrba, J. Tesarik, D. B. Rodrigues, and J. Vrba, "Anatomically and dielectrically realistic 2.5D 5-layer reconfigurable head phantom for testing microwave stroke detection and classification," *Int. J. Antennas Propag.*, vol. 2019, 2019, doi: 10.1155/2019/5459391.

[128] A. Thielscher and T. Kammer, "Electric field properties of two commercial figure-8 coils in TMS: Calculation of focality and efficiency," *Clin. Neurophysiol.*, 2004, doi: 10.1016/j.clinph.2004.02.019.

[129] P. Rastogi, E. G. Lee, R. L. Hadimani, and D. C. Jiles, "Transcranial Magnetic Stimulation-coil design with improved focality," *AIP Adv.*, vol. 7, no. 5, May 2017, doi: 10.1063/1.4973604.

[130] P. Rastogi, Y. Tang, B. Zhang, E. G. Lee, R. L. Hadimani, and D. C. Jiles, "Quadruple Butterfly Coil with Passive Magnetic Shielding for Focused Transcranial Magnetic Stimulation," *IEEE Trans. Magn.*, vol. 53, no. 11, Nov. 2017, doi: 10.1109/TMAG.2017.2711962.

APPENDICES

Appendix A – MATLAB Code for Simulation of the High-Frequency Neuromodulation System

```matlab
clear all,
close all,
clc;

load("W:\Hadimani Group\Ivan Carmona\Research\In-Progress Work\3 -
Neuromodulation\carrier.mat",'efield_t');

efield_t_c = efield_t;
clear efield_t;

% Preliminary Calculations:
% =========================

% Modulation Parameters:
% *************************************************************************
m = 1;%0              % AM modilation index
fc = 25500            % FM carrier frequency
fstim = 1500;         % Frequency of the rectified message
fm = fstim;%/2;       % Stimulation tone (message frequency)
% *************************************************************************


% Time vector and sampling rate:

Fs = 1000*fc               % sampling rate
tsim = 10E-3;              % simulation time
t = linspace(0,tsim,Fs+1); % time vector
dt = t(2)-t(1);            % differential of time
tplot = 3/fstim;

% Coil parameters:
% ----------------------------------------------------
N = 20      % number of turns
l = 10E-3;  % length

uo = 4*pi*1E-7;
ur = 12;
% ur = 778.4936;

% Area = 7.42E-6; %equvalent area for the QCC
Area = pi*(1.5E-3)^2;

L_calculated = uo*ur*(N^2)*Area/l
% L = L_calculated;
L = 5E-6;

% B-H curve:
load('W:\Hadimani Group\Ivan Carmona\Research\In-Progress Work\3 -
Neuromodulation\BH_steel_1010.mat');
% ----------------------------------------------------

% Target area:
% r = 0.5E-3; %radious of the targeted area
% r = 1E-3; %radious of the targeted area
r = sqrt(Area/pi);
% r = 5E-3;
% ----------------------------------------------------

% Efield desired in the targeted area:
Etarget = 100 %V/m


% *************************************************************************
% *************************************************************************
%                 VOLTAGE SHAPING (dV/dt(FM PRE-MODULATED))
% *************************************************************************
```

```matlab
% *************************************************************************
% -------------------------------------------------------------------------

% Output voltage from the stimulator:
Vstim = 1*cos(2*pi*fc*t).*(1+cos(2*pi*fm*t));        % below the saturation point
% Vstim = (2/1.5)*0.2*Etarget*cos(2*pi*fc*t).*(1+cos(2*pi*fm*t)); % in the saturation point
% Vstim = (3/1.5)*0.2*Etarget*cos(2*pi*fc*t).*(1+cos(2*pi*fm*t)); % % above the saturation point
% Vstim = (5/1.5)*0.2*Etarget*cos(2*pi*fc*t).*(1+cos(2*pi*fm*t)); % % above the saturation point

% % Magnitude of the Output Voltage:
Vstim_mag = max(abs(Vstim));
Vstim_rms = rms(Vstim);


% Fourier Transform of the AM Output Voltage Signal:
[V_AM_ORIG,f_vect_AM_ORIG] = get_FFT(Vstim,length(Vstim),Fs/max(t),'um');


% FIGURE 2:
% =========
figure,
subplot(3,1,1),
plot(t,Vstim,'k');
title('Amplitude Modulated Voltage (Stimulator Output)');
ylabel('Voltage (V)');
xlabel('Time (sec)');
axis([0 tplot -1.1*abs(min(Vstim)) 1.1*max(Vstim)]);

subplot(3,1,2),
stem(f_vect_AM_ORIG,V_AM_ORIG,'k','Marker','.','LineWidth',1.5);
title('Spectrum of Magnitudes of the Original AM Voltage Signal');
xlabel('Frequency (Hz)');
ylabel('Voltage (V)');
axis([0 500E3 0 1.1*max(V_AM_ORIG)]);

subplot(3,1,3),
stem(f_vect_AM_ORIG,V_AM_ORIG,'k','Marker','.','LineWidth',1.5);
title('Spectrum of Magnitudes of the Original AM Voltage Signal');
xlabel('Frequency (Hz)');
ylabel('Voltage (V)');
axis([0 3500 0 1.1*max(V_AM_ORIG)]);

% *************************************************************************
% *************************************************************************
%                      PULSE WIDTH MODULATION (PWM)
% *************************************************************************
% *************************************************************************

fpwm = 13*fc;

pwm_c = sawtooth(2*pi*fpwm*t,0.5);

% VDC = 52.9423;
VDC = 40;

pwm = VDC * (2*( Vstim >= pwm_c)-1);

figure,
subplot(3,1,1),
plot(t,pwm,'b');
title('PWM Voltage');
ylabel('Voltage (V)');
xlabel('Time (sec)');
axis([0 tplot -1.1*abs(min(pwm)) 1.1*max(pwm)]);

[PWM,f_PWM] = get_FFT(pwm,length(pwm),Fs/max(t),'um');

subplot(3,1,2),
plot(f_PWM,PWM,'b');
title('PWM Spectrum');
ylabel('Voltage (V)');
xlabel('Frequency (Hz)');
axis([0 5E6 0 1.1*max(PWM)]);
```

```matlab
subplot(3,1,3),
plot(f_PWM,PWM,'b');
title('PWM Spectrum');
ylabel('Voltage (V)');
xlabel('Frequency (Hz)');
axis([0 50E3 0 1.1*max(PWM)]);




% ****************************************************************************
% ****************************************************************************
%                         CURRENT IN THE COIL
% ****************************************************************************
% ****************************************************************************


Vstim = pwm;

int_V_dt = zeros(1,length(Vstim));

for(a=1:length(Vstim)-1)
    int_V_dt(a+1) = int_V_dt(a) + 0.5*(Vstim(a)+Vstim(a+1))*dt;
end

Istim = (1/L)*int_V_dt;   %Current in the coil

Istim = Istim *8.48;
% Istim = Istim - mean(Istim); %Eliminating any existing DC level

% Fourier Transform of the Current Through the Coil:
[I,f_vect_I] = get_FFT(Istim,length(Istim),Fs/max(t),'um');

Istim_mag = mean(I)*length(I);
Istim_rms = rms(Istim);

% FIGURE 3:
% =========
figure,
subplot(3,1,1),
plot(t,Istim,'g');
title('Current Through the Coil');
ylabel('Current (A)');
xlabel('Time (sec)');
axis([0 tplot -1.1*abs(min(Istim)) 1.1*max(Istim)]);

subplot(3,1,2),
stem(f_vect_I,I,'g','Marker','.','LineWidth',1.5);
title('Spectrum of Magnitudes of the Current Through the Coil');
xlabel('Frequency (Hz)');
ylabel('Current (A)');
axis([0 500E3 0 1.1*max(I)]);

subplot(3,1,3),
stem(f_vect_I,I,'g','Marker','.','LineWidth',1.5);
title('Spectrum of Magnitudes of the Current Through the Coil');
xlabel('Frequency (Hz)');
ylabel('Current (A)');
axis([0 3500 0 1.1*max(I)]);




% ****************************************************************************
% ****************************************************************************
%                 MAGNETIC FLUX DENSITY IN THE TARGET (Bt)
% ****************************************************************************
% ****************************************************************************


Ht = N*Istim/l;
Ht_pos = Ht.*(Ht>=0);
Ht_neg = Ht.*(Ht<0);
Bt_pos = BH_cfit(Ht_pos)';
Bt_neg = -BH_cfit(-Ht_neg)';
Bt = Bt_pos + Bt_neg;
```

```
Bt = uo*ur*Ht;

Btsat = sign(Bt).*2.*(abs(Bt)>=2);
Btnonsat = Bt.*(abs(Bt)<2);

Bt = Btnonsat + Btsat;



[max_Bt I_max_Bt] = max(Bt);
ur_max = (Bt(I_max_Bt) / Ht(I_max_Bt))/(4*pi*1E-7);

% Fourier Transform of the Current Through the Coil:
[Bfreq,f_vect_B] = get_FFT(Bt,length(Bt),Fs/max(t),'um');

P_Bt_mag = mean(Bfreq.^2)*length(Bfreq);


% FIGURE 4:
% =========
figure,
subplot(3,1,1),
plot(t,Bt,'k');
title('Magnetic Flux Density in the Targeted Plane');
ylabel('Magnetic Flux Density (T)');
xlabel('Time (sec)');
axis([0 tplot -1.1*abs(min((Bt))) 1.1*max(Bt)]);

subplot(3,1,2),
stem(f_vect_B,Bfreq,'k','Marker','.','LineWidth',1.5);
title('Spectrum of Magnitudes of the Magnetic Flux Density');
xlabel('Frequency (Hz)');
ylabel('Magnetic Flux Density  (T)');
axis([0 500E3 0 1.1*max(Bfreq)]);

subplot(3,1,3),
stem(f_vect_B,Bfreq,'k','Marker','.','LineWidth',1.5);
title('Spectrum of Magnitudes of the Magnetic Flux Density');
xlabel('Frequency (Hz)');
ylabel('Magnetic Flux Density  (T)');
axis([0 3500 0 1.1*max(Bfreq)]);


% ************************************************************************
% ************************************************************************
%                    ELECTRIC FIELD IN THE TIP (E-field)
% ************************************************************************
% ************************************************************************

% Time derivative of the magnetic flux:
dB_dt = [0 diff(Bt)/dt];

% Electric field in the tip:
efield_t = (1/2)*r*dB_dt; % E-field induced at the plane z=0

% Fourier Transform of the Derivative of the Original FM Voltage Signal:
[EFIELD,f_vect_EFIELD] = get_FFT(efield_t,length(efield_t),Fs/max(t),'um');

E_25_5_kHz = EFIELD(256)

efield_t_mag = mean(EFIELD)*length(EFIELD)

% FIGURE 5:
% =========
figure,
subplot(3,1,1),
plot(t,efield_t,'r');
title('Electric Field in the Target');
ylabel('Electric Field (V/m)');
xlabel('Time (sec)');
axis([0 3/fstim -1.1*abs(min(efield_t)) 1.1*max(efield_t)]);
```

```matlab
subplot(3,1,2),
stem(f_vect_EFIELD,EFIELD,'r','Marker','.','LineWidth',1.5);
title('Spectrum of Magnitudes of the Electric Field');
xlabel('Frequency (Hz)');
ylabel('Electric Field (V/m)');
axis([0 500E3 0 1.1*max(EFIELD)]);

subplot(3,1,3),
stem(f_vect_EFIELD,EFIELD,'r','Marker','.','LineWidth',1.5);
title('Spectrum of Magnitudes of the Electric Field');
xlabel('Frequency (Hz)');
ylabel('Electric Field (V/m)');
f_zoom = 3000;
% UPPER_LIMIT = find( (f_vect_EFIELD >= f_zoom-5) & (f_vect_EFIELD <= f_zoom+5) );
% MAX_UPPER_LIMIT = max(EFIELD(1:UPPER_LIMIT));
% axis([0 f_zoom 0 1.1*MAX_UPPER_LIMIT]);
axis([0 f_zoom 0 1.1*max(EFIELD)]);

[yupper,ylower] = envelope(efield_t,2000,'peak');
rect_envt = yupper - mean(yupper);




% ************************************************************************
% ************************************************************************
%             LOW-PASS FILTERING REPRESENTING THE NEURON RESPONSE
% ************************************************************************
% ************************************************************************


% fcutoff = 3500;
%
% tao = 24.49E-3;
% fcutoff = 1/(2*pi*tao)
%
% [B,A] = butter(1,tsim*fcutoff/(Fs/2),'low');
%
% UGain = (3*Fs);
% impulse = [zeros(1,250000) 1];
% impulse = UGain*[impulse zeros(1,length(t)-length(impulse))];
%
% e_field_filt = filter(B,A,impulse);
%
% % Fourier Transform of the Impulsive Response of the Neuron (Frequency Response):
% [NEURON_RESP,f_vect_NEURON_RESP] = get_FFT(e_field_filt,length(e_field_filt),Fs/tsim,'um');
%
%
% % FIGURE 6:
% % =========
% figure,
% subplot(2,1,1),
% % stem(f_vect_NEURON_RESP,NEURON_RESP,'g','Marker','.','LineWidth',1.5);
% % hold on,
% plot(f_vect_NEURON_RESP,NEURON_RESP,'k','LineWidth',1.5);
% hold on,
% area(f_vect_NEURON_RESP,NEURON_RESP,'FaceColor','g');
% title('Low Pass Filter Representing the Frequency Response of Neurons');
% xlabel('Frequency (Hz)');
% ylabel('Gain');
% axis([0 1000 0 1.1*max(NEURON_RESP)]);
%
% subplot(2,1,2),
% % stem(f_vect_NEURON_RESP,NEURON_RESP,'g','Marker','.','LineWidth',1.5);
% % hold on,
% plot(f_vect_NEURON_RESP,NEURON_RESP,'k','LineWidth',1.5);
% hold on,
% area(f_vect_NEURON_RESP,NEURON_RESP,'FaceColor','g');
% title('Low Pass Filter Representing the Frequency Response of Neurons');
% xlabel('Frequency (Hz)');
% ylabel('Gain');
% axis([0 100 0 1.1*max(NEURON_RESP)]);
% ========================================================================
```

```
%
% =========================================================================

% e_field_filt = filter(B,A,(UGain/Fs)*efield_t);
%
% figure,
%
% subplot(3,1,1),
% plot(t,e_field_filt,'k');
% title('E-field Seen by the Neurons');
% xlabel('Time (sec)');
% ylabel('Electric Field (V/m)');
% axis([0 3/fstim -1.1*abs(min(rect_envt)) 1.1*max(rect_envt)]);
%
% [E_FIELD_FILT,f_vect_E_FILT] = get_FFT(e_field_filt,length(e_field_filt),Fs/max(t),'um');
%
% E_FIELD_FILT = E_FIELD_FILT;
%
% subplot(3,1,2),
% plot(f_vect_E_FILT,E_FIELD_FILT,'k','Marker','.','LineWidth',1.5);
% title('Spectrum of Magnitudes of the E-field Seen by the Neurons');
% xlabel('Frequency (Hz)');
% ylabel('Electric Field (V/m)');
% axis([0 500E3 0 1.1*max(E_FIELD_FILT)]);
%
% subplot(3,1,3),
% plot(f_vect_E_FILT,E_FIELD_FILT,'k','Marker','.','LineWidth',1.5);
% title('Spectrum of Magnitudes of the E-field Seen by the Neurons');
% xlabel('Frequency (Hz)');
% ylabel('Electric Field (V/m)');
% f_zoom = 3000;
% % UPPER_LIMIT = find( (f_vect_env >= f_zoom-5) & (f_vect_env <= f_zoom+5) );
% % MAX_UPPER_LIMIT = max(RECT_ENV(1:UPPER_LIMIT));
% % axis([0 f_zoom 0 1.1*MAX_UPPER_LIMIT]);
% axis([0 f_zoom 0 1.1*max(E_FIELD_FILT)]);
%
% % [E_max_upto_3500Hz,i] = max(EFIELD_NEURON(1:(3500/f_vect_EFIELD_NEURON(2))+1));
% [E_max_upto_3500Hz,i] = max(E_FIELD_FILT);
% fmax = f_vect_E_FILT(i)
%
%
% % Vstim = efield_t;
% % =====================================================================

r
fc
fstim
% Vstim_mag
Vstim_rms

% Istim_mag
Istim_rms

P_Bt_mag
% E_max_upto_3500Hz = round(E_max_upto_3500Hz,2)

E_theoretical = pi*r*fc*max(Bfreq)

error = 100*(E_theoretical - max(EFIELD)) / E_theoretical

Etarget = max(EFIELD) *exp(-4.25E-3/((0.03)/5))
```

Appendix B – Polarization Modes Using *Space-varying E-field Vector Modulation*

Note 1: In all the following tables, the use of "1" and "-1" indicates the polarization of the coils with the maximum current, which will depend on the setup and specific application. The "+" and "-"signs indicate a phase shifting of 180 degrees in the sinusoidal waveform. This means that when one coil reaches the positive maximum (for instance, 5 kA), the other one should reach a minimum (i.e., -5 kA). "0" indicates a coil turned-off. However, the system has been thought to work with multi-level DC power source when possible, which should also allow obtaining variable amplitude AC currents using a standard H-bridge configurations for the power electronics. This should allow adjusting the current as an independent variable. However, this can also be done with time switching if a multi- level system is not available in the H-bridge.

Table XVII - Polarization Patterns for Blue Zones

Note 2: These patterns require the addition of coils 1' to 6'. They could be physically connected –or not– to the same port as coils 1 to 6, but this configuration requires additional switching devices to disconnect the one petal and connect the other one (e.g., connect coil 1' and disconnect 1, and vice-versa).

#	Zone to be Stimulated	E-field Direction	Coil 1' (T1)	Coil 1 (T2)	Coil 2' (T1)	Coil 2 (T2)	Coil 3' (T1)	Coil 3 (T2)	Coil 4' (T1)	Coil 4 (T2)	Coil 5' (T1)	Coil 5 (T2)	Coil 6' (T1)	Coil 6 (T2)	Coil 0 (T1)	Coil 0 (T2)
67	A	↗	1	0	0	0	0	0	0	0	0	0	0	0	-1	1
68	A	↙	-1	0	0	0	0	0	0	0	0	0	0	0	1	-1
69	C	↘	0	0	1	0	0	0	0	0	0	0	0	0	-1	1
70	C	↖	0	0	-1	0	0	0	0	0	0	0	0	0	1	-1
71	E	↓	0	0	0	0	1	0	0	0	0	0	0	0	-1	1
72	E	↑	0	0	0	0	-1	0	0	0	0	0	0	0	1	-1
73	G	↙	0	0	0	0	0	0	1	0	0	0	0	0	-1	1
74	G	↗	0	0	0	0	0	0	-1	0	0	0	0	0	1	-1
75	I	↖	0	0	0	0	0	0	0	0	1	-1	0	0	-1	1
76	I	↘	0	0	0	0	0	0	0	0	-1	1	0	0	1	-1
77	K	↑	0	0	0	0	0	0	0	0	0	0	1	-1	-1	1
78	K	↓	0	0	0	0	0	0	0	0	0	0	-1	1	1	-1
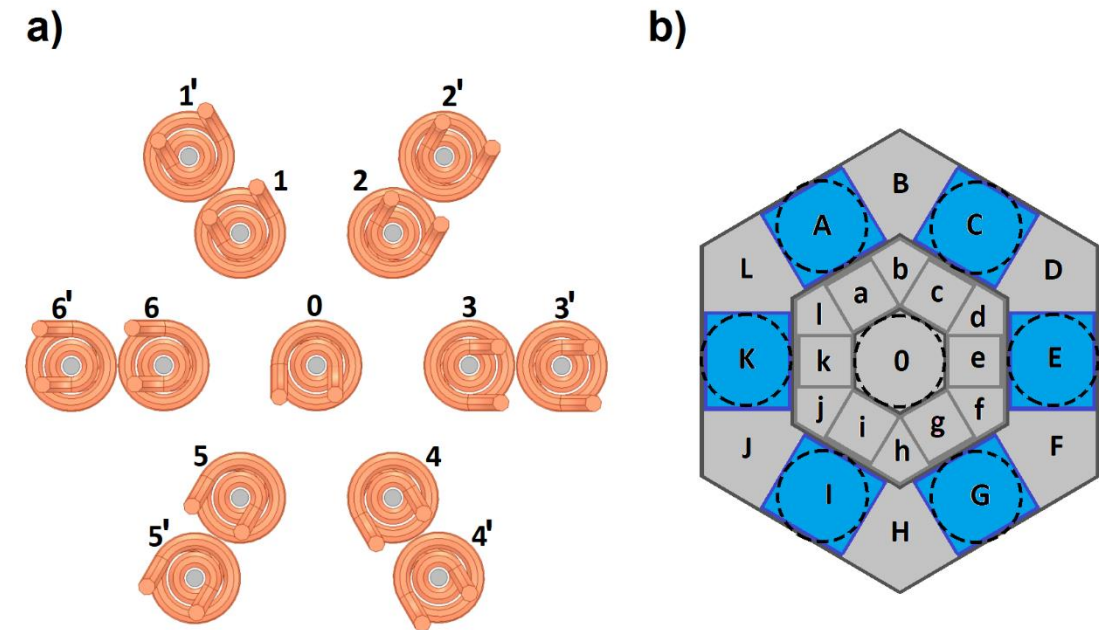
Note 3: A very large number of other patterns can be obtained with the combined polarization of the different coils and the use of direct patterns or time-switched patterns in different periods. However, due to the extensive set of combinations, we show the basic patterns to be produced in the coverage area for a wide range of usability. Other patterns are in study and in publication process. Nevertheless, any pattern that can be produced with this *Figure-of-Flower coil* (*FFC*) and *Space-varying E-Field Vector Modulation* method (*SVEVM*), though not studied yet, is consider to be part of this invention, being an inherent capability of the system and operation mode. That includes variations in amplitude, frequency, phase and waveforms of the feeding currents in the coils.

Table XVIII - Polarization Patterns for Green and Pink Zones

DIRECT STIMULATION PATTERNS									
#	Zone to be Stimulated (target	E-field Direction	Coil 1	Coil 2	Coil 3	Coil 4	Coil 5	Coil 6	Coil 0
1	B	↑	1	-1	0	0	0	0	0
2	B	↓	-1	1	0	0	0	0	0
3	D	↗	0	1	-1	0	0	0	0
4	D	↙	0	-1	1	0	0	0	0
5	F	↘	0	0	1	-1	0	0	0
6	F	↖	0	0	-1	1	0	0	0
7	H	↓	0	0	0	1	-1	0	0
8	H	↑	0	0	0	-1	1	0	0
9	J	↙	0	0	0	0	1	-1	0
10	J	↗	0	0	0	0	-1	1	0
11	L	↖	-1	0	0	0	0	1	0
12	L	↘	1	0	0	0	0	-1	0
13	a	↗	1	0	0	0	0	0	-1
14	a	↙	-1	0	0	0	0	0	1
15	c	↘	0	1	0	0	0	0	-1
16	c	↖	0	-1	0	0	0	0	1
17	e	↓	0	0	1	0	0	0	-1
18	e	↑	0	0	-1	0	0	0	1
19	g	↙	0	0	0	1	0	0	-1
20	g	↗	0	0	0	-1	0	0	1
21	i	↖	0	0	0	0	1	0	-1
22	i	↘	0	0	0	0	-1	0	1
23	k	↑	0	0	0	0	0	1	-1
24	k	↓	0	0	0	0	0	-1	1

Table XIX - Polarization Patterns for Purple Zones

DIRECT STIMULATION PATTERNS (...continuation)									
#	Zone to be Stimulated (target	E-field Direction	Coil 1	Coil 2	Coil 3	Coil 4	Coil 5	Coil 6	Coil 0
25	b	→	1	1	0	0	0	0	-1
26		←	-1	-1	0	0	0	0	1
27		↘	1	-1	0	0	0	0	1
28		↖	-1	1	0	0	0	0	-1
29		↙	-1	1	0	0	0	0	1
30		↗	1	-1	0	0	0	0	-1
31	d	↘	0	1	1	0	0	0	-1
32		↖	0	-1	-1	0	0	0	1
33		←	0	-1	1	0	0	0	1
34		→	0	1	-1	0	0	0	-1
35		↗	0	1	-1	0	0	0	1
36		↙	0	-1	1	0	0	0	-1
37	f	↙	0	0	1	1	0	0	-1
38		↗	0	0	-1	-1	0	0	1
39		←	0	0	-1	1	0	0	-1
40		→	0	0	1	-1	0	0	1
41		↖	0	0	-1	1	0	0	1
42		↘	0	0	1	-1	0	0	-1
43	h	←	0	0	0	1	1	0	-1
44		→	0	0	0	-1	-1	0	1
45		↖	0	0	0	-1	1	0	-1
46		↘	0	0	0	1	-1	0	1
47		↗	0	0	0	-1	1	0	1
48		↙	0	0	0	1	-1	0	-1
49	j	↖	0	0	0	0	1	1	-1
50		↘	0	0	0	0	-1	-1	1
51		→	0	0	0	0	1	-1	1
52		←	0	0	0	0	-1	1	-1
53		↙	0	0	0	0	1	-1	1
54		↗	0	0	0	0	-1	1	-1
55	l	↗	1	0	0	0	0	1	-1
56		↙	-1	0	0	0	0	-1	1
57		→	1	0	0	0	0	-1	-1
58		←	-1	0	0	0	0	1	1
59		↘	1	0	0	0	0	-1	1
60		↖	-1	0	0	0	0	1	-1
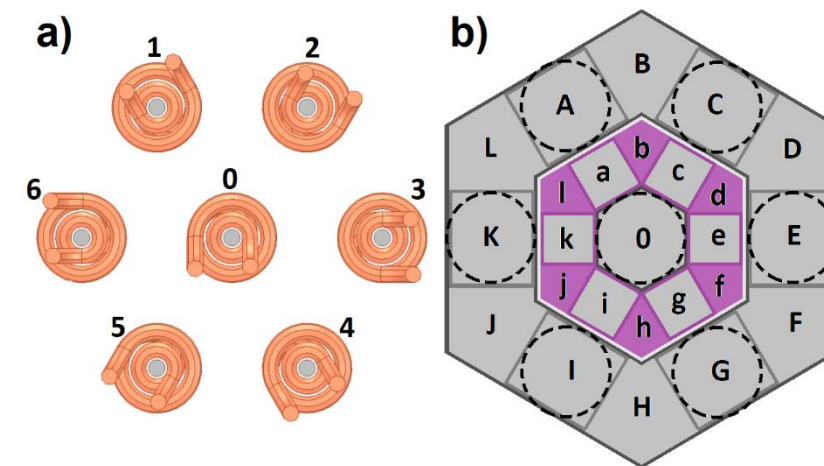
Table XX - Polarization Patterns for Yellow Zone

Note 4: The following patterns are time-switched in intervals T1 and T2 to produce an average E-field. T1 + T2 create a total period T, which should be the reciprocal of the high-frequency current or carrier used to modulate the stimulating signal (T = 1/f_H). Then, the ratios T1/T and T2/T determines the weight of each pattern in the final pattern. Most of the time T1 can be equal to T2 (i.e. case 61 to 66). However, for other cases in which the pattern in T2 aims to attenuate the *E*-field in and area produced in T1, in order to make it focal (i.e. case 67 to 78), T1 and T2 can be manipulated and made different to control the final location of the hotspot and magnitude of the E-field.

		INDIRECT SWITCHED STIMULATION PATTERNS (TIME-AVERAGED)													
#	Zone to be Stimulated (target	Average E-field Direction Toward (x)	Coil 1		Coil 2		Coil 3		Coil 4		Coil 5		Coil 6		Coil 0	
			T1	T2	T1	T2	T1	T2	T1	T2	T1	T2	T1	T2	T1	T2
61	0	↗(c)	1	0	-1	1	0	-1	-1	0	1	-1	0	1	0	0
62	0	→(e)	0	1	1	0	-1	1	0	-1	-1	0	1	-1	0	0
63	0	↘(g)	1	-1	0	1	1	0	-1	1	0	-1	-1	0	0	0
64	0	(i)↙	-1	0	1	-1	0	1	1	0	-1	1	0	-1	0	0
65	0	(k)←	0	-1	-1	0	1	-1	0	1	1	0	-1	1	0	0
66	0	(a)↖	-1	1	0	-1	-1	0	1	-1	0	1	1	0	0	0

a)

b)